université
PARIS-SACLAY

Leibniz
Universität
Hannover

Theoretical study of quantum gas experiments in an Earth-orbiting research laboratory

Étude théorique d'expériences de gaz quantiques dans un laboratoire en orbite terrestre

Thèse de doctorat de l'université Paris-Saclay et de l'université Leibniz Universität Hannover

École doctorale n° 572 : Ondes et Matière (EDOM)
Spécialité de doctorat : Physique Quantique
Graduate School : Physique. Référent : Faculté des sciences d'Orsay

Thèse préparée dans l'unité de recherche **Institut des Sciences Moléculaires d'Orsay (ISMO)** (Université Paris-Saclay, CNRS), sous la direction d' **Éric Charron**, Professeur, et dans l'unité de recherche **Institut für Quantenoptik** (Leibniz Universität Hannover) sous la co-direction de **Ernst M. Rasel**, Professeur, le co-encadrement de **Naceur Gaaloul**, Group leader

Thèse soutenue à Hanovre, le 01 Mars 2024, par

Annie PICHERY

Composition du jury
Membres du jury avec voix délibérative

Elina FUCHS Professeur, Leibniz Universität Hannover	Présidente
Baptiste BATTELIER Ingénieur de recherche, Université de Bordeaux	Rapporteur & Examinateur
Nick PROUKAKIS Professeur, Newcastle University	Rapporteur
Klemens HAMMERER Professeur, Leibniz Universität Hannover	Examinateur
Goulven QUÉMÉNER Chargé de recherche CNRS, Université Paris-Saclay	Examinateur

Theoretical study of quantum gas experiments in an Earth-orbiting research laboratory

Von der QUEST-Leibniz-Forschungsschule

der Gottfried Wilhelm Leibniz Universität Hannover

zur Erlangung des Grades

Doktorin der Naturwissenschaften
Dr. rer. nat.

genehmigte Dissertation von

M. Sc. Annie Pichery

2024

Title : Theoretical study of quantum gas experiments in an Earth-orbiting research laboratory

Keywords : Bose-Einstein condensate, quantum-degenerate mixtures, microgravity

Abstract : One of the major goals of fundamental physics is to unify general relativity, which describes macroscopic phenomena driven by the influence of gravity, with quantum mechanics, which focuses on effects at microscopic scales. Ensembles of cold atoms, as massive quantum objects, lie at the crossroads of both theories and appear as a test object of choice. They can be used to test theories that postulate a violation of Einstein's Equivalence Principles, in particular a violation of the Universality of Free Fall (UFF).

Recent proposals suggest using mixtures of Bose-Einstein condensates (BEC) as sources for precision atom interferometry to perform UFF. These have the potential to match the precision of the best tests with classical test masses performed during the MICROSCOPE mission, and may even provide better results in the long term. The realization of experiments in microgravity, where atoms can float for long periods of time, allows longer interrogation times, thus increasing the performance of matter-wave sensors. To optimize the implementation of UFF tests, one needs exquisite control of the atoms due to stringent requirements on the error budget. In this work, we focus on the design of the input state with control over the position and velocity of the atom clouds, as well as their size evolution.

The experiments studied here are designed with atom chip setups that manipulate atoms with magnetic traps. Most of the applications presented are experiments performed in the NASA Cold Atom Laboratory (CAL) aboard the International Space Station as part of the Consortium for Ultracold Atoms in Space (CUAS). This multi-user BEC machine allows the manipulation of single species BEC at its installation as well as dual species mixtures after upgrades. Following this chronology, we first study the dynamics of single species BEC and then extend the work to the manipulation of an interacting mixture of two BECs. The first step after calibrating the chip model is to design a fast and robust transport protocol to move the atoms away from the atom chip. We present and use a Shortcut-To-Adiabaticity (STA) protocol, based on reverse engineering, to transport the BEC and meet the requirements of position control at the sub-μm level and velocity control at the hundreds of μm/s level. The free expansion of the atom cloud with its inherent atomic density drop makes signal detection difficult. By analogy with light, it is possible to collimate the atom cloud with atomic lenses using the Delta-Kick Collimation (DKC) technique. Application to CAL resulted in expansion energies in the tens of pK level. To simulate the imaging process and to support the data analysis, theoretical models are presented that take into account the resolution effects of the camera and the frame transformations associated with the orientation of the camera or the orientation of the trapping potential with respect to the atom chip.

Space allows the operation of Bose-Einstein condensate mixtures under miscibility conditions not possible on the ground. The colocation of the trap center for the different species in microgravity can lead to different topologies of the trap ground state. Moreover, the interaction energy between the species, which is almost negligible in the ground state, plays a significant role in the dynamics of the mixture during its transport. However, the simulation of the dynamics of interacting dual-species BEC mixtures is computationally challenging, particularly due to the long expansion times. In this work, scaling techniques to overcome these limitations are presented and illustrated in the case of space experiments in CAL and aboard sounding rockets. Such scaled-grid approaches make it possible to simulate long transports with free expansion times on the order of seconds, which would not be feasible with a fixed-grid approach on reasonable time scales, not to mention the problems of memory usage.

ÉCOLE DOCTORALE
Ondes et matière
(EDOM)

Leibniz
Universität
Hannover

Titre : Étude théorique d'expériences de gaz quantiques dans un laboratoire en orbite terrestre

Mots clés : Condenstat de Bose-Einstein, mélanges dégénérés quantiques, microgravité

Résumé : Un des principaux objectifs de la physique fondamentale est d'unifier la relativité générale, qui décrit les phénomènes macroscopiques régis par l'influence de la gravité, à la mécanique quantique, qui se concentre sur les effets à l'échelle microscopique. Les ensembles d'atomes froids, en tant qu'objets massifs quantiques, se trouvent au croisement de ces deux théories et paraissent comme des sujets de tests idéaux. Ils peuvent être utilisés pour tester des théories qui postulent une violation des principes d'équivalence d'Einstein et en particulier une violation de l'universalité de la chute libre (UFF).

Des propositions récentes suggèrent d'utiliser des mélanges de condensats de Bose-Einstein (BEC) comme sources d'interféromètres atomiques de précision pour implémenter des tests UFF. Ces expériences ont le potentiel d'atteindre et même de dépasser la précision des meilleurs tests réalisés avec des masses classiques durant la mission MICROSCOPE. L'exécution d'expériences en microgravité permet des temps d'interrogation plus longs, améliorant par conséquent les performances des capteurs à ondes de matière. Pour optimiser l'implémentation des tests UFF, il est nécessaire d'avoir un contrôle parfait des atomes dû aux exigences strictes sur le budget d'erreurs. Dans ce travail, nous nous concentrons sur la conception d'états d'entrée avec un contrôle en position et vitesse des nuages d'atomes, ainsi que leurs évolutions en taille.

Les expériences étudiées ici sont conçues avec des montages avec puce atomique qui manipulent les atomes à l'aide de pièges magnétiques. La plupart des applications présentées sont des expériences réalisées dans le Cold Atom Laboratory (CAL) de la NASA à bord de la Station Spatiale Internationale dans le cadre du Consortium for Ultracold Atoms in Space. Cette machine à BEC multi-utilisateur permet la manipulation de BEC simple-espèce à son installation ainsi que celle de mélanges de BEC double-espèces après des améliorations. En suivant cette chronologie, nous étudions d'abord la dynamique de BEC simple-espèce puis étendons ce travail à la manipulation d'un mélange de deux BECs en interaction. La première étape après la calibration du modèle à puce est de concevoir un transport rapide et robuste pour éloigner les atomes de la puce. Nous présentons et utilisons un protocole de raccourci à l'adiabaticité sur la base de rétro-ingénierie, pour transporter le BEC et atteindre les exigences sur le contrôle de la position et vitesse finale. L'expansion libre du nuage atomique avec la chute inhérente de densité rend la détection du signal difficile. Par analogie avec la lumière, il est possible de collimater le nuage atomique avec une lentille atomique à l'aide de la technique de Delta-Kick Collimation. Les applications à CAL ont abouti à des énergies d'expansion de l'ordre de la dizaine de pK. Pour simuler le processus d'imagerie et soutenir l'analyse de données, des modèles théoriques qui prennent en compte les effets de résolution de la caméra et les changements de repères associés à l'orientation de la caméra ou l'orientation du potentiel de piégeage par rapport à la puce atomique sont présentés.

L'espace permet la manipulation de mélanges de condensats de Bose-Einstein sous des conditions de miscibilité impossibles à obtenir au sol. La colocation des centres des pièges pour les différentes espèces en microgravité peut mener à des topologies différentes de l'état fondamental du piège. De plus, l'énergie d'interaction entre les espèces peut jouer un rôle significatif dans la dynamique du mélange lors de son transport. Cependant, la simulation de la dynamique de mélanges de BEC double-espèces en interaction est un défi sur le plan des ressources informatiques, surtout à cause des longues durées d'expansion. Dans ce travail, des méthodes de mise à l'échelle pour dépasser ces limitations sont présentées et illustrées dans des cas d'expériences dans l'espace dans CAL et à bord de fusées-sondes.

Titel : Theoretische Untersuchung von Quantengasexperimenten in einem Forschungslabor in der Erdumlaufbaum

Schlagwörter : Bose-Einstein Kondensate, quantentartete Mischungen, Mikrogravitation

Zusammenfassung : Eines der wichtigsten Ziele der Grundlagenphysik ist die Vereinheitlichung der allgemeinen Relativitätstheorie, die makroskopische Phänomene unter dem Einfluss der Schwerkraft beschreibt, mit der Quantenmechanik, die sich auf mikroskopische Effekte konzentriert. Als massive Quantenobjekte scheinen kalte Atome prädestinierte Testobjekte an der Schnittstelle beider Theorien zu sein. So können atomare Ensembles benutzt werden, um die Universalität des freien Falls (UFF) zu testen und somit Theorien zu überprüfen, die eine Verletzung des Einstein'schen Äquivalenzprinzips postulieren.

Es gibt aktuell Vorschläge, Mischungen aus Bose-Einstein Kondensaten (BEC) als Quellen für präzise Atominterferometrie-Tests zu verwenden. Diese haben das Potenzial, mit der Präzision der besten Tests mit klassischen Testmassen im Rahmen der MICROSCOPE-Mission gleichzuziehen, und könnten langfristig sogar bessere Ergebnisse liefern. Die Realisierung derartiger Experimente in Mikrogravitation verspricht längere Abfragezeiten und erhöht damit die Performance der Materiewellensensoren. Zur Optimierung dieser UFF-Tests ist aufgrund der strengen Anforderungen an die Fehlerbudgets eine präzise Kontrolle der Atome erforderlich. In dieser Arbeit konzentrieren wir uns auf die Präparation des initialen Zustands mittels der Kontrolle über die Position und Geschwindigkeit der Atomwolken sowie deren Expansionsverhalten.

Die in dieser Arbeit untersuchten Experimente nutzen Atomchips, die die Atome mittels magnetischer Fallen manipulieren. Die meisten Versuche wurden im NASA Cold Atom Laboratory an Bord der Internationalen Raumstation als Teil des Consortium for Ultracold Atoms in Space durchgeführt. Die sich dort befindliche Multi-User-BEC-Maschine erlaubt die Manipulation von Bose-Einstein Kondensaten (BEC) einer atomaren Spezies sowie nach Verbesserungen auch die Kontrolle von Mischungen aus zwei Spezies. Dieser Chronologie folgend untersuchen wir zuerst die Dynamik von Einzel-BECs und dann die Manipulation einer wechselwirkenden Mischung aus zwei BECs.

Im Anschluss an die Kalibrierung des Chipmodells besteht der erste Schritt darin, ein schnelles und robustes Protokoll zu entwerfen, um das atomare BEC vom Atomchip weg zu transportieren. Um dabei die Anforderungen an die Positionskontrolle und die Geschwindigkeitskontrolle zu erfüllen, stellen wir ein auf Reverse-Engineering basierendes Shortcut-To-Adiabaticity (STA)-Protokoll vor. Die freie Expansion der Atomwolke mit ihrem inhärenten Dichteabfall erschwert die Signaldetektion. Mittels der Delta-Kick-Kollimationstechnik ist es möglich, die Atomwolke mit atomaren Linsen in Analogie zu Lichtwellen zu kollimieren. Deren Anwendung im CAL-Experiment führte zu Expansionsenergien im zweistelligen pK-Bereich. Zur Simulation des Abbildungsprozesses und zur Unterstützung der experimentellen Datenanalyse stellen wir theoretische Modelle vor, die sowohl die Auflösungseffekte und Ausrichtung der Kamera, als auch die Ausrichtung des Fallenpotenzials in Bezug auf den Atomchip in der Bildtransformation berücksichtigen.

Schwerelosigkeit ermöglicht spezielle Eigenschaften für Mischungen aus Bose-Einstein Kondensaten, die unter Gravitation nicht realisierbar sind. Die räumliche Übereinstimmung des Fallenzentrums für die verschiedenen atomaren Spezies in Mikrogravitation kann beispielsweise zu unterschiedlichen Topologien des Fallengrundzustands führen. Außerdem spielt die Wechselwirkungsenergie zwischen den Spezies, die im Grundzustand nahezu vernachlässigbar ist, eine wichtige Rolle für die Dynamik der Mischung während des Transports. Die Simulation der Dynamik von wechselwirkenden BEC-Mischungen mit zwei Spezies ist mit großem numerischen Rechenaufwand verbunden, insbesondere aufgrund der langen Expansionszeiten. In dieser Arbeit werden Skalierungstechniken vorgestellt, um diese Einschränkungen zu überwinden. Ihre Anwendung wird anhand von Weltraumexperimenten in CAL und an Bord von Höhenforschungsraketen erläutert.

Acknowlegements

This section is the last one that I write in this manuscript and announces the end of my PhD project. I would like to take this opportunity to express my gratitude to all the people I interacted with during my journey. The different exchanges that we had made this experience unique and helped me realize what it means to be a PhD student and a member of a scientific community in a research laboratory.

First, I would like to thank my thesis directors Eric Charron and Ernst M. Rasel for giving me the chance to work on this joint PhD thesis between the universities in France and Germany. I would also like to thank Naceur Gaaloul, who supervised my work in the theoretical group in Hannover. They provided a great working environment to ensure that everything went well during this thesis. Eric and Naceur were always there to guide me on this journey, sharing their thoughts on our work, answering my interrogations when I was not quite sure about what I was doing. I learned many skills under their supervision, from programming to developing a physical model, as well as the art of making a scientific presentation. It was a great privilege to work with them on many stimulating projects, and their role was crucial to the success of this thesis.

I am very grateful to my referees Baptiste Battelier and Nick Proukakis, as well as my examiners Klemens Hammerer and Goulven Quéméner, and Elina Fuchs, who chaired the jury committee, for their time and engagement to my thesis. Their comments on the manuscript and questions offered very precious insights on the field of cold atoms physics.

I would like to thank the people with whom I interacted with as part of the DIRAM group in France, starting with the permanent members Annie Klisnick, Osman Atabek, Fabien Gatti, Denis Cubaynes, Danielle Dowek, Raluca Cireasa, Lionel Poisson, Lou Barreau, for their valuable advice and support, as well as the rich discussions that we had during lunch and other breaks. I would also like to thank my fellow PhD students, Robin Corgier, Jennifer Joseph, Sirine Amri, Samrit Mainali, Laila Dakroub, Lei Shi, Jean-Nicolas Vigneau, Timothé Estrampes, for the great time together in the lab and I enjoyed how we could discuss about anything at each opportunity that came by. I deeply thank Thomas Pino, the director of the institute, for all his advice and time, as he made sure that my thesis could be done in the best conditions.

I am very grateful to the members of the theory group in Hannover, the T-SQUAD. Our group now has a new name, "Theory of Quantum Sensing" and a new logo, but I think we will keep referring to ourselves as theory squad for a long time. I would like to thank the former and present members : Sina Loriani, Jan-Niclas Kirsten-Siemß, Florian Fitzek, Stefan Seckmeyer, Matthew Glaysher, Gabriel Müller, Christian Struckmann, Rui Li, Victor Martinez, Gina Kleinsteinberg, Matthieu Bruneau, Ashkan Alibabaei. Most of you were already around when I started my journey, forming a very stimulating environment, and it was great to integrate this group as it expanded. Thank you very much for the awesome time together, in and out of the lab. I could always count on you for your support when I had questions, be it on scientific topics or not. I would also like to thank specially Robin, for sharing his tips about the cotutelle between the two groups and for his guidance when I started this project, the transmission of his knowledge on the theoretical support of a cold atom experiment.

Financial support

x

Contents

Chapter 1

Introduction

Space is a very special environment which offers a variety of experimental conditions that are difficult to reproduce on Earth, such as extreme low scale energies or vanishing values of gravity. It can be considered as the best playground for microgravity experiments, where objects can float for long periods of time. It motivates countless technological developments to better understand the universe by studying the fundamental laws of physics.

The Universality of Free Fall (UFF) is one of the fundamental principles that has been tested in space, and each realization of its tests is making use of different capabilities provided by the environment. For example, the lunar atmosphere is similar to a vacuum chamber and was used during the Apollo-15 mission in 1971 to perform the Galileo experiment by dropping a hammer and a feather at the same time. The video recording of the drop shows that the two objects fall simultaneously. Another example is the MICROSCOPE mission on board an Earth-orbiting satellite, which realised tests of the UFF with different masses between 2016 and 2018. Taking advantage of the low-vibration environment, it measured the relative acceleration of the objects with state-of-the-art precision.

Ultra-cold atomic ensembles are a prime choice for sources in quantum sensing experiments. By sending them into space, we can study them for longer periods of time, increasing the precision of these sensors. This makes them ideal candidates for future UFF tests, where instead of measuring their acceleration directly by dropping them, we obtain it by measuring phase shifts in atom interferometry experiments.

In precision experiments, the initial state plays a crucial role. Indeed, the knowledge of the initial conditions, as well as of all the parameters that play a role during the experiment, makes it possible to retrace its history, to interpret the results, and to minimize errors. In this work, we focus on the preparation of the source for precision atom interferometry experiments by controlling the position, velocity and size dynamics of Bose-Einstein condensates.

1.1 . Interferometry and applications to fundamental physics

Interferometry is a measurement technique based on the interference phenomenon resulting from the superposition of two waves. An interferometer typically involves a coherent source that is
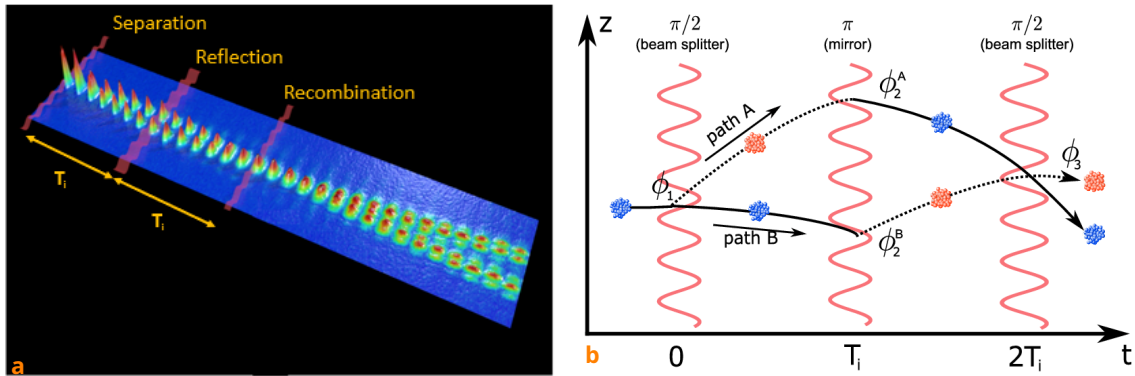
Figure 1.1 – Mach-Zehnder Interferometry with Cold Atoms. Panel **a** : Realisation of the experiment with a Bose-Einstein condensate source split and recombined with laser light beam-splitters by the QUANTUS collaboration in Germany. Panel **b** : Mach-Zehnder type atom interferometer sequence under the influence of gravity (figure taken from [9]).

split and then recombined. The waves involved take different paths and accumulate a phase difference that can be measured from the resulting interference fringes, from which we can extract information about the system. It can be used to reveal the quantum properties of an object. An emblematic experiment is Young's double-slit experiment, which demonstrated the wave nature of light. In 1927, Davisson and Germer published their work on experiments showing the diffraction pattern of electrons by a crystal of nickel metal [1, 2]. This adaptation of Young's double-slit experiment revealed the wave nature of electrons, confirming its wave-particle duality, and led to the attribution of the Nobel prize to Louis de Broglie in 1929 [3].

The first interferometers used light sources as they are easy to set up and manipulate. There are various configurations such as Fresnel mirrors, Fabry-Pérot interferometers, Michelson interferometers, Mach-Zehnder interferometers or Sagnac interferometers. The applications are also very diverse, ranging from industry, where it can be used for surface quality control, to fundamental physics. The Michelson and Morley interferometry experiments of 1887 [4], which had concluded on the constant speed of light, had a major impact in fundamental physics, being one of the elements that led to the theory of general relativity. Modern applications in fundamental physics using laser are dedicated to measuring phenomena with increased precision, such as LIGO for the detection of gravitational waves [5].

The wave-particle duality of quantum objects is not limited to light, and other objects can be used as sources for interferometry, such as atoms or ions. As with light, there are various types of matter-wave interferometers. However, as these quantum objects have mass, they are subject to the gravitational force. The first observation of a phase shift induced by gravity was made in a neutron interferometer, in the work of Colella, Overhauser and Werner published in 1975 [6]. Later the experiment was reproduced with different atomic species, for example with sodium atom interferometers [7], or with rubidium atom interferometers [8].

These gravimetry experiments use a Mach-Zehnder configuration, as shown in Figure 1.1. This

2
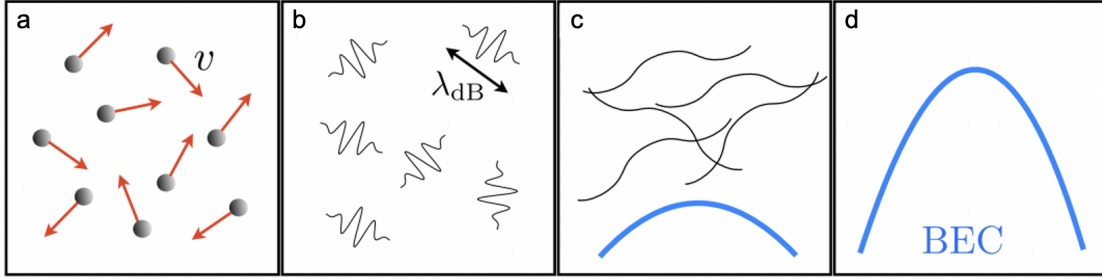
Figure 1.2 – Schematic description of the atomic Bose-Einstein condensation process. At high temperatures (panel **a**) atoms behave like particles and their dynamics can be described by kinetic theory. At low temperatures (panel **b**) atoms start to behave like waves and can be described by wave packets whose spatial extent is of the order of the de Broglie wavelength λ_{dB} of Eq. (1.2). At the critical temperature $T = T_C$ (panel **c**), the wave packets start to overlap and form a macroscopic quantum state. At zero temperature (panel **d**) the atoms form a coherent ensemble, the Bose-Einstein Condensate. Figure adapted from [15].

setup, which spatially splits the wave packets before recombining them, is very versatile. These atom interferometers use laser light to change the internal states and the momentum of the atoms, creating mirrors and beam splitters. As shown in the panel **b** of Figure 1.1, the atom clouds are separated, reflected and recombined by $(\pi/2; \pi; \pi/2)$ Raman or Bragg pulse sequences, which are separated by a duration T_i. The calculation of the gravitational phase shift can be realised using Feynman path integrals [10]. This phase shift ϕ is given by

$$\phi = k_{\text{eff}} \, g \, T_i^2 \tag{1.1}$$

where k_{eff} is the effective wave vector of the laser pulses, which is proportional to the momentum difference gained during the splitting, g is the gravitational acceleration, and T_i is the time between each interferometer pulse, also called the interrogation time.

To optimise the contrast of the fringes, it is important to ensure that the matter-wave source is coherent and that it has a long lifetime. Bose-Einstein Condensates (BEC) are therefore good candidates. BECs were first theorised in 1924 [11] by Satyendra Nath Bose and Albert Einstein, and the first experimental realisations in 1995 are the fruit of several experimental and theoretical developments as well as technical innovations [12–15]. It was rewarded by the attribution of the Nobel Prize in Physics in 2001.

The formation of a BEC by cooling a dilute atom gas can be summarized in a few steps as shown in Figure 1.2 [15]. At high temperatures, the atoms can be described as particles moving around at a certain velocity using kinetic theory. As the system temperature decreases, the atoms begin to exhibit wave-like behaviour, and can be described by wave packets of spacial extent of the order of the thermal de Broglie wavelength

$$\lambda_{dB} = \sqrt{\frac{2\pi\hbar^2}{mk_B T}}. \tag{1.2}$$

3

In this expression $\hbar$ is the reduced Planck constant and k_B the Boltzmann constant. The de Broglie wavelength thus depends on the atom mass m, and it increases when the temperature of the ensemble T decreases. At a certain critical temperature $T = T_C$, the average distance between the atoms is of the same order as the de Broglie wavelength, and their associated wave packets begin to overlap. At the same time, as the temperature decreases, the atoms start populating the lowest energy quantum state. Under such conditions, the atoms undergo a quantum mechanical phase transition and form a coherent macroscopic state, the Bose-Einstein condensate.

BEC sources are now a common choice in atom interferometry for high precision gravimetric measurements [16–18]. One application is to test the Universality of Free Fall (UFF), which postulates that two objects of different mass or composition experience the same acceleration when subjected to the same gravitational field. In the theory of general relativity [19], it corresponds to the Weak Equivalence Principle (WEP), which is the equivalence between the inertial mass and the gravitational mass. This principle, together with Local Lorentz Invariance (LLI) and Local Position Invariance (LPI), form Einstein's Equivalence Principles (EEP). These principles are a cornerstone of general relativity, but some theories attempting to unify general relativity and quantum mechanics predict a violation of these principles at some particular scale [20, 21]. To test the UFF, one can compare the acceleration of two test masses in free fall. For this we use the Eötvös coefficient η, defined by

$$\eta = \frac{|a_1 - a_2|}{(a_1 + a_2)/2} \tag{1.3}$$

where a_1 and a_2 are the accelerations of the two masses.

Tests of the UFF using classical test masses have been performed on Earth and in space [22]. One example is the torsion-balance experiment [23–25], which considers two objects of different composition connected by a rod or placed on a tray and suspended in a horizontal orientation by a fine wire. The measurement of the torque induced during the torsion yields measurements of the Eötvös coefficient at the level of 2×10^{-13} [26–28]. Another example is the Lunar Laser Ranging experiments, which use laser telemetry to measure the distance between the Earth and the Moon [29, 30]. The measurement of the Eötvös coefficient in these experiments is also on the order of 10^{-13} [31, 32]. The state-of-the-art measurement of the UFF test with classical test masses was conducted during the MICROSCOPE mission [33, 34]. This experiment measured the force required to keep two masses of different compositions (titanium and platinum alloys) in equilibrium on a quasi-circular trajectory around the Earth. The use of an orbiting satellite has removed many sources of systematic error from the measurement. The final data analysis shows the measurement of $\eta = [1.5 \pm 2.3(\text{stat}) \pm 1.5(\text{syst})] \times 10^{-15}$. By quadratically combining the stochastic error (*i.e.*, the statistical error) and the systematic errors, there is no EEP violation at the level of $[\sigma_{\text{stat}}^2 + \sigma_{\text{syst}}^2]^{\frac{1}{2}} = 2.7 \times 10^{-15}$ [34].

Using cold atoms for UFF tests imposes many constraints on the experimental setup [35]. It is necessary to perform simultaneous interferometry experiments with the two atomic sources so that they are subjected to the same conditions during the experiment. This requires exquisite control of the interactions between the two components, as well as different sources of error. The state-of-the-art measurements were performed with cold atom clouds of ^{85}Rb and ^{87}Rb in a 10 m fountain, resulting in a measurement of $\eta = 1.6 \pm 1.8(stat) \pm 3.4(syst) \times 10^{-12}$ [36]. This shows that quantum

Figure 1.3 – Different platforms for experiments in microgravity. From left to right : Zero-g plane (credits ESA), Bremen ZARM drop tower (credits ZARM), MAIUS-1 sounding rocket (credits DLR), International Space Station (credits NASA), HiTech building of the University of Hannover with the Einstein elevator highlighted (credits LUH).

tests of the weak equivalence principle are consistent with the observation of no violation at the level of 10^{-12}. This also demonstrates the potential of cold atom sources, more specifically in our case the potential of BECs, to provide results with uncertainties of a similar order of magnitude to classical tests, and which may improve further in the longer term. For instance, the STE-QUEST proposal for experiments aboard an Earth-orbiting satellite [17] aims to reach a precision of 10^{-17} in an UFF test using dual-species interferometry with ^{87}Rb and ^{41}K condensates.

1.2 . Microgravity, an ideal environment for cold atom experiments

The resolution of the acceleration measurement with atom interferometry is related to that of the measured phase of Eq. (1.1) according to

$$\frac{\delta g}{g} = \frac{\delta \phi}{\phi} \ . \tag{1.4}$$

Therefore, it is desirable to maximize the value of the measured phase. Since $\phi = k_{\text{eff}} \, g \, T_i^2$, the first solution is to increase the momentum transferred by the lasers in the beam-splitting phase. This requires high laser powers in specific experimental setups. It is the strategy adopted in the Large Momentum Transfer (LMT) interferometers [37–39] that can be applied to inertial sensing and gravitational wave detection.

The second solution is to increase the interrogation time T_i. In the case of the 10 m fountain of Ref. [36], the total interrogation time is $2T_i = 1.91\,$s. Using a longer baseline is technically complex and restricts the location of the setup. There are plans to use long baselines from 10 m up to 100 m in the Matter-wave Atomic Gradiometer Interferometric Sensor (MAGIS) project in the USA [5] and even up to 1 km in the Atom Interferometric Observatory and Network (AION) project in the UK [40].

Microgravity appears as the best answer to increase the interrogation time, since in microgravity atoms float for extended times. Several microgravity platforms are currently in use, as shown in Figure 1.3. These platforms make it possible to study certain physical phenomena on time scales that are not accessible in the presence of the gravitational sag. This is the case, for example, with the

creation of perfect BEC bubbles or BEC mixtures that share a co-localized magnetic trap centre [41]. On Earth, this is achieved by dropping the entire experimental setup in free fall, so that the frame associated with the setup is in microgravity. It can be done, for example, in a zero-g plane executing parabolic flights, which is the case of the ICE experiment [42]. Another example is to build a structure high enough to provide adequate free fall time, which is the purpose of a drop tower. The ZARM drop tower has a drop height of 110 m, providing 4.7 s of free fall for experiments, which can be extended to 9 s in a catapult mode at a rate of 3 drops per day. The QUANTUS collaboration is one of the users of this tower [43–46]. To achieve higher repetition rates, other structures have been built, such as the Einstein elevator from the Hannover Institute of Technology (HITec) at the Leibniz University of Hannover, Germany [47].

Microgravity can also be achieved by launching the experimental setup directly into space [48]. The MAIUS collaboration launched its experiment on the MAIUS-1 sounding rocket in 2017. This rocket provided 6 minutes of microgravity, enough time to carry out 110 experiments, including the first realization of a BEC in space [49] and the first interferometry experiments in space [50]. The International Space Station (ISS) has been hosting orbiting experiments with the Cold Atom Laboratory (CAL) since 2018 [51–53]. In the near future, the STE-QUEST project also plans to conduct cold atom experiments with UFF tests on board Earth-orbiting satellites [17, 54].

Each platform has its own advantages and disadvantages that must be considered. In practical terms, it can be, for example, the ease or difficulty of accessing the setup to make adjustments or replace various parts when necessary. The repetition rate and the vibration levels can also be limiting factors. However, most of the setups share the same issue of weight and volume constraints, especially when the experiments have to be launched into space. This has led to the development of compact setups using atom chips to trap and manipulate the atoms in many projects such as QUANTUS, MAIUS or CAL mentioned above.

1.3 . The Cold Atom Laboratory, one of the coolest spots in the Universe

The Cold Atom Laboratory (CAL) is a NASA multi-user facility launched to the International Space Station (ISS) on May 21, 2018. It is installed on the US Destiny Module and it is operated on ground by the Jet Propulsion Laboratory (JPL) in Pasadena, California, USA. The project website [55] provides information and news to the scientific community and to the general public. One of the objectives presented to the general public is to become the coolest spot in the universe by producing and manipulating BECs. This machine enables various types of cold atom experiments for the different consortia involved in the project (more details can be found in the introduction of Chapter 3). Figure 1.4 illustrates the fruitful cooperation between astronauts and JPL ground crews during the installation and upgrades of the machine. It was an opportunity to test new communication tools developed to facilitate the work of astronauts, with for example the test of augmented reality (AR) headsets during the upgrade of the machine shown in Figure 1.4**d**. On a daily basis, the machine is fully remote-controlled by the JPL operator team on ground. Regular meetings between the research teams and the operator team determine the experiments to be realized.

Figure 1.4 – The Cold Atom Laboratory aboard the ISS. Panel **a** : CAL in the US module Destiny. Panel **b** and **c** : Astronaut Christina Koch welcoming the SM3 module aboard the ISS during the week of December 9, 2019, and installing it in January 2020. Panel **d** : Astronaut Megan McArthur using augmented reality headsets to upgrade the SM3 module in July 2021. (Credits ESA and NASA).

The first module installed on CAL was the Science Module 2 (SM2), which was launched in May 2018. It produced the first in-orbit BECs in July 2018 [51] and was operational for scientific investigations in October 2018. This module was able to implement experiments with ^{87}Rb BECs. The SM2 module was later replaced by the SM3 module, which was launched in December 2019 and installed in January 2020. This new module enables the realisation of atom interferometry. In July 2020, the SM3 module was upgraded to enable dual species experiments with the possibility of condensing ^{39}K and ^{41}K atoms.

This manuscript presents results investigated by the Consortium for Ultra-cold Atoms in Space (CUAS), led by Nick Bigelow from the University of Rochester, New York in the USA. The consortium proposal, developed in 2016, included several types of experiments : the implementation of a space atom laser, the control of quantum gases and mixtures, and atom interferometry. As part of the consortium, my main contribution was the simulation of the dynamics of single species BECs and dual-species BEC mixtures to control the evolution of their size and position. This work also involved data analysis of the images obtained from the experiments.

1.4 . Quantum engineering and simulations at the service of experiments

Experiments require careful preparation with a detailed sequence plan, especially in cases where the number of measurements that can be realized is limited, as in the case of the MAIUS-1 mission, where the total available experiment duration is only 6 minutes [49]. To achieve the best performance during the experimental campaigns, very robust models of the system and a well defined experimental strategy are required. Theoretical simulations provide insight into the dynamics of the cold atoms, and data analysis from the experiments allows to gauge the models. In this context, exchanges between experience and theory are not only fruitful, they are absolutely necessary. In our case, the simulations are based on an atom chip model for the magnetic traps induced by the different current drivers of the setup, and we need their characteristics such as the orientation of the trap eigenaxes, the position of the trap minimum, and the trapping frequencies.

Once the model is calibrated, the scientific investigation can start. In the case of an atom interferometry experiment, there are several steps to consider : source preparation, wave packet splitting, recombination and detection. During my Ph.D. project, I focused on the first steps, which are the displacement of the BEC to bring it to the expected position of the beam-splitting laser beam, and on the collimation of the BEC size expansion. Most of the simulations that I performed were dedicated to applications on the CAL machine. User time on the CAL machine is shared among the different consortia, and the number of experiments that can be realized is limited, fluctuating between 100 and 200 runs per week, depending on the active period. This has an impact on the number of parameters scanned, for example to design a complete transport sequence.

In atom chip experiments, the final evaporation trap of the BEC is very close to the atom chip. Since the atom cloud is very dense, in-situ imaging is not possible. In addition, during its expansion, atoms can collide with the atom chip, and the wires on the chip structure can heat up the atom cloud, reducing its lifetime. Therefore, almost all experiments start with a transport to move the BEC away from the chip. Moreover, constraints on the system, which will be discussed later in the text, impose a non-adiabatic transport. To simulate the dynamics of the BEC during the sequence, we can lean on textbooks and a large scientific literature (*e.g.* [56–58]). However, there are no generic experimental sequences designed to engineer the optimal transport adapted to the situation. The methods to transport a BEC in experiments have been extensively studied in atom optics after the first experimental realizations, and have evolved with the technical advances as shown in Ref. [59], which shows the evolution of the use of wires from atom guides to the creation of a BEC with an atom chip. Methods used to transport atoms or ions can also be applied to BECs, such as the use of optical tweezers [60] or moving lattices [61]. With atom chips, we can directly transport the atoms by moving the minimum of the trapping potential by modulating the currents in the different structures involved in the setup. In my work, I considered the Shortcut-to-Adiabaticity method using reverse-engineering to implement the transport sequence [62, 63].

1.5 . Thesis outline

The guiding objective of my Ph.D. project is the engineering of an optimal BEC source for a dual species atom interferometry experiment in space. Most of the simulations performed were dedicated to the CAL experiments in the frame of the CUAS consortium. The upgrades of the machine from ^{87}Rb condensate experiments to dual mixtures of ^{41}K and ^{87}Rb condensates, led to the development of a new simulation method allowing the treatment of multi-species mixture dynamics. This simulation method was also applied to dual-species mixture experiments from the MAIUS collaboration.

Chapter 2 presents different simulation tools to study single species BEC experiments in the case of an atom chip setup. It defines some ingredients for the gauging process of the model, for example to extract information about the centre of mass evolution or the trapping frequency. It then presents methods used to control the position and size evolution of the BEC. It also presents some aspects of the imaging process that need to be considered in order to reconcile the simulation results with the experimental data.

Chapter 3 corresponds to applications of the different models presented in the previous chapter to experiments in microgravity realized with the Cold Atom Laboratory on board the International Space Station. It follows the investigations of the CUAS consortium with the SM2 module in order to implement a fast and controlled transport of a BEC, as well as the control of the size evolution of the BEC after such a transport.

Chapter 4 is dedicated to the study of interacting BEC mixtures. It consists of two main parts : The first one presents the simulation models and a grid scaling method developed for an efficient description of the dynamics of BEC mixtures, and The second part shows the numerical and experimental applications to BEC mixtures of K and Rb atoms. These applications include results from experiments performed with the CAL SM3 module.

Chapter 5 concludes my work with a summary of the different chapters and presents some future prospects.

Finally, I would like to point out that the work presented in this thesis has resulted in contributions to the following peer-reviewed journal articles [1] :

— Ref. [52] : Naceur Gaaloul, Matthias Meister, Robin Corgier, **Annie Pichery**, Patrick Boegel, Waldemar Herr, Holger Ahlers, Eric Charron, Jason R. Williams, Robert J. Thompson, Wolfgang P. Schleich, Ernst M. Rasel, and Nicholas P. Bigelow, "A space-based quantum gas laboratory at picokelvin energy scales", *Nature Communications*, **13**, 7889 (2022).

— Ref. [64] : **Annie Pichery**, Matthias Meister, Baptist Piest, Jonas Böhm, Ernst Maria Rasel, Eric Charron, and Naceur Gaaloul, "Efficient numerical description of the dynamics of interacting multispecies quantum gases", AVS Quantum Science **5**, 044401 (2023).

---

1. Some results concerning the simulations and data analysis are developed in more details in Chapters 3 and 4, as indicated in the introduction of each chapter.

— Ref. [53] : Ethan R. Elliott, David C. Aveline, Nicholas P. Bigelow, Patrick Boegel, Sofia Botsi, Eric Charron, José P. D'Incao, Peter Engels, Timothé Estrampes, Naceur Gaaloul, James R. Kellogg, James M. Kohel, Norman E. Lay, Nathan Lundblad, Matthias Meister, Maren E. Mossman, Gabriel Müller, Holger Müller, Kamal Oudrhiri, Leah E. Phillips, **Annie Pichery**, Ernst M. Rasel, Charles A. Sackett, Matteo Sbroscia, Wolfgang P. Schleich, Robert J. Thompson, and Jason R. Williams, "Quantum Gas Mixtures and Dual-Species Atom Interferometry in Space", *Nature,* **623**, 502-508 (2023).

— Ref. [65] : Jason R. Williams, Charles A. Sackett, Holger Ahlers, David C. Aveline, Patrick Boegel, Sofia Botsi, Eric Charron, Ethan R. Elliott, Naceur Gaaloul, Enno Giese, Waldemar Herr, James M. Kohel, Matthias Meister, Gabriel Müller, Holger Müller, Kamal Oudrhiri, Leah Phillips, **Annie Pichery**, Ernst M. Rasel, Albert Roura, Matteo Sbroscia, Wolfgang P. Schleich, Christian Schneider, Christian Schubert, Bejoy Sen, Robert J. Thompson, and Nicholas P. Bigelow, "Interferometry of Atomic Matter-Waves in a Cold Atom Lab onboard the International Space Station", arXiv:2402.14685 (2024).

2 Manipulation of BEC with an atom chip

2.1 . Introduction

Since the experimental realisation of the first Bose-Einstein Condensates (BEC) [12, 13], there has been a wealth of applications in theoretical and experimental studies. In our work, we focus on their use in quantum metrology, exploiting the coherence properties of BECs for atom interferometry experiments performed on ground and in space.

Many types of theoretical work can be done around cold atom experiments. For example, it can be the modeling of an experimental sequence to check its feasibility and to evaluate the physical quantities whose measurement is of interest. It can also be a kind of detective work, trying to trace the process leading to the measured data. For this purpose, a constant exchange with experimentalists is essential, since the comparison with experimental results allows to refine the models and to better understand the system under study. In this context, one of the main objectives of my thesis was to obtain a good agreement between the simulation results and their experimental realisation, thus allowing us to better understand and control the dynamics of these atomic ensembles, while validating the different theoretical approaches we had chosen.

Chapter outline

In this chapter, I present the theoretical tools that I developed and used during my thesis to design experimental sequences, to simulate them, and to analyse the experimental results. First, a brief overview of atom chip experiments is given in Section 2.2 with the modeling of the trapping potential used to manipulate the atoms. The next section 2.3 introduces the Shortcut-to-Adiabaticity (STA) method, which allows a fast and controlled transport of a BEC. Section 2.4 focuses on the study of the centre-of-mass motion of the BEC and on its use for characterising the system. Section 2.5 introduces the Delta-Kick Collimation (DKC) method, that I use to control the size evolution of the BEC during its free expansion. The following section 2.6 presents a scaling method that is useful for simulating the size evolution of the atom clouds during their dynamics. Finally, the sections 2.7 and 2.8 deal with some aspects of the BEC imaging process and analysis, such as the orientation of the camera or the rotation of the trapping potential.
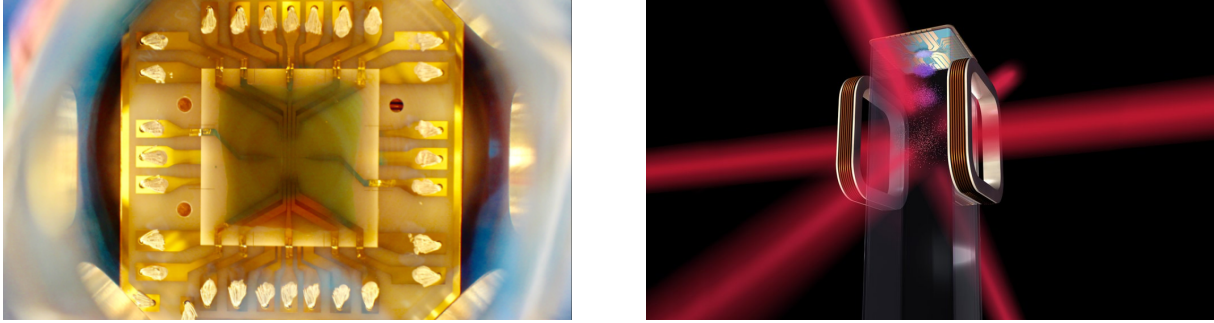
Figure 2.1 – Atom chips, the wire structure is painted with gold. On the left, the atom chip used in the MAIUS-1 experiment. On the right, artist's view of the CAL setup, with the atom chip on top, the magnetic coils on the side, and the laser beams that can be used for imaging, among other things. Credits to the DLR and NASA.

2.2 . Experimental setup : atom chip and magnetic trap

We are interested in the part dedicated to the manipulation of the atoms when they are cooled to the condensed stage, and the first step is to understand the role of the main components of the setup on the experiments. The experimental setup on which we base our simulations works with a magnetic trap featuring atom chips [66]. The atom chip is a micro-fabricated, integrated device that allows the design of small and compact setups that can be embedded in mobile devices where the volume and the weight are limited. It is even more the case for applications to space experiments in rockets, such as the MAIUS-1 experiment [49], or CAL on board of the ISS [51]. Another advantage of using atom chips is the high flux of atoms that can be achieved, with creations of ensembles of 10^5 atoms in the span of a second [8].

The manipulation of the atoms in the system relies mainly on two main elements : the atom chip and the Helmholtz coils. The atom chip is a structure with many wires, as it can be seen on the left side of Figure 2.1. These wires carry currents inducing magnetic fields that can be calculated using the Biot-Savart law

$$\mathbf{B}(\mathbf{r}) = \frac{\mu_0}{4\pi} \int_C \frac{I d\mathbf{l} \times \mathbf{r}'}{|\mathbf{r}'|^3} \tag{2.1}$$

where $d\mathbf{l}$ is a vector along the path C whose magnitude is the length of the differential element of the wire in the direction of conventional current. $\mathbf{r}' = \mathbf{r} - \mathbf{l}$ is the full displacement vector from the wire element $d\mathbf{l}$ at point l to the point at which the field is being computed (r), and μ_0 is the magnetic constant.

The magnetic field induced by the chip currents can be combined with the quasi-linear magnetic field produced by the coils $\mathbf{B}_{bias}$, that can be referred to as the bias field. This creates a magnetic potential, and its minimum can be used to trap neutral atoms, as shown for example in the artist's view of the CAL SM2 atom chamber on the right side of Figure 2.1 for instance. In the weak field approximation and in the absence of gravity, the trapping potential that is experienced by an atom

can be expressed as

$$V(x, y, z, t) = m_F \, g_F \, \mu_B \, B(x, y, z, t) \tag{2.2}$$

where μ_B is the Bohr magneton, g_F is the Landé factor, m_F is the azimuthal quantum number and $B(x, y, z, t)$ is the total magnetic field.

Depending on the geometry of the wires used on the atom chip, we can obtain different trapping potentials. One of the configurations is the Z-shape chip configuration, where it takes a wire tracing a Z-shape on the chip [67]. It is the one used for the application to STA transport, and the experiments realized with the first module of CAL, SM2. It is chosen because of the cigar-shaped trap that it can create.

Using the CAD design of the chip and information on the experimental setup, we can model the different wires of the chip and the coils used during the experiment. By plugging this information into a code solving the Biot-Savart law in a software such as Mathematica, we can get an overview of the trap configurations that can be achieved during the experiments. Usually, the potential created is fitted by a harmonic potential centered on the trap minimum. Defining the centre of the trap as (x_t, y_t, z_t), the potential is expressed as

$$V(x, y, z, t) = \frac{1}{2} m \Big[\omega_x^2(t)(x - x_t)^2 + \omega_y^2(t)(y - y_t)^2 + \omega_z^2(t)(z - z_t)^2 \Big] \tag{2.3}$$

where $\omega_\alpha = 2\pi f_\alpha$ for $\alpha = x, y, z$ with f_x, f_y and f_z the trap frequencies. x, y, z are the eigenaxes of the trap and can be rotated with respect to the axes of the chip.

The result of the trapping potential simulation depends on the presence or absence of gravity, since the real trap is not a perfect parabolic trap. In the presence of gravity, the trapping potential is distorted, and if we fit a harmonic potential to the trap bottom, the frequency changes compared to the case without gravity, and the eigenaxes of the trap can experience a rotation that can be more or less important in a case-by-case situation.

The trap characteristics, such as the position of the minimum and the trapping frequencies, can then be used to simulate the dynamics of the atom cloud. However, some approximations have to be made to simplify the calculations, such as how to account for the form of the wires, the width and position of the coils. It is necessary to compare these values with experimental data, hence a calibration phase is required. This calibration is also very important to simulate experimental protocols that cannot be performed directly in the laboratory, *e.g.* planning for experiments to be realized during a rocket launch.

2.3 . STA : control of the final position and velocity of the BEC

The idea is to achieve a fast, precise and controlled transport of a BEC. Constraints such as the initial position, final position and duration are linked to the experimental requirements. In our case, we want to study the expansion of a cloud and perform operations leading to interferometry from a configuration where the BEC is at rest in the initial trap. This requires a fast transport during which the BEC will be excited. There are many methods to perform a shortcut to adiabaticity (STA) protocol

depending on the object to move from a single atom to a cloud of atoms condensed in a BEC [68]. The method we use is the reverse engineering method that was studied by Robin Corgier during his PhD thesis [62, 63]. This work assumes a 1D transport with a Z-wire chip trap. It uses the same formulas and calculation process as in these works, and more details on some demonstrations can be found in the references above.

In the harmonic potential approximation and in the absence of gravity, the trajectory of the centre of mass of the atom cloud z_a can be described by Newton's equation (see section 2.4 for more details)

$$\ddot{z}_a(t) + \omega_z^2(t)(z_a(t) - z_t(t)) = 0 \tag{2.4}$$

with z_t the position of the trap centre, and $\omega_z(t)$ the time-dependent angular frequency of the trap. This equation links the atom trajectory to the trap trajectory.

2.3.1 . Polynomial approach for the atoms trajectory

Using the constraints on the trajectory of the atoms, such as the initial position, velocity and acceleration, as well as the final ones, we can design an ideal trajectory for the atom cloud. We consider a transport along the z direction of the cloud. $z_a(t)$ describes the trajectory of the atom cloud we want to obtain. Here we want to transport atoms that are initially at rest to a final trap where the atoms should also be at rest. The boundary conditions at initial and final time are

$$z_a(0) = z_i, \qquad \dot{z}_a(0) = 0, \qquad \ddot{z}_a(0) = 0 \tag{2.5}$$

$$z_a(t_f) = z_f, \qquad \dot{z}_a(t_f) = 0, \qquad \ddot{z}_a(t_f) = 0 \tag{2.6}$$

where z_i and z_f are the initial and final positions of the cloud, respectively. Using our knowledge of the system, we can create the trap evolution that gives us this trajectory as a solution to Newton's equations. Since we can experimentally tune the currents so that the traps are at rest at both ends of the transports, we have similar boundary conditions on the trap trajectory $z_t(t)$

$$z_t(0) = z_i, \qquad \dot{z}_t(0) = 0, \qquad \ddot{z}_t(0) = 0 \tag{2.7}$$

$$z_t(t_f) = z_f, \qquad \dot{z}_t(t_f) = 0, \qquad \ddot{z}_t(t_f) = 0 \tag{2.8}$$

By taking into account these boundary conditions on the trap trajectory with Newton's equation 2.4, we obtain new constraints on the 3rd and 4th derivatives of the atom trajectory with respect to time.

$$z_a^{(3)}(0) = 0, \qquad z_a^{(4)}(0) = 0 \tag{2.9}$$

and

$$z_a^{(3)}(t_f) = 0, \qquad z_a^{(4)}(t_f) = 0 \tag{2.10}$$

This gives us a total of 10 constraints to satisfy. Using Lagrange's theorem on polynomials, there is a unique polynomial of degree 9 that satisfies these conditions. Solving the equations with this polynomial and its derivative, we find the coefficients for the atom trajectory

$$z_{poly}(t) = z_i + (z_f - z_i) \left[126 \left(\frac{t}{t_f} \right)^5 - 420 \left(\frac{t}{t_f} \right)^6 + 540 \left(\frac{t}{t_f} \right)^7 - 315 \left(\frac{t}{t_f} \right)^8 + 70 \left(\frac{t}{t_f} \right)^9 \right] \tag{2.11}$$

This polynomial form for the atom trajectory is convenient to get a first impression of the calculations and to learn the techniques of this reverse engineering STA protocol. It is also a way to systematically find a function that satisfies all the boundary conditions, thanks to the properties of polynomials.

In Figure 2.2 we see an application to a transport from $z_i = 0.453$ mm to $z_f = 1.654$ mm in $t_f = 75$ ms. The blue curve corresponds to the polynomial anzatz from equation 2.11. However, the polynomial function lacks flexibility, and it is not easy to modulate it to account for other criteria of atom transport, such as controlling the offset to the trap minimum.

2.3.2 . Flexible approach with sinusoidal functions

After finding the polynomial function that satisfies the boundary conditions, it is possible to think about other categories of functions that have similar properties for the 1st and 2nd derivatives like the sinusoidal functions. Another ansatz is presented in [63]. It is the one that will be used in our numerical and experimental applications. It is based on the observation that the transport requires an acceleration followed by a deceleration of the atom cloud. This suggests the use of a function whose acceleration has a sinusoidal shape with the possible introduction of some chirping parameters

$$z_a(t) = z_i + \left(\frac{z_f - z_i}{12\pi} \right) \left[6\nu - 8\sin(\nu) + \sin(2\nu) \right] \tag{2.12}$$

where

$$\nu = \nu(t) = 2\pi \left(\frac{1 + a(t/t_f) + b(t/t_f)^2}{1 + a + b} \right) \frac{t}{t_f} \tag{2.13}$$

The parameters a and b are control parameters that can be adjusted to optimise the transport. We see in Figure 2.2 that for $(a, b) = (0, 0)$, this ramp, which corresponds to the dashed red line, has a shape close to that of the polynomial ramp in blue. Optimizing to minimize the offset from the trap minimum throughout the transport results in the optimized parameters $(a, b) = (-1.37, 0.78)$. This optimized ramp is shown in green in Figure 2.2.

2.3.3 . Design of the trap evolution by reverse engineering

In some cases, we can analytically reverse-engineer the trap trajectory that provides the atom trajectory [62]. This is the case when we can write the dependence of the trap frequencies on the trap position with, for instance, simple Padé functions, which are quotients of polynomial functions

$$\omega_z^2(z_t) = \frac{\alpha + \beta z_t}{1 + \gamma z_t + \zeta z_t^2} \tag{2.14}$$

By inserting this expression into Newton's equation of motion 2.4 with the chosen ramp for $z_a(t)$, we can indeed easily calculate $z_t(t)$. Finally, by reversing the calculation of our chip model, we can obtain the evolution of the experimental currents that will implement this trap evolution.

These calculations assume that the trap is harmonic throughout the whole dynamics. This is an approximation that is sometimes difficult to hold when studying the transport in practice, especially if the atoms move away from the centre of the trap during the dynamics. The anharmonicity of the
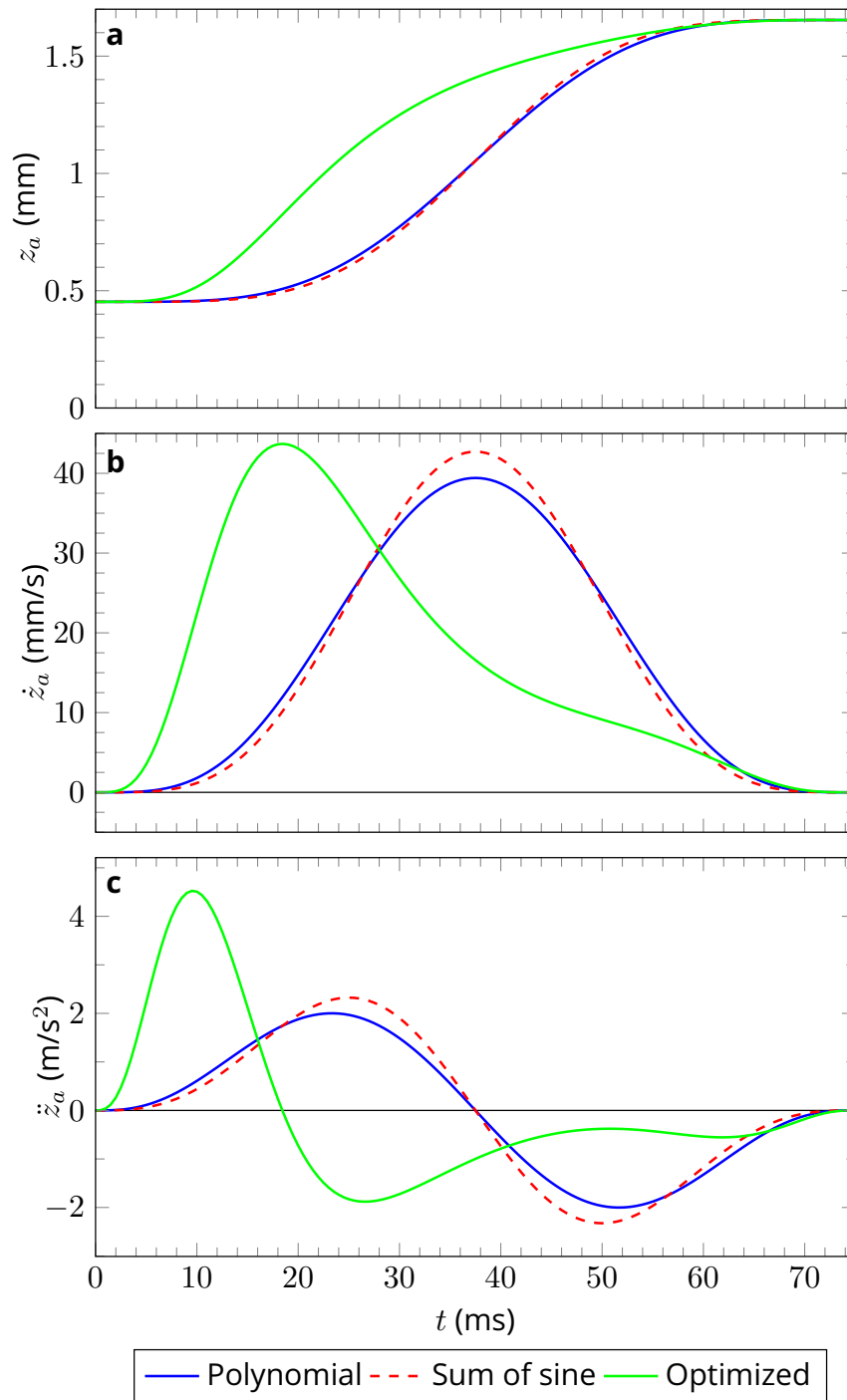
Figure 2.2 – Different atom trajectories satisfying the conditions for a STA transport for a duration of $t_f = 75$ ms, from $z_i = 0.453$ mm to $z_f = 1.654$ mm. The blue curve corresponds to the polynomial ansatz. The dashed red curve corresponds to the sinusoidal ansatz with $(a, b) = (0, 0)$. The green curve corresponds to the same flexible ansatz, but for a different, optimized couple of parameters $(a, b) = (-1.37, 0.78)$.

trap can be described by taking a third order term from the Taylor expansion of the potential around the trap minimum

$$V_a(x, y, z, t) = V(x, y, z, t) + \frac{1}{3} m \omega_z^2(t) \frac{(z - z_t)^3}{L_3(t)} \tag{2.15}$$

where $V(x, y, z, t)$ is the harmonic potential seen in equation 2.3, and $L_3(t)$ is the characteristic length associated with the 3rd order anharmonic term. For typical chip geometries as reported in [8], the cubic term is by far the largest correction term to the harmonic order.

We can visualize the influence of this third-order correction by inserting the new expression for the potential into Newton's equation of motion. For the transport along z that we are considering, the new equation of motion reads

$$\ddot{z}_a(t) + \omega_z^2(t)(z_a(t) - z_t(t)) \left(1 + \frac{z_a(t) - z_t(t)}{L_3(t)}\right) = 0 \tag{2.16}$$

To limit the effects of the anharmonic component on the dynamics, the following criterion must be met [62]

$$\chi(t) = \left| \frac{z_a(t) - z_t(t)}{L_3(t)} \right| \ll 1, \forall t \tag{2.17}$$

In Figure 2.3 we see that for the polynomial trajectory and for the sinusoidal ramp with $(a, b) = (0, 0)$ the offset is more than 30 µm near the end of the transport. For the particular, optimized choice $(a, b) = (-1.37, 0.78)$, this offset is minimized and is less than 13.6 µm along the trajectory. We can see in Figure 2.2 that by choosing this particular set of parameters, the aspect of the ramp is very different. The shape of the atoms velocity $\dot{z}_a$ and acceleration $\ddot{z}_a$ also shows a different strategy for the transport : the atoms are initially launched faster thanks to the higher and more constraining trap frequency in the beginning, and then the deceleration occurs earlier to allow the trap to "catch up" with the atoms earlier in order to minimize the offset in the remaining part of the transport. Another way to minimize the offset would be to choose a longer transportation time, and therefore a more adiabatic transport, but this transportation time would then have to be significantly lengthened to achieve similar results in terms of maximum offset.

Once the trap trajectory is determined as a function of the experimental parameters, it is necessary to take into account the constraints on the parameter variations imposed by the experimentalists. For example, the limit on the step size and on the number of steps for the ramp. These are limits imposed by the software and the hardware of the experimental setup. We will see more about the study of the robustness of the STA ramp in the next chapter, where we will apply this 1D STA transport to the CAL machine in space.

2.4 . Study of the center of mass (COM) motion with Newton's equation of motion

The BEC is a quantum object that can be modeled by a 3D wavefunction $\phi(x, y, z)$. In the frame of the mean-field theory, its dynamics is described by the Gross-Pitaevskii equation [56]. In this section we will focus on the spatial dynamics of the wavefunction. By definition, the position of the quantum
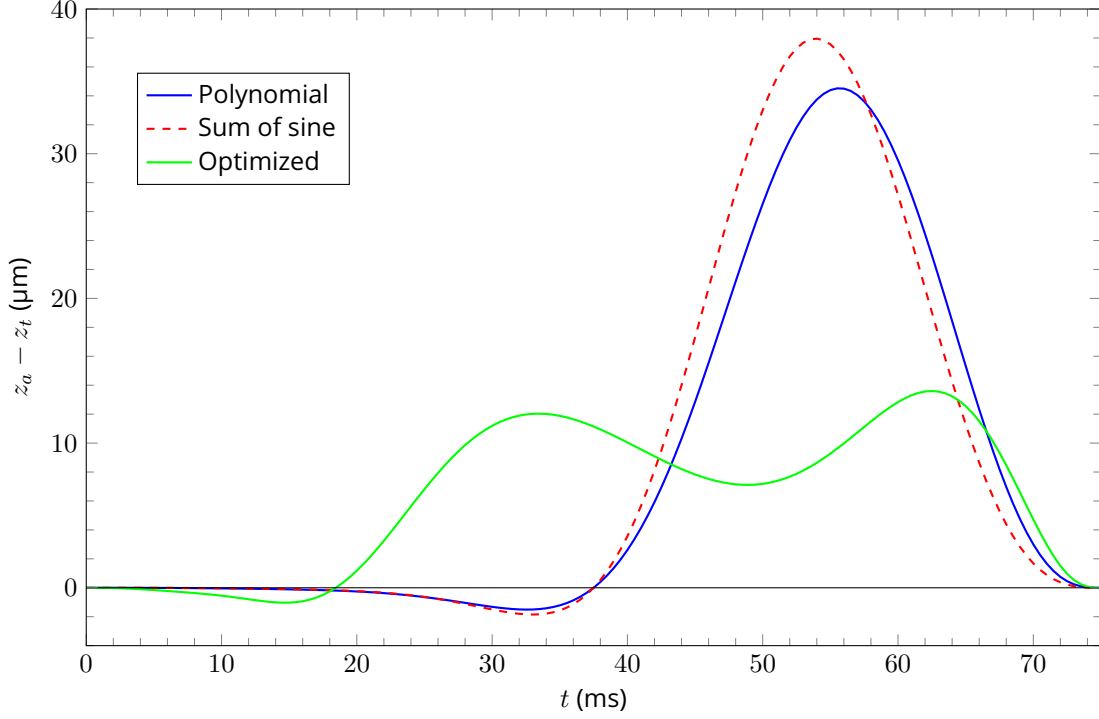
Figure 2.3 – Offset between the atom trajectory and the trap trajectory, using the same ramps and color codes as for Figure 2.2. The green curve is optimized to minimize the offset over the ramp.

object is calculated using the probability density associated with the wavefunction. For example, to get the average position $\langle x \rangle$ along the x direction we use

$$\langle x \rangle = \int_x \int_y \int_z x \, |\phi(x,y,z)|^2 \, dx \, dy \, dz \tag{2.18}$$

This method requires knowledge of the full wavefunction at all times, in case we want to follow the displacement of the BEC during the dynamics. This requires a lot of computational resources, either in terms of computational memory for the data storage, or in terms of computation time. The Gross-Pitaevskii equation can also be referred to as a non-linear Schrödinger equation, since the equation includes the kinetic energy and potential energy terms as in the Schrödinger equation, along with an additional term which is the interacting term $Ng \, |\phi(x,y,z)|^2 \, \phi(x,y,z)$, which is cubic with respect to the wavefunction.

$$\text{Schrödinger:} \quad i\hbar \, \partial_t \phi(x,y,z) = \left[-\frac{\hbar^2}{2m} \Delta + V(x,y,z) \right] \phi(x,y,z) \tag{2.19}$$

$$\text{Gross-Pitaevskii:} \quad i\hbar \, \partial_t \phi(x,y,z) = \left[-\frac{\hbar^2}{2m} \Delta + V(x,y,z) + Ng|\phi(x,y,z)|^2 \right] \phi(x,y,z) \tag{2.20}$$

Due to the similarity between the Gross-Pitaevskii equation and the Schrödinger equation, many studies have been conducted to show that similar numerical methods can be used to solve both equations. These studies have been largely successful, such as in [69–71].

18

Here we first want to use the same approach as in the case of single particles to study the trajectory of the object without going through the solution of the equations describing the dynamics of the wavefunction. For an atom in a harmonic potential, the dynamics is found by solving the Schrödinger equation. In this case, the Ehrenfest theorem [72] shows that the centre of mass dynamics is described, as in classical mechanics, by the solution of Newton's equation of motion. This greatly simplifies the study, since solving this simple second-order differential equation is much easier. Now we want to extend this approach to the GPE by adding the nonlinear term. This term depends only on the probability density of the wavefunction, which is symmetric with respect to the center of mass of the system in a harmonic well. As a result, the interactions (repulsive in our case) will simply tend to broaden the wave function, without changing the position of the center of mass. In the harmonic approximation we can therefore still apply the Ehrenfest theorem to the BEC to describe the spatial dynamics of the center of mass. This is one of the main reasons why we can use the reverse engineering method to design the ramp that will move the BEC along the desired trajectory. Now we will see applications of this equation of motion such as measuring trap frequencies, or modeling of the final position and velocity of a cloud at the end of a transport.

2.4.1 . Characterisation of an atom trap

In this part, we will see how to extract the frequency and position of a trap from a sloshing experiment where the BEC is imaged after a fixed time-of-flight (TOF). We will also calculate the in-trap oscillation amplitude from the signal.

Let us consider the trajectory along the z direction of a BEC oscillating in a trap centered at z_0 with frequency ω_z. We note $z_{in}(t)$ the trajectory in the trap and $z_{TOF}(t)$ the trajectory observed on the camera after a short free expansion time t_{TOF}. The trajectory in the trap is found by solving Newton's equation for a harmonic oscillator.

$$z_{in}(t) = A_{in} \sin(\omega_z t + \phi_{in}) + z_0 \tag{2.21}$$

with A_{in} the in-trap oscillation amplitude and ϕ_{in} the phase of the signal. It is of course also possible to express this oscillation with a cosine function by changing the definition of the initial phase ϕ_{in}.

We assume that the atoms expand freely and that the expansion time is short, so that the motion of the cloud is defined only by the release velocity. Thus, similar to a first-order Taylor expansion, we find the expression of the trajectory measured by the camera using

$$z_{TOF}(t_r + t_{TOF}) = z_{in}(t_r) + \dot{z}_{in}(t_r)\, t_{TOF} \tag{2.22}$$
$$= A_{in}\left[\sin(\omega_z t_r + \phi_{in}) + \omega_z t_{TOF} \cos(\omega_z t_r + \phi_{in})\right] + z_0 \tag{2.23}$$

It corresponds to the uniform linear motion after the release at $t = t_r$ from the trap followed by the free expansion of t_{TOF}. We can see from the expression of z_{TOF} that it has the same period $T_z = 2\pi/\omega_z$ as the in-trap motion z_{in}. Therefore, the frequency ω_z can be determined by measuring z_{TOF}. Note that we can also fit the in-trap amplitude A_{in} and the position of the trap minimum z_0 from the measurement of z_{TOF}.

19

2.4.2 . Tools to study the robustness of a transport

Let us consider the case of a transport experiment realised in orbit, such as an STA transport. We assume that the atoms are initially oscillating in the initial trap, and we fix the initial time $t = 0$ of the transport after a fixed initial holding time $t_{hold,i}$. The initial conditions of the atoms trajectory $z_{at}(t; t_{hold,i})$ are

$$z_{at}(0; t_{hold,i}) = A_i \cos(\omega_z(0) t_{hold,i} + \phi_i) \tag{2.24}$$

and

$$\dot{z}_{at}(0; t_{hold,i}) = -A_i \omega_z(0) \sin(\omega_z(0) t_{hold,i} + \phi_i) \tag{2.25}$$

for the equation of motion

$$\ddot{z}_{at} + \omega_z^2(t) \left[z_{at}(t; t_{hold,i}) - z_{trap}(t) \right] = 0 \tag{2.26}$$

At the end of the transport, we can define the release velocity of the atoms $\dot{z}_{at}(t_f; t_{hold,i})$, which is the velocity of the atoms when we switch off the trap at $t = t_f$. In the case where the experiment continues with the holding of the BEC in the final trap of frequency $\omega_z(t_f)$, we can deduce the final oscillation amplitude $A_f(t_{hold,i})$ from the motion of a particle in a harmonic trap. This amplitude is easily obtained from the position and velocity of the centre of mass of the condensate at the end of the transport by the following formula

$$A_f(t_{hold,i}) = \sqrt{\left[\dot{z}_{at}(t_f; t_{hold,i}) / \omega_z(t_f) \right]^2 + \left[z_{at}(t_f; t_{hold,i}) - z_{trap}(t_f) \right]^2} \tag{2.27}$$

Experimentally, we want to control the final position of the cloud so that it is as close as possible to the final trap minimum. We also want to keep its velocity as low as possible, so that the centre of mass motion can be controlled when releasing the cloud. This is why we try to minimize the amplitude of the oscillation $A_f(t_{hold,i})$ by choosing the optimal initial holding time $t_{hold,i}$. The transport is considered robust if the final amplitude remains below a threshold of the order of microns for a small offset from the initial position, expressed here as a function of the holding time in the initial trap.

2.5 . DKC : control of the expansion

During the free expansion of a BEC, its size can grow very quickly, and since the total atom density is conserved, the cloud becomes more and more dilute. This leads to a loss of contrast in the imaging process after a certain time of flight, resulting in very poor signal to noise ratio in the data. The growing size of a BEC is also a limiting factor for performing experiments on the cloud after its creation, such as atom interferometry. The laser beams interacting with the cold ensemble have a finite size, and if the cloud is too large, the interaction between light and atoms across the cloud is not the same, and the defects over the wavefront introduce errors. Similar to the collimation of a light beam at the beginning of an optics experiment, we want to control the size of the atom clouds by lensing the atoms with an atom lens. The idea introduced in the paper from Hubert Ammann and Nelson Christensen [58], is to use of a short pulse of a potential to narrow the momentum distribution of the atom cloud. To the term "Delta Kick Cooling" introduced in the paper, we will prefer the term "Delta Kick Collimation" (DKC) due to the fact that we do not consider temperatures as defined in thermodynamics in the BEC.

At first sight, we can use an analogy to classical mechanics with atoms in a harmonic oscillator. During the dynamics of atoms in a trap, the total energy of the system is conserved. The potential energy oscillates in phase with the motion of the atoms, and the kinetic energy oscillates out of phase. By turning off the trapping potential when the potential energy is maximal, we obtain a free expansion of the ensemble with a low kinetic energy.

In practice, after a short free expansion of the atom cloud, we turn on the trapping potential for a very short time. This short pulse corresponds to the "delta kick", and is of the order of milliseconds when the trapping frequency is of the order of tens of Hertz. This duration depends on the expansion time before the application of the delta-kick. In the seminal paper on the DKC method, the pulse duration can be found when the following condition $\kappa_{cl} \approx 1$ is satisfied, where

$$\kappa_{cl} = \sqrt{2\pi}\, \Delta t_{lens}\, \omega^2\, t_{exp} \qquad (2.28)$$

with Δt_{lens} the duration of the kick, t_{exp} the duration of the free expansion before the kick, and ω the angular frequency of the trap. Observing the expression of κ_{cl}, we can see that the parameters are all related, and for a fixed trapping frequency, the pulse duration to apply shortens as the expansion before the pulse gets longer.

For a BEC in ballistic expansion, *i.e.* for a long time of flight when the size of the condensate evolves linearly, we can estimate the optimal lens duration Δt_α to control the size evolution in the direction $\alpha = x, y$ or z using a very simplified model. When the BEC is trapped again during the DKC process, different collective excitation modes can coexist with various frequencies [56, 73]. Suppose that we can express the size oscillation $R_\alpha(t)$ of the BEC in the direction α as the solution of a harmonic oscillator of frequency $q\omega_\alpha$, with q a real factor depending on the excitation mode. Then

$$R_\alpha(t) = R_\alpha(t_{exp}) \cos\left(q\omega_\alpha(t - t_{exp})\right) + \frac{\dot{R}_\alpha(t_{exp})}{q\omega_\alpha} \sin\left(q\omega_\alpha(t - t_{exp})\right) , \qquad (2.29)$$

and

$$\dot{R}_\alpha(t) = -R_\alpha(t_{exp})q\omega_\alpha \sin\left(q\omega_\alpha(t - t_{exp})\right) + \dot{R}_\alpha(t_{exp}) \sin\left(q\omega_\alpha(t - t_{exp})\right) . \qquad (2.30)$$

The lens time duration Δt_α is chosen so that the size derivative is zero. By using the size velocity from Eq. (2.30) we obtain

$$\Delta t_\alpha = \frac{1}{q\omega_\alpha} \arctan\left(\frac{\dot{R}_\alpha(t_{exp})}{R_\alpha(t_{exp})q\omega_\alpha}\right) . \qquad (2.31)$$

We can therefore obtain a reasonable initial estimate of the lens duration from the expression

$$\Delta t_\alpha \sim \frac{1}{\omega_\alpha} \left(\frac{\dot{R}_\alpha(t_{exp})}{R_\alpha(t_{exp})\omega_\alpha}\right) , \qquad (2.32)$$

which can then be refined by scanning the values of Δt_α around that value.

The upper graph from Figure 2.4 shows qualitatively the effect of the same lens duration over a cloud with different initial trap frequencies and dynamics, as well as different frequencies for the lens. The lens duration Δt_{lens} is too short for the red curve with only a small reduction of the expansion

rate of the cloud in this direction. On the other hand, Δt_{lens} is too long for the blue curve with an over-focusing of the cloud, followed by a "rebound" in the size evolution due to atomic interactions, which are repulsive and more important when the cloud is dense. For the longer time, the cloud expansion is faster than before the lensing process, which is analogous to a diverging lens in optics. Finally the lens is optimized for the green curve that is well collimated. This shows that if we are not in a spherical symmetry, it is difficult to control the expansion of the BEC in all the directions, and sometimes the optimization of one direction has to be done at the expense of the others. One way to overcome this limitation is to control the initial release from the trap, and to introduce a second DKC to act as a telescope.
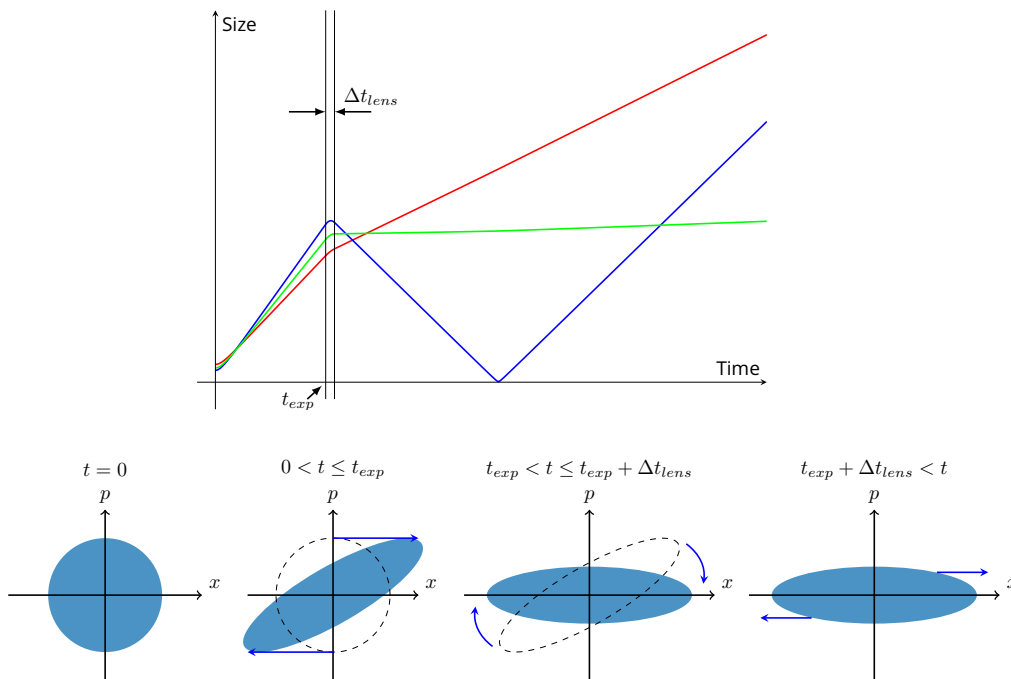
Figure 2.4 – Principle of DKC, effect of the lensing time on the expansion and visualisation in phase space. In the upper part, we observe the effect of the same lensing time on an expansion with different frequencies. The lensing time is collimating for the green curve, too short for the red curve, and too long for the blue curve that shows overfocusing. In the lower part we see the representation of the wavefunction in the phase space domain at different times during the lensing.

The lower part of Figure 2.4 shows the effect of DKC on a BEC in phase space. Initially, the trapped BEC is represented by a disk in phase space. Then, after a long enough free expansion stage, the momentum of the cloud remains constant, stretching the disk into an ellipse. The trapping potential during the DKC corresponds to a rotation of the ellipse in phase space, and the switch-off time is optimal when the momentum width of the cloud Δp is minimized. With this small momentum width, the kinetic energy of the cloud is reduced, and the cloud expands slower after this process. The size of the condensate at the end of an ideal kick will never be perfectly constant due to the presence of the remaining atomic interaction energy in the BEC. However, a good control of this expansion can allow the observation of the cloud after seconds of expansion in some special cases [45].

To quantify the expansion rate of the condensate at the end of the DKC, we define the 3D expansion temperature by analogy to the definition of the temperature in the Maxwell-Boltzmann statistics

$$\frac{3}{2}k_BT = \frac{m}{2}\left[\left(\frac{d\Delta x}{dt}\right)^2 + \left(\frac{d\Delta y}{dt}\right)^2 + \left(\frac{d\Delta x}{dt}\right)^2\right] \tag{2.33}$$

where k_B is the Boltzmann constant. We can also define a 1D temperature for each direction as

$$\frac{1}{2}k_BT_\alpha = \frac{m}{2}\left(\frac{d\Delta\alpha}{dt}\right)^2 \tag{2.34}$$

where $\alpha \in \{x,y,z\}$.

2.6 . Scaling equations and GPE simulations

In the mean-field approach, the dynamics of a Bose-Einstein Condensate is described by the time-dependent Gross-Pitaevskii equation (GPE) [56]. The equation shown below assumes that the wave function $\psi(\boldsymbol{r},t)$ representing the condensate is normalised to 1

$$i\hbar\,\partial_t\psi(\boldsymbol{r},t) = \left[-\frac{\hbar^2}{2m}\boldsymbol{\nabla}^2 + V(\boldsymbol{r},t) + Ng\left|\psi(\boldsymbol{r},t)\right|^2\right]\psi(\boldsymbol{r},t) \tag{2.35}$$

Here m is the mass of an atom, $V(\boldsymbol{r},t)$ corresponds to the external potential, N is the atom number in the cloud, $\hbar = h/2\pi$ is the reduced Planck constant and the interaction term g is related to the s-wave scattering length a of the species considered by

$$g = \frac{4\pi\hbar^2 a}{m} \tag{2.36}$$

At equilibrium, it is possible to write a time-independent version of the Gross-Pitaevskii equation, which can also be derived using the Lagrange equation

$$\left[-\frac{\hbar^2}{2m}\boldsymbol{\nabla}^2 + V(\boldsymbol{r},0) + Ng\left|\psi(\boldsymbol{r},0)\right|^2\right]\psi(\boldsymbol{r},0) = \mu\,\psi(\boldsymbol{r},0) \tag{2.37}$$

where μ is a Lagrangian multiplier corresponding to the chemical potential of the system.

In the case where the atom number is sufficiently large, *i.e.* N usually of the order of at least 10^5, it is possible to neglect the kinetic energy of the cloud compared to the other terms of the GPE. This is called the Thomas-Fermi (TF) approximation. Under this approximation, the atomic density can be written as

$$\rho(\boldsymbol{r},0) = N\left|\psi_{TF}(\boldsymbol{r},0)\right|^2 = \begin{cases} \dfrac{\mu - V(\boldsymbol{r},0)}{g} & \text{if } V(\boldsymbol{r},0) \leqslant \mu \\ 0 & \text{otherwise} \end{cases} \tag{2.38}$$

The chemical potential μ is determined by the normalisation of the wavefunction.

$$\iiint \rho(\boldsymbol{r},0)\,d\boldsymbol{r} = N \tag{2.39}$$

In the case of an external harmonic potential, this normalisation yields

$$\mu = \frac{\hbar\tilde{\omega}(0)}{2}\left(15Na\sqrt{\frac{m\tilde{\omega}(0)}{\hbar}}\right)^{2/5} \tag{2.40}$$

where $\tilde{\omega}(0) = (\omega_x(0)\omega_y(0)\omega_z(0))^{1/3}$ is the geometric mean of the three trapping frequencies. In this Thomas-Fermi approximation, the probability density has the shape of an ellipsoid in 3D space, and we can define the size or radius of the wavefunction in all directions $\alpha \in \{x, y, z\}$ by

$$R_\alpha(0) = a_{osc}\left(\frac{15Na}{a_{osc}}\right)^{1/5}\frac{\tilde{\omega}(0)}{\omega_\alpha(0)} \tag{2.41}$$

where $a_{osc} = \sqrt{\hbar/(m\tilde{\omega}(0))}$ is the characteristic quantum mechanical length scale of the 3D harmonic oscillator.

The Gross-Pitaevskii equation (GPE) can be used to get the size evolution of the atomic clouds to see how the density evolves. This is useful to find out if the cloud is small enough when interacting with a laser beam during an interferometry sequence, or if we have a high enough atomic density to keep the cloud visible. However, this can require numerical calculations that can be long and tedious, sometimes memory intensive [69, 71, 74]. A simpler model is welcome to obtain fast results. In our case, we use a set of scaling equations [57, 75]. These equations rely on a few constraints on the system : having a harmonic trap and having enough atoms so that the Thomas-Fermi approximation holds. In this scaling approach, we make the analogy between the Bose-Einstein condensate and an ellipsoidal balloon that inflates or deflates during the dynamics. We define scaling functions $\lambda_\alpha(t)$ in each direction $\alpha \in \{x, y, z\}$ such that

$$R_\alpha(t) = \lambda_\alpha(t)\,R_\alpha(0) \tag{2.42}$$

These scaling functions are the solutions of coupled second-order differential equations

$$\ddot{\lambda}_\alpha + \omega_\alpha^2(t)\,\lambda_\alpha = \frac{\omega_\alpha^2(0)}{\lambda_\alpha\lambda_x\lambda_y\lambda_z} \tag{2.43}$$

that can be solved numerically with different methods such as the Verlet algorithm.

This method provides a good description of the size dynamics of a condensate and is used to anticipate the behaviour of a condensate when designing sequences for diverse experiments on ground or in space. When the atom number gets too low, we can underestimate the size of the condensate with this method. We then have to fully solve the Gross-Pitaevskii equation to describe the dynamics more accurately. The scaling equations can be used in this case to have a suitable, adapted grid at all times by performing an appropriate frame transformation, which makes Gross-Pitaevskii calculations much more efficient, as shown for exemple in the references [74, 76]. This scaled grid method is used in our codes and it will be described in more detail in Chapter 4.

We have seen that with the Thomas-Fermi approximation and with the scaling equations we can define the radius of the BEC to measure its typical size evolution. Using the parabolic shape of the

wave function, we can show that there is a scaling relation between the radius $R_\alpha(t)$ and the standard deviation $\Delta\alpha(t)$ in each direction [62]. For $\alpha \in \{x, y, z\}$ we have

$$R_\alpha(t) = \sqrt{7}\, \Delta\alpha(t) \tag{2.44}$$

where

$$(\Delta\alpha)^2 = \langle \alpha^2 \rangle - \langle \alpha \rangle^2 \tag{2.45}$$

This last relation is used when we numerically evaluate the widths $\Delta x(t)$, $\Delta y(t)$ and $\Delta z(t)$ from the solution of the Gross-Pitaevskii equation.

2.7 . Rotations and frame changes

Expression of the rotation matrix

When modeling the system to solve its dynamics, we are sometimes confronted with the fact that the eigenaxes of the trap are not the same as the laboratory frame. In the case of a magnetic trap created by the combination of the magnetic fields induced by a chip and by magnetic coils, this laboratory frame is where we define the position of these elements. We must also take into account the fact that the system is imaged in a camera frame, which can also be rotated with respect to this laboratory frame. In this case, we need to know how to measure the size of the cloud on the camera and how to compare the experimental data with the simulation, knowing that the calculations are simpler using the eigenaxes of the trap.

In this section we will introduce rotation matrices, which are unitary matrices in the case of orthonormal frames, used to go from one frame to another. For a BEC with Thomas-Fermi approximation, we can consider that the BEC is an ellipsoid and we need to get its size from its projection on the camera. A way to handle the plane projections mathematically is described in the reference [77].

In the simulations, we consider the trapping potential for the atom clouds in the laboratory frame, which can also be called the "chip frame". Due to the geometry of the system, the eigenaxes of the trap are rotated with respect to the axes of the laboratory frame. The first step is to define the rotation matrix that goes from the trap frame to the laboratory frame. We note $\{\boldsymbol{x}, \boldsymbol{y}, \boldsymbol{z}\}$ the unitary vectors of the coordinates in the trap frame and $\{\boldsymbol{X}, \boldsymbol{Y}, \boldsymbol{Z}\}$ the unitary vectors of the coordinates in the laboratory frame. In addition, let P_{trap}^{chip} be the rotation matrix that makes the transformation from the chip frame to the trap frame such that

$$\begin{pmatrix} x \\ y \\ z \end{pmatrix} = P_{trap}^{chip} \begin{pmatrix} X \\ Y \\ Z \end{pmatrix} \tag{2.46}$$

We now want to reconstruct the rotation matrix using the notation of [77] and to obtain the values of the rotation angles θ, ϕ, ψ defined in Figure 2.5, knowing that the simulations will give us the 3 quantities θ_x, θ_y and θ_z defined by

$$\boldsymbol{x}.\boldsymbol{X} = \cos(\theta_x), \quad \boldsymbol{y}.\boldsymbol{Y} = \cos(\theta_y), \quad \boldsymbol{z}.\boldsymbol{Z} = \cos(\theta_z) \tag{2.47}$$

25
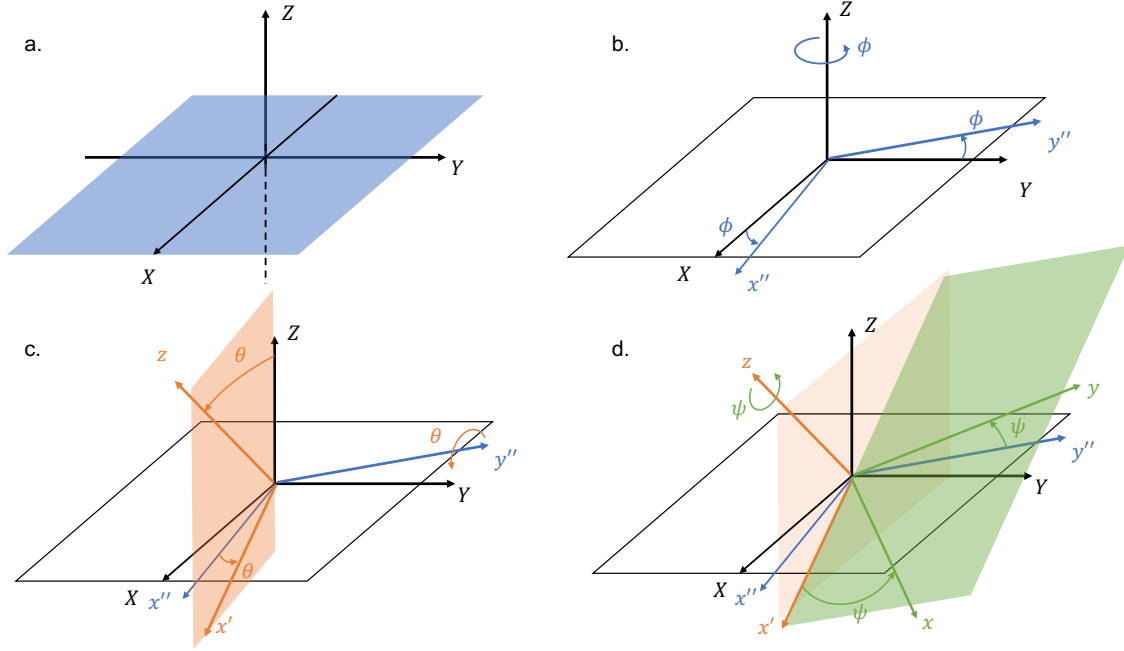
Figure 2.5 – Definition of the coordinate system. (XYZ) is the reference frame in the laboratory, and (xyz) is the rotated frame. Panel **b** shows the rotation of angle ϕ around the Z axis and x'' and y'' are the new orthogonal axes in the (XY) plane. Panel **c** shows the rotation of the angle θ around the y'' axis, and z and x' correspond to the new orthogonal axes in the (Zx'') plane. Panel **d** shows the final rotation of angle ψ around the z axis with x and y as the new orthogonal axes in the $x'y''$ plane.

For this, we consider the rotation matrix with the angles θ, ϕ and ψ defined by the successive rotations from Figure 2.5

$$P_{trap}^{chip} = \begin{pmatrix} \cos\psi & \sin\psi & 0 \\ -\sin\psi & \cos\psi & 0 \\ 0 & 0 & 1 \end{pmatrix} \begin{pmatrix} \cos\theta & 0 & -\sin\theta \\ 0 & 1 & 0 \\ \sin\theta & 0 & \cos\theta \end{pmatrix} \begin{pmatrix} \cos\phi & \sin\phi & 0 \\ -\sin\phi & \cos\phi & 0 \\ 0 & 0 & 1 \end{pmatrix} \tag{2.48}$$

This leads to

$$P_{trap}^{chip} = \begin{pmatrix} \cos\theta\cos\phi\cos\psi - \sin\phi\sin\psi & \cos\theta\sin\phi\cos\psi + \cos\phi\sin\psi & -\sin\theta\cos\psi \\ -\cos\theta\cos\phi\sin\psi - \sin\phi\cos\psi & -\cos\theta\sin\phi\sin\psi + \cos\phi\cos\psi & \sin\theta\sin\psi \\ \sin\theta\cos\phi & \sin\theta\sin\phi & \cos\theta \end{pmatrix} \tag{2.49}$$

Identifying the diagonal terms of this matrix with the results of the scalar products from equation 2.47 we obtain

$$\cos\theta_x = \cos\theta\cos\phi\cos\psi - \sin\phi\sin\psi \tag{2.50a}$$

$$\cos\theta_y = -\cos\theta\sin\phi\sin\psi + \cos\phi\cos\psi \tag{2.50b}$$

$$\cos\theta_z = \cos\theta \tag{2.50c}$$

Our goal is now to find expressions for the angles ϕ and ψ as a function of θ_x, θ_y and θ_z in the case of a non-trivial rotation where

$$\cos^2(\theta_z) \neq 1 \tag{2.51}$$

26

Replacing $\cos\theta$ with $\cos\theta_z$ in Eq. (2.50) we get

$$\cos\theta_x = \cos\theta_z \cos\phi \cos\psi - \sin\phi \sin\psi \tag{2.52a}$$
$$\cos\theta_y = -\cos\theta_z \sin\phi \sin\psi + \cos\phi \cos\psi \tag{2.52b}$$

and this leads to

$$\cos\phi \cos\psi = \frac{\cos\theta_y - \cos\theta_z \cos\theta_x}{1 - \cos^2\theta_z} \equiv A \tag{2.53a}$$
$$\sin\phi \sin\psi = \frac{\cos\theta_x - \cos\theta_z \cos\theta_y}{\cos^2\theta_z - 1} \equiv B \tag{2.53b}$$

Using the notations A and B to refer to the various expressions on the right side of the previous Eq. (2.53) and some trigonometry formulas, we finally obtain the following expressions used for the determination of the angles ϕ and ψ

$$\cos(\phi - \psi) = A + B \tag{2.54a}$$
$$\cos(\phi + \psi) = A - B \tag{2.54b}$$

Because of the parity of the cosine function, to determine the sign of the angles θ, ϕ, and ψ it is necessary to check these results against the expression of a rotation matrix whose angles are known to have the correct sign. As shown in Figure 2.5, when $\cos(\theta) = \pm 1$ the frame transformation consists in a simple rotation around the z axis. In the special case where $\cos(\theta) = -1$, the axes are also reversed. As an example, let us consider the simple case where $\theta_x = \theta_y = \phi$ and $\theta_z = 0$. In that case $\cos\theta = +1$. The rotation matrix is then simplified to

$$P_{trap}^{chip} = \begin{pmatrix} \cos\phi & \sin\phi & 0 \\ -\sin\phi & \cos\phi & 0 \\ 0 & 0 & 1 \end{pmatrix} \tag{2.55}$$

Note that in most cases, it is sufficient to consider this matrix, since we can neglect angles of the order of degrees in the experiments.

In the following numerical example, which is used for applications to the mixture experiments performed in the presence of gravity studied in Section 4.6, we have $(\theta_x, \theta_y, \theta_z) = (4.1640, 4.8630, 2.5196)$ degrees, and we want to find the expressions of the angles (θ, ϕ, ψ) that correspond to the expression of the matrix

$$P_{trap}^{chip} = \begin{pmatrix} 0.997 & -0.073 & 0.001 \\ 0.072 & 0.0996 & 0.043 \\ -0.004 & -0.004 & 0.993 \end{pmatrix} \tag{2.56}$$

Using trigonometry, we find that we must make the following choices, with A and B defined in Eq. (2.53)

$$\theta = -\theta_z \tag{2.57a}$$
$$\phi = [\arccos(A + B) - \arccos(A - B)]/2 \tag{2.57b}$$
$$\psi = [\arccos(A - B) - \arccos(A + B)]/2 \tag{2.57c}$$

We can see that the numerical value of the rotation matrix P_{trap}^{chip} is very close to the identity matrix. Therefore, except for simulations that require a higher accuracy in the calculations, we often simplify the simulation process by neglecting the rotation of the trap and, at the same time, the rotation of the BEC in the chip frame.

Once we have determined the transformation matrix from the chip frame to the trap frame, we can proceed to calculate the dynamics of the BEC. Experimentally, however, we sometimes have to consider an additional frame transformation due to the imaging setup. In the experiments we have studied, we know the camera position with respect to the atom chip, *e.g.* the sensor is orthogonal to the chip. As shown in Figure 2.6, the third axis of the camera frame (which is by definition orthogonal to the sensor plane) is along the imaging beam.
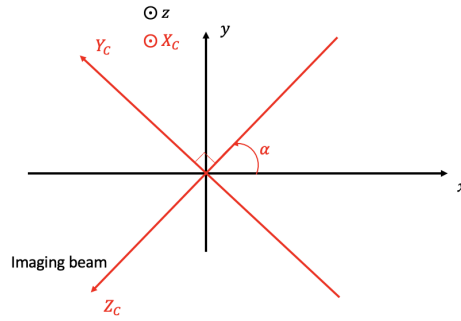
Figure 2.6 – Definition of the camera frame with respect to the atom chip frame. The imaging beam is orthogonal to the camera plane (OX_CY_C).

Similar to the definition in Eq. (2.46), this new frame transformation can be written as follows

$$\begin{pmatrix} x \\ y \\ z \end{pmatrix} = P_{chip}^{cam} \begin{pmatrix} X_C \\ Y_C \\ Z_C \end{pmatrix} \tag{2.58}$$

where (X_C, Y_C, Z_C) are the coordinates in the camera frame. We obtain

$$P_{chip}^{cam} = \begin{pmatrix} 0 & -\sin\alpha & -\cos\alpha \\ 0 & \cos\alpha & -\sin\alpha \\ 1 & 0 & 0 \end{pmatrix} \tag{2.59}$$

with the angle α defined in Figure 2.6. The numerical value of the α angle is fixed by the experimental setup. Now, using these transformations, we will connect the size of the atom cloud on the camera to the theoretical size of the cloud calculated in another frame.

Expression of the size of an atom cloud after a frame transformation

The previous section explained how to define the rotation matrices that allow the transition from the chip frame or the trap frame in which the calculations are performed, to the camera frame where

the images are captured. Now we will show how, once we have the expression of the rotation matrix, we can express the wavefunction width in the new frame.

The geology article [77] describes in detail how to obtain the width of the projection of an ellipsoid on a 2D plane. This recipe can be used to obtain the radius of a BEC cloud on a camera when we use the Thomas-Fermi approximation to describe a BEC in a harmonic trap. A step-by-step calculation using this method is described in Appendix A.

Using integrations and variance properties, we can express the width a bit more easily and get the same final expressions. For a general calculation, let us consider the following transformation

$$\begin{pmatrix} X_C \\ Y_C \\ Z_C \end{pmatrix} = P_{cam}^{chip} \begin{pmatrix} x \\ y \\ z \end{pmatrix} = \begin{pmatrix} P_{11} & P_{12} & P_{13} \\ P_{21} & P_{22} & P_{23} \\ P_{31} & P_{32} & P_{33} \end{pmatrix} \begin{pmatrix} x \\ y \\ z \end{pmatrix} \tag{2.60}$$

We want to express $\sigma_X^2 = \langle X_C^2 \rangle - \langle X_C \rangle^2$ and $\sigma_Y^2 = \langle Y_C^2 \rangle - \langle Y_C \rangle^2$ as a function of σ_x, σ_y and σ_z. To do this, we first calculate

$$\begin{align} \langle X_C^2 \rangle &= \langle (P_{11}x + P_{12}y + P_{13}z)^2 \rangle \tag{2.61a} \\ &= P_{11}^2 \langle x^2 \rangle + P_{12}^2 \langle y^2 \rangle + P_{13}^2 \langle z^2 \rangle + 2(P_{11}P_{12}\langle xy \rangle + P_{11}P_{13}\langle xz \rangle + P_{12}P_{13}\langle yz \rangle) \tag{2.61b} \\ \langle X_C \rangle^2 &= \langle P_{11}x + P_{12}y + P_{13}z \rangle^2 \tag{2.61c} \\ &= P_{11}^2 \langle x \rangle^2 + P_{12}^2 \langle y \rangle^2 + P_{13}^2 \langle z \rangle^2 + 2(P_{11}P_{12}\langle x \rangle \langle y \rangle + P_{11}P_{13}\langle x \rangle \langle z \rangle + P_{12}P_{13}\langle y \rangle \langle z \rangle) \tag{2.61d} \end{align}$$

As (x, y, z) is a Cartesian frame, the variables are independent from each other and thus the covariance is null

$$\langle xy \rangle = \langle x \rangle \langle y \rangle, \quad \langle xz \rangle = \langle x \rangle \langle z \rangle, \quad \langle yz \rangle = \langle y \rangle \langle z \rangle \tag{2.62}$$

Therefore

$$\sigma_X^2 = P_{11}^2 \sigma_x^2 + P_{12}^2 \sigma_y^2 + P_{13}^2 \sigma_z^2 \tag{2.63}$$

In a similar way, we obtain

$$\sigma_Y^2 = P_{21}^2 \sigma_x^2 + P_{22}^2 \sigma_y^2 + P_{23}^2 \sigma_z^2 \tag{2.64}$$

2.8 . Imaging process and camera considerations

Almost every experiment in which atom clouds are manipulated has an imaging sequence so that measurements can be made. Atom clouds, which can sometimes be a few tens of microns in size, are imaged by optical systems, including lenses and a sensor. Even in cases where optics are considered as perfect or not limited by aberrations, one has to consider optical effects due to diffraction [78]. These effects are measured experimentally during calibration phases using test targets. An example presenting the setup of the MAIUS experiment can be found in [79]. Works on optical design and sensor theory introduce the Optical Transfer Function (OTF) of optical systems. Using Fourier optics relationships from the object to the image, the Optical Transfer Function provides the physical
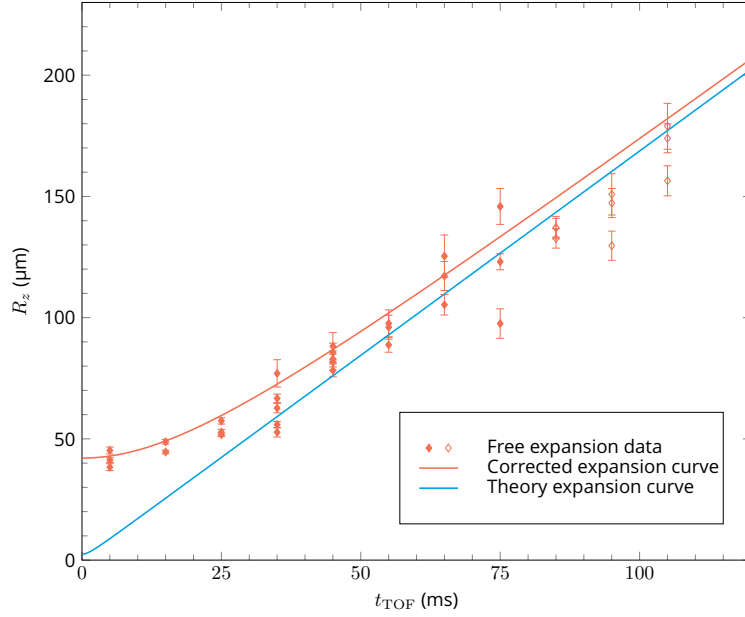
Figure 2.7 – Free expansion of a cloud after an experimental sequence performed in microgravity with the CAL apparatus. The raw simulation results are plotted in blue. The correction applied with $\sigma_{cam} = 42$ µm makes the theoretical data match to the experimental points.

equations used to define the optical system [80, 81]. These equations take the form of the convolution of a function representing the signal to be observed with a function representing the effects of the system. A detailed description of the optical effects of the camera on the imaging of the atom cloud is beyond the scope of our work, but it is not possible to neglect these effects when analysing the experimental images. We drastically simplify this approach by modeling the images on the camera $D_{cam}(x, y)$ by convolution of the computed probability density integrated in the camera plane $D(x, y) = \int |\psi(x, y, z)|^2 dz$ with a 2D Gaussian of width σ_{cor}

$$D_{cam}(x, y) = \iint D(x', y')G(x - x', y - y') \, dx'dy' \tag{2.65}$$

where

$$G(x, y) = \frac{1}{2\pi\sigma_{corr}^2} \ \exp\left(-\frac{x^2 + y^2}{2\sigma_{corr}^2}\right) \tag{2.66}$$

The width of the Gaussian is measured experimentally, for example, when checking the Rayleigh criterion. A typical value of σ_{corr} that is used in $\sigma_{cor} \sim 10 - 20$ µm, which is confirmed empirically by comparing results of simulations and experiments. An illustration of this can be found in the comparison with experimental data of BEC mixtures in Chapter 4.

There is another way to account for the resolution effects of the camera when measuring the size of a cloud. In Figure 2.7, which shows the evolution of the size of a BEC during its free expansion in microgravity, we see that the measured radius of the BEC, represented by the red dots, is larger than what is simulated by the theory, plotted as the blue curve, especially at the beginning of the expansion

when the cloud is small. The size threshold is determined by the optical resolution of the camera. We introduce a heuristic correction for the size evolution of the cloud

$$R_{corr} = \sqrt{R^2 + \sigma_{cam}^2} \tag{2.67}$$

where σ_{cam} is adjusted to the signal as a free parameter, by comparing the distance between the simulation and the data point. In Figure 2.7, the applied correction is $\sigma_{cam} = 42$ µm. We can see that the corrected expansion, plotted in red, matches the variation of the data points.

In 1D, the convolution of two Gaussian functions is also a Gaussian, whose variance is the sum of the original variances. Furthermore, we have seen in section 2.6 that the BEC radius is related to its width by a factor of $\sqrt{7}$. We can see that the results between the two different approximations of the resolution effects of the imaging process can be linked to each other by the relation $\sigma_{cam} \sim \sqrt{7}\,\sigma_{corr}$.

2.9 . Conclusion

This chapter can be seen as a toolbox containing the main theoretical elements that I had to use or develop during the course of my thesis in order to study the dynamics of single-species BECs and to analyze the results of experimental measurements carried out on these systems. The next chapter will show how they can be applied to certain experiments carried out in-orbit. This chapter has shown that a good knowledge of the characteristics of the experimental setup can provide useful insights for the development of theoretical models. In particular, knowing which parameters can be varied experimentally gives a hint as to which physical quantities should be included when developing simulation models, such as the current intensity in the atom chip drivers and coils that create the magnetic potential used to trap the cold atoms. We have seen that the trajectory of a BEC can be easily simulated by solving Newton's equation of motion. Solving this equation, we can deduce, by studying the evolution of the centre of mass of the BEC, the characteristics of the trap, such as its position and frequency.

Regarding the size dynamics of the BEC, we have an alternative to the resolution of the Gross-Pitaevskii equation used in the mean-field approach, with scaling equations. The scaling equations presented in Section 2.6 provide a quick result to the simulations, that describes very well the size evolution for a number of atoms large enough to successfully apply the Thomas-Fermi approximation. It can be used, for example, with the DKC method to find the optimal lensing time that leads to collimation of the BEC during a free expansion stage. Since the analysis of the experiment is done by fitting the fluorescence images of the atom cloud captured by the camera sensors, we have also seen in this chapter how to extract the size of the cloud from the fit, and how to define the rotation matrices that allow us to account for frame transformations in the case of rotations.

To implement the transport of a BEC that is required in some experiments, we presented a protocol for a Shortcut-to-Adiabaticity (STA) transport in the case of a transport in 1D. For a transport in more dimensions, this analytical method is limited, which leads to the necessity of defining another type of ansatz that takes into account the dependence of the coordinates between each other. A solution would be to refine the trajectory by trial and error, using methods such as the Optimal Control Theory (OCT) [82].

Quantum State Engineering of a BEC in an Earth-orbiting laboratory

3.1 . Introducing the Cold Atom Laboratory

In order to achieve the precision required for tests of Einstein's equivalence principle with atom interferometry, a list of requirements has been developed in addition to the study of different sources of uncertainty [17, 54]. A microgravity environment such as space is highly desirable for quantum sensing experiments because atom clouds can then float for extended times of several seconds. It makes possible longer interferometry times thus boosting the precision of these sensors. The interferometry experiments considered use laser beams to perform the splitting, reflecting, and recombining steps. To avoid diffraction effects by the atom chip on the beam [50], it is placed at a certain distance from the chip and at the same time away from the BEC evaporation trap. In order to get the atom cloud to interact fully with the atom beam, one has thus to develop an experimental sequence aimed at displacing the atom cloud and controlling its size evolution.

The Cold Atom Laboratory (CAL) is a NASA-funded BEC machine on board of the International Space Station (ISS). It is a multi-user facility operated by the Jet Propulsion Laboratory (JPL) in Pasadena (CA, USA). It was launched on May 21st 2018, and is operational since June 2018. The Science Module 2 (SM2) is the first CAL science module to be sent on board of the International Space Station (ISS). This machine enables many research applications of the different consortia involved in the project, such as the study of quantum bubbles [83–86], space atom lasers [87–89], few-body physics [90], quantum reflection from material surfaces [91] or entangled state preparation [92, 93]. The details of the experimental setup of the machine which was designed to manipulate BECs of ^{87}Rb can be found in Ref. [51], which reports on the creation of the first BEC in an Earth-orbiting laboratory.

The work conducted during my Ph.D. project was in the frame of the Consortium for Ultracold Atoms in Space (CUAS) led by Nick Bigelow (University of Rochester, New York). It is a US-German collaboration proposing CAL experiments. The aim of the consortium is to control and manipulate quantum gases in space, to implement precision atom interferometry experiments. A first objective was to implement a precise and controlled transport of the BEC, with a control of the position to the µm level, and a control of the velocity to a µm/s level. The second objective was to implement delta-kick collimation to reduce the expansion of the cold ensemble and allow the observation of long free

expansions.

Chapter outline

This chapter develops the results of the CUAS consortium paper [52] in which I participated in the data analysis with other members of the consortium and performed the simulation of the BEC dynamics. The section 3.2 describes the process of gauging the chip model associated with the experiment. It is followed by Section 3.3, which is dedicated to the elaboration of a controlled ramp to move the BEC in its evaporation trap away from the atom chip, with the help of the STA method, and to its characterisation after experimental realisation. This is an application of the scheme proposed in the previous chapter (see Section 2.3). Section 3.4 shows the design of an atomic lens using the DKC method introduced in the previous chapter, in order to control the size expansion of the BEC after its transport. The realisation of an optimal DKC resulted in a lower expansion energy of the order of the tens of pK and in an increased time of flight after which the atoms could be observed on the camera.

3.2 . Chip gauging and first experiments from the CUAS consortium with CAL

Following the installation of the Cold Atom Laboratory (CAL) with the SM2 module on the ISS, began a commissioning phase for NASA's Jet Propulsion Laboratory (JPL). The consortium then started the first experiments with CAL.

The first step was to design a trapping configuration for the atoms, as the possible magnetic field distributions produced by the different structures of the chips and by the magnetic coils are very diverse. Our choice was fixed on a Z-shape trap configuration, combined with two Helmoltz coils aligned on the y-direction, as shown on the left side of figure 3.1**a**. The properties of the trap were first studied using the chip model presented in the previous chapter, section 2.2. According to this model, the Z-shape configuration allows the production of cigar-shaped traps with $\omega_x < \omega_y \approx \omega_z$, which can be shifted along the z-axis by keeping the chip current I_{chip} constant while varying the coil current I_{coil}.

The principle of the experiments realised with CAL is presented in the figure 3.1. The panel **a** describes the transport away from the chip along the z-direction of a BEC from a tight trap where the cloud is oscillating to a weaker trap within a total time t_{ramp}. As the atoms are oscillating during $t_{hold,i}$ in the initial trap or $t_{hold,f}$ in the final trap, the atoms are displaced by Δz_i or Δz_f from the centre of the trap. The experiments realised are divided in two main categories : holding or sloshing experiments to study the in-trap dynamics (see fig 3.1**b** and **c**), and free expansion releases for the release dynamics (see fig. 3.1**d**). For the holding experiments, the atoms are imaged after a fixed expansion time t_{TOF} as the clouds are too dense and the signal would be limited by the diffraction for in-situ imaging. This expansion time gives more margin for the fluorescence imaging process as there is a minimum response time for this process. It also amplifies the oscillations of the cloud, making the fits more accurate. The length of the expansion time depends also on the trap studied. The initial trap shown in the panel **b** is imaged after the short TOF $t_{TOF} = 4$ ms as the trap is very close to the chip surface, and if the expansion time is too long, there is a risk of having the atoms hitting the chip as the cloud
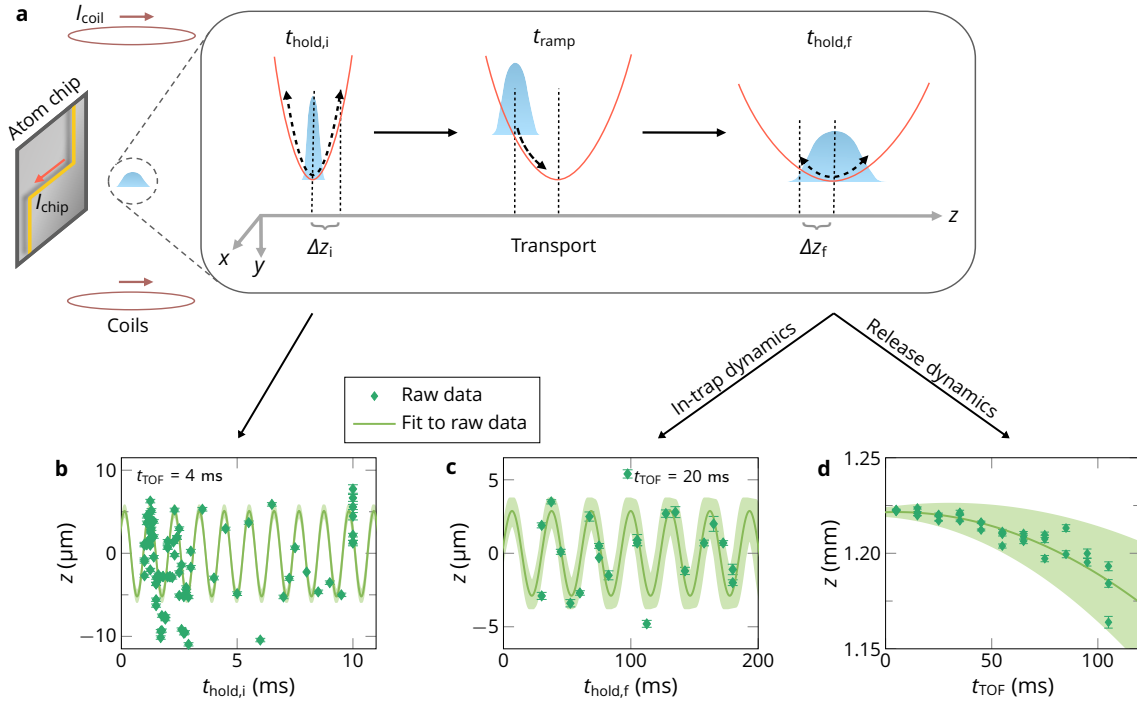
Figure 3.1 – Experiments for the characterization of a BEC in orbit. (**a**) Description of the transport process in the z-direction orthogonal to the chip, and definition of the chip coordinate system. The bottom figures show examples of data measured experimentally with the study of the centre of mass motion in the z-direction. To study the in-trap dynamics, we use sloshing experiments where the holding time in the trap is varied, (**b**) $t_{hold,i}$ for the initial trap and (**c**) $t_{hold,f}$ for the final trap. Then the atoms are imaged at a fixed time of flight t_{TOF}. The periodicity of the signal is used for the frequency calibration of the model, and the amplitude of the signal can be used to judge the performances of a transport. The release dynamics is obtained by scanning the free expansion time t_{TOF} after the release (**d**). The centre of mass parabolic motion in (**d**) shows the effects of the release velocity from the transport combined to those of the residual magnetic fields. The green shaded areas show the 1σ-confidence bounds of the fits and the error bars reflect the single-shot detection noise.

expands quickly. The final trap after transport is further away from the chip, enabling a longer TOF of $t_{TOF} = 20$ ms.

The camera observes the projection of the atom cloud on the (Oxz) plane, but here we are mainly showing the results along the z-direction where the transport happens.

The results of the experiments are analysed and used differently depending on the information we need. For the calibration stage we focus on the holding experiments. The average position and the period of the signal are used to extract the position of the trap minimum and its frequency. The result is then plotted on a graph and compared to the current model as shown for instance in the figure 3.2. Once the trap characteristics are known, we use the holding experiments in specific traps to get more information on the design of the transport. The oscillations in the initial trap used for the transport (see fig 3.1**b**) are due to the transfer of the condensed BEC from the facility trap to a

simplified trap determined by only two currents from the Z-shape chip trap and the bias coils. The presence of these oscillations imposes a choice on the initial holding time to minimize the effect of the offset to the trap minimum, and must be taken into account since it affects the robustness of the transport. The oscillations in the trap at the end of the transport (see fig 3.1**c**) give information on the final velocity of the atoms, and are used to evaluate the performance of the transport. The release dynamics experiments (see figure 3.1**d**) are a more direct method to obtain the release velocity of the atoms at the end of the transport. It can be observed that the trajectory does not follow a linear uniform motion as expected in microgravity, because residual magnetic field gradients accelerate the atoms during the free expansion.

During the calibration, we focused on different values of the coil current, from the initial trap after the formation of the BEC, to the further range of displacement of the cloud, for decreasing values of the current. The choice of a simple trap configuration, such as the one used here, makes the calibration more efficient by reducing the number of parameters to be tested. It is also important because the number of experiments that can be realised by the consortium is limited. Moreover, having the coil current as the only variable parameter simplifies the model.
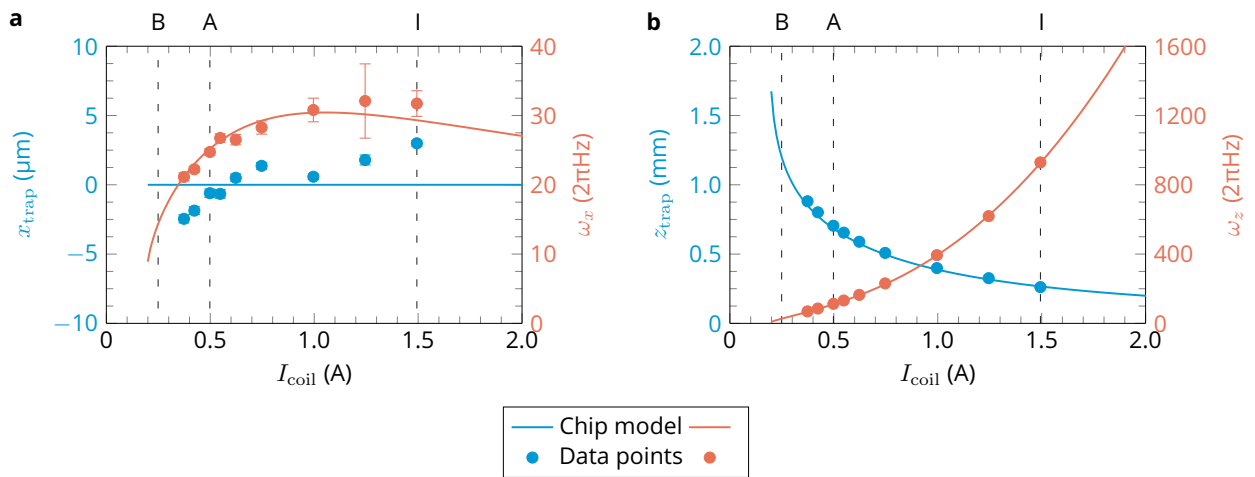
Figure 3.2 – Experimental gauging of the chip model : Plots of the trap minimum positions (blue, left vertical scale) and frequencies (red, right vertical scale) along the x-axis (**a**) and along the z-axis (**b**) as a function of the current I_{coil} in the Helmoltz bias coils. The aim is to calibrate the model such that the theoretical curves match the experimental points. The error bars correspond to the 1σ-confidence bounds of the measurements.

It is usually necessary to introduce simplifications when modeling a real system. For example, the chip model assumes square wires with smooth edges and perfect regular coils. In addition, the microgravity environment of the Cold Atom Laboratory can introduce effects that cannot be anticipated by simply setting the variable associated with the gravitational acceleration to 0. The gauging campaign realised by studying the BEC behaviour in the traps created for different values of coil current I_{coil}, while the other settings are not modified, allowed to adapt the model and improve its accuracy. The aim is to calibrate the model so that for the given intensity value I_{coil}, we obtain the same position

or frequency that is measured. This may involve modifying the intensity value in the model with a scaling factor to get the effective current in the application of the Biot-Savart law. Figure 3.2 shows the results of this gauging campaign, where we observe a very good agreement between the results predicted by the final model and the experimental data. The next section presents the use of these results to achieve the objectives set by the consortium.

On figure 3.2 **b**, we see that the variations of the frequency ω_z and of the trap position z_{trap} are strictly monotonous as a function of the coil current. This enables the definition of a function $\omega_z(z_{trap})$ that will be used for the design of a STA ramp as seen in section 2.3. After calibrating the chip model, which takes into account all the currents in the chip and in the coil, we further simplify it by using a Padé approximant function [94] to express the trap characteristics as a function of the coil current I_{coil} only. A Padé function $R(x)$ is a rational function of the form

$$R(x) = \frac{\sum\limits_{j=0}^{m} a_j\, x^j}{1 + \sum\limits_{k=1}^{n} b_k\, x^k} \tag{3.1}$$

where m and n are two integers chosen to minimize the fitting error.

Once the trap parameters are defined as a function of this master parameter I_{coil}, the designed ramp can be generated by this variable. Then the time variation of this current can be put into tables by the operators at JPL for execution.

3.3 . STA and robustness

3.3.1 . STA ramp design

Once we have a calibrated model of the experiment, we can look at the properties of the trap that can be used. The blue curves in figure 3.2, combined with the chip model for the evolution of the trap minimum y_{trap} in the direction orthogonal to the camera, show that as the bias coil current decreases, the trap moves away from the chip only in the z-direction. The starting point of the experiments is the trap indicated by the dashed line labeled as "I" in figure 3.2, with $I_{coil} = 1.5$ A. This trap "I" is 267 μm away from the atom chip. Its angular frequencies are $(\omega_x, \omega_y, \omega_z) = 2\pi \cdot (29.3, 922, 926)$ Hz. The information from the model is complemented by a scan of the holding time $t_{hold,i}$ shown in figure 3.1**b**. The in-trap cloud oscillation amplitude in the z-direction is of 0.22 ± 0.05 μm, which corresponds to a maximum in-trap velocity of 1.3 ± 0.3 mm.s^{-1}.

The first experiment we want to implement is the shortcut to adiabaticity (STA) transport, as presented in the previous chapter (see section 2.3). The motivation of the transport is to manipulate and control the position and final velocity of the atomic cloud at the μm and μm/s level [52]. This control on the position is necessary to have a cloud that does not move too much so that we can apply pulses for interferometry. The transport should also be robust, since experimentally the cloud is initially not perfectly in the ground state of the trap and can oscillate slightly.

To do this, we designed ramps to two different final trap configurations, Trap A and Trap B. The position and frequency evolution to realize both transports are shown in figure 3.3.

The transport to Trap A takes place over a distance of 0.42 mm, for a duration of 100 ms. The final trap frequencies are $(\omega_x, \omega_y, \omega_z) = 2\pi(f_x, f_y, f_z) = 2\pi \cdot (25.2, 109, 110)$ Hz. This is an ideal configuration for matter-wave lensing experiments, *i.e.* DKC experiments, because the quasi-cylindrical symmetry allows the control of 2 dimensions at the same time.

The transport to Trap B goes to a further distance of 0.93 mm in 150 ms. This longer distance highlights the advantages of the STA method and helps to explore a region further away from the chip. The trapping frequencies of Trap B are weaker, and lose the cylindrical symmetry, with $(\omega_x, \omega_y, \omega_z) = 2\pi \cdot (14.4, 35.1, 26.9)$ Hz. This shallow trap can be used in space because there is no gravitational pull to make the atoms fall like on Earth.
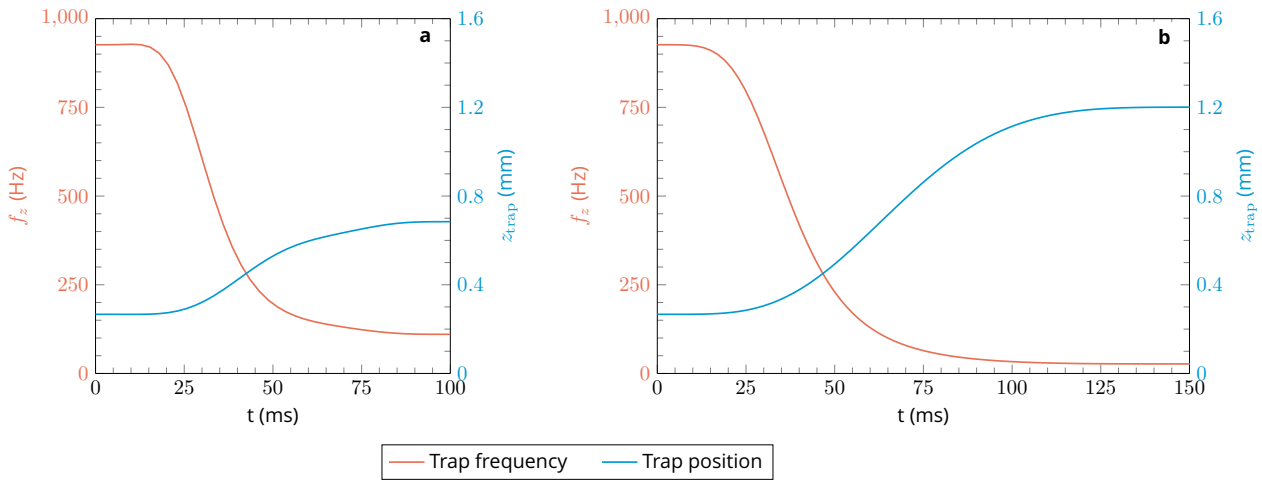
Figure 3.3 – Evolution of the trap minimum position z_{trap} (blue) and frequency f_z (red) during the fast transport in 100 ms to Trap A in the left panel **a**, and in 150 ms to Trap B in the right panel **b**. The trap position z_{trap} is shifted by 0.4 (0.93) mm, while the frequency is reduced from $f_z = 926$ Hz to $f_z = 110\,(26.9)$ Hz for the transport A (B).

The STA ramp design with the reverse engineering method is done by using the equation with the sum of sine functions as in equation 2.12, with the variable parameters (a, b) from equation 2.13.

Once the trap trajectory is found, it is converted into a current variation table for the execution by the operators of the CAL machine at JPL. The execution tables are tables in which each column contains the current to be applied to the different elements of the machine (chip wires, coil, etc.), as well as the intensity of the laser used and the state of the cameras, for example. Each line of the table gives the timing of the operation, and in our case a certain number of lines are dedicated to the variation of the coil current I_{coil} per linear steps. The time step is limited by the machine, since the possible current variation cannot be too fast. The main constraint on the sequence is the number of steps dedicated to the transport due to memory issues. Indeed, the total number of lines possible in an experimental sequence is limited. This is why the ramp to Trap A has only 40 steps, whereas the

ramp to Trap B has 80 steps. The limited number of steps of the current ramps leads to a deviation of the real trajectory of the atoms compared to the theoretical prediction, so that at the end of the transport the atoms do not arrive at rest in the final trap.

Another source of fluctuations and errors in the ramp design is linked to fluctuations in the experimental setup and to imperfect knowledge of all the parameters present. Small fluctuations of currents in some wires can induce variations of magnetic fields, and these small errors can ultimately change the frequency and position of the magnetic traps. It is important to estimate the effect of these errors and control their sources, as small differences in conditions can make the ramp fail its purpose. However, we consider that the main source of error, after the discrete nature of the current variation, is the small oscillation of the BEC in the initial trap. A timing error in the sequence, which corresponds to the instant that defines $t = 0$, is translated into a small offset of the initial position of the cloud, with $z_{trap}(t = 0) \neq z_i$. If the error on the final position or velocity of the BEC at the end of the transport is less than what can be experimentally distinguished or tolerated by the error budget, the ramp and its parameters are considered as robust.

The figure 3.4 shows different theoretical ramps obtained by using different values of (a, b) for the transport to Trap B. In the panel **a** we see the different ramps of the coil current $I_{coil}(t)$ that vary with the parameter that we seek to optimize : the blue curve corresponds to the case where the current variation is the smoothest and the closest to a linear variation. The red curve attempts to minimize the effect of the trap anharmonicity, which is represented by the L_3 term (see equation 2.15). The yellow curve is the optimal trajectory for our case, as it minimizes the offset to the trap center, and minimizes the residual oscillation in the trap in case of fluctuations in the initial trap. In order to quantify the effect of the anharmonic correction, we define the term $P_3(t)$ as a function of $L_3(t)$ in the expression of the effective potential with the anharmonic correction

$$V_\alpha(z_a, t) = \frac{1}{2} m \omega_z^2(t)(z_a(t) - z_t(t))(1 + P_3(t)) \tag{3.2}$$

where

$$P_3(t) = \frac{2}{3} \frac{|z_a - z_t|}{L_3(t)} \ . \tag{3.3}$$

The evolution of this quantity $P_3(t)$ is shown in panel **b**. It shows, in percentage, the effect of the third-order anharmonic correction in the expression of the potential by calculating the percentage of the cubic term on the total potential explored by the centre of mass of the BEC during the transport. The higher $P_3(t)$, the further the BEC explores the anharmonicities of the trap, which can induce perturbations in the condensate dynamics. On this panel, the red curve is the one that minimizes it. The optimised yellow curve shows a good compromise, with a maximum around 2%, compared to the blue curve which peaks around 4%. Panels **c** and **d** show the robustness of the STA ramps by showing the consequence of an offset of the initial position at the beginning of the ramp on the final position and velocity of the cloud. A small initial shift at the beginning of the transport can lead to a big shift in position and velocity at the end if the ramp is not robust enough. The final position of the cloud is controlled at a precision of less than 4 µm, which is comparable to the size of a camera pixel. The final velocity variation is on average less than 0.5 mm.s^{-1}, and we see that the yellow curve, corresponding to the optimal STA ramp chosen, is the most robust to the perturbations in the initial trap.
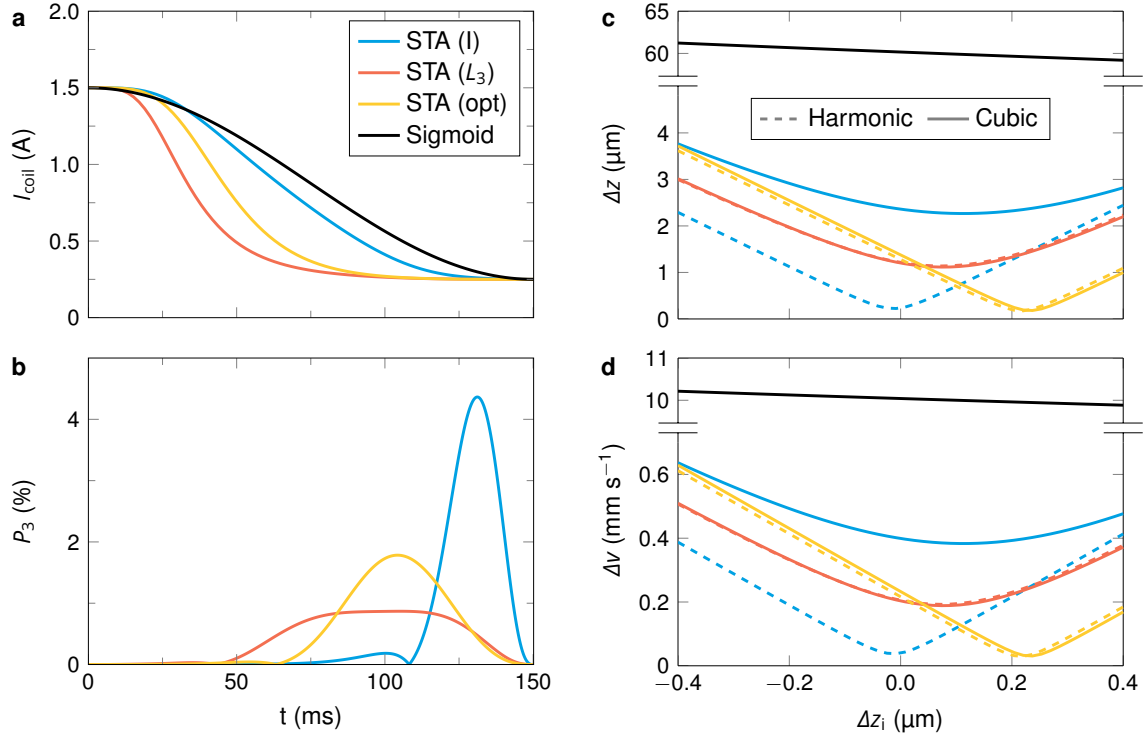
Figure 3.4 – Robustness analysis of different transport ramps leading to Trap B, with the comparison between 3 ramps obtained by the STA method (blue, red and orange lines) and a specific sigmoid function (black line). Panel (**a**) shows the different coil current ramps $I_{coil}(t)$ as a function of time. Each STA ramp is optimised for a different criterion : The blue curve aims at a smooth current evolution, the red curve minimises the contribution of the cubic term in an anharmonic potential and thus minimises the oscillation amplitude, the yellow curve corresponds to a compromise between both constraints. The black curve is a sigmoid centered in time and current. Panel (**b**) shows the evolution of the contribution of the cubic term in the approached anharmonic potential in percents of the harmonic potential term for different choices of optimisation for the STA ramp. Residual position offset (**c**) and velocity (**d**) at the end of the transport for the different ramps as a function of an initial offset in position with respect to the minimum position of the initial trap. The dashed lines correspond to the simulation with a harmonic potential, whereas the solid lines include the cubic term in the potential energy calculation that comes from the fit of the potential minimum.

The black curve in figure 3.4 corresponds to a sigmoid and serves as a control ramp. It is a common test function that can be used experimentally because of its simple S-shape. The coil current sigmoid $I_{sig}(t)$ is defined from the initial $I_0 = I_{coil}(0)$ and final $I_f = I_{coil}(t_f)$ intensities by

$$I_{sig}(t) = I_0 + \left[\frac{s(t) - s(0)}{s(t_f) - s(0)} \right] (I_f - I_0) \tag{3.4}$$

where

$$s(t) = \left[1 + e^{-2\pi \left(\frac{t}{t_f} - \frac{1}{2} \right)} \right]^{-1}. \tag{3.5}$$

We can see that this sigmoid current ramp does not fulfill the requirements for the transport, since the atoms are displaced 60 μm away from the target position z_f at final time, and the residual velocity of the order of 10 mm.s^{-1} is also too high. By playing around with the parameters of the sigmoid, it may be possible to get a better transport, but it is not as systematic as using the reverse engineering method used in our STA approach.

3.3.2 . STA ramp experimental characterization

After designing a robust STA transport for the BEC, we get to the experimental realisation. This is needed to characterise the transport and confirm the simulation results. We first want to check the final position of the atoms at the end of the transport. In-situ imaging of the cloud is not very precise because the atomic cloud is too dense to extract its size on the camera, and the precision is limited to the time at which the images are taken. We prefer a more reliable measurement based on the study of the oscillation amplitude in the final trap.

For this first set of experiments, different holding times in the initial trap $t_{hold,i}$ were considered. Then, for each initial condition, the holding time in the final trap $t_{hold,f}$ was scanned and an image of the BEC was taken after a fixed time of flight (TOF), typically 20 ms. The centre of mass information in the z-direction is then plotted in a graph like the one in panel **c** of figure 3.1. The oscillation of the atoms is then fitted by a sinusoid, and knowing the value of the TOF, we can deduce the in-trap oscillation amplitude (see section 2.4). The results of this experiment are shown in figure 3.5, where we see that the maximum in-trap oscillation amplitude is lower for Trap A than for Trap B. This can be explained by the fact that Trap A is more confining than Trap B in the z-direction.

The theoretical curves (solid lines) in figure 3.5 correspond to an ab-initio simulation of the sequence, and are an application of the analytical considerations from the previous chapter in section 2.4. The initial position $z_{at}(0; t_{hold,i})$ is a sinusoid in $t_{hold,i}$ defined by

$$z_{at}(0; t_{hold,i}) = A_i \cos(\omega_{z,i}\, t_{hold,i} + \phi_i) \qquad (3.6)$$

where $A_i = 0.22 \pm 0.05$ μm is determined from the experimental fit, $\omega_{z,i} = 2\pi \cdot 926$ Hz, and ϕ_i is a phase adjusted such that the residual oscillation amplitude curve is in phase with the experimental data. Using the initial position of the atoms as a boundary condition of Newton's equation of motion, we obtain the amplitude of the oscillation in the final trap. We consider the error in the oscillation measurement in the initial trap as the main source of uncertainty. The shaded area on the theoretical plot are the results of the simulations using the maximum and minimum values of the oscillation amplitude in the initial trap, which are given by the confidence bounds on the experimental measurement. Due to the periodicity of the initial conditions of the experiment, we observe that the in-trap oscillation amplitude at the end of the transport share the same period, and are just shifted in phase.

We finally see a good agreement between the data and the simulations, especially for the transport to Trap A. The measured oscillation amplitudes are of the order of 1 μm and lower, and the minimum value is 0.068 ± 0.072 μm for $t_{hold,i} = 2.4$ ms. The simulations for the transport to Trap B slightly overestimate the oscillation amplitude, but it shows that in the worst case the cloud oscillates in the final trap with an amplitude of about 2.5 μm. The minimum oscillation amplitude measured in
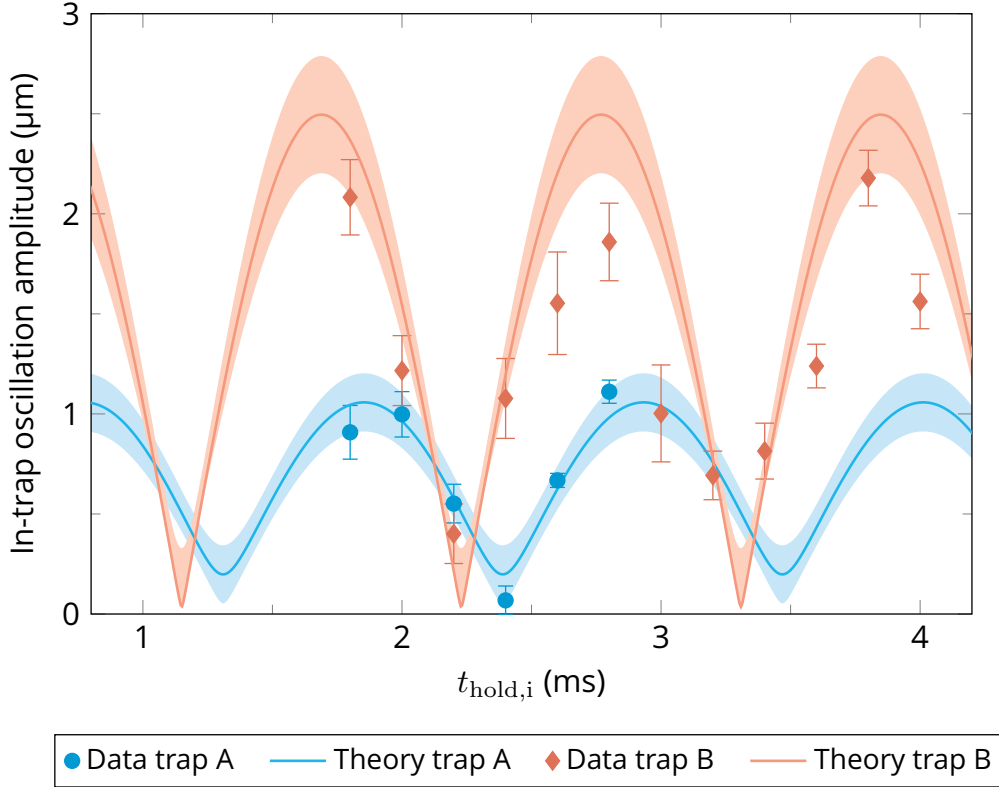
Figure 3.5 – In-trap oscillation amplitude in the final trap after the STA ramp to Trap A (blue dots) and to Trap B (red dots), as a function of the holding time in the initial trap $t_{hold,i}$. The measurements were taken after 20 ms of TOF. The solid lines show the results of the theoretical model. The error bars and shaded areas correspond to the 1σ confidence bound on the fits and on the model, respectively.

Trap B at the end of the transport is 0.40 ± 0.15 µm for $t_{hold,i} = 2.2$ ms. This shows that it is possible to control the position of the BEC at the end of the transport better than the 1 micron level required for precision interferometry tests [95].

After checking the robustness of the STA ramps in terms of control of the final position, we study the release velocity from the final trap as a function of the initial holding time. Numerically, it is obtained by calculating the final velocity of the atom cloud at the end of the transport $\dot{z}_{at}(t_f; t_{hold,i})$. Experimentally, the COM of the atom cloud follows a parabola during its free expansion at the end of the transport, and we extract the release velocity from the fitted parabola. As an example, we see the data and the corresponding fit from such an experiment in the panel **d** of figure 3.1.

Figure 3.6 shows the result of the measurement of the release velocity at the end of the STA as a function of the holding time in the initial trap $t_{hold,i}$, where the atoms initially oscillate. The error bars are larger due to the statistical noise, and to the limited extent for the time of flight over which the atomic cloud signal can be measured. The theoretical curves are the results from the simulations, and the shaded area correspond to the behaviour of the atoms when we take the extreme amplitude

values from the initial oscillation of the cloud. Both curves have the same period as the initial trap, and a different phase.
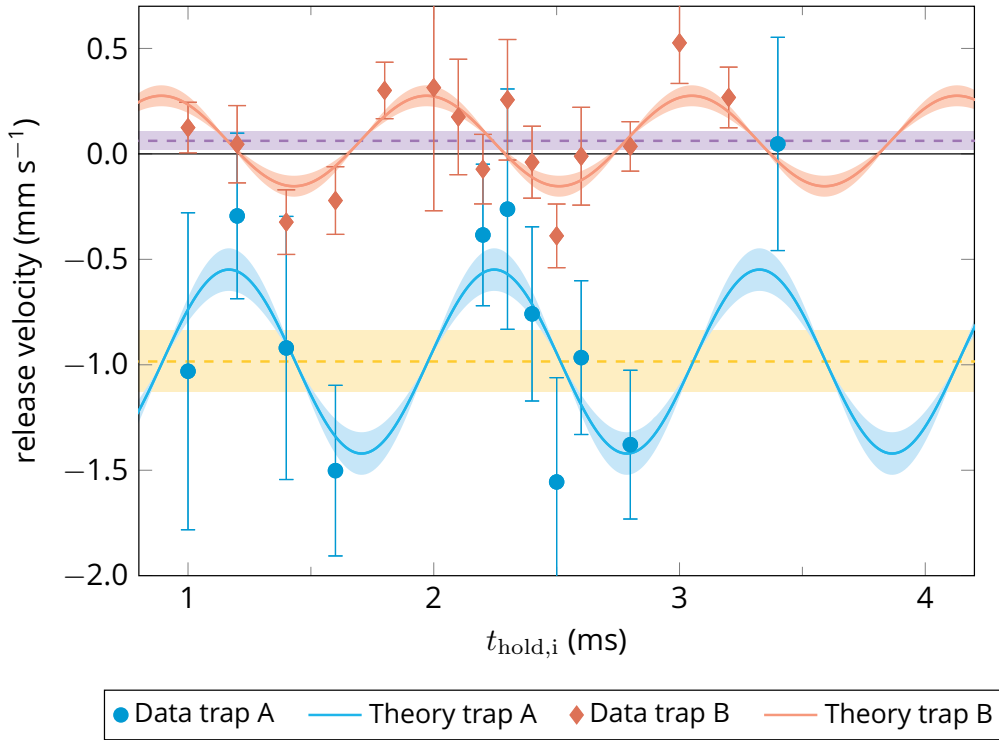
Figure 3.6 – Release velocity from the final trap after the STA transport to Trap A (blue) and Trap B (red) as a function of the initial hold time $t_{hold,i}$. The solid lines show the results of the theoretical model. The horizontal dashed lines (yellow for Trap A, purple for Trap B) show the offset applied to the theory curves to match the experimental data. This velocity offset is a trap-dependent systematic shift of $\Delta v_A = -0.98 \pm 0.15$ mm.s^{-1} and $\Delta v_B = +0.062 \pm 0.045$ mm.s^{-1} and is caused by the finite switch-off of the trap. The error bar for the experimental points and the shaded areas show the 1σ-confidence bounds of the fits and the model respectively.

In an ideal world, the simulations predict that the release velocity will follow a sinusoid centered at 0. To match the experimental results, the curves were shifted by $\Delta v_A = -0.98 \pm 0.15$ mm.s^{-1} for Trap A and $\Delta v_B = +0.062 \pm 0.045$ mm.s^{-1} for Trap B. These trap-dependent shifts are represented respectively by the yellow and the purple dashed lines in figure 3.6, and are caused by the finite switch-off time of the trap. This kick is more important for Trap A because the distance to the atom chip is closer than for Trap B. The error bar for the experimental points is smaller around the inflection points of the theoretical curves, around the average release velocity. For Trap B, the minimum uncertainty is of 0.117 mm.s^{-1} for $t_{hold,i} = 2.8$ ms. These curves show that it is possible to tune the release velocity at the end of the transport in a range between -1.5 mm.s^{-1} and 0.5 mm.s^{-1}.

For the next sequence of experiments where we aim to control the expansion of the cloud, we focus on the sequence to Trap A, that leads to a cylindrical trap.
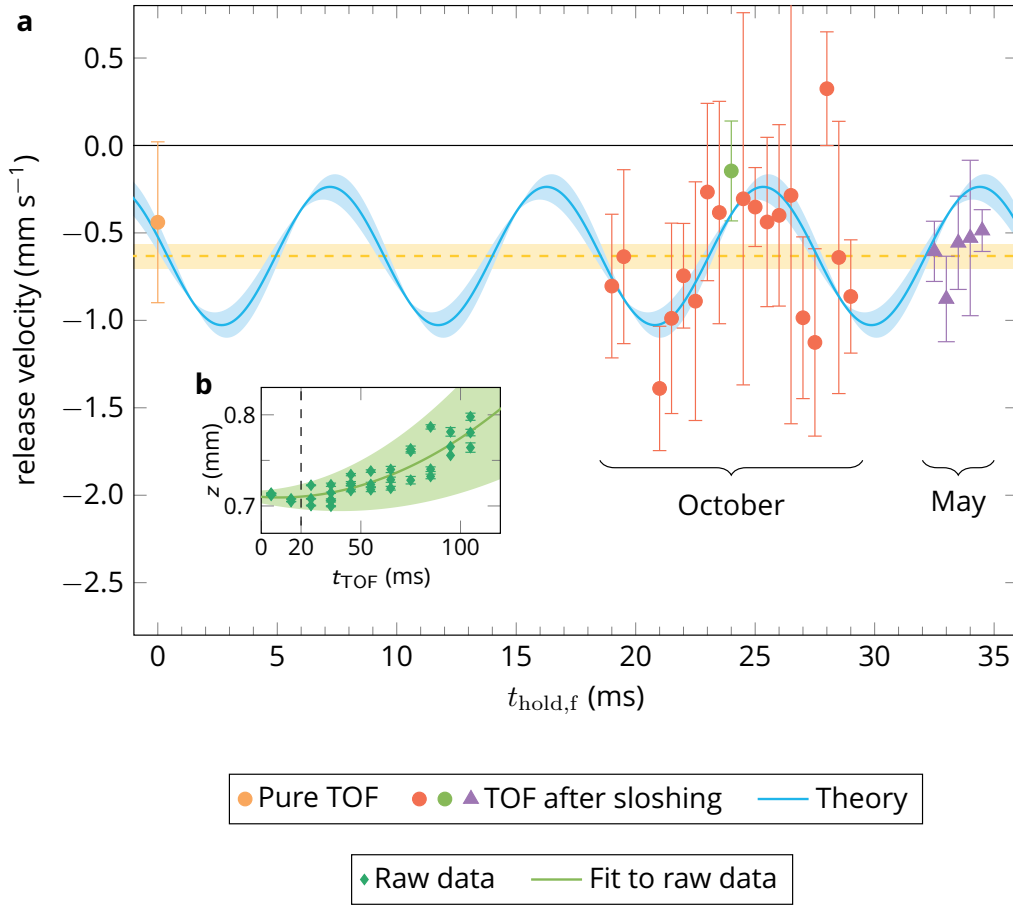
Figure 3.7 – Long term stability of the BEC release and preparation of atomic lensing. **a** Evolution of the release velocity in the z-direction as a function of the holding time in the final trap $t_{hold,f}$ after the STA transport to trap A. The data from May 2019 (purple triangles) is compared to the data collected during a two-week campaign in October 2019 (orange, red and green points), showing a good agreement with the model although the average altitude of the ISS was increased by 7 km between both campaigns due to regular orbit adjustments. The velocity offset (yellow dashed line) $\Delta v_A = -0.63 \pm 0.07$ mm.s^{-1} is solely caused by the switch-off of the final trap. **b** Centre of mass evolution along the z-direction during the free expansion after $t_{hold,f} = 24$ ms in the final trap associated to the green data point in the main figure. The error bars and shaded areas correspond to the 1σ confidence bound on the fits and the model, respectively.

Figure 3.7 shows the long-term stability of the BEC release with CAL. The data were taken over two main experimental campaigns from May 2019 and October 2019. The sequence starts with an optimal hold time of $t_{hold,i} = 2.4$ ms, which leads to a minimum oscillation amplitude of the atom cloud in the final trap. In these campaigns, we scan the holding time in the final trap and measure the release velocity from the trap from the centre of mass evolution during the free expansion. The processing is the same as for the study of the release velocity at the end of the transport as a function of the initial holding time from figure 3.6. We can see from figure 3.7 that there is a good agreement of the May

and October data with the theoretical model. This shows the robustness of this model with respect to the conditions of the ISS, whose average altitude increased by 7 km between the two campaigns due to regular orbit adjustments. We also observe the effects of the final trap switch-off, i.e. a kick from the chip, with the velocity offset $\Delta v_A = -0.63 \pm 0.07$ mm.s^{-1}, represented by the yellow dashed line. The green data point on the main graph at $t_{hold,f} = 24$ ms corresponds to the optimal configuration we will use for the next part of the atomic lensing sequence.

The panel **b** from Figure 3.7 shows the centre of mass evolution in the z-direction after release from the trap for the case $t_{hold,f} = 24$ ms. Fitting the data by a parabola, which is plotted with a solid green line, gives us the value of the minimum release velocity $v_z = -0.146 \pm 0.286$ mm.s^{-1}. This low release velocity gives the atom cloud a wider range of time of flight before which we can trap it in a potential centred at z_f and "catch" it again near the trap minimum. The combination of the effective velocity from the release and the residual magnetic gradients in the setup results in a small displacement of the BEC of only 0.2 ± 5.9 µm within the first 20 ms of free expansion. This provides an ideal setup for a delta-kick collimation.

3.4 . DKC, control of size expansion

3.4.1 . Preparation of the experimental sequence

We continue this transport sequence with a holding for a control of the release, that we will complete with a small free expansion followed by a DKC, and ending with a final free expansion for the imaging. For the realisation of the lensing sequence, we need to fix a few parameters, such as the frequency used for the lensing, the duration of the free expansion before the lensing, and the duration of the lensing. All of these parameters are chosen after simulating the sequence using the chip model and the knowledge of the experiment obtained from the sequences performed on board of the ISS. The first simulations use the Thomas-Fermi approximation and the scaling equations from the paper of Castin and Dum [57], because they are fast to implement and make it easy to scan the various parameters. Once we have a first idea on these parameters, we can simulate the sequence with more accuracy.

The lensing sequence is performed using Trap A, which is cylindrical, because it allows to control the size of the BEC in the y- and z-directions at the same time. We note that, according to equation 2.32, the trapping frequencies of Trap A $(\omega_x, \omega_y, \omega_z) = 2\pi(f_x, f_y, f_z) = 2\pi \cdot (25.2, 109, 110)$ Hz are too high to give a reasonable lens duration that can be performed in the experiment. The magnetic potential in the setup is related to the currents in the different wires by the law of Biot and Savart. In the harmonic approximation around the trap centre, it can be shown that there is a quadratic law relating these intensities to the trap frequencies. According to this model, we divided all currents (from the chip and the bias coil) by the same number, here 16, and get a trapping potential sharing the same position, and frequencies divided by the square root of the scaling factor, here 4.

The choice of this trap, that we will call the DKC trap, sets boundary conditions on the duration of the free expansion t_{exp} before the lensing, since we need to capture the atoms near the trap centre. The results of the sloshing experiment in Trap A shown in figure 3.7**b** show us that we can consider

the first 20 ms of the free expansion. In addition, a longer expansion time is problematic because the cloud size evolves rapidly, and a large cloud before the DKC will continue to grow after the DKC. For the lowest bound of t_{exp}, it should be long enough not to be in the hydrodynamic regime of the BEC size evolution. However, since the lensing time decreases with the expansion time t_{exp} (as seen in equation 2.32), we prefer to set this expansion time near its upper bound. After simulations in the case of 15 ms and 20 ms of expansion, we decide to set $t_{exp} = 20$ ms.

The last parameter to fix is the lens duration t_{lens}. It is found by simulating the sequence with a software such as Mathematica and keeping it as a free parameter. Since the calculations have to be done in a short time, we use the scaling approach for the size dynamics and we scan the possible lens durations using the "Manipulate" function of Mathematica. According to this simplified model, the optimal lens time is $t_{lens} = 1.6$ ms. Finally, we simulate the whole sequence and solve the dynamics determined by the Gross-Pitaevskii equation to confirm that we have a reduction in the expansion rate of the BEC in the y- and z-directions as expected.
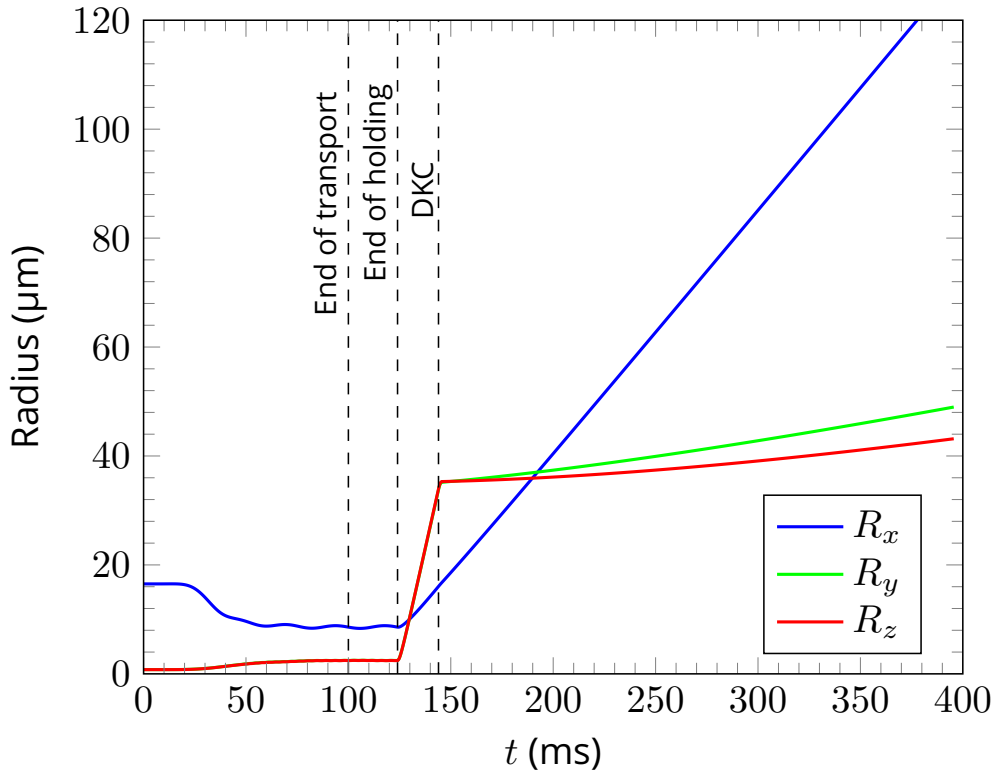
Figure 3.8 – Simulation of the BEC size evolution for a sequence controlling the size expansion of the BEC with CAL using an atom lens. The sequence is divided into different phases, separated by a dashed line : the STA transport to Trap A, followed by a holding in the final trap, a short free expansion, the DKC and the final free expansion.

Figure 3.8 shows the evolution of the BEC radii given by the GPE for the sequence using the optimized parameters we found. This sequence is a bit simplified compared to the one realised with CAL

and is decomposed in the following steps :
— $t = 0$ ms the ground state is calculated in the initial trap using the imaginary time propagation algorithm.
— For $0 \leq t \leq t_f$, transport dynamics using the STA ramp, which moves the atoms to Trap A. The end of the transport is materialised by the first vertical dashed line.
— During $t_{hold,f} = 24$ ms, the trap frequencies are constant and keep the values from Trap A. This phase, which is ended by the second vertical dashed line, is necessary in the experiment to control the atoms velocity during the release of the atoms due to the effect of the chip currents and of the residual magnetic fields in the setup.
— For $t_{exp} = 20$ ms, free expansion of the BEC until the lensing starts.
— For $t_{lens} = 1.6$ ms, the DKC trap is switched on. Since it is very short, it is represented by a simple vertical dashed line in the figure.
— Final free expansion of the cloud. The time of flight ends with the imaging sequence in the experiments.

For the simulation, the choice of the atom number in the BEC plays a minor role, since it appears to be of little influence. In the case of the Thomas-Fermi approximation, we have $R \propto N^{1/5}$, which corresponds to a small scaling factor that is global to the whole size dynamics and that is not affecting the timing of all the steps of the sequence.

3.4.2 . Experimental results and analysis

Now that we have found the optimal sequence for the control of the BEC, we can proceed to execute it and analyze the experimental data. When the sequence written above is sent to the JPL for the creation of the execution table, we add at the beginning an initial holding time of $t_{hold,i} = 2.4$ ms to compensate for the fact that we do not start with a condensate in its ground state in the initial trap. To get a better overview of the effect of the DKC in microgravity, we scan different lensing durations. This helps to check if there are other phenomena that need to be considered in the simulations. We will study the results of the following DKC pulse durations : 1.4 ms, 1.6 ms, 1.7 ms, and 1.8 ms, which were also presented in our paper and its supplementary material [52].

Figure 3.9 provides a lot of information. First, we can see from the free expansion without DKC (in red) and the expansion after DKC (in green) that the lensing trap accomplished its mission. Each plot shows a different behaviour of the lensed atoms, showing the effect of the pulse duration. The expansion rate of the lensed cloud is smaller, and it extended the TOF after which the atom cloud was observed from $t_{TOF} \approx 105$ ms for the free expansion, to $t_{TOF} \approx 300$ ms for the 1.8 ms lens.

The fit of the atomic clouds observed on the camera is challenging due to different experimental constraints. This is highlighted by the choice of different shades of green for the DKC data, as well as the representation of some data points by empty circles. For the light green empty circles we observe split clouds. The BEC is in a magnetically sensitive state $m_F = 2$, and after applying the lensing potential, the BEC is split into two individual clouds in the $m_F = 1$ and $m_F = 2$ hyperfine sublevels by non-adiabatic spin-flip transitions due to magnetic field switching, similar to what was observed by another CAL consortium in the article [96]. The splitting occured in the x-direction and the majority of the atoms remained in the $m_F = 2$ state and were fitted to obtain the data from the empty
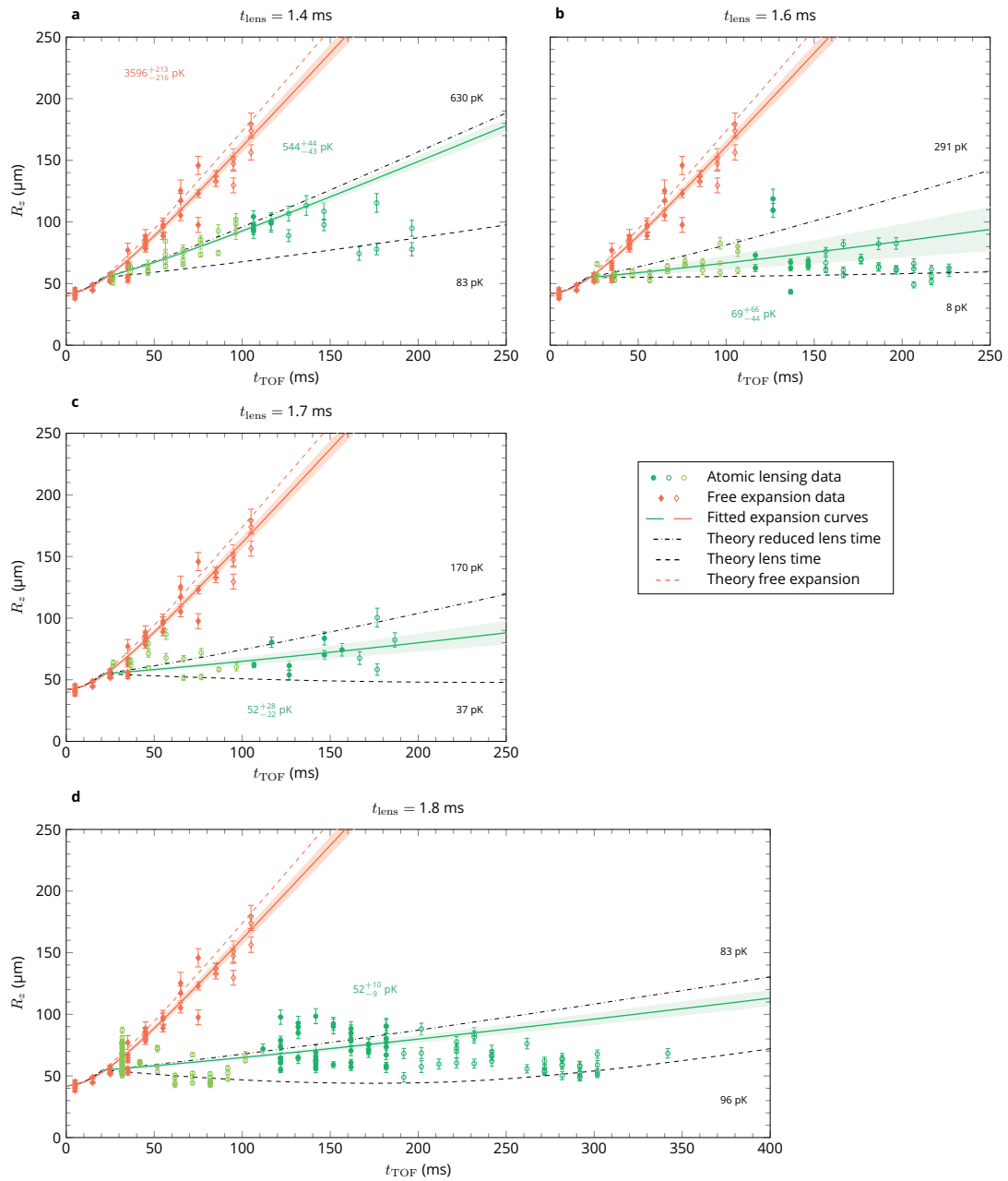
Figure 3.9 – Evolution of the BEC radius along the z-direction for different DKCs realised with CAL (green), compared to the free expansion curve (red). The error bars combine the standard deviation of the 1σ confidence bound of the data points averaged over many shots. The reduced lens time (see text) corresponds to the indicated lens time shortened by 0.4 ms. The indicated expansion temperatures are calculated from the slopes of the linear fits to the data points, and from the slopes of the linear expansion regime of the theoretical simulations.

circles. Moreover, this splitting only affected the atomic lens experiment, but not the pure free expansion experiment. This affects the clouds mainly for $t_{TOF} \leq 100$ ms and makes the fitting of nearly overlapping clouds challenging, especially for the fitting of the size R_x in the x-direction. For the long expansion times, the decrease of the contrast and the lower signal-to-noise ratio make the detection of the cloud difficult. The minimum density that can be detected experimentally is estimated to be $2 \cdot 10^{11}$ atoms/m^2, and using our simulation models, the data points where the density falls below this threshold are represented by dark green empty circles. The cutoff time depends on the lens duration due to the lensing effect, and increases from 120 ms to 190 ms as the lensing time increases. The most reliable points in medium time-of-flights are represented by the full dark green circles and are used to fit a linear expansion curve.

For greater consistency between the plots, all the data points for the size evolution are renormalized to the same number of atoms. Since the fit uses the definition of the Thomas-Fermi radius, this renormalization is done using the relation $R \propto N^{1/5}$. In all the plots, we consider $N = 2,000$ condensed atoms. This is also the number of atoms used for the simulations solving the Gross-Pitaevskii equation. This number is close to experimental realizations, where about 2,000 to 4,000 atoms are condensed, with a BEC fraction of 10 to 25%. For information, during the calibration measurements, the BEC fraction was less than 10% and the number of condensed atoms reached a maximum of 12,000.

We observe that the size of the cloud measured in the z-direction is limited to about 45 μm, creating a kind of plateau effect for some expansions. This experimental limitation does not allow to accurately measure the short time behaviour of the BEC, since its initial size is of the order of $R_z \sim 10\,\mu$m. Therefore, we introduced a correction factor $\sigma_{cam} = 42$ μm to account for the effects of the camera optics on the resolution, as seen in the previous chapter and in Figure 2.7. This correction factor was found by calibrating the simulation model to match free expansion curves where the overall atom density is sufficient for reliable measurements of the BEC size.

We observe on the DKC data (Fig. 3.9) that the measured size of the atom cloud is systematically larger than what is expected by the simulation with the theoretical lens time, which is the lower dashed line. This means that the effective lens is weaker than expected. There are several reasons for this, such as the finite switching time and the response time of the current drivers. A realistic simulation of this would be to describe the rise and fall of the currents with exponential decay functions for which the characteristic time depends on the nature of the object (coil or chip wire). However, this would require both better knowledge of the machine and calibration experiments, which cannot be done due to limited user time on the device. In addition, this knowledge is not crucial for the understanding of the experiment. There are also some analytical problems in the chip model when simulating the exponential decay of the currents, since the frequencies diverge to infinity as the trap minimum approaches the chip. The solution we chose for the DKC simulation was to simulate the lensing using a potential with constant frequencies, i.e. keeping the current values constant, but for a shorter effective time. We simulated the sequence and gradually reduced the lens time from $t_{lens} - 0.1$ ms to $t_{lens} - 0.5$ ms. We then compared the average standard deviation between the theoretical curve and the data points (taking into account the resolution correction). Finally we find that the optimal reduced lens time is $t_{lens} - 0.4$ ms, as shown by the upper dashed-dotted lines on the graphs.

To quantify the difference in expansion between the different sequences, we compare the slopes of the expansion curves at long time-of-flights where we reach a linear expansion regime. For easier comparisons, we convert these slopes to pK temperatures by analogy with the definition of the thermodynamic energy. We also change the equation (2.34) to the following definition

$$\frac{k_B T}{2} = \frac{m}{2} \left(\frac{dR}{dt} \frac{1}{\sqrt{7}} \right)^2 \tag{3.7}$$

where the factor $\sqrt{7}$ relates the Thomas-Fermi radius to the standard deviation of the cloud [62, 97]. We see that experimentally the 1D expansion slows down as the DKC time increases. We can also notice that for the theoretical curve of the 1.8 ms lens, the expansion temperature increases again. This is due to an overfocusing effect of the lens. In the best case, the expansion temperature goes from $3,596^{+213}_{-216}$ pK for the free expansion to 52^{+10}_{-9} pK for the 1.8 ms lens. This 70-fold reduction in expansion energy nearly triples the observation time of the BEC on the camera.

3.5 . Conclusion

This chapter has presented experiments in a modular, multi-user quantum gas laboratory, demonstrating cold atom applications in space. Compared to ground-based experiments, there are more constraints to consider, such as the inability to make hardware changes to the module, remote operations and limitations on the sequences that can be run depending on the capabilities of the software interface, as well as delays in data retrieval. However, regular exchanges between the teams and JPL scientists helped overcome these challenges. Regular feedback from the simulations guided the choice of parameters for the implementation of the experiments. The first campaigns on the CAL machine were dedicated to the development of the chip model and resulted in well gauged chip traps. This gauging was essential for the development of the following experimental campaigns as well as for the data analysis and simulations. Consequently, there was a very good agreement between the simulations and the experimental results on all data plots presented.

Taking advantage of the microgravity environment, we could engineer transports of BECs to traps with frequencies as low as tens of Hertz, which cannot be implemented on Earth due to the gravitational force pulling down the atoms. With the STA method, it was possible to implement the transport of a BEC at a velocity of 6 mm/s over a distance roughly 1,000 times its size. The precision with which this was done allowed us to fully achieve our objectives, with a control of the final position of the BEC achieved to within 70 nm. By playing with the holding time in the final trap, we have shown that it is possible to tune the release velocity at the level of 100 μm/s. The DKC was also successful in reducing the expansion energy to about 50 pK. This enabled the observation of the atom cloud after a longer time of flight, almost tripling it compared to the direct observation at the end of a transport in the case of the 1.8 ms lens. It also demonstrated the possibility to observe freely expanding gases on time scales inaccessible to ground experiments.

We can conclude that the objectives of the consortium were satisfied at the end of the campaigns with CAL. It also proved the robustness of the implemented method with a stability of the results

observed over months and millions of km of operation on a 90-minute orbit of the ISS. In order to perform state-of-the-art measurements testing the universality of free fall with dual-species atom interferometry [33], the control on the initial state would require the positioning uncertainty to be no greater than 1 µm and the expansion energy to be in the order of a few tens of pK. These two stringent requirements have been met by the quantum state engineering achieved here with single-species condensates of Rb. It demonstrates the feasibility of fundamental physics missions in space that could be conducted in future satellite tests of Einstein's equivalence principle with the STE-QUEST project [17, 98] aiming for a precision of the measurements at the 10^{-17} level in the Eötvös ratio.

Low atom numbers in the system made the data analysis challenging in some cases due to the low signal-to-noise ratio. We expect a major improvement with the next generation CAL machine and the envisioned BECCAL payloads [41] on the ISS. By increasing the atom numbers to 10^5 instead of 10^4 in the BEC, the measured signal strength would increase greatly, allowing better measurements. Software upgrades with more flexible current controllers would enable even smoother transport ramps (using ramps of a few hundred discrete steps instead of the 80 used here) for a better control of the transport. Finally, dedicated studies with atoms in the magnetically insensitive Zeeman states will allow for an undisturbed free expansion of the floating atoms. These technical improvements could already make it possible to access positioning accuracies at the nm level and observation times of several seconds, compatible with the most ambitious quantum technology applications in space [48].

The experiments presented in this chapter ended with the replacement of the new CAL science module SM3 on the ISS in January 2020. The lessons learnt from the machine concerning its operation and the data analysis were very rich. They gave us a blueprint of the different steps to follow for characterising the experimental setup and gauging the chip models. The next step is then to explore the new capabilities provided by the SM3 module, such as atom interferometry and dual-species experiments with the addition of K atoms to the system.

Study of dual species BEC mixture and its applications

4.1 . Introduction

The study of cold atom mixtures is very rich and has inspired many theoretical [97, 99–107] and experimental research [108–116]. Mixtures may consist of two (or more) components, which can be internal states of a single species Bose-Einstein condensate [101], two isotopes of a single species [112], or two different species [102, 103, 115]. In recent years, interest in binary mixtures has spread from theoretical studies to applications in diverse domains like metrology, with, for example, their use in high-precision atomic interferometry experiments. Proposals of realisations of Einstein's Equivalence Principle [17, 18, 54, 95] suggest the use of dual-species BEC mixtures to implement simultaneous interferometry experiments in order to benefit from the precision brought by these quantum objects.

In our work, we consider mixtures of ^{41}K and ^{87}Rb as they are used in the microgravity projects MAIUS-2 and CAL. The choice of these species is mainly due to experimental feasibility [97, 108–110], with for instance advantages brought by the existence of interspecies Feshbach resonances at low values of magnetic fields. The MAIUS-2 team plans to send a sounding rocket into space to create BEC mixtures and to realise dual-species atom interferometry [79]. During ground tests of the payload, experiments with BEC mixtures were realised and some detection images could be used for comparison with our models. The Science Module 3 (SM3) of CAL, which is operational on board of the ISS since 2020, offers the possibility to perform dual species experiments. One objective of the CUAS consortium is to study the dynamics of a mixture of K and Rb in order to control it for future dual species interferometry experiments. These two projects share common features such as the use of atom chips for magnetic traps to manipulate the atoms, and imaging systems placed with the sensor plane orthogonal to the chip. Regarding the trap geometry, both have a quasi-cylindrical configuration with cigar-shaped traps. This allows the use of similar theoretical approaches for the simulation of the experimental sequences and for the comparison with experimental results.

As for theoretical studies, researchers have started by considering the Thomas-Fermi approach and by applying methods similar to single-species calculations [97]. Many calculations have focused on homonuclear mixtures or binary mixtures that are composed of two internal states of the same atomic species or two isotopes of the same species (e.g ^{85}Rb and ^{87}Rb) , which make it possible to simplify certain analytical expressions, the main variable parameter then being the interaction between the two species, given that the masses are the same. Some calculations simplify the potential term

further by considering the same trapping frequencies for both species [99]. From both an analytical and numerical point of view, it is also easier to start with spherical symmetry, since with spherical coordinates calculations are then reduced to a single dimension [99, 103]. However, due to the absence of such a symmetry in our problem, our calculations are best performed using a generic 3D Cartesian coordinate system, which makes analytical calculations too complex to implement. Therefore, in our problem the ground state of the system is calculated numerically using the imaginary time propagation method [70, 117] solving the time-independent coupled Gross-Pitaevskii equations for the binary mixture. In addition, problems with the study of displacements and fast condensate expansion are also expected with BEC mixtures, since the additional interaction between the two species makes the choice of the computational grid more complex. Indeed, the evolution of the two-species condensate can be described with the help of a scaling approach only under very specific conditions [63, 97]. The numerical method presented in this chapter takes a different approach. First, an affine transformation of the grid allows it to be translated over time, following a specific displacement associated with the centre of mass of one of the species. Next, the coordinates are scaled to account for any expansion or contraction of the dual-species condensate during the dynamics. This is an extension of the change of variables previously introduced in Sections 2.4 and 2.6 for the single-species case.

Depending on the interaction strength between two species in a BEC mixture, it is possible to classify these mixtures in two different categories : miscible or immiscible [56]. In miscible cases, the atomic densities can overlap and respect the geometry of the trap in the ground state. On the other hand, an immiscible mixture does not allow overlap, and the spatial distribution of the condensate is strongly affected, usually breaking the geometry of the trap. In microgravity, the different distributions can be even more diverse with a co-located trap centre for both species compared to the presence of gravity, where the trap minima are shifted due to the gravitational sag. In simulations, these different cases can be studied by numerically tuning parameters such as the trap characteristics, atom numbers or interaction strengths. Experimentally, it is possible to tune the inter-species scattering length to have different interactive behaviours for the mixtures with the help of Feshbach resonances [113]. For short-term applications to space experiments, we are limited to the triplet scattering length, which makes the mixture of K and Rb non-miscible.

Chapter outline

This chapter is divided into two main parts, which contain some results and discussions already presented in Refs. [64] and [53], of which I am co-author.

The first part of this chapter presents the theoretical tools I developed to treat the dynamics of a BEC mixture for the transport or expansion of the system. After defining the notations I will use and the reference frame for the calculations (Section 4.2), I introduce the grid transformations (Section 4.3). Finally, in Section 4.4, I will present some issues that arise when simulating the ground state of a dual-species mixture in microgravity.

The second part of this chapter presents numerical applications of the theoretical approach as well as applications to experiments on ground and in microgravity. In the first application (Section 4.5), which is only numerical, I implement a transport of the mixture confined in an atom chip trap for a shift of the trap minimum over a distance of about 20 µm in 10 ms, followed by a holding period

of 20 ms in the final trap. The second application (Section 4.6) aims to simulate the free expansion of a BEC mixture on ground to test the handling of a grid expansion by our codes using the scaled-grid approach. These applications contrast a fixed-grid approach with our theoretical approach in order to validate the model. Then I compare the numerical result with experimental measurements obtained by the MAIUS team [79]. I continue with the study of mixtures produced in orbit with the CAL experiment, and end with simulations aimed at preparing future experiments with the same device (Section 4.7).

4.2 . Presentation of the theoretical model for multi-species interacting mixtures

We consider an ensemble of n_{sp} different Bose-Einstein condensates interacting in a multispecies mixture. These could correspond to different species as what we will study in later applications where species 1 is Rubidium-87 and species 2 is Potassium-41. In the literature, we can also have the case of different isotopes of the same species [111, 112] or different internal states of the same species [118, 119] for dual interacting mixtures. At zero temperature and within the mean-field approximation, the time evolution of this multispecies mixture of BEC is described by the time-dependent coupled Gross-Pitaevskii equation

$$i\hbar\partial_t\psi_j(\boldsymbol{r},t) = \left[-\frac{\hbar^2}{2m_j}\boldsymbol{\nabla}_{\boldsymbol{r}}^2 + U_j(\boldsymbol{r},t) + \sum_{j'=1}^{n_{sp}} N_{j'}g_{jj'}|\psi_{j'}(\boldsymbol{r},t)|^2\right]\psi_j(\boldsymbol{r},t) \tag{4.1}$$

where j and $j' = 1, 2, ..., n_{sp}$. As we will use matrix notations for the following calculations, we use $\boldsymbol{r} = (x, y, z)^T$ to denote the position vector in a fixed frame of reference (for example the lab frame) and ^{T} is a standard notation used to indicate the transposition. We use the convention where the wave function of species j, $\psi_j(\boldsymbol{r},t)$, is normalised to 1, and m_j corresponds to the mass. N_j is the atom number in the condensate and U_j corresponds to the external potential of species j. The scattering amplitudes $g_{jj'}$ are related to the corresponding s-wave scattering lengths $a_{jj'}$ by the relation

$$g_{jj'} = \frac{2\pi\hbar^2 a_{jj'}}{m_{jj'}} \tag{4.2}$$

with $m_{jj'}$ being the reduced mass

$$m_{jj'} = \frac{m_j m_{j'}}{m_j + m_{j'}} \tag{4.3}$$

We consider situations where the multispecies condensate is trapped in a general external potential described by the functions $U_j(\boldsymbol{r},t)$ that we decompose in the sum of a harmonic and an anharmonic part, similarly to the Taylor expansion of a function fitting the potential, with

$$U_j(\boldsymbol{r},t) = V_j(\boldsymbol{r},t) + W_j(\boldsymbol{r},t), \tag{4.4}$$

where

$$V_j(\boldsymbol{r},t) = \frac{1}{2}m_j\left(\boldsymbol{r} - \boldsymbol{r}_j(t)\right)^T\boldsymbol{\Omega}_j^2(t)\left(\boldsymbol{r} - \boldsymbol{r}_j(t)\right) \tag{4.5}$$
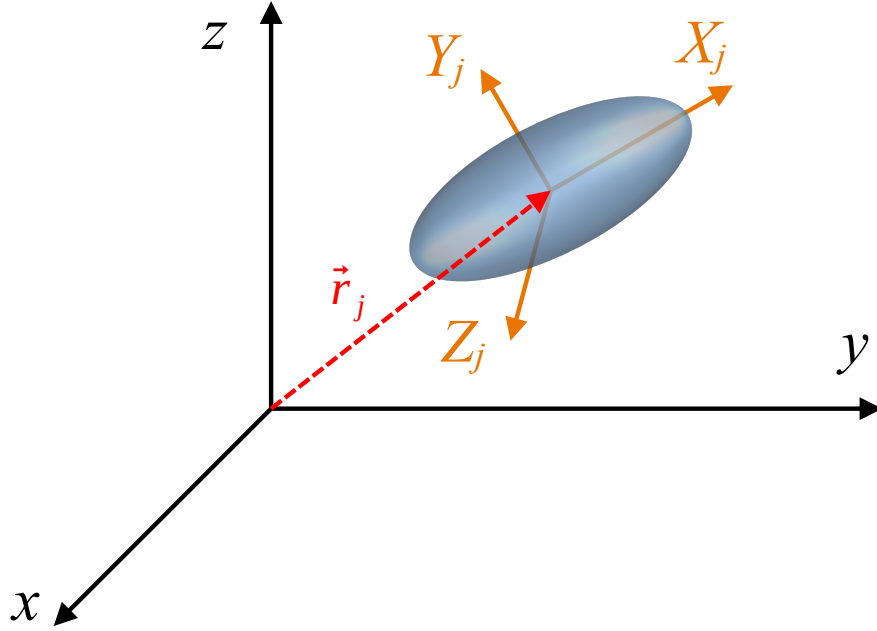
Figure 4.1 – Representation of the condensate (in blue) associated with the species j, centred on the point of coordinates $\boldsymbol{r_j} = (x_j, y_j, z_j)^T$ in the fixed reference frame (x, y, z). The frame (X_j, Y_j, Z_j) shown in orange is associated with the eigenaxes of the harmonic trap V_j.

In this expression, $\boldsymbol{r}_j(t) = (x_j(t), y_j(t), z_j(t))^T$ is the position of the trap minimum for species j at time t in the reference frame. In many cases, the atom cloud and the trap eigenaxes are rotated with respect to the fixed frame associated generally to the lab frame. It leads to the use of multiple axis and coordinate systems as showed schematically on Figure 4.1. We assume that at each time t the harmonic traps $V_j(\boldsymbol{r}, t)$ associated with the different species are characterized by eigenaxes pointing in the directions $X_j(t)$, $Y_j(t)$ and $Z_j(t)$. We can define the unitary rotation matrix $\boldsymbol{M}_j(t)$ that allows to pass from the particular system of eigenaxes $(X_j(t), Y_j(t), Z_j(t))$ to the fixed frame of reference (x, y, z) at time t. We can find examples of such rotation matrices in section 2.7. The 3×3 squared harmonic frequency matrices $\boldsymbol{\Omega}_j^2(t)$ are then defined in the fixed reference frame (x, y, z) as

$$\boldsymbol{\Omega}_j^2(t) = \boldsymbol{M}_j(t) \begin{pmatrix} \omega_{j,X_J}^2(t) & 0 & 0 \\ 0 & \omega_{j,Y_j}^2(t) & 0 \\ 0 & 0 & \omega_{j,Z_j}^2(t) \end{pmatrix} \boldsymbol{M}_j(t)^T \tag{4.6}$$

The eigenvalues of $\boldsymbol{\Omega}_j^2(t)$ thus coincide with the squared instantaneous eigenfrequencies $\omega_{j,X_j}^2(t)$, $\omega_{j,Y_j}^2(t)$ and $\omega_{j,Z_j}^2(t)$ of the traps along their principal axes $(X_j(t), Y_j(t), Z_j(t))$. In the codes that I implemented it is important to choose a particular species to define a reference frame for the calculations, so all the equations to be solved are in the same coordinate system to take into account the coupled interaction terms conveniently. This particular index $j = j^*$ can, in principle, be chosen freely. However it is preferable to choose as j^* the species that would expand the fastest without inter-species interactions. Empirically, in the case of a mixture of two species, the species indexed by

j^* is the one with the largest Thomas-Fermi radius (see Eq. 2.41). In all that follows, we will assume that for this particular species, the eigenaxes of the trap do not rotate during the dynamics. Thus, the rotation matrix $M_{j^*}(t)$ will be simply denoted by M_{j^*} and will be assumed to be independent of time. In practice, this approach can be used as long as the rotation of these eigenaxes is sufficiently small and slow so that the effect of non-inertial forces due to the rotation of the eigenaxes associated to this reference species j^* can be neglected. This is the case in most situations, especially when the rotation is slow enough not to induce the appearance of vortices, as shown for instances in references [74, 120, 121].

In the reference frame associated with the eigenaxes of the species j^*, the matrix of the squared harmonic frequencies associated with each species j writes

$$\mathbf{\Omega}_j'^2(t) = \mathbf{M}_{j^*}^T \mathbf{\Omega}_j^2(t) \mathbf{M}_{j^*} \tag{4.7}$$

This matrix is symmetric, but not always diagonal. Actually, the matrix $\mathbf{\Omega}_j'^2(t)$ is diagonal only if the trap associated with the species j has the same principal axes as the trap associated with the reference species j^*. With the help of equations (4.6) and (4.7) we can check that $\mathbf{\Omega}_{j^*}^2(t)$ is the diagonal matrix of the squares of the instantaneous eigenfrequencies $\omega_{j*,X_{j^*}}(t)$, $\omega_{j*,Y_{j^*}}(t)$ and $\omega_{j*,Z_{j^*}}(t)$, as expected.

4.3 . Grid transformation for efficient numerical simulations

4.3.1 . Shifting the grid

The numerical simulations of the GPE describing the BEC mixture start with the definition of a grid. We can first study the dynamics of collective mode excitations in a stationary trap using a grid centered on the trap minimum. Even if we can numerically vary the initial position of the condensate or modulate the frequency of the trap, the range of modeled experiments is limited. Let us now consider more general experiments where both the position and the frequency of the trap vary. Such variations induce a displacement of the multispecies condensate, which can be of high amplitude with respect to the trap minimum. Mathematically, we can define a moving reference frame that follows either the trap minimum or the centre of mass of the BEC. However, since the condensate can move far away from the trap minimum during a transport, it is better to follow the centre of mass of the BEC. The choice of the appropriate grid displacement is crucial for the optimisation of the computations, since the computational time scales with the grid size. Indeed, the computation time grows at least as $N_{\mathrm{grid}} \log_2(N_{\mathrm{grid}})$, where $N_{\mathrm{grid}} = N_x \times N_y \times N_z$ is the total number of grid points in 3 dimensions.

The frame change is especially important when implementing transport dynamics over distances significantly larger than the characteristic size of the condensate, as in the recent space atom chip manipulation of a BEC described in the previous chapter and in Ref. [52]. In this context, we transform the computational grid such that it follows the global displacement dictated by the classical evolution of the condensate centre of mass of the reference species $j = j^*$. This approach is a further

development of techniques used to deal with single BEC dynamics that have been presented in references [74, 76, 107, 122] and used in the previous chapter. The change of variable associated with this transformation is tied to the introduction of the new coordinate

$$\boldsymbol{R} = \boldsymbol{r} - \boldsymbol{r}_{cm,j^*}(t) \tag{4.8}$$

where $\boldsymbol{r}_{cm,j^*}(t)$ denotes the classical position of the centre of mass of the condensate associated with the species j^* at time t. It is computed by solving Newton's equation of a classical particle of mass m_{j^*}, initially at rest in the case where the dynamics start with a condensate in its ground state, and subjected to the time-dependent harmonic potential $V_{j*}(\boldsymbol{r}, t)$ of Eq. (4.5).

– General approach with the displacement operator

In a general approach aimed at tackling the frame change, we can define the quantum displacement operator in coordinate representation

$$\hat{D}_j(\boldsymbol{r}, t) = \exp\left(i\left[\boldsymbol{k}_{\mathrm{cm},j}(t) \cdot \boldsymbol{r} - \boldsymbol{r}_{\mathrm{cm},j^*}(t) \cdot \hat{\boldsymbol{k}}\right]\right) \tag{4.9}$$

where $\hat{\boldsymbol{k}} = -i\,\boldsymbol{\nabla_r} = \hat{\boldsymbol{p}}/\hbar$ and $\boldsymbol{k}_{\mathrm{cm},j}(t) = \boldsymbol{p}_{\mathrm{cm},j}(t)/\hbar$. The variable $\boldsymbol{p}_{\mathrm{cm},j}(t)$ is homogeneous to a momentum, and will be determined later. The displacement operator is a unitary operator. It has the following properties

$$\hat{D}_j(\boldsymbol{r}, t)\,\phi(\boldsymbol{r}, t) = \exp\left[-\frac{i}{2}\,\boldsymbol{r}_{cm,j^*} \cdot \boldsymbol{k}_{cm,j}\right]\,\exp\left[i\,\boldsymbol{k}_{cm,j} \cdot \boldsymbol{r}\right]\,\phi(\boldsymbol{r} - \boldsymbol{r}_{cm,j^*}, t) \tag{4.10}$$

and

$$\hat{D}_j(\boldsymbol{r}, t)^\dagger f(\boldsymbol{r}, \hat{\boldsymbol{k}})\,\hat{D}_j(\boldsymbol{r}, t) = f(\boldsymbol{r} + \boldsymbol{r}_{cm,j^*}, \hat{\boldsymbol{k}} + \boldsymbol{k}_{cm,j}) \tag{4.11}$$

for any smooth functions $\phi(\boldsymbol{r}, t)$ and $f(\boldsymbol{r}, \hat{\boldsymbol{k}})$.

Using the same steps as in [74], we introduce the unitary transformation of the wavefunction

$$\Psi_j(\boldsymbol{r}, t) = e^{i\,S_j(t)/\hbar}\,\hat{D}_j(\boldsymbol{r}, t)\,\Psi_j^D(\boldsymbol{R}, t) \tag{4.12}$$

where $S_j(t)$ is a global phase term that will be defined later in the calculation. As we insert this ansatz in the coupled Gross-Pitaevskii equation (4.1) we obtain

$$
\begin{aligned}
i\hbar\partial_t\Psi_j^D(\boldsymbol{R}, t) = \Bigg[&-\frac{\hbar^2}{2m_j}\nabla^2 + \frac{m_j}{2}\boldsymbol{R}^T\boldsymbol{\Omega}_j'^2(t)\boldsymbol{R} + W_j(\boldsymbol{r} - \boldsymbol{r}_{cm,j*}, t) + \sum_{j'=1}^{n_{sp}} N_{j'}g_{jj'}|\Psi_{j'}^D(\boldsymbol{R}, t)|^2 \\
&+ \left(\frac{\boldsymbol{p}_{cm,j}}{m_j} - \frac{d\boldsymbol{r}_{cm,j*}}{dt}\right)\hat{\boldsymbol{p}} + \left(m_j(\boldsymbol{r}_{cm,j*} - \boldsymbol{r}_j)^T\boldsymbol{\Omega}_j'^2(t) + \frac{d\boldsymbol{p}_{cm,j}^T}{dt}\right)\boldsymbol{R} \\
&+ \frac{dS_j}{dt} + \frac{d\boldsymbol{p}_{cm,j}}{dt}.\boldsymbol{r}_{cm,j*} - \frac{1}{2}\frac{d}{dt}\left(\boldsymbol{r}_{cm,j*}.\boldsymbol{p}_{cm,j}\right) + \frac{\boldsymbol{p}_{cm,j}^T\boldsymbol{p}_{cm,j}}{2m_j} \\
&+ \frac{m_j}{2}(\boldsymbol{r}_{cm,j*} - \boldsymbol{r}_j)^T\boldsymbol{\Omega}_j'^2(t)(\boldsymbol{r}_{cm,j*} - \boldsymbol{r}_j)\Bigg]\Psi_j^D(\boldsymbol{R}, t)\,.
\end{aligned} \tag{4.13}
$$

To cancel out the term depending on $\hat{p}$, we define

$$\boldsymbol{p}_{cm,j}(t) = m_j \, \dot{\boldsymbol{r}}_{cm,j^*} \,, \quad \forall j \,. \tag{4.14}$$

This dependence in j^*, the reference species, is due to the fact that we follow this particular species. In the particular case of the reference species, it corresponds to the definition of the classical momentum of that species $\boldsymbol{p}_{cm,j^*}(t) = m_{j^*}\dot{\boldsymbol{r}}_{cm,j^*}$. We can also get the expression of Newton's equation of motion since in this case

$$\dot{\boldsymbol{p}}_{\text{cm},j^*}(t) = -m_{j^*} \, \boldsymbol{\Omega}_{j^*}'^2(t) \, [\boldsymbol{r}_{\text{cm},j^*}(t) - \boldsymbol{r}_{j^*}(t)] \,. \tag{4.15}$$

The scalar terms in Eq. (4.13) can also be canceled by choosing an adapted global phase term $S_j(t)$ which satisfies

$$\frac{dS_j}{dt} = -\frac{d\boldsymbol{p}_{cm,j}}{dt}.\boldsymbol{r}_{cm,j^*} + \frac{1}{2}\frac{d}{dt}[\boldsymbol{r}_{cm,j*}.\boldsymbol{p}_{cm,j}] - \frac{\boldsymbol{p}_{cm,j}^2}{2m_j} - \frac{m_j}{2}(\boldsymbol{r}_{cm,j*} - \boldsymbol{r}_j)^T\boldsymbol{\Omega}_j'^2(t)(\boldsymbol{r}_{cm,j*} - \boldsymbol{r}_j) \tag{4.16}$$

Finally, we consider the terms that are linear in $\boldsymbol{R}$ as a corrective potential term $V_j^{cor}(\boldsymbol{R},t)$, which can be reorganized with the help of Eqs. (4.14) and (4.15)

$$V_j^{cor}(\boldsymbol{R},t) = \left[m_j(\boldsymbol{r}_{cm,j^*} - \boldsymbol{r}_j)^T \boldsymbol{\Omega}_j'^2(t) + \frac{d\boldsymbol{p}_{cm,j}^T}{dt} \right] \boldsymbol{R} \tag{4.17}$$

$$= \left[m_j(\boldsymbol{r}_{cm,j^*} - \boldsymbol{r}_j)^T \boldsymbol{\Omega}_j'^2(t) + \frac{m_j}{m_{j^*}}\frac{d\boldsymbol{p}_{cm,j^*}^T}{dt} \right] \boldsymbol{R} \tag{4.18}$$

$$= \left[m_j(\boldsymbol{r}_{cm,j^*} - \boldsymbol{r}_j)^T \boldsymbol{\Omega}_j'^2(t) - \frac{m_j}{m_{j^*}}m_{j^*}(\boldsymbol{r}_{\text{cm},j^*}(t) - \boldsymbol{r}_{j^*}(t))^T\boldsymbol{\Omega}_{j^*}'^2(t) \right] \boldsymbol{R} \tag{4.19}$$

$$= m_j \left[(\boldsymbol{r}_{cm,j^*} - \boldsymbol{r}_j)^T\boldsymbol{\Omega}_j'^2(t) - (\boldsymbol{r}_{\text{cm},j^*}(t) - \boldsymbol{r}_{j^*}(t))^T\boldsymbol{\Omega}_{j^*}'^2(t) \right] \boldsymbol{R} \tag{4.20}$$

We also use a new notation for the term associated with the anharmonicities of the potential, using $\overline{W}_j(\boldsymbol{R},t) = W_j(\boldsymbol{r} - \boldsymbol{r}_{cm,j^*},t)$. Combining all the simplified terms of Eq. (4.13), we finally obtain the following transformed Gross-Pitaevskii equation

$$i\hbar\,\partial_t\Psi_j^D(\mathbf{R},t) = \left[-\frac{\hbar^2}{2m_j}\boldsymbol{\nabla}_R^2 + \frac{m_j}{2}\,\mathbf{R}^T\,\boldsymbol{\Omega}_j'^2(t)\,\mathbf{R} + \overline{W}_j(\mathbf{R},t) + V_j^{\text{cor}}(\mathbf{R},t) \right.$$

$$\left. + \sum_{j'=1}^{n_{sp}} N_{j'}\,g_{jj'}|\,\Psi_{j'}^D(\mathbf{R},t)|^2 \right]\Psi_j^D(\mathbf{R},t)\,. \tag{4.21}$$

The equation (4.21) now depends on an unique coordinate, which is the translated coordinate $\boldsymbol{R} = \boldsymbol{r} - \boldsymbol{r}_{cm,j^*}(t)$. This allows us to see that the new computational grid follows the global motion of the centre of mass of the condensate associated with the reference species j^*. We can also see that

for the particular case of the reference species $j*$, the correction term of equation (4.20) disappears, and consequently for this particular species the equation (4.21) reduces to

$$i\hbar\,\partial_t\Psi_{j*}^D(\mathbf{R},t) = \left[-\frac{\hbar^2}{2m_{j*}}\boldsymbol{\nabla}_R^2 + \frac{m_{j*}}{2}\mathbf{R}^T\boldsymbol{\Omega}_{j*}'^2(t)\mathbf{R} + \overline{W}_{j*}(\mathbf{R},t) \right.$$
$$\left. + \sum_{j'=1}^{n_{sp}} N_{j'}\,g_{j*j'}|\,\Psi_{j'}^D(\mathbf{R},t)|^2 \right]\Psi_{j*}^D(\mathbf{R},t)\,. \tag{4.22}$$

We can thus consider equation (4.21) as a general equation applicable to any species, whether or not it is the reference species, for the displacement operation being performed.

– Particular approach using Cartesian coordinates

The matrix notation and the displacement operator are very compact and versatile, since we can use their properties to write simpler equations. However, the displacement operator can be a bit difficult to handle when you need to use commutators with the momentum operator $\hat{\boldsymbol{p}}$. In the special case where the trap potential for each species is oriented along the same principal axis as the reference species, we can use a different approach to transform the GPE. This approach considers the use of Cartesian coordinates and the coordinate system transformation $\{\boldsymbol{r}, t\} \to \{\boldsymbol{R}, \tau\}$ where $\boldsymbol{R} = \boldsymbol{r} - \boldsymbol{r}_{cm,j*}$ with $\boldsymbol{R} = (X, Y, Z)$ and $t = \tau$. But first we need to redefine the differential operators using the chain rule

$$\frac{\partial}{\partial X} = \frac{\partial}{\partial x}, \quad \frac{\partial}{\partial Y} = \frac{\partial}{\partial y}, \quad \frac{\partial}{\partial Z} = \frac{\partial}{\partial z} \tag{4.23}$$

and

$$\frac{\partial}{\partial t} = \frac{\partial}{\partial \tau} - \dot{x}_{cm,j*}\frac{\partial}{\partial X} - \dot{y}_{cm,j*}\frac{\partial}{\partial Y} - \dot{z}_{cm,j*}\frac{\partial}{\partial Z}\,. \tag{4.24}$$

The ansatz of the wavefunction to be introduced in the GPE is then

$$\psi_j(\boldsymbol{r},t) = \exp\left[-i\boldsymbol{\kappa}_j.\boldsymbol{R} - i\varphi_j(\tau) + i\overline{S}_j(\tau) \right]\psi_j^D(\boldsymbol{R},\tau)\,, \tag{4.25}$$

where $\boldsymbol{\kappa}_j = (\kappa_{X,j}, \kappa_{Y,j}, \kappa_{Z,j})$, $\varphi_j(\tau)$ and $\overline{S}_j(\tau)$ are chosen to simplify the GPE after inserting the ansatz into Eq. (4.1). We finally obtain

$$\kappa_{\alpha,j} = -\frac{m_j}{\hbar}\dot{\alpha}_{cm,j*}(\tau) \quad \text{for } \alpha \in \{X, Y, Z\}, \tag{4.26}$$

and

$$\varphi_j(\tau) = -\frac{m_j}{2\hbar}\int_0^\tau \left[\dot{x}_{cm,j*}^2(\tau') + \dot{y}_{cm,j*}^2(\tau') + \dot{y}_{cm,j*}^2(\tau') \right]d\tau'\,. \tag{4.27}$$

And the second phase term $\overline{S}_j(t)$ encloses the remaining scalar terms, such that

$$\frac{\partial \overline{S}_j}{\partial \tau} = -\frac{m_j}{2}\left(\omega_{x,j}^2(x_{cm,j*} - x_j)^2 + \omega_{y,j}^2(y_{cm,j*} - y_j)^2 + \omega_{z,j}^2(z_{cm,j*} - z_j)^2 \right)\,. \tag{4.28}$$

This approach finally ends up with the same simplified GPE for the displaced wave function $\psi_j^D(\boldsymbol{R},\tau)$, as in equation (4.21).

4.3.2 . Expanding or compressing the grid

During the dynamics, the size of the condensate can vary a lot and it would be very useful to have a grid that compresses or expands accordingly during the propagation to save computational time. This approach is even more important when considering a free expansion of the condensate, when its size scales very fast and the fixed-grid approach cannot keep up with this in terms of memory storage and computational time. Similar to what was implemented for single species calculations in Refs. [74, 76, 107, 122] we define a new frame transformation. To define the time-dependent scaling factors applied to the computational grid, we choose the same reference species as before, corresponding to the index $j = j^*$, and we define a new rescaled coordinate $\boldsymbol{\xi}$ satisfying

$$\boldsymbol{\Lambda}(t)\boldsymbol{\xi} = \boldsymbol{R}\,, \tag{4.29}$$

where

$$\boldsymbol{\Lambda}(t) = \begin{pmatrix} \lambda_{X_{j^*}}(t) & 0 & 0 \\ 0 & \lambda_{Y_{j^*}}(t) & 0 \\ 0 & 0 & \lambda_{Z_{j^*}}(t) \end{pmatrix} \tag{4.30}$$

is a diagonal matrix whose elements are three scalar and adimensional time-dependent scaling functions $\lambda_{X_{j^*}}(t)$, $\lambda_{Y_{j^*}}(t)$ and $\lambda_{Z_{j^*}}(t)$ that we apply to the three coordinates associated with the eigenaxes of the potential trapping the species number j^*. In principle, any scaling function could be chosen, but we can be inspired by functions that bring the calculations closer to already known cases. This is why we have chosen to force the computational grid to compress or expand according to the dynamics predicted by the so-called "scaling law" approximation developed for a single species in the Thomas-Fermi regime [57, 75]. In the case of a single species condensate with a large number of atoms, such that the Thomas-Fermi approximation holds, we can use this scaling approach to describe the 3D size evolution dynamics of the BEC in a time-dependent harmonic trap. This leads to the coupled differential equations (2.43) shown in the previous chapter (see section 2.6), that we will write here in a matrix form for a diagonal 3×3 scaling matrix $\boldsymbol{\Lambda}(t)$

$$\boldsymbol{\Lambda}^T(t)\ddot{\boldsymbol{\Lambda}}(t) + \boldsymbol{\Lambda}^T(t)\,\boldsymbol{\Omega}_{j^*}'^2(t)\,\boldsymbol{\Lambda}(t) = \frac{\boldsymbol{\Omega}_{j^*}'^2(0)}{\det[\boldsymbol{\Lambda}(t)]}\,, \tag{4.31}$$

where $\det[\boldsymbol{\Lambda}(t)] = \lambda_{X_{j^*}}(t)\lambda_{Y_{j^*}}(t)\lambda_{Z_{j^*}}(t)$ is the determinant of the diagonal matrix $\boldsymbol{\Lambda}(t)$. By fixing at initial time $t = 0$ the boundary conditions of the matrix to $\boldsymbol{\Lambda}(0) = \mathbb{1}$ and $\dot{\boldsymbol{\Lambda}}(0) = \mathbb{0}$, we can get a good estimate of the evolution of the BEC size in 3D. To take into account the introduction of the scaled coordinate $\boldsymbol{\xi}$ we now need to transform the wave function associated with each species as

$$\Psi_j^D(\boldsymbol{R}, t) = \frac{\exp\left(\frac{i}{\hbar}\left[\boldsymbol{\xi}^T \boldsymbol{A}_j(t)\,\boldsymbol{\xi} - \beta_j(t)\right]\right)}{\sqrt{\det[\boldsymbol{\Lambda}(t)]}}\,\Psi_j^S(\boldsymbol{\xi}, t)\,, \tag{4.32}$$

where $\boldsymbol{A}_j(t)$ and $\beta_j(t)$ will be determined later. This coordinate transformation $\{\boldsymbol{R}, t\} \to \{\boldsymbol{\xi}, \tau\}$, with $\boldsymbol{R} = \boldsymbol{\Lambda}(t)\boldsymbol{\xi}$ and $t = \tau$, requires the definition of the associated differential operators, and using the chain rule we get $\boldsymbol{\nabla}_{\boldsymbol{X}} = (\boldsymbol{\Lambda}^{-1})^T \boldsymbol{\nabla}_{\boldsymbol{\xi}}$ and

$$\frac{\partial}{\partial t} = \frac{\partial}{\partial \tau} - \left(\boldsymbol{\Lambda}^{-1}(\tau)\frac{d\boldsymbol{\Lambda}(\tau)}{d\tau}\boldsymbol{\xi}\right)^T \boldsymbol{\nabla}_{\boldsymbol{\xi}}\,. \tag{4.33}$$

Finally, the time derivative of $\Psi_j^D(\boldsymbol{R}, t)$ can be calculated using Jacobi's formula

$$\frac{d}{d\tau}\det[\boldsymbol{\Lambda}(\tau)] = \det[\boldsymbol{\Lambda}(\tau)]\,\mathrm{Tr}\left[\boldsymbol{\Lambda}^{-1}\frac{d\boldsymbol{\Lambda}}{d\tau}\right],\tag{4.34}$$

where $\mathrm{Tr}\,[\boldsymbol{M}]$ is the trace of the matrix $\boldsymbol{M}$. Let us now insert the ansatz (4.32) into the transformed GPE (4.21). This results in

$$
\begin{aligned}
i\hbar\partial_\tau\Psi_j^S(\boldsymbol{\xi},\tau) = &\left(-\frac{\hbar^2}{2m_j}\boldsymbol{\nabla}_\xi^T\boldsymbol{\Lambda}^{-1}(\boldsymbol{\Lambda}^{-1})^T\boldsymbol{\nabla}_\xi + V_j^{cor}(\boldsymbol{\Lambda}\boldsymbol{\xi},\tau) + \overline{W}_j(\boldsymbol{\Lambda}\boldsymbol{\xi},\tau) + \sum_{j'=1}^{n_{sp}}\frac{g_{jj'}N_{j'}}{\det[\boldsymbol{\Lambda}]}|\Psi_j|^2\right)\Psi_j^S(\boldsymbol{\xi},\tau)\\
&+ i\hbar\left[Tr\left(\frac{\boldsymbol{\Lambda}^{-1}}{2}\left(\frac{d\boldsymbol{\Lambda}}{d\tau} - \frac{2}{m_j}(\boldsymbol{\Lambda}^{-1})^T\boldsymbol{A}_j\right)\right) + \frac{i}{\hbar}\frac{d\beta_j}{d\tau}\right]\Psi_j^S(\boldsymbol{\xi},\tau)\\
&+ \boldsymbol{\xi}^T\left(\frac{d\boldsymbol{A}_j}{d\tau} - 2\boldsymbol{A}_j\boldsymbol{\Lambda}^{-1}\left(\frac{d\boldsymbol{\Lambda}}{d\tau} - \frac{1}{m_j}(\boldsymbol{\Lambda}^{-1})^T\boldsymbol{A}_j\right) + \frac{m_j}{2}\boldsymbol{\Lambda}^T\boldsymbol{\Omega}_j'^2(\tau)\boldsymbol{\Lambda}\right)\boldsymbol{\xi}\,\Psi_j^S(\boldsymbol{\xi},\tau)\\
&+ i\hbar(\nabla_\xi\Psi_j^S)^T\left(\boldsymbol{\Lambda}^{-1}\frac{d\boldsymbol{\Lambda}}{d\tau} - \frac{2}{m_j}\boldsymbol{\Lambda})^{-1}(\boldsymbol{\Lambda}^{-1})^T\boldsymbol{A}_j\right)\boldsymbol{\xi}
\end{aligned}\tag{4.35}
$$

To simplify the terms from the second and fourth lines of the right-hand side of Eq. (4.35), we choose

$$\boldsymbol{A}_j(\tau) = \frac{m_j}{2}\boldsymbol{\Lambda}^T(\tau)\frac{d\boldsymbol{\Lambda}(\tau)}{d\tau},\tag{4.36}$$

which implies

$$\frac{d\boldsymbol{\Lambda}}{d\tau} - \frac{2}{m_j}(\boldsymbol{\Lambda}^{-1})^T\boldsymbol{A}_j = 0.\tag{4.37}$$

The phase term $\beta_j(\tau)$ has less constraints and could be zero. However, similar to the choices made in single species calculations [74], we define $\beta_j(\tau)$ as a function of the chemical potential μ_j of the ground state of species j

$$\beta_j(\tau) = \int_0^\tau \frac{\mu_j}{\det[\boldsymbol{\Lambda}(\tau')]}d\tau'\tag{4.38}$$

This choice, which makes the equation consistent with what we could get when calculating the ground state of the mixture, leads to

$$\frac{d\beta_j}{d\tau} = \frac{\mu_j}{\det(\boldsymbol{\Lambda}(\tau))}.\tag{4.39}$$

Now let us look at the third line of equation (4.35) by defining

$$C_j(\tau) = \frac{d\boldsymbol{A}_j}{d\tau} - 2\boldsymbol{A}_j\boldsymbol{\Lambda}^{-1}\left(\frac{d\boldsymbol{\Lambda}}{d\tau} - \frac{1}{m_j}(\boldsymbol{\Lambda}^{-1})^T\boldsymbol{A}_j\right) + \frac{m_j}{2}\boldsymbol{\Lambda}^T\boldsymbol{\Omega}_j'^2(\tau)\boldsymbol{\Lambda}.\tag{4.40}$$

62

Using the definitions of $\boldsymbol{A}_j(\tau)$ and $\boldsymbol{\Lambda}(\tau)$, and the scaling law (4.31), we obtain

$$
\begin{aligned}
C_j(\tau) &= \frac{m_j}{2}\frac{d}{d\tau}\left(\boldsymbol{\Lambda}^T\frac{d\boldsymbol{\Lambda}}{d\tau}\right) - 2\frac{m_j}{2}\boldsymbol{\Lambda}^T\frac{d\boldsymbol{\Lambda}}{d\tau}\boldsymbol{\Lambda}^{-1}\left(\frac{d\boldsymbol{\Lambda}}{d\tau} - \frac{1}{m_j}(\boldsymbol{\Lambda}^{-1})^T\boldsymbol{\Lambda}^T\frac{d\boldsymbol{\Lambda}}{d\tau}\frac{m_j}{2}\right) + \frac{m_j}{2}\boldsymbol{\Lambda}^T\boldsymbol{\Omega}_j'^2(\tau)\boldsymbol{\Lambda} \\
&= \frac{m_j}{2}\left(\frac{d\boldsymbol{\Lambda}^T}{d\tau}\frac{d\boldsymbol{\Lambda}}{d\tau} + \boldsymbol{\Lambda}^T\frac{d^2\boldsymbol{\Lambda}}{d\tau} - 2\boldsymbol{\Lambda}^T\frac{d\boldsymbol{\Lambda}}{d\tau}\boldsymbol{\Lambda}^{-1}\left(\frac{d\boldsymbol{\Lambda}}{d\tau} - \frac{1}{2}\frac{d\boldsymbol{\Lambda}}{d\tau}\right) + \boldsymbol{\Lambda}^T\boldsymbol{\Omega}_j'^2(\tau)\boldsymbol{\Lambda}\right) \\
&= \frac{m_j}{2}\left(\frac{d\boldsymbol{\Lambda}^T}{d\tau}\frac{d\boldsymbol{\Lambda}}{d\tau} + \boldsymbol{\Lambda}^T\frac{d^2\boldsymbol{\Lambda}}{d^2\tau} - \frac{d\boldsymbol{\Lambda}^T}{d\tau}\boldsymbol{\Lambda}\boldsymbol{\Lambda}^{-1}\frac{d\boldsymbol{\Lambda}}{d\tau} + \boldsymbol{\Lambda}^T\boldsymbol{\Omega}_j'^2(\tau)\boldsymbol{\Lambda}\right) \\
&= \frac{m_j}{2}\left(\boldsymbol{\Lambda}^T\frac{d^2\boldsymbol{\Lambda}}{d^2\tau} + \boldsymbol{\Lambda}^T\boldsymbol{\Omega}_j'^2(\tau)\boldsymbol{\Lambda}\right) \\
&= \frac{m_j}{2}\left(\frac{\boldsymbol{\Omega}_{j*}'^2(0)}{\det[\boldsymbol{\Lambda}]} - \boldsymbol{\Lambda}^T\boldsymbol{\Omega}_{j*}(\tau)'^2\boldsymbol{\Lambda} + \boldsymbol{\Lambda}^T\boldsymbol{\Omega}_j'^2(\tau)\boldsymbol{\Lambda}\right) \tag{4.41}
\end{aligned}
$$

By combining all these elements, we finally obtain an adapted set of coupled time-dependent Gross-Pitaevskii equations for all species, which reads

$$
\begin{aligned}
i\hbar\,\partial_t\Psi_j^S(\boldsymbol{\xi},t) = \Bigg[&-\frac{\hbar^2}{2m_j}\boldsymbol{\nabla}_{\boldsymbol{\xi}}^T\boldsymbol{\Lambda}^{-1}(\boldsymbol{\Lambda}^{-1})^T\boldsymbol{\nabla}_{\boldsymbol{\xi}} + \frac{m_j}{2}\boldsymbol{\xi}^T\boldsymbol{\Lambda}^T\left(\boldsymbol{\Omega}_j'^2(t) - \boldsymbol{\Omega}_{j*}'^2(t)\right)\boldsymbol{\Lambda}\,\boldsymbol{\xi} + V_j^{\mathrm{cor}}(\boldsymbol{\Lambda}\,\boldsymbol{\xi},t) \\
&+ \overline{W}_j(\boldsymbol{\Lambda}\,\boldsymbol{\xi},t) + \frac{\frac{m_j}{2}\boldsymbol{\xi}^T\boldsymbol{\Omega}_{j*}'^2(0)\,\boldsymbol{\xi} + \sum_{j'}N_{j'}\,g_{jj'}|\,\Psi_{j'}^S(\boldsymbol{\xi},t)|^2 - \mu_j}{\det[\boldsymbol{\Lambda}(t)]}\Bigg]\Psi_j^S(\boldsymbol{\xi},t)\,, \tag{4.42}
\end{aligned}
$$

where μ_j is the chemical potential associated with the species j at time $t = 0$. We can note that for the reference species $j = j^*$, this equation simplifies to

$$
\begin{aligned}
i\hbar\,\partial_t\Psi_{j*}^S(\boldsymbol{\xi},t) = \Bigg[&-\frac{\hbar^2}{2m_{j*}}\boldsymbol{\nabla}_{\boldsymbol{\xi}}^T\boldsymbol{\Lambda}^{-1}(\boldsymbol{\Lambda}^{-1})^T\boldsymbol{\nabla}_{\boldsymbol{\xi}} + \overline{W}_{j*}(\boldsymbol{\Lambda}\,\boldsymbol{\xi},t) \\
&+ \frac{\frac{m_{j*}}{2}\boldsymbol{\xi}^T\boldsymbol{\Omega}_{j*}'^2(0)\,\boldsymbol{\xi} + \sum_{j'}N_{j'}\,g_{j*j'}|\,\Psi_{j'}^S(\boldsymbol{\xi},t)|^2 - \mu_{j*}}{\det[\boldsymbol{\Lambda}(t)]}\Bigg]\Psi_{j*}^S(\boldsymbol{\xi},t)\,. \tag{4.43}
\end{aligned}
$$

We now have tools to describe the dynamics of interacting BEC mixtures with the coupled differential equations (4.42) and (4.43). These equations are solved numerically using the second-order split-operator technique [123]. This technique is first used in imaginary time [70, 117] to compute the ground state of the mixture, which is taken as the initial state of the system at $t = 0$. We then solve the equations in real time to compute the translation and expansion dynamics of the system [62, 97]. The chosen time step is equal to one thousandth of the shortest time period associated with the highest trapping frequency in the system (typically associated to the K atom in our numerical applications). We can also note that for the reference species j^* only the interaction terms need to be calculated at each iteration of the split-operator propagation. The other terms can be defined at the beginning of the code, after the declaration of the variables, making the computations simpler and more efficient. The term describing the contribution of the trap anharmonicities $\overline{W}_j(\boldsymbol{\Lambda}\boldsymbol{\xi},t)$ is the only term (apart from the corrective potential $V_j^{cor}(\boldsymbol{\Lambda}\boldsymbol{\xi},t)$) that is not modified except for the change of variable $\boldsymbol{R} = \boldsymbol{\Lambda}\boldsymbol{\xi}$, since we have no other relation or physical property that can be used to simplify this term. If

the condensate does not move too far from the center of the trap, the trap anisotropy $\overline{W}_j(\boldsymbol{\Lambda\xi}, t)$ can be neglected, but we chose to include it in all calculations to allow the description of a broader range of situations.

Although in a multi-species mixture the individual species j are typically trapped in potentials with different trapping frequencies, leading to unequal expansion dynamics and requiring the computation of additional correction terms such as $V_j^{cor}(\boldsymbol{\Lambda\xi}, t)$ at each iteration of the code, the scaling introduced in the equations (4.42) and (4.43) still absorbs most of the dynamics so that the numerical solution of the time evolution can be obtained much faster compared to a static grid. Moreover, in the special case where the trap frequencies are equal for both species in a binary mixture, which could be realised with dedicated optical traps [107], the equations (4.42) and (4.43) further simplify.

4.4 . The issue of mixture ground state simulations in microgravity

In this section we discuss some of the problems encountered when studying a dual species non-miscible BEC mixture of ^{41}K and ^{87}Rb in microgravity.

In microgravity, or under certain conditions where we can compensate for the gravitational sag, the trap minimum for the two species are co-located and the trapping frequencies associated with the two species are related by their mass ratio. Let us define for $j = 1, 2$ the trapping potential $V_j(\boldsymbol{r}, t)$

$$V_j(\boldsymbol{r}, t) = \frac{m_j}{2}(\omega_{x,j}\, x^2 + \omega_{y,j}\, y^2 + \omega_{z,j}\, z^2) \tag{4.44}$$

We consider that

$$\omega_{\alpha,2} = \sqrt{\frac{m_1}{m_2}}\, \omega_{\alpha,1}\,, \quad \text{for } \alpha \in \{x, y, z\}. \tag{4.45}$$

The two species are not miscible, *i.e.* their respective scattering lengths verify the following condition [1]

$$a_{11}a_{22} < a_{12}^2\,. \tag{4.46}$$

As mentioned in the previous section, we calculate the ground state of the binary mixture by solving the coupled Gross-Pitaevskii equation with the imaginary time propagation method. However, during the testing of the codes, it was important to compare the results with existing examples from the literature, in addition to "holding tests", where we verify that the computed state is stationary. For the analytical studies of the coupled GPE, the calculations start with the Thomas-Fermi approximation, but the inter-species interaction term makes the resolution of the GPE equation more challenging. Reducing the system to spherical symmetry simplifies the wave functions, which then become one-dimensional functions, greatly reducing the complexity of the calculations. These calculations show for the ground state a phase separation where the 1D atomic density is a symmetric function, with one species in the center and the other sandwiching it on the outside, creating a "hamburger-like" configuration [97, 99].

---

1. Note that this condition is strictly valid for homogeneous gases only [56]. We therefore use it here as a simple approximate guidance.

4.4.1 . Ground state calculation for various interspecies scattering lengths

The interaction between the two species is experimentally tunable using Feshbach resonances [111, 113]. This suggested a first set of simulations in which we observe the effect of varying the interspecies scattering length on the ground state of a mixture of K and Rb in a quasi-cylindrical trap. The trapping frequencies for the Rubidium cloud are $(f_{x,1}, f_{y,1}, f_{z,1}) = (24.8, 378.2, 384.0)$, and the mixture is composed of $N_1 = 2 \times 10^4$ atoms of Rb and $N_2 = 5 \times 10^4$ atoms of K. We consider the mixture in microgravity and vary the scattering length a_{12} between 0 and 8.747 nm, value observed naturally in the absence of any Feshbach resonance. The ground state is computed iteratively, *i.e.* we first find the ground state of the mixture with $a_{12} = 0$. This ground state is then used as the initial state for the imaginary time propagation to find the ground state for an increased interspecies scattering length. Figure 4.2 shows for a limited set of interspecies scattering lengths the probability density P_x integrated along the y- and z-directions. In this example, x is the weak axis, with $f_x \ll f_y \simeq f_z$. It is along this weak axis direction that the splitting of the mixture happens. On the top row of this Figure we see mainly two types of configurations, with overlapping distributions with bell-shaped curves in most of the miscible cases $a_{12} \leq 3.5$ nm, and the "hamburger-like" split distribution with the clouds of K on both sides of the Rb cloud for $a_{12} \geq 4$ nm. Let us define $a_{12,\text{lim}}$ the value for which we get from a miscible mixture to an immiscible mixture from the definition of Eq. (4.46). In our application for a mixture of K and Rb, we have

$$a_{12,\text{lim}} = \sqrt{a_{11}a_{22}} = \sqrt{5.237 \times 3.204} = 4.10 \, \text{nm} \qquad (4.47)$$

On Figure 4.2 and for $a_{12} = 4$ nm, where the mixture approaches the phase transition, we observe that the K cloud is split along x, with the Rb cloud in the centre. The change in the structure of the mixture is more visible in the lower panels of the Figure, where we focus on the values around the transition from $a_{12} = 3.0$ nm to $a_{12} = 4.5$ nm. For $a_{12} = 3$ nm and $a_{12} = 3.5$ nm, both species have a distribution similar to an inverted parabola centered on the trap minimum. The difference in shape is small, and can be approached by the Thomas-Fermi distribution that models the ground state with $a_{12} = 0$. Moreover, the variation of the atomic densities is smoother for $a_{12} = 4.0$ nm than for $a_{12} = 4.5$ nm, especially in the region where the two species touch each other. For $a_{12} = 4.0$ nm there is an overlap of the atomic densities at the transition between the two species, as both species are still partially miscible. Finally, the transition between the atomic density distributions becomes sharper as the interspecies scattering length increases, with nearly vertical boundaries for the highest interspecies scattering lengths.

Intuitively, and considering Noether's theorem, the ground state of the system should be symmetric, since the trapping potential is symmetric. However, theoretically, the repulsive interaction in the non-miscible mixture introduces some instability in the solution of the GPE [99]. As a consequence, we can observe in simulations the convergence of the imaginary time propagation (or other algorithms) leading to states of different geometries, such as an asymmetric configuration where the two species sit side by side [100, 102, 103, 111, 112]. In some models studying the structure of the mixture during the evaporation process, it is possible to obtain different configurations with bubbles of one species trapped within the other one, leading to alternating peaks of the different species in the plots of the 1D probability density as in [112, 124]. Some studies classify different phase diagrams, where
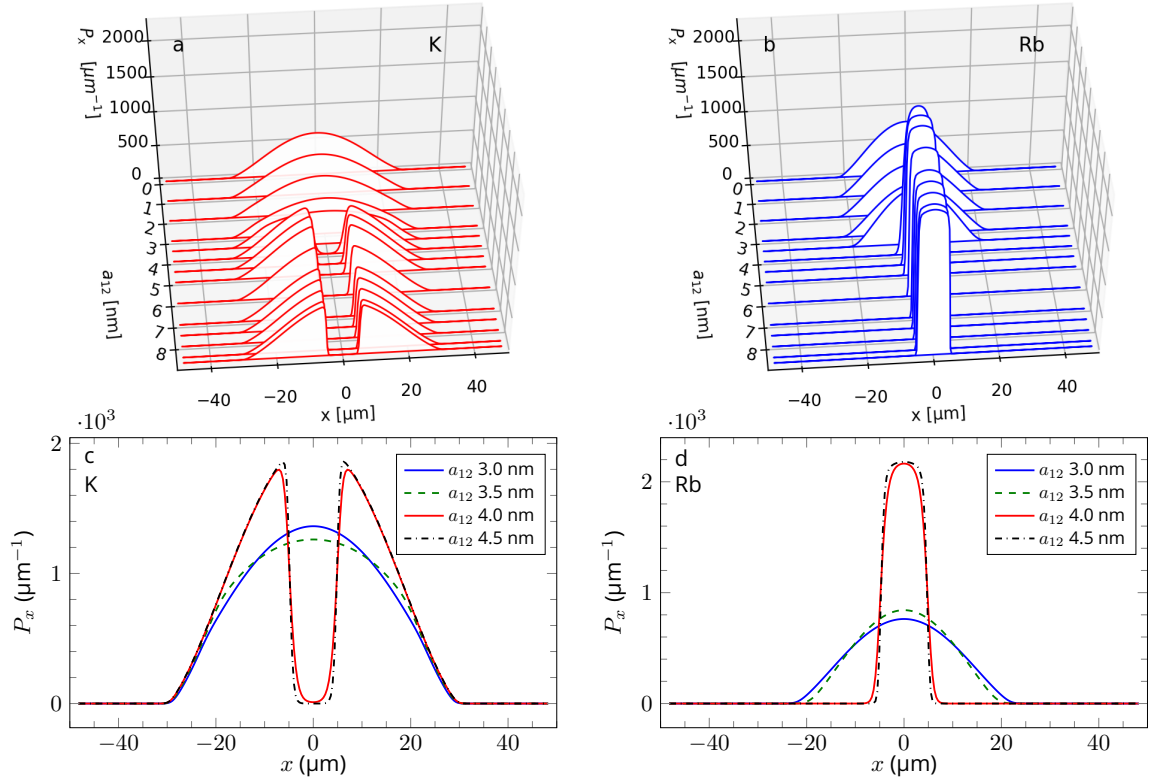
Figure 4.2 – Probability density P_x integrated along the y- and z-directions in the ground state of a BEC mixture in microgravity. Top row : Cascade plot of this integrated density profile as a function of x for a BEC mixture with $N_2 = 5 \times 10^4$ atoms of K (panel **a**) and $N_1 = 2 \times 10^4$ atoms of Rb (panel **b**) for different interspecies scattering lengths a_{12}. Bottom row : Plots of the density profile for interspecies scattering length values at which the phase transition from miscible ($a_{12} = 3.0, 3.5$ nm) to immiscible ($a_{12} = 4.0, 4.5$ nm) takes place, with the profile of the K BEC in panel **c** and that of the Rb BEC in panel **d**. The trapping potential is almost cylindrical and the frequencies for the Rb cloud are $(f_{x,1}, f_{y,1}, f_{z,1}) = (24.8, 378.3, 384.0)$ Hz.

the result depends on the fraction of atoms of each species in the mixture as well as the interspecies scattering length [104, 125]. In the end, these states are often considered as nearly degenerate metastable states, even if they are stationary in the potential in which we search for the ground state.

4.4.2 . Comparison between two simulations in microgravity

In our codes considering quasi-cylindrical traps, after fixing the number of atoms in the mixture, we can obtain two types of results, depending on the symmetry of the initial state used in the imaginary time propagation algorithm. We can thus converge two configurations : a symmetric stationary state where one species is sandwiched between two clouds of the second species, and a pair of asymmetric stationary states where the two species are side-by-side. For the symmetric state, we start with

two functions centered on the trap minimum, which is identical for both species. To force the appearance of the asymmetric state, we start with the two initial probability densities shifted side by side. Actually, for the asymmetric state, we have two mirror states for symmetry reasons.

Here we focus first on two different examples of K and Rb mixtures in a trap in microgravity. The first example is related to a future sounding rocket mission with MAIUS, and the second has already been implemented in space with CAL. We want to see how different the two configurations are. Both traps are implemented with atom chip setups, and we will refer to them as the MAIUS chip trap and the CAL chip trap. They also have a quasi-cylindrical geometry, where $\omega_{x,j} \ll \omega_{y,j} \simeq \omega_{z_j}$.

For the CAL chip trap, we consider a mixture of $N_1 = 1,400$ atoms of Rubidium and $N_2 = 1,900$ atoms of Potassium and the trapping frequencies characterized for the Rb cloud are $(f_{x,1}, f_{y,1}, f_{z,1}) = (26.0, 922.1, 927.6)$ Hz. For the MAIUS chip trap we consider a mixture of $N_1 = 43,900$ atoms of Rubidium and $N_2 = 14,400$ atoms of Potassium and the trapping frequencies characterized for the Rb cloud are $(f_{x,1}, f_{y,1}, f_{z,1}) = (24.8, 378.3, 384.0)$ Hz. The trap aspect ratios are different in the two cases, and are characterized by a more pronounced "cigar-shaped" one-dimensional character for the CAL configuration. In terms of atom number, there are an order of magnitude more atoms in the MAIUS configuration, and the dominant species is different in each case. Finally, since there is no Feshbach resonance present in the setups, the interspecies scattering length is $a_{12} = 8.747$ nm.
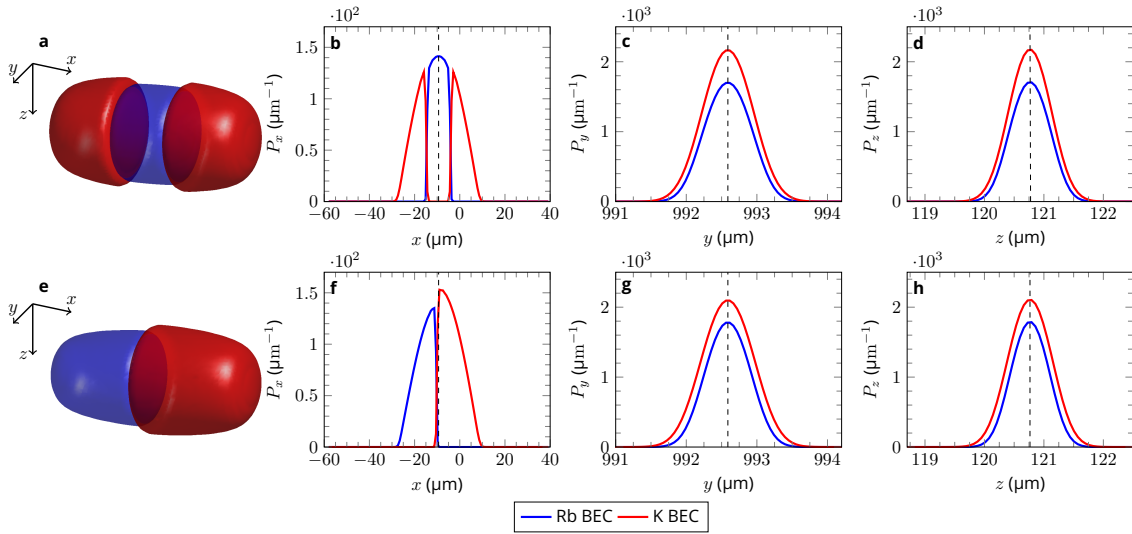

Figure 4.3 – Results from the imaginary time propagation for the CAL chip trap in microgravity after choosing a symmetric ansatz (top row) or an asymmetric ansatz (bottom row). We have 1,400 Rb atoms and 1,900 K atoms. The first column shows a 3D representation of the mixture with K in red and Rb in blue, and the other columns show the integrated profiles P_x, P_y and P_z.

Nonetheless, the simulation process is the same for both configuration, and we present the results in Figures 4.3 and 4.4. In each Figure, panels **a** and **e** in the first column show a 3D representation of the BEC mixture, with the Rb BEC in blue and the K BEC in red. The next 3 columns show the average
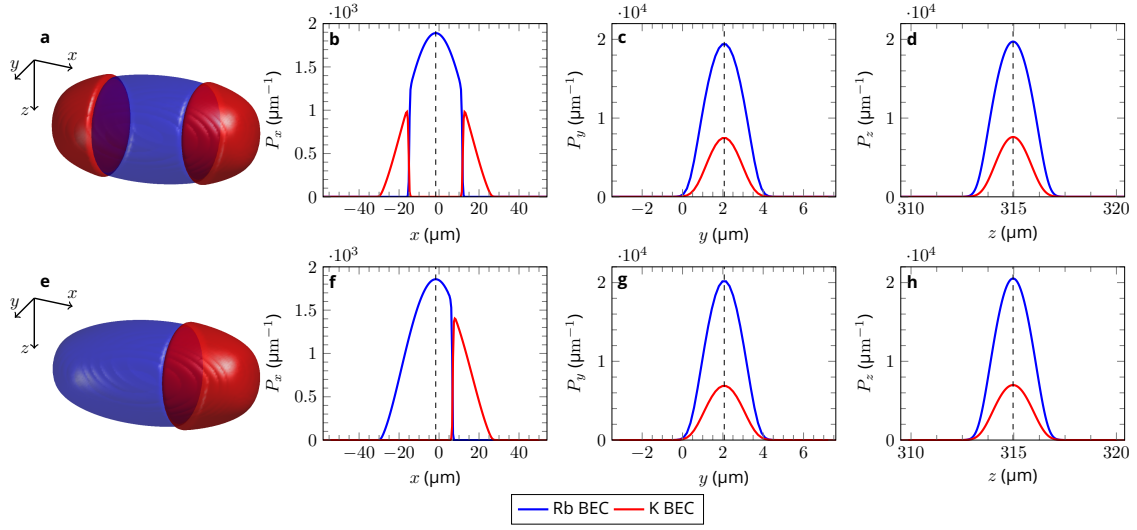
Figure 4.4 – Results from the imaginary time propagation for the MAIUS chip trap in microgravity after choosing a symmetric ansatz (top row) or an asymmetric ansatz (bottom row). We have 43,900 Rb atoms and 14,400 K atoms.

atomic densities

$$P_x(x,t) = \int_{-\infty}^{+\infty} \int_{-\infty}^{+\infty} N_j \left| \psi_j(\boldsymbol{r},t) \right|^2 dy \, dz \,, \tag{4.48a}$$

$$P_y(y,t) = \int_{-\infty}^{+\infty} \int_{-\infty}^{+\infty} N_j \left| \psi_j(\boldsymbol{r},t) \right|^2 dx \, dz \,, \tag{4.48b}$$

and

$$P_z(z,t) = \int_{-\infty}^{+\infty} \int_{-\infty}^{+\infty} N_j \left| \psi_j(\boldsymbol{r},t) \right|^2 dx \, dy \,, \tag{4.48c}$$

for Rb (blue) and K (red) along the three directions x, y and z. The vertical dashed lines correspond to the position of the trap centre, which is shared by both species since the system is in microgravity. The first row corresponds to the result obtained with the symmetric ansatz, and all the plots are symmetric : the vertical line representing the position of the trap centre acts as a symmetry axis. The second row shows the result obtained with an asymmetric ansatz, and in both Figures the shift between the species was such that the K cloud is positioned toward the positive x-direction, and the Rb cloud is positioned toward the negative x-direction. If we take the mirror of this initial ansatz with respect to the yz-plane, we end up with the mirror of this state with the same energy. We can see that the segregation between the two species exists only along the x-direction, $i.e.$ along the weak axis direction. Comparing the density plots along the x-direction with those along the other directions ($i.e.$ the y- and z-directions), we see that this characteristic segregation is visible along x only. The similarities between the plots of panels **c** and **d** with those of panels **g** and **h** in Figures 4.3 and 4.4 show that experimentally the orientation of the camera is crucial to discriminate the different possible states that can exist, and the best orientation is one where the weak axis is parallel to one of the sensor directions.

68

Looking at the 3D representation of the BEC mixtures in Figures 4.3 and 4.4, we see that the species with the largest atom number in the mixture will be the most prominent in the plot. In the asymmetric configuration it is also the one that will sit in the trap minimum, as seen for the blue Rb cloud in Figure 4.4**e**, where there are almost 3 times more Rb atoms than K atoms. The study of the energy per atom in the mixture will indicate the contribution of each species to the total energy of the mixture.

The imaginary time propagation algorithm used to find the ground state of the mixture in micro-gravity is designed so that the final converged states have a relative energy variation between two consecutive time iterations of less than 10^{-12}. We can also verify that this state is stationary by propagating it in real time for a given holding period. The atomic density along the x-direction shows an almost vertical transition from one species to the other, similar to a potential wall that prevents any overlap between the two species, leading to a quasi-perfect segregation. As mentioned above, the symmetric state should normally be the ground state, and the two asymmetric states should normally be stationary states that can be referred to as metastable states of the trap [102].

Table 4.1 – Table comparing the energies per atom for the symmetric and asymmetric configurations in the CAL and MAIUS chip traps in microgravity. The minimum values are given in blue. For the MAIUS (CAL) chip trap, we have 43,900 (1,400) Rb atoms and 14,400 (1,900) K atoms, respectively.

	MAIUS chip trap		CAL chip trap	
Energy per atom	Symmetric (nK)	Asymmetric (nK)	Symmetric (nK)	Asymmetric (nK)
Kinetic Energy Rb	2.23	2.24	6.50	6.88
Potential Energy Rb	33.36	35.56	14.96	17.26
Interaction Energy Rb-Rb	26.17	24.68	8.03	6.63
Kinetic Energy K	1.83	1.61	15.32	14.49
Potential Energy K	17.99	16.15	32.14	29.55
Interaction Energy K-K	5.60	6.99	8.25	10.23
Interaction Energy K-Rb	0.25	0.16	0.31	0.19
Total Energy	87.43	87.49	85.50	85.23

Table 4.1 shows the contribution of each species and energy term to the total energy of the states obtained from the imaginary time propagation for the symmetric and asymmetric configurations for both chip traps. All energies are converted to nK per atom, which correspond to the energies divided by the total number of atoms in the system. For each row, we compare the energies between the two columns corresponding to the symmetric and asymmetric states, and the value in blue corresponds to the minimum. On the last row of the table we see that the total energy per atom in the symmetric and asymmetric states are very close, with a difference of $|\Delta E_{MAIUS}| = 0.06$ nK/atom, which is 0.07 % of the total energy per atom and $|\Delta E_{CAL}| = 0.27$ nK/atom, which is 0.32 % of the total energy per atom. These energy differences are thus extremely small compared to the total energy in the mixture. It shows that both states are nearly degenerate in energy. We also observe that the lowest energy configuration can differ, depending on the system. For the MAIUS chip trap, the symmetric state has the lowest energy with $E_{tot,MAIUS} = 87.43$ nK/atom, whereas for the CAL chip trap the

asymmetric state has the lowest energy with $E_{tot,CAL} = 85.23$ nK/atom. The second to last row of the table shows that the asymmetric state achieves the lowest interspecies interaction. This could be due to the presence of a single "contact surface" between the two species when side by side, compared to when the Rb cloud is sandwiched between two clouds of K. This also results in a lower intraspecies interaction for K in the symmetric configuration. Ultimately, the total energy of the symmetric and asymmetric configurations results in a trade-off between intraspecies and interspecies interactions.

Since the states are almost degenerate in energy, they have a similar probability to appear experimentally. In addition to that, these states are very sensitive to the environment and all potential asymmetries of the fields in the system, so they are very fragile. It suggests that it might be difficult to get the perfect symmetric state experimentally, and it would be even more difficult to predict what is the state that is produced.

4.5 . Numerical application : BEC dynamics with different scattering lengths

After deriving in the previous sections the scaling equations used to solve the coupled time-dependent Gross-Pitaevskii equations for BEC mixtures, we implemented them in Fortran codes. Our first objective was to check whether we obtain the same numerical results using a fixed-grid method and our scaled-grid method. The second one was to numerically observe the effect of a dynamical sequence on a dual-species mixture in microgravity for different interspecies scattering lengths.

In this application, we assume that the atoms are trapped by the magnetic field produced by a Z-shape atom chip configuration [59, 62, 66, 67, 126] in the presence of a time-dependent homogeneous magnetic field generated by magnetic coils through which a tunable current flows. Here we implement the transport induced by a linear variation of the coil currents during 10 ms followed by a holding of 20 ms in the final trap. Since the relative variation of the current during the transport is small, the trajectory followed by the trap is one-dimensional and linear along the z-direction, and the evolution of the trapping frequencies over time is also linear. The dynamics is assumed to take place in microgravity, and the position of the trap centre is therefore the same for potassium and rubidium. At time $t = 0$, its initial position is 314.97 μm above the atom chip. The transport consists of a translation in the z-direction, perpendicular to the chip, moving the centre of the trap to 333.56 μm above the chip. The transport then has a total length of 18.59 μm, to be compared with the initial width (FWHM) of the atomic density distribution along z of about 2 μm. As in the other applications, we associate the index $j = 1$ with rubidium and the index $j = 2$ with potassium. For rubidium, the trapping frequencies vary linearly from

$$\omega_{1,X_1}(0) \quad = 2\pi \times 24.8 \text{Hz} \tag{4.49a}$$
$$\omega_{1,Y_1}(0) \quad = 2\pi \times 378.3 \text{Hz} \tag{4.49b}$$
$$\omega_{1,Z_1}(0) \quad = 2\pi \times 384.0 \text{Hz} \tag{4.49c}$$

to

$$\omega_{1,X_1}(t_f) \quad = 2\pi \times 24.9 \text{Hz} \tag{4.50a}$$

$$\omega_{1,Y_1}(t_f) \quad = 2\pi \times 340.9 \text{Hz} \tag{4.50b}$$

$$\omega_{1,Z_1}(t_f) \quad = 2\pi \times 346.4 \text{Hz} \tag{4.50c}$$

The initial and final trapping frequencies ω_{2,Σ_2} for potassium with $\Sigma \in \{X, Y, Z\}$ are given by

$$\omega_{2,\Sigma_2}(t) = \left(\frac{m_1}{m_2}\right)^{\frac{1}{2}} \omega_{1,\Sigma_1}(t) \tag{4.51}$$

We consider a mixture of 43,900 rubidium atoms with 14,400 potassium atoms, similar to what can be regularly achieved with the MAIUS-2 experiment on ground [79]. To explore different miscibility regimes, we consider 3 different cases with the following interspecies scattering length values $a_{12} = 0$, 1 and 8.747 nm. In principle, this variation of the scattering length can be realized experimentally using the Feshbach resonances observed in K-41 and Rb-87 mixtures around 35 G and 79 G using a dipole trap [113]. The last value $a_{12} = 8.747$ nm corresponds to the natural scattering length between K-41 and Rb-87 in the absence of any Feshbach resonance.

The first step in the simulation is to determine the ground state of the mixture confined in the initial trap using the imaginary time propagation method. We can see in Figure 4.5 that the spatial distribution of the two species in the ground state is different depending on the value of the inter-species scattering length a_{12}. The first two columns correspond to two miscible cases associated with $a_{12} = 0$ nm and $a_{12} = 1$ nm, respectively. The third column corresponds to the immiscible case $a_{12} = 8.747$ nm calculated with the same trapping parameters and shown in the previous section 4.4. The first line shows the 3D representation of the atomic density associated with Rb (blue) and K (red). As seen in the previous section for the $a_{12} = 8.747$ nm case, we see that its immiscible nature is clearly visible in a distinctive hamburger-like structure. On the other hand, we see that the two miscible cases show a large spatial overlap of the two condensates. The last three rows in Figure 4.5 show the 1D integrated atomic densities for Rb (blue) and K (red) along the three directions x, y and z at the initial time $t = 0$. The dashed line on all plots indicates the position of the trap minimum and draws a symmetry axis. These plots also show that the two miscible cases considered here are very similar, with a complete overlap of the densities in all directions. Therefore, the introduction of a weak repulsive interaction between Rb and K ($a_{12} = 1$ nm, middle column of Fig. 4.5) has very little impact on the initial spatial distribution of the atomic densities compared to the non-interacting case ($a_{12} = 0$ nm, left column of Fig. 4.5). Comparing the last two rows of the Figure, we see that the spatial distributions in y and z for the non-miscible case (panels **i** and **l** in Fig. 4.5) are relatively unaffected by the introduction of a strong repulsion between Rb and K atoms. Indeed, the spatial discrimination is only observed in the direction of the weak trapping axis, *i.e.* the x-direction (see panel **f** in Fig. 4.5).

Figure 4.6 shows the calculated probability densities for K and Rb at the end of the transport and holding sequence, at time $t = t_f = 30$ ms. The first row shows a 3D representation of the atomic densities. The next three rows show the averaged probability densities P_x, P_y and P_z calculated with the scaled-grid method described in section 4.3 (red and blue solid lines for K and Rb, respectively) and
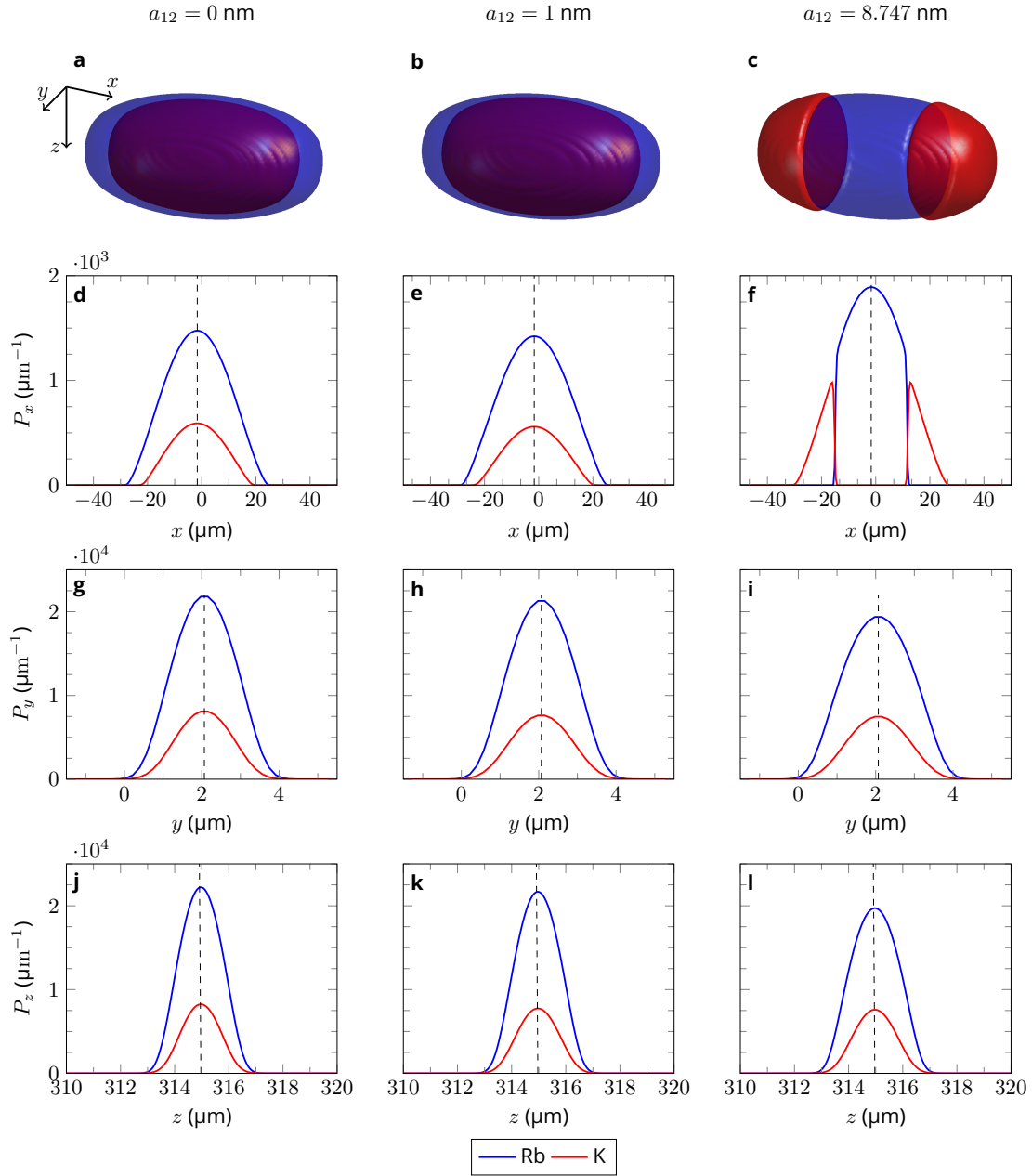
Figure 4.5 – Calculated ground state of a dual species condensate of K and Rb in microgravity in two miscible phases (left and middle columns) and one immiscible phase (right column) in a cigar-shaped trap. The 3D representations are shown in the first row (panels **a**, **b** and **c**) and the integrated density profiles P_x, P_y and P_z for Rb (blue) and K (red) are shown in the next three rows. The intraspecies scattering lengths are $a_{11} = 5.237$ nm and $a_{22} = 3.204$ nm. The interspecies scattering length is $a_{12} = 0$ nm in the left column, $a_{12} = 1$ nm in the middle column and $a_{12} = 8.747$ nm in the right column. The trap frequencies are given in Eqs. (4.49) and (4.50). The number of rubidium and potassium atoms is 43,900 and 14,400 respectively. The centre of the trap is marked by a black vertical dotted line in each subplot.
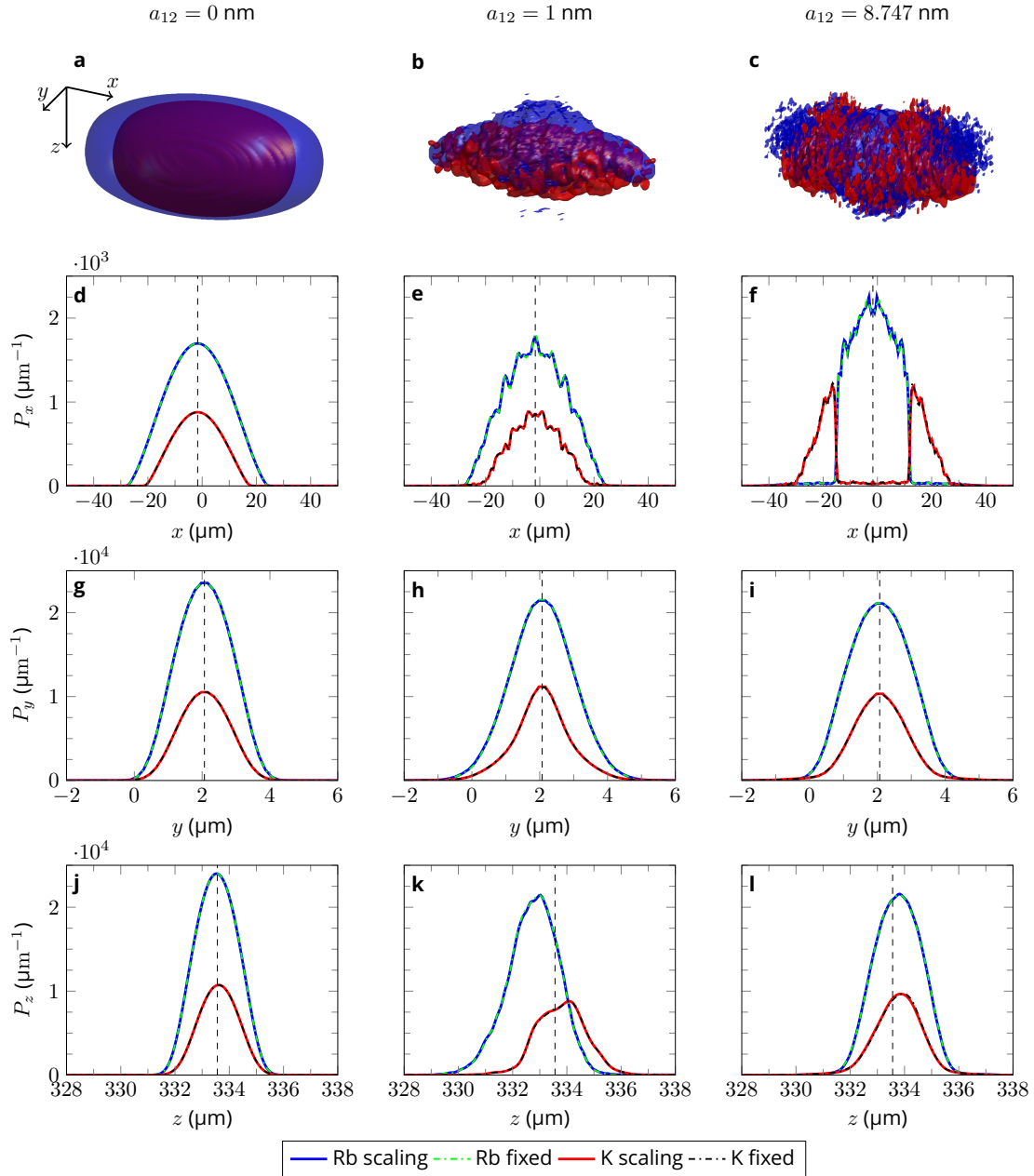
Figure 4.6 – Probability density of a dual Rb-K condensate in microgravity after 10 ms of transport and 20 ms of holding. The first row shows the 3D representations and the next 3 rows show the density profiles P_x, P_y and P_z for K (red) and Rb (blue). The interspecies scattering length is $a_{12} = 0$ nm in the left column, $a_{12} = 1$ nm in the middle column and $a_{12} = 8.747$ nm in the right column. The number of Rb and K atoms is 43,900 and 14,400, respectively. The centre of the trap at the final time is marked by a black vertical dotted line in each subplot. In panels **d** to **l**, the Rb probability densities calculated with the scaled-grid approach and with a fixed grid are shown as solid blue lines and dashed green lines, respectively. Similarly, the K probability densities calculated with the scaled-grid approach and with a fixed grid are shown as solid red lines and dashed black lines, respectively.

Table 4.2 – Transport dynamics computation (cpu) time. The calculations were performed in parallel using 16 cores of an Intel Xeon Gold 6230 processor running at 2.1 GHz. The real calculation time is roughly the displayed values shown in the table divided by the number of cores.

a_{12} (nm)	Ground State Calculation		Ramp & Holding Dynamics	
	Fixed Grid	Scaled Grid	Fixed Grid	Scaled Grid
0	9 h 10 min	3 h 02 min	9 h 25 min	3 h 03 min
1	9 h 39 min	3 h 00 min	9 h 37 min	2 h 58 min
8.747	24 h 19 min	8 h 03 min	9 h 23 min	3 h 04 min

with a fixed grid (black and green dashed lines for K and Rb, respectively). The probability densities calculated with these two different methods are perfectly superimposed, demonstrating the validity of the scaled-grid approach regardless of the chosen interaction regime, *i.e.*, miscible or not. These results confirm that the two approaches are identical in principle, since they stem from calculations that are mathematically equivalent. However, they could differ due to numerical errors induced by the limited precision of the calculations and interpolation to different spatial grid points. A comparison of the first two columns of Figure 4.6, and in particular of panels **d** and **e**, shows that the introduction of a weak interaction between Rb and K induces significant perturbations during the dynamics in the spatial density profile in the x-direction corresponding to the weakest trapping axis, whereas the effect of this small interaction is negligible in the ground state (see panels **d** and **e** in Fig. 4.5). We can conclude that here, the transport acts as a detector of these interspecies interactions, even if they are relatively weak. Comparing panels **j** and **k**, we also see that this weak interspecies interaction induces a shift of the average position of the two atomic species in the z-direction of the transport as well as a deformation of the density profile, which is not the case here for the non-interacting mixture.

In order for the calculation to converge, it is necessary to use a larger grid with a larger number of grid points in the fixed-grid approach than in the scaled-grid approach. The fixed grid must be at least longer than the total displacement of about 18.6 μm along the z-direction of the sequence, so that the wave function can be accurately described at all times. The fixed-grid approach uses $(N_x = 256, N_y = 64, N_z = 576)$ grid points, while the scaled-grid approach uses $(N_x = 256, N_y = 64, N_z = 192)$ grid points. The total number of $N_x \times N_y \times N_z$ grid points required is thus 3 times larger for the fixed-grid approach than for the scaled-grid approach. As shown in Table 4.2, this variation in the number of grid points has a strong impact on the computational time. In fact, the computational time, either for obtaining the ground state using the imaginary time approach [70, 117] or for calculating the dynamics, is on average 3 times longer with the fixed-grid approach than with the scaled-grid approach. The ratio of 3 obtained here is due to the necessity of increasing the size of the grid in the z-direction, *i.e.* in the direction along which the transport takes place. Here, the transport was designed in such a way that we limit the range of the displacement so that it is not too large (about 18.6 μm) compared to the initial size of the condensate (about 2 μm FWHM in the z-direction, as shown in panels **j**, **k** and **l** of Fig. 4.5), in order to keep the computational time reasonable for the fixed-grid approach. However, many experiments in the past have required the realisation of condensate displacements over distances of the order of a millimeter [45, 49, 52]. Thus, it can be estimated that the calculation
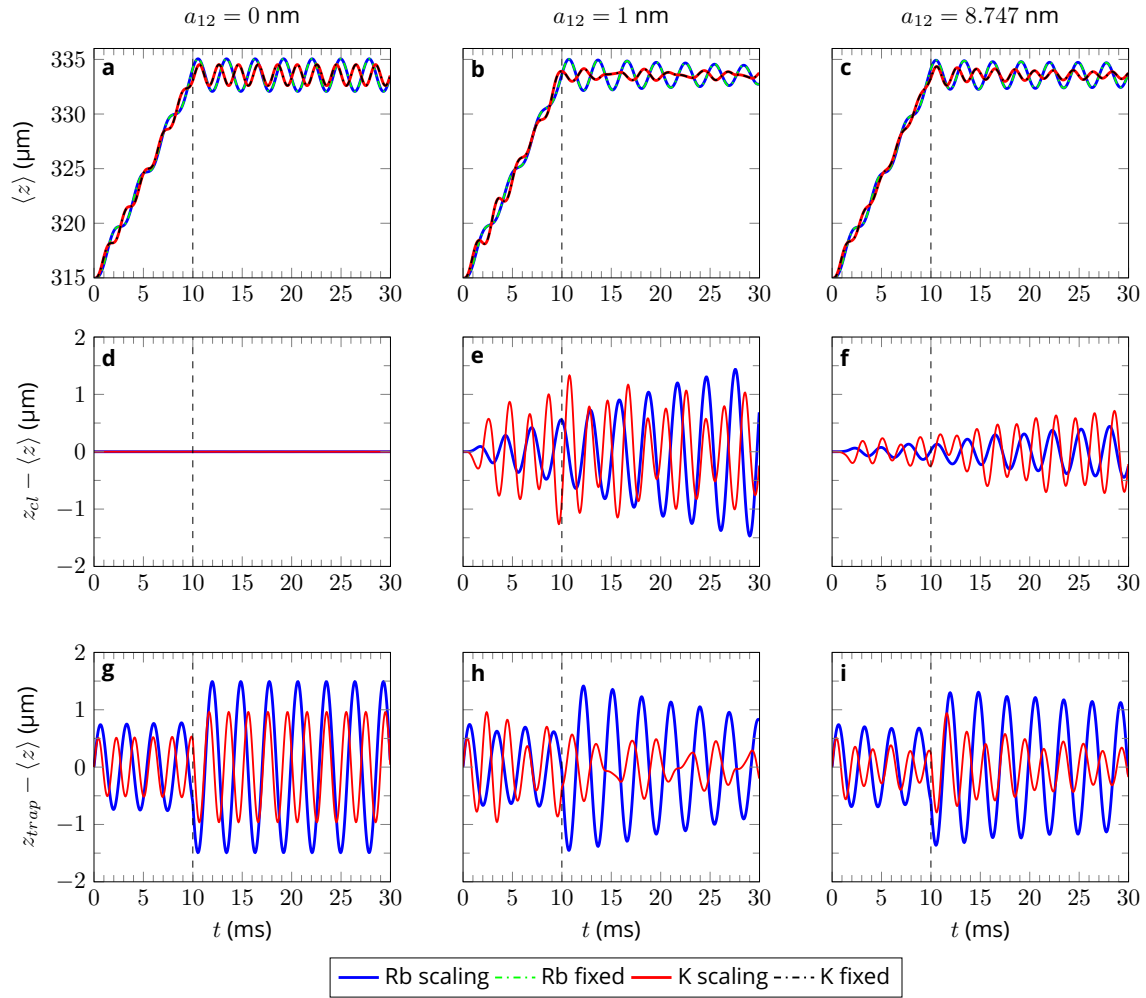
Figure 4.7 – Evolution of the position of the atom clouds along the z direction during the dynamics of transport and holding for the 3 values of the interspecies scattering length considered here : $a_{12} = 0$ in the left column, $a_{12} = 1$ nm in the middle column and $a_{12} = 8.747$ nm in the right column. The first row shows the average position $\langle z \rangle$ for Rb and K as a function of time. The second row shows the offset between the average position $\langle z \rangle$ and the expected trajectory $z_{cl}(t)$ when Newton's law is applied independently for each species. The third row shows the offset between the average position $\langle z \rangle$ and the centre of the trap. The color code associated with Rb and K is the same as in Figure 4.6. The end of the transport is marked by a black vertical dashed line in each subplot.

of transport dynamics in such situations would require the use of 100 or 200 times more grid points in a fixed-grid calculation than in the scaled-grid approach, making this type of calculation extremely demanding in terms of memory resources as well as computational time, or even impossible with standard computing facilities. We can also see that in the case of the immiscible mixture, the calculation of the ground state takes more time because it requires more iterations to separate the different geometries of this state (see section 4.4.2 for details).
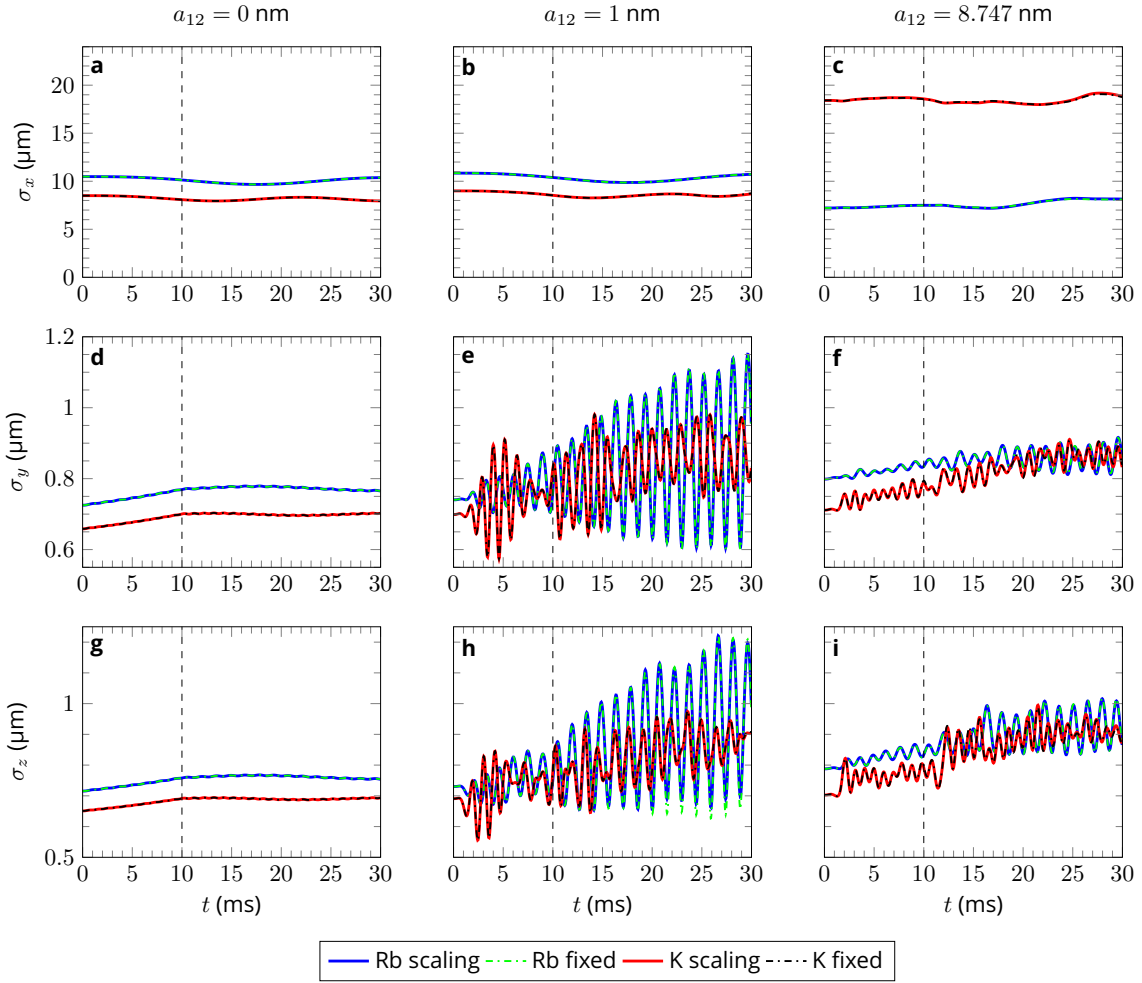
Figure 4.8 – Size evolution of the Rb and K clouds along x, y and z during the transport and holding for $a_{12} = 0$ (left column), $a_{12} = 1$ nm (middle column) and $a_{12} = 8.747$ nm (right column). The color code associated with Rb and K is the same as in Figure 4.6. The end of the transport is marked by a black vertical dashed line in each subplot.

Let us now study in more detail the displacement dynamics of the mixture by calculating the average positions of the two condensates over time, which will be referred to as the "trajectories" followed by the two atomic clouds, and by calculating the evolution of the average "size" of the two condensates, which will be defined as the standard deviations of the Rb and K atomic densities. Since the transport is unidirectional, we only need to focus on the z direction. The average trajectories followed by the two condensates are defined as $\langle z \rangle = \langle \Psi_j | z | \Psi_j \rangle$. They are shown in the first row of Figure 4.7 using the same colour coding as in Figure 4.6. In panels **a**, **b** and **c** we see that the fixed-grid and scaled-grid calculations lead to the same results regardless of the interaction regime considered. In panels **g**, **h** and **i**, it can be seen that the condensates start to oscillate in the trapping potentials as the transport unfolds. This is due to the fact that it is too fast to be adiabatic. Furthermore, these oscillations, which occur at different frequencies for Rb and K, continue into the holding phase. In panel **g**

we see that these oscillations are regular, similar to what could be obtained by solving the dynamics of a harmonic oscillator. However, in the presence of interactions, the collisions between the species perturb the trajectories followed by the two condensates. Consequently, even if the average positions of the condensates obey classical laws of motion when the interspecies interaction is suppressed (see panel **d**), this is no longer the case in the presence of an interaction (see panel **f**), even if this inter-action is relatively weak (see panel **e**). Finally, panels **g**, **h** and **i** show that the remaining oscillations observed during the holding phase are characterized by multiple modes that differ as a function of the interspecies scattering length.

The evolution of the average sizes of the two condensates, defined as the standard deviations of the Rb and K atomic densities along the x, y and z directions, are shown in Figure 4.8 using the same colour coding as in Figure 4.6. In this figure we see that the fixed-grid and scaled-grid approaches also give the same results for the evolution of the sizes, regardless of the interaction regime. During the transport, the trapping frequency for Rb and K remains almost constant along the x-direction, while the trapping frequencies along the y- and z-directions decrease by slightly less than 10 %. This relatively small variation of the trapping frequencies leads to a smooth evolution of the size of the two atomic clouds in the absence of interspecies interactions ($a_{12} = 0$ in the left column of Fig. 4.8). On the other hand, panels **e**, **f**, **h** and **i** show that the presence of a non-zero interspecies interaction ($a_{12} = 1$ nm in the middle column and $a_{12} = 8.747$ nm in the right column) leads to relatively strong collective excitations of the two condensates in the y- and z-directions, which continue into the holding phase. Since the change of the trap frequency along the x-direction is negligible, no such perturbation effect is observed in this particular direction (see panels **b** and **c** in fig. 4.8).

4.6 . Application to the MAIUS experiments on ground : Free expansion of a BEC mixture in the presence of gravity

4.6.1 . Presentation of the experiment and verification of the scaled-grid code

In this application of the multi-species scaled-grid approach, we study the free expansion of a dual-species BEC mixture of K-41 and Rb-87 in the presence of gravity. After testing the code for a short expansion time, we will compare the results of the simulation with experimental data taken in the laboratory by the MAIUS team in Hannover (Germany) [79]. The number of atoms considered is again 43,900 for Rb and 14,400 for K. We simulate the free expansion of the K-Rb mixture, starting at $t = 0$ from the ground state of this dual-species mixture. Due to the gravitational sag, the centres of the trapping potentials associated with each species are shifted, mainly in the z-direction, which is the direction in which gravity acts. In addition, the eigenaxes of the traps associated with Rb and K are rotated very slightly. This rotation is taken into account in the calculations using transformation matrices as presented in Chapter 2 (see section 2.7). The initial trap uses the same electric current flowing through the magnetic coils and chip wires as in the example presented earlier in section 4.5, which discussed the dynamics of transport and holding in microgravity. In the case of Rb, the initial
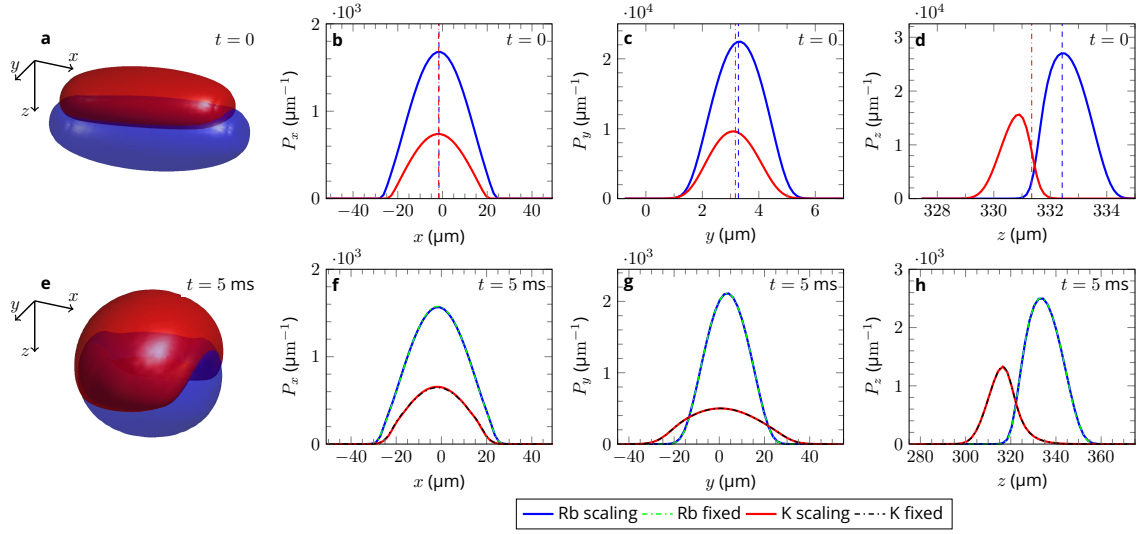
Figure 4.9 – Probability density of a dual Rb-K condensate in the presence of gravity. Shown are the 3D representations (first column) and the integrated density profiles P_x, P_y and P_z (second column : along x, third column : along y, fourth column : along z). The first row shows the initial ground state. The second row shows the same density after 5 ms of free expansion. The scattering lengths are $a_{11} = 5.237$ nm, $a_{22} = 3.204$ nm and $a_{12} = 8.747$ nm. In the first row the centres of the Rb and K traps are marked by blue and red vertical dashed lines, respectively. The number of Rb and K atoms is 43,900 and 14,400, respectively. Gravity points in the positive z direction. In the second row, the Rb probability calculated with the scaled-grid approach and with a fixed grid are shown as solid blue and dashed green lines, respectively. Similarly, the K probability densities calculated with the scaled-grid approach and with a fixed grid are shown as solid red and dashed black lines, respectively.

trap is positioned at $(x_1, y_1, z_1) = (-1.62, 2.23, 332.43)$ µm and the initial trapping frequencies are

$$\omega_{1,X_1}(0) \quad = 2\pi \times 25.3 \text{Hz} \tag{4.52a}$$

$$\omega_{1,Y_1}(0) \quad = 2\pi \times 345.1 \text{Hz} \tag{4.52b}$$

$$\omega_{1,Z_1}(0) \quad = 2\pi \times 347.1 \text{Hz} \tag{4.52c}$$

For K, the initial trap is positioned around $(x_2, y_2, z_2) = (-1.76, 2.24, 331.35)$ µm, and the initial trapping frequencies are

$$\omega_{2,X_2}(0) \quad = 2\pi \times 36.5 \text{Hz} \tag{4.53a}$$

$$\omega_{2,Y_2}(0) \quad = 2\pi \times 504.1 \text{Hz} \tag{4.53b}$$

$$\omega_{2,Z_2}(0) \quad = 2\pi \times 509.8 \text{Hz} \tag{4.53c}$$

The first row of Figure 4.9 shows the spatial distribution of the dual-species condensate at time $t = 0$, to be compared with the distribution shown in the last column of Figure 4.5, which shows the data for the same trap implementation in a microgravity environment. From this comparison

we can already conclude that the presence of gravity affects significantly the initial structure of the condensate. The most notable change is that the symmetry of the hamburger-like structure of the condensate is broken in the presence of gravity. Due to the segregation along the z-direction, both species can sit in the trap minimum along the x-direction as seen in panel **b**, which was not the case in microgravity. We can see that along the z-direction the maximum density of the Rb cloud is at the trap minimum, while the peak of the K density is slightly shifted due to the repulsive interaction between the two species.

Since the size of the two-species condensate increases rapidly as it is released from the trap, we have limited the duration of the time-of-flight to 5 ms so that a fixed-grid calculation remains feasible. The second row of Figure 4.9 shows the spatial distributions of the atom clouds at time $t = 5$ ms, *i.e.* at the end of the free expansion. It can be seen that during this time the sizes of the Rb and K clouds grow by a factor of about 10 in both the y and z directions. On the contrary, the size along the weak axis x remains almost unchanged. In this second row, we also compare the probability densities calculated at the end of the expansion with the scaled-grid method (blue and red solid lines for Rb and K, respectively) with those obtained using a fixed grid (green and black dashed lines for Rb and K, respectively). The probability densities calculated with both methods are in perfect agreement, confirming the validity of the scaled-grid approach in this example, where the atomic expansion dynamics occurs in the presence of gravity.

As with the transport and holding example discussed in the previous section 4.5, achieving convergence when describing the expansion with a fixed grid requires a larger number of grid points than with the scaled-grid approach. In fact, in this example, the fixed-grid approach uses $(N_x = 64, N_y = 256, N_z = 256)$ grid points, while the scaled-grid approach uses $(N_x = 64, N_y = 64, N_z = 64)$ grid points. The total number of $N_x \times N_y \times N_z$ grid points required is therefore 16 times greater for the fixed-grid calculation (4,194,304) than for the scaled-grid approach (262,144). As shown in Table 4.3, this variation in the number of grid points has a strong impact on the computation time, dramatically favouring the scaled-grid approach in terms of both CPU time and, of course, memory consumption. It can be seen that the increase in the number of points affects the y and z directions along which the condensate expansion is most significant. The computational time in this 5 ms expansion, both for obtaining the ground state and for computing the dynamics, is on average 18 times larger with the fixed grid than with the scaled-grid approach, which is consistent with the ratio of grid sizes. Of course, this factor of 18 depends on the expansion time, since the size of the condensate increases linearly with time after the initial acceleration phase. As shown in Table 4.3, for an expansion time of 8 ms, the computation time in a fixed grid is on average 68 times larger than in the scaled-grid approach. Actually, this computation requires $64 \times 512 \times 512$ grid points, *i.e.* 64 times more than with the scaled-grid approach. On the one hand, the scaled-grid approach is characterized by a computation time that grows linearly with the free expansion time since the number of grid points does not need to change. On the other hand, the fixed-grid approach has a grid size that scales with $\lambda_x(t_{TOF})\lambda_y(t_{TOF})\lambda_z(t_{TOF})$, the product of the scaling factors of the BEC size in all directions, and the dynamics code has a duration of the order of $O(N_{ngp} \log(N_{ngp}))$ where $N_{ngp} = N_x \times N_y \times N_z$. In practice, many free expansion experiments are performed over durations of tens of milliseconds [45, 49, 52]. A simple extrapolation of the results obtained here gives a gain in computational time of the order of 600 for a free expansion of 25 ms and of 10,000 for a time of flight of 100 ms. Such calculations quickly become

79

Table 4.3 – Computation (cpu) time for the calculation of a dual-species condensate free expansion dynamics in gravity. The calculations were performed parallelizing 16 cores of an Intel Xeon Gold 6230 processor running at 2.1 GHz. The real calculation time is roughly the displayed values of the table divided by the number of cores.

| | Ground State | | Expansion Dynamics | |
TOF (ms)	Fixed Grid	Scaled Grid	Fixed Grid	Scaled Grid
5	11 h 06 min	31 min	55 min	3 min 40 s
8	39 h 07 min	31 min	6 h 12 min	6 min 06 s
25	16 days*	31 min	7 days*	18 min 32 s
100	266 days*	31 min	432 days*	78 min 31 s
1000	N/A	31 min	N/A	16 h 23 min

* Estimation based on the number of grid points required.

cumbersome in the standard fixed-grid approach, which confirms the importance of developing the scaled-grid approach presented in this work for an efficient treatment of the expansion dynamics of multispecies quantum mixtures. Reaching the regime of a few seconds of free expansion is also within reach, since we have seen that the scaled-grid computation time scales linearly with the expansion time, and would amount to about 16 hours of CPU time, which can be easily reduced by parallelization to about one hour of real computation time for 1 s of free expansion using, as in our case, 16 or more cores (see Table 4.3). Using more parallel cores for the calculations would reduce the real computation time even more.

4.6.2 . Comparison with experimental data

After the validation of our scaled-grid code for dynamics including displacements and free expansion with and without gravity, we can now compare the results of a BEC mixture simulation with experimental data. Here we study the results of the free expansion during 25 ms of a BEC mixture of K and Rb atoms obtained during a calibration campaign in Hannover in preparation for the MAIUS-2 and MAIUS-3 missions [79]. During these experiments, quantum degenerate mixtures with variable proportions of Rb and K atoms were prepared and several free expansions of the mixtures were realized. Our goal is first to verify the applicability of our computational method by comparing its predictions with experimental measurements, and second to gain a better understanding of the multi-species dynamics.

In the first column of Figure 4.10 we see the experimental absorption images of the K (first row, panel **a**) and Rb (second row, panel **d**) clouds after a free expansion of 25 ms. For each image, the bright red colour corresponds to the highest measured atomic density, and the dark blue regions correspond to low atomic densities. The number of condensed Rb and K atoms, calibrated by experimental measurements, is 43,900 and 14,400, respectively. Comparing panels **a** and **d** we can see that the experimental image of K shows more background noise than for Rb because there are about 3 times fewer atoms of K than of Rb. The intensity of the peak of K is therefore lower than for Rb, decreasing the signal-to-noise ratio. The vertical direction X_C of the camera corresponds to the direction z of
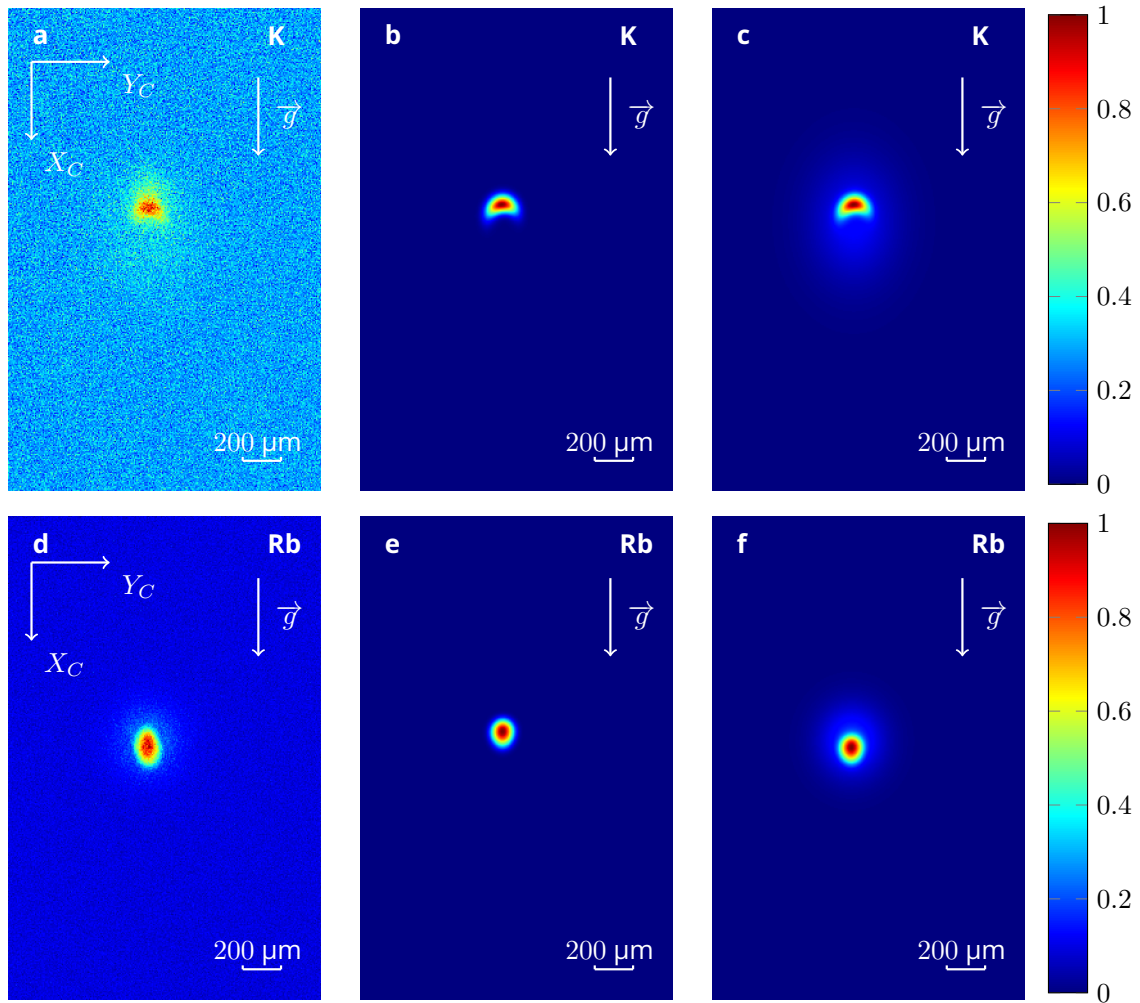
Figure 4.10 – Normalized 2D atomic densities of K (first row) and Rb (second row) after a free expansion of 25 ms, starting from the initial trap described by Eqs. (4.52) and (4.53). First column : false-colour absorption images measured by the MAIUS-2 apparatus in a ground-based experiment [79]. The direction of gravity, indicated by white arrows, is vertical along the camera axis X_C, orthogonal to the atom chip. The Rb and K images are normalized for better visibility. The fitted atom numbers are 43,900 for Rb and 14,400 for K. Second column : Condensate probability densities calculated with the scaled-grid approach in the plane (X_C, Y_C) of the camera. The theoretical images **b** and **e** have been translated so that the position of the maximum of the K density is the same for the experimental and simulated signals, and convoluted with a Gaussian of width 15 μm. Third column : Calculated total probability densities including thermal atoms (see text for details).

gravity. The horizontal axis Y_C of the camera is in the (x, y) plane, and makes an angle of 46° with the x-axis of Figure 4.9. The initial Rb and K frequencies are given by Eqs. (4.52) and (4.53), and the initial state of the condensed dual-species mixture has already been shown in the first row of Figure 4.9. The second column of Figure 4.10 shows the projection in the camera plane of the atomic densities

81

calculated after 25 ms of free expansion by the numerical solution of the coupled Gross-Pitaevskii equations (4.1) in the scaled-grid approach, with K in the first row (panel **b**) and Rb in the second row (panel **e**). The grid used in the numerical calculations has been translated so that the position of the maximum K density is the same for the experimental and simulated data. Comparing the position of the Rb cloud in panel **d** with that in panel **e** shows a slight shift between the measured and calculated positions of the Rb cloud. This shift is about 81.6 µm in the X_C direction of gravity and about 16.3 µm in the transverse Y_C direction. Compared to the distance of about 3 mm covered by the atoms during the 25 ms free fall, this global shift of 83.2 µm between experiment and theory is relatively small, since it represents only 2.7% of the total displacement. This small shift may be due to an initial oscillation of the atoms before the expansion stage in the experiment, or to an additional kick experienced by the atoms during the switch-off of the trap-inducing currents, two effects not considered in the simulation. Still, it can be concluded that the comparison between the experimental measurements and the numerical simulation shows a good qualitative agreement between theory and experiment in the region of interest of the CCD camera. It should also be noted that an efficient simulation of the 3D dynamics of the mixture was only possible using the scaled-grid method, with a grid that adapts over time to the centre-of-mass motion and size expansion of the condensate, as presented in Section 4.3.

Let us perform a more quantitative study to refine this comparison. The size of the image shown in Figure 4.10 corresponds to the region of interest taken for data analysis. The intensity information given by each pixel of the camera region was integrated in each direction to obtain the integrated 1D signals shown as blue solid lines in Figure 4.11. These integrated experimental data are characterized by bimodal structures, with quasi-Gaussian pedestals corresponding to the presence of a thermal cloud. The 2D camera recorded data shown in panels **a** and **d** of Figure 4.10 for Rb and K have therefore been fitted by a fit function constructed as the sum of a 2D Gaussian with an inverted 2D parabola. The 2D Gaussians associated with Rb and K are used to represent the thermal cloud, and their integrals are shown as green dash-dotted lines in each subplot of Figure 4.11. For the 2D plots of the coupled GPE solutions, these images were numerically convoluted to a 2D Gaussian function with a standard deviation (RMS width) of $\sigma = 15$ µm in all directions to mimic the effect of camera resolution. These convoluted 2D images were then integrated along the two camera axes. The simulated Rb peak was shifted by 81.6 µm in the X_C direction and by 16.3 µm in the Y_C direction to match its position with the observation from panel **d** of Figure 4.10. This shift was introduced to account for the initial velocity difference between the Rb cloud and the K cloud during the expansion, which is not included in our simulation model. We combine the integration of the convoluted simulation results, representing the condensed part of atom cloud, with the Gaussian-fit, representing the thermals atom, to get the total simulated atomic density, and plot it as the solid red lines in Figure 4.11. The comparison between the experimental measurement (solid blue line) and the results of the numerical simulation using the scaled-grid approach (solid red line) shows a very good agreement. The result of this numerical model taking into account the simulated condensed atoms and the fitted thermal atoms is also shown in the right column of Figure 4.10, which also compares very favorably with the images taken by the camera (see left column of Figure 4.10). We can conclude that our numerical approach using the scaled-grid method to solve the coupled GPE enables an efficient and accurate simulation of the BEC mixtures. We can also observe that the centres of the condensed and thermal fraction distributions do not coincide, especially for the lighter K species (see Figure 4.11). This non-
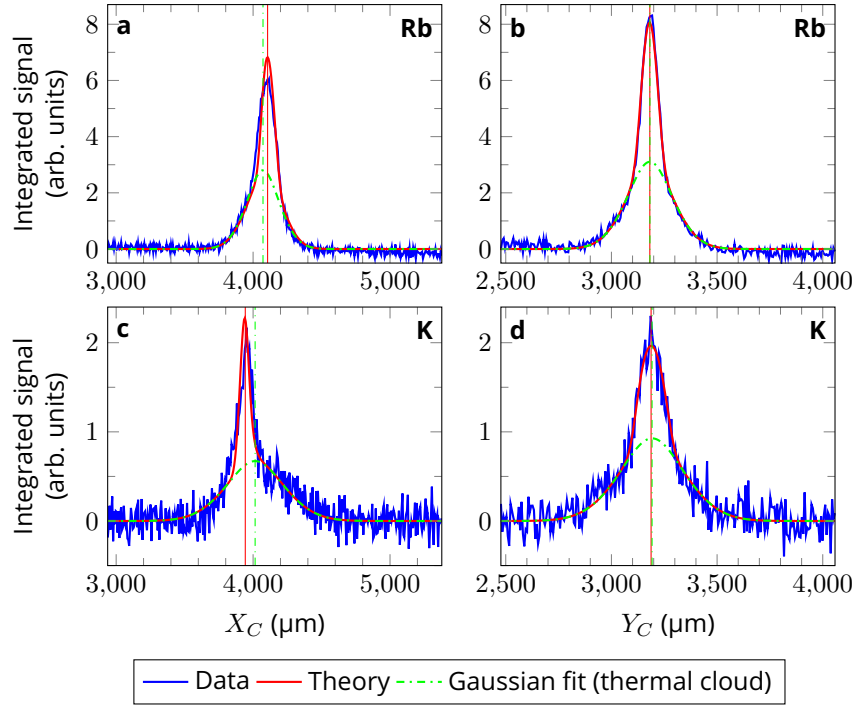
Figure 4.11 – Integrated atomic densities of Rb (first row) and K (second row) in arbitrary units along the camera directions X_C and Y_C in the MAIUS experiment on ground after 25 ms of free fall. In the first column the integration of the 2D images shown in Figure 4.10 is performed along Y_C and in the second column the integration is performed along X_C. The solid blue line is the experimental measurement and the dashed green line is the Gaussian fit describing the thermal component of the atomic cloud. The solid red line is the adjusted numerical simulation, which includes both the computed condensed and the fitted thermal components. The vertical lines correspond to the average position of the condensed part of the atomic cloud for the solid red line, and to the centre of the thermal part for the dash-dotted green line. The offsets between the positions of the condensed and thermal parts in the directions (X_C, Y_C) are $(+33.54, -0.41)$ µm for Rb and $(-40.93, -5.25)$ µm for K.

obvious, unexpected effect is due to the repulsion between the dense, interacting, degenerate parts of the clouds, which causes a shift of the centre of each BEC with respect to its more dilute thermal counterpart. This shift is thus a signature of the bimodal distributions of interacting mixtures.

To give more technical details about the simulations, the time step used in the calculations corresponds to one thousandth of the shortest time period associated with the trap of the K atom, which is lighter than Rb and therefore generally undergoes faster dynamics. This corresponds to a time step of 1.96 µs for a total propagation time of 25 ms. For an alternative visualisation of the time step, this results in 510 steps of time propagation for each ms of simulated dynamics. It should also be noted that in this calculation the volume of the computational grid increases from 107 µm $\times$ 7.84 µm $\times$ 9.16 µm, or 7.68×10^3 µm^3 at the beginning, to 172 µm $\times$ 617 µm $\times$ 734 µm, or 7.79×10^7 µm^3 at the end of the 25 ms TOF. The increase in volume therefore corresponds to a factor of about 10^4, which is extremely challenging to simulate. This increase is so large that a simulation with a fixed grid would not have

been feasible, as the required number of grid points is a hard limiting factor (see Table 4.3).

The experimental setup used by the MAIUS collaboration in Hannover has the possibility to rotate the trapping components, offering the opportunity to study the influence of gravity on different trapping configurations [79] for a mixture of K and Rb. The setup is tilted by an angle α defined between the direction of the gravity axis and the X_C axis of the camera, which is orthogonal to the atom chip. Due to the gravitational sag, the trapping potential for each condensate is rotated in the chip frame and redefined for the different values of the α angle, which ranges here from $0°$ to $60°$ by increments of $15°$. Repeating the same data analysis and simulation process as in the first part of this section, we compare the experimental data with the results of the simulation (simulated condensed and fitted thermal atoms) in Figure 4.12. The first and third columns correspond to the experimental data, while the second and fourth columns are the results of the simulation. For each row of the figure we have a different orientation of the gravitational acceleration, and the first row is another representation of the panels **a**, **c**, **d** and **f** of Figure 4.10. Comparing each pair of images, we can see a good agreement between the simulation and the experiment for all α angles. A more quantitative comparison between the experimental images and the simulation results can be found in Appendix B. It also validates the chip model and the use of rotation matrices to handle the rotation of the setup.

4.7 . Application to CAL – Scientific Module SM3

4.7.1 . Experimental results

In this section, the simulations follow a similar procedure as in the previous section with the MAIUS free expansion on ground. However, in CAL, microgravity makes the process a bit more delicate due to the quasi-degenerate steady states of the initial trap. Here we study the dual-species microgravity experiments realised by the JPL team with the CAL SM3 machine in the International Space Station during the commissioning phase. This corresponds to the calibration and verification of various aspects of the setup. More details on the experimental setup and procedure can be found in the following publication [53]. Here we focus on the comparison between the mixture model and the experimental results presented in that article.

The CAL SM3 machine has a similar setup to the previous SM2 machine, with the same orientation of the camera with respect to the atom chip. Let us recall the orientation of the (x, y, z) frame. The atom chip is in the (xy) plane, and the z-direction is orthogonal to the chip, pointing away from it. The camera is in the (xz) plane, orthogonal to the chip. Since we do not need the absolute position of the atomic clouds after the expansion for data analysis, the simulations will redefine the centre of the K cloud fitted from the camera images as the origin of the frame. For the imaging of the mixture, the Potassium cloud is first imaged after 12 ms of time-of-flight, and considering the imaging duration, the Rubidium cloud is observed 2.1 ms later (with a total TOF of 14.1 ms). These different expansion times are taken into account in the simulation.

A data analysis problem is the low signal-to-noise ratio due to the low atomic densities in the mixtures. To improve the quality of data analysis, a Principal Component Analysis (PCA) technique was
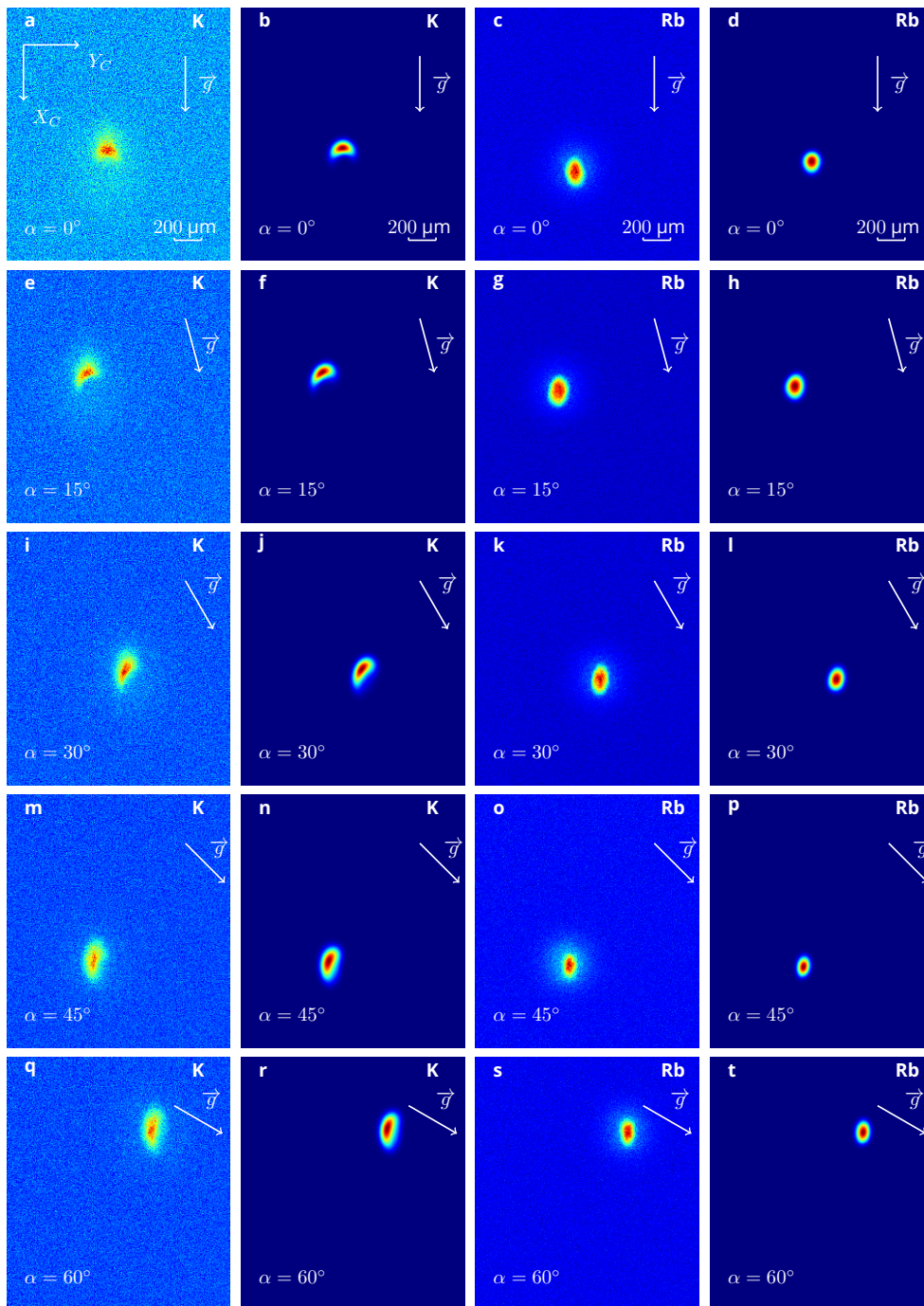
Figure 4.12 – Effects of the experimental setup rotation with respect to the gravity direction. The first and third columns correspond to experimental results and the second and fourth columns correspond to the calculated total probability densities including thermal atoms. Each line corresponds to a different value of the angle α between the X_C camera axis and the gravity direction (indicated by a white arrow), from 0° to 60° by increments of 15°.

applied to reduce the noise in the image. This technique identifies and enhances the most significant structures on the image [127–129]. The data from these images were averaged over the number of experimental realizations (5 for the mixture case, 3 for the single K BEC case), and a bimodal fit was applied. The extracted information, such as the number of condensed atoms, the position of the clouds, or the characteristics of the background thermal cloud, was then used in the simulation. Here we compare the results of the same experimental sequence, a short decompression of the evaporation trap followed by a short time-of-flight, with a dual-species mixture of K-41 and Rb-87 on one side, and only K-41 atoms on the other side.

In the dual species mixture, the data measured $N_{Rb} = 1,400$ condensed atoms of Rubidium and $N_K = 1,900$ of Potassium. In the single species experiment with only Potassium atoms, the fits from the data counted $N_K = 2,200$ condensed atoms. For the simulation process, we proceeded in the same way as in the previous section for the MAIUS experiments on ground. We solved the coupled GPE with the fitted atom number and used the data from the chip simulation to know the temporal evolution of the trap parameters. After projection to the camera plane, the 2D atom densities are convoluted to a Gaussian of size $\sigma = 15$ µm in both directions.

In microgravity we have the problem of calculating the ground state of the initial trap : we obtain different density distributions that are almost degenerate in energy. These states are shown in Figure 4.3, Section 4.4. The two species are separated along the weak axis x, and we can have a symmetric state that is hamburger-like, or an asymmetric state with both species side by side. In addition, we can get the left-right mirror version of the asymmetric state, since there is no reason to tilt more to one side than the other, except in the case of experimental fluctuations. In practice, after propagating these different initial states, we obtain almost identical results in the camera plane. Assuming that the three configurations are the most likely obtainable states, we averaged the three final densities to plot the simulation results, as we can see on panels **d** and **e** of Figure 4.13. Comparing the simulation results (bottom row of Figure 4.13) with the experimental images (top row), we can see a good agreement between the two. Since the atom number is lower than in the ground experiment from the previous section, the signal-to-noise ratio decreases and the background noise is more visible. The small ring around the K atom cloud in panel **b** is an imaging artifact due in part to the high density at the centre of the atom cloud.

To obtain a more quantitative comparison between our model and the experimental data, we integrate the atom densities along the camera directions as done previously. The atom clouds are not fully condensed and we can fit a bimodal distribution to them. The thermal atoms are accounted for in our model by fitting a 2D Gaussian to the pedestal of the cloud, and are represented by green dashed lines in Figure 4.14. We have plotted the simulation results as solid red lines and the integrated experimental densities as solid blue lines. In all panels we can see a good agreement between the two curves. Similar to what was observed on the ground (see section 4.6.2), the centre of the condensed atoms of the interacting mixture is shifted with respect to the centre of the non-condensed thermal distributions (panels **a**,**b**,**c** and **d** of Figure 4.14). The position difference, which corresponds to the distance between the vertical lines on the plots (red for the condensed part and dashed green for the thermal part), is $\Delta x_K = 23.97$ µm and $\Delta z_K = 23.98$ µm for the K cloud and $\Delta x_{Rb} = 12.37$ µm and $\Delta z_{Rb} = 1.59$ µm for the Rb cloud. This shift is more pronounced for the Potassium cloud than for
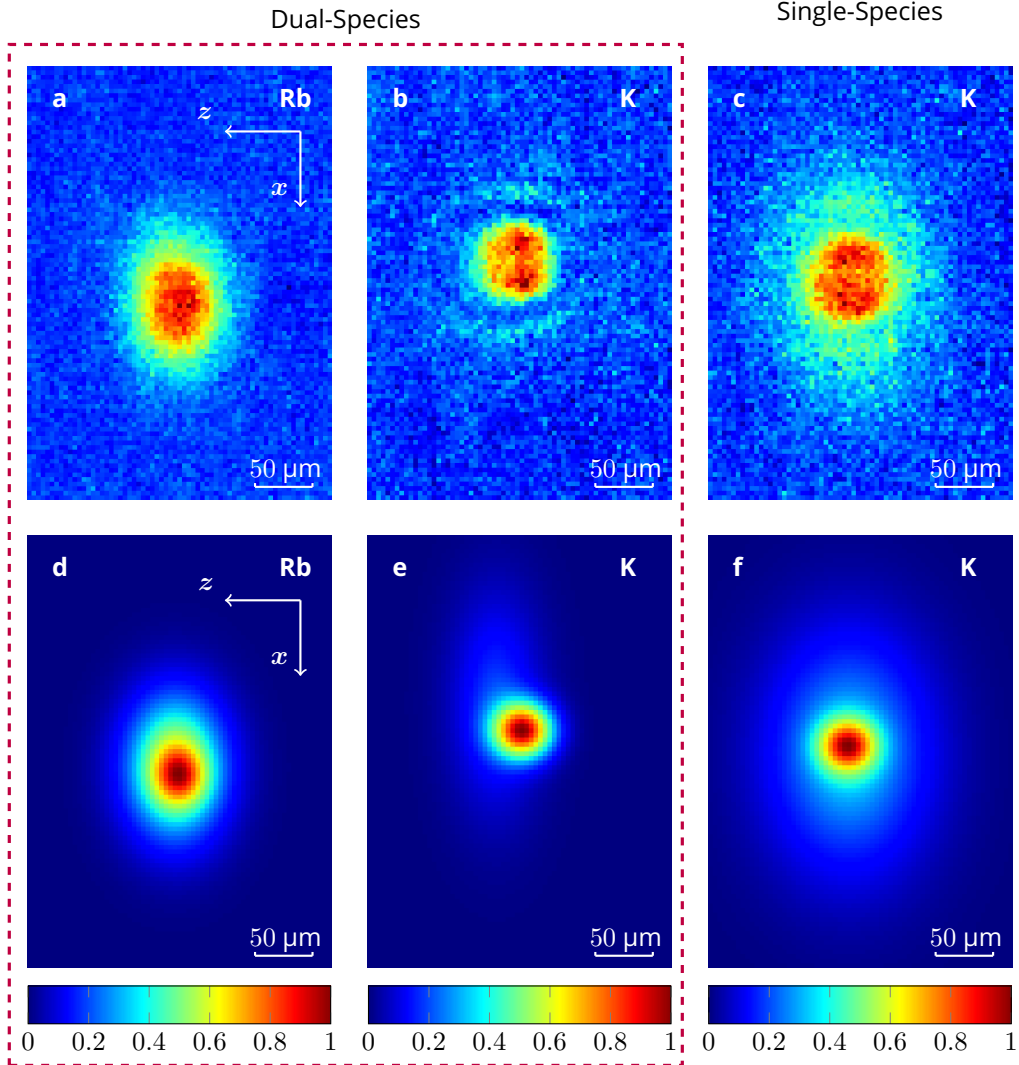
Figure 4.13 – Normalized atomic densities of K and Rb in microgravity, imaged after a 12 ms free expansion for K and a 14.1 ms free expansion for Rb. The top row corresponds to the analysed experimental data, the bottom row to the simulation results combining the solution of the GPE and the fitted thermal cloud. The theoretical results are interpolated on a grid where the spatial step corresponds to the effective pixel size of the camera. On the left side (panels **a**, **b**, **d** and **e**) we consider a non-miscible BEC mixture of K and Rb with the interspecies scattering length $a_{12} = 8.747$ nm. On the right side (panels **c** and **f**), we observe a single species K BEC. The Rb and K images are normalized for better visibility. The fitted atom numbers for the mixture are $N_1 = 1,400$ atoms of Rb and $N_2 = 1,900$ atoms of K, and in the case of the single K BEC, $N_2 = 2,000$. The atom chip is in the (xy) plane, orthogonal to the camera plane, on the right hand side of the images.

the Rubidium cloud. When there is only Potassium in the system (see panels **e** and **f**), the differences in the positions of the components of the atomic clouds are negligible, with $\Delta x'_K = -5.76$ µm and $\Delta z'_K = -0.38$ µm. We can therefore attribute the shift between the condensed and non-condensed

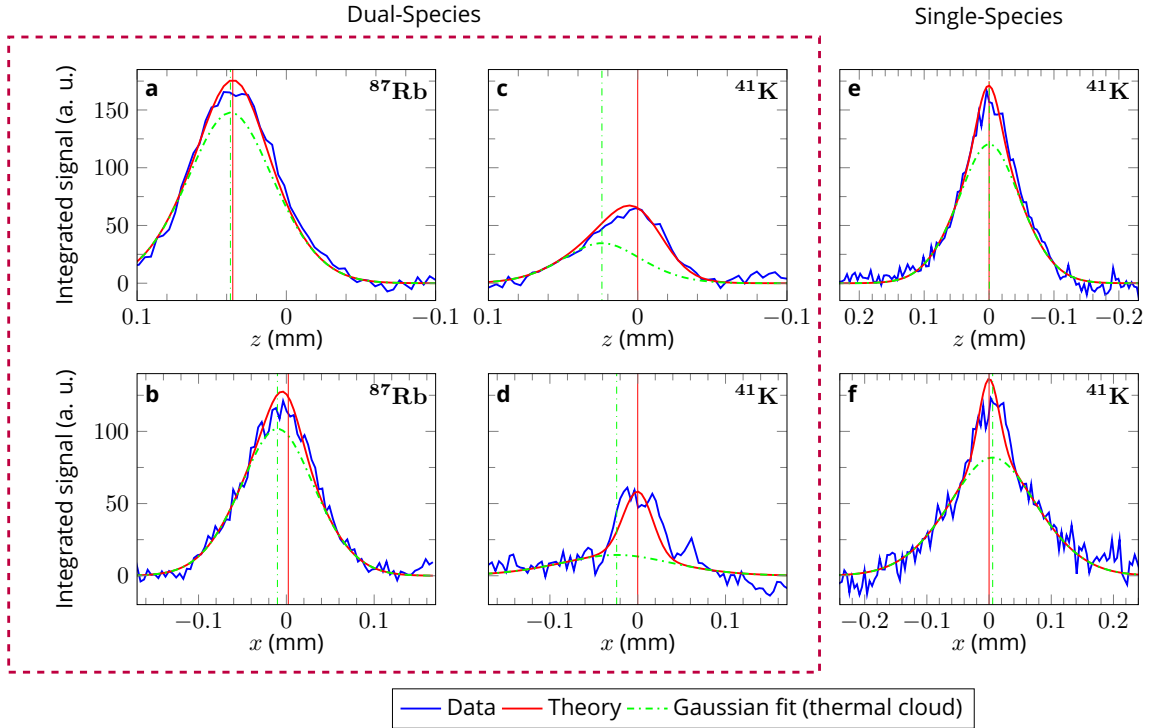atoms to the effects of the interactions between the two species.

Figure 4.14 – Integrated atomic densities in arbitrary units. In the first row the integration of the 2D images shown in Figure 4.13 is performed along the z axis and in the second row the integration is performed along the x axis. Note that in these plots, the extent of the horizontal axis is smaller than that shown in the 2D camera images. Shown are the experimental data (solid blue line), the Gaussian-fits of the thermal clouds (green dashed line), and the total simulation results (solid red line). The position $(0,0)$ is defined as the centre of the K cloud on the camera, and the positive z-direction is orthogonal to the chip and points away from it. The centre of the condensed cloud (thermal cloud) is marked by a vertical red line (green dashed line). Panels **a**, **b**, **c** and **d** show the interacting dual mixture, and panels **e** and **f** correspond to the single K condensate. In the case of the mixture, the offsets between the positions of the condensed and thermal clouds in the (x, z) directions are $(23.97, 23.98)$ µm for K and $(12.37, 1.59)$ µm for Rb. For the single-species K BEC, this offset amounts to $(-5.76, -0.38)$ µm.

4.7.2 . Planning mixture experiments in microgravity

We have seen in the previous section the capabilities of the CAL-SM3 machine to create and manipulate dual species BEC mixtures of K-41 and Rb-87. A future objective is to observe the ground state of the mixture in a trap in microgravity. The atoms are condensed in an evaporation trap near the atom chip. Due to the expansion of the clouds and to some residual magnetic fields that move the atoms towards the atom chip, it is very difficult to do in-situ imaging or observation after free expansion from the evaporation trap. So we need to move the atoms away from the chip before imaging. The chip used in this science module is similar to the one used in SM2, with which we carried out

several experiments with a single Rb BEC, but its structure is different with the addition of a small window for the implementation of atom interferometry experiments. This led to the use of more wires to create the trapping potential used to manipulate the cold atoms. After the commissioning phase of the machine, different experiments were realised by the consortium, such as atom interferometry experiments. These experiments were designed for the displacement of a single species Rb BEC, moving the atoms away from the atom chip. However, this transport is not unidimensional, with a shift mainly in the y and z directions. In this case, the Shortcut to Adiabaticity (STA) method studied earlier in this work could not be applied to optimize the ramps.

Experimental constraints limited the choice of transport implementation to a relatively simple base ramp. The only parameters that could be modified are those related to the time scale, in the sense that the time step separating two successive values of the current could be stretched or shortened. It was also possible to remove some current values by interrupting the ramp before its end. Using the scaled-grid approach, we modeled the transport of a mixture of $N_1 = 10,000$ atoms of Rb and $N_2 = 2,000$ atoms of K using this base ramp. For the initial state we used the symmetric hamburger-like state. The goal is to keep the shape of the initial state, *i.e.* to have a symmetric state at the end of the transport. Since this transport is non-adiabatic, the atoms are excited and the shape of the mixture changes. Looking at the simulation results as a function of time, it appears that by cutting off the ramp at $t = 80$ ms, the mixture gets far enough away from the chip while maintaining its shape. A few ms later the mixture gets distorted with the appearance of many bubbles of K in the Rb part of the mixture and vice versa.
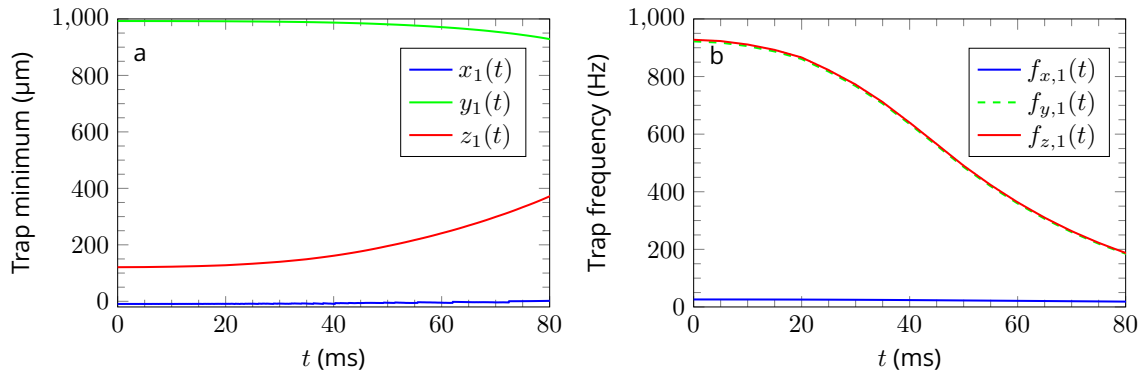

Figure 4.15 – Characteristics of the modeled transport for a mixture of K and Rb in microgravity. Panel a : Evolution of the position of the trap minimum during the transport. Panel b : Evolution of the trap frequencies for the Rb cloud during the transport.

Figure 4.15 shows the evolution of this base ramp shortened to $t_f = 80$ ms. The left panel (a) shows the evolution of the position of the trap minimum, which will be shared by the two species in microgravity. The initial position is $(x_1(0), y_1(0), z_1(0)) = (-9.4, 992.6, 120.8)$ µm. The final position is $(x_1(t_f), y_1(t_f), z_1(t_f)) = (1.7, 928.6, 371.9)$ µm. The atoms are mainly shifted in the z-direction by 251.1 µm. There is also a small shift of 11.1 µm in the x-direction and 64.0 µm in the y-direction. Another thing to note is the non-negligible slope at the end of the evolution ($t = t_f = 80$ ms) mainly along the z-direction, which could induce a motion of the atoms away from the chip along the z-direction during

the free expansion of the cloud after the trap is turned off. The right panel (b) of Figure 4.15 shows the evolution of the trap frequencies seen by the Rubidium cloud during the transport. The evolution of the atom chip trap is such that the frequencies decrease as the distance to the chip increases. The initial frequencies are $(f_{x,1}(0), f_{y,1}(0), f_{z,1}(0)) = (26.0, 922.1, 927.6)$ Hz, and the final frequencies are $(f_{x,1}(t_f), f_{y,1}(t_f), f_{z,1}(t_f)) = (18.5, 184.7, 187.6)$ Hz. Since the setup is in microgravity, we can deduce the frequency evolution seen by the K atom by multiplying the frequencies by $\sqrt{m_1/m_2}$. On the plot, the evolution of the frequency along the y-direction $f_{y,1}(t)$ is almost superimposed with that along the z-direction, showing that the trap can be considered quasi-cylindrical at all times. Consequently, the initial state will have a shape similar to that shown in the first row of Figure 4.3. Finally, as the trap decompresses, the size of the mixture is expected to grow.
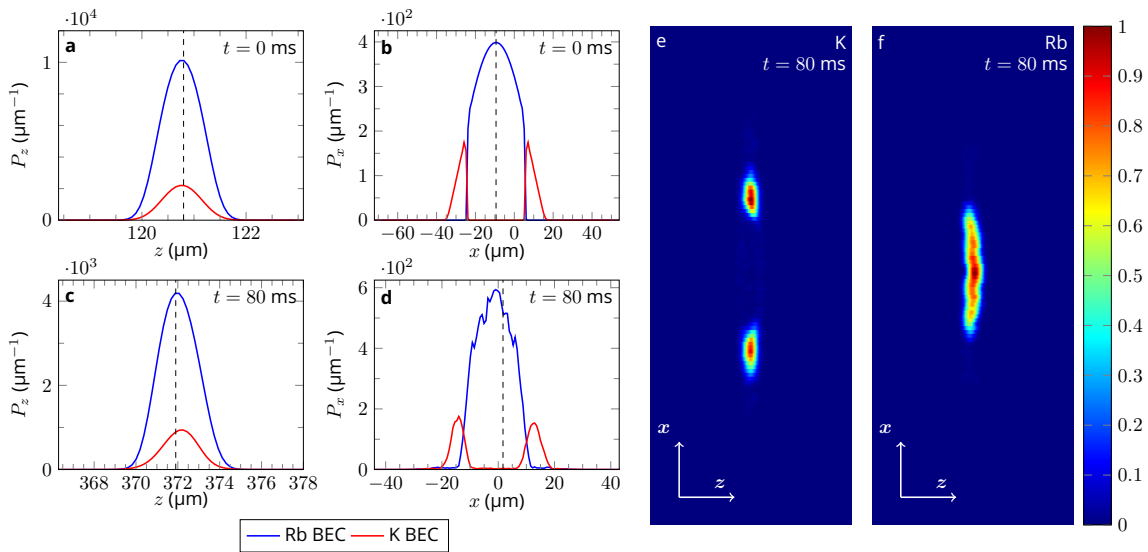

Figure 4.16 – Various representations of the atomic densities of a mixture of K and Rb in the (x, z) camera plane orthogonal to the atom chip. Here the atom chip is in the negative z direction, at the left of the 2D images. Panels **a** and **b** show the integrated atomic densities along the camera axis of the initial state at $t = 0$. Panels **c** to **f** show the integrated densities in the camera plane and at the end of the 80 ms transport. The vertical dashed line correspond to the position of the trap minimum at initial and final time of the transport. The Rb and K images are normalized for better visibility.

To illustrate the simulation results, the calculated atomic densities in the (xz) camera plane are plotted in Figure 4.16. The four panels on the left (**a**, **b**, **c**, **d**) show the integrated densities along each camera direction for Rb (blue) and K (red). The first row (panels **a** and **b**) shows the initial ($t = 0$) integrated densities and the second row (panels **c** and **d**) show the same integrated densities at final time ($t = t_f$). Panels **c** and **d** were obtained by integrating the 2D densities from panels **e** and **f** along the x and z axes. Initially, the mixture is centred at the trap minimum, indicated by a vertical dashed line. We see that at the end of the transport the mixture is shifted with respect to the trap minimum, as expected from the non-adiabatic nature of the transport. There is also a slight deformation of the Rb density in panel **d**, caused by the interactions between the atoms during the transport. However, the global shape of the mixture is still present with the clouds of K on both sides of the Rb cloud

as in the initial state shown in panel **b**. For a better visualisation, panels **e** and **f** show the K and Rb condensates at the end of the transport. The irregularities in the Rb cloud in panel **f** lead to the dents in the Rb density in panel **d**. However, the small size of the variations suggests that they could be blurred by the camera due to resolution effects.

Theoretically, this 80 ms ramp should allow the mixture to be transported away from the chip in a way that preserves the structure of the initial state of the evaporation trap. This ramp was sent to the JPL operators for implementation on the CAL machine. However, the low atomic densities in the mixture resulted in images with a low signal-to-noise ratio, which made data analysis difficult. After a short time-of-flight, it was difficult to distinguish condensed atoms from background noise. Overall, we do not have conclusive experimental results for this transport sequence at this time.

4.8 . Conclusion

In this chapter we presented an efficient method for describing the dynamics of interacting quantum mixtures. It is based on an affine transformation of the computational grid with a translation and rescaling of the coordinate system. We have seen in numerical simulations that the transformed GPE resulting from the dynamical grid change gives the same results as the simulation of the GPE with a fixed grid in a much shorter computational time, validating our approach. This perfect agreement between the different methods has been observed under realistic conditions. We also have a very good agreement with camera images from experiments on Earth and in space. Comparing the computational times, we see that the use of a scaled-grid approach makes the computation very efficient and short. The use of small grids makes these simulations adapted to available computing resources, ranging from personal computers to relatively small clusters. The computation times benefit from the parallelisation of the computations, and the real computation time is roughly equal to the CPU time divided by the number of cores assigned to the job. We can imagine that the use of GPU setups can further accelerate the computation due to the large number of operations that can be parallelised. The smaller grid size in the computations also makes them less memory intensive, with smaller and lighter files to deal with for data management. In addition, with a fixed-grid approach, the memory capacity of the computer is reached much earlier due to the rapid increase in the number of grid points required to capture the dynamics of the system.

The validity of our method allows its implementation in the context of microgravity and space experiments, where transports over long distances are realized with traps reaching low frequencies down to a few Hz and for long free expansion times of seconds, necessary in metrology applications such as fundamental physics tests [17, 54] or for Earth observation with space quantum gravimeters [130]. In the latter cases, our method would take a few hours of computation, while fixed-grid approaches cannot be implemented on reasonable time scales.

In order to use a minimal model adapted to the experiments we are simulating, some assumptions have been made about the transformations of the mixture, such as no time-dependent rotations. Rotations and other perturbations of the system can introduce more complex dynamics such as vortices

[74, 120, 121], whose dynamics does not scale linearly. Another aspect is that our model does not include the behaviour of the non-condensed atoms that form the thermal cloud. It is assumed to be an independent component of the system, fitted by a Gaussian function. This approach thus relies on the fact that we neglect the interactions between the condensed and non-condensed atoms and the losses of condensed atoms during the dynamics. The agreement between the integrated atomic densities from the camera images and this model validates this hypothesis in the experiments we have studied.

We have seen that the ground state of a BEC mixture in a harmonic potential is different depending on the presence of gravity, especially for immiscible mixtures. For these immiscible mixtures in microgravity, there are different low-energy steady states that are quasi-degenerate. One interpretation of the different geometries is that due to the repulsive interaction between the two species in the mixtures, the boundaries between two domains act as potential barriers and there is almost no tunneling of atoms to get from an asymmetric configuration to a symmetric configuration. As a result, it could be challenging to predict the state obtained experimentally when a mixture is created, since small perturbations may or may not force such tunneling. Choosing a different ansatz for the mixture before using our imaginary time propagation method to find the ground state of a trap is a good way to find out if there are other stable configurations of the mixture. Another method presented in [112] is to develop a model that simulates the evaporation process in the trap in order to create the BEC mixtures. An alternative to describe the dynamics of the condensed cloud and the thermal cloud together would be to use the Zaremba–Nikuni–Griffin (ZNG) method that consider the GPE coupled to a quantum Boltzmann equation [131].

For future experiments in microgravity, a good knowledge of the system is very important. Mixtures are sensitive to variations in the trapping potential, and the atomic dynamics is therefore difficult to predict. The number of atoms and the ratio between species play a role in the structure of the ground state, which can be characterised by different topologies of the mixture. We hope to gain in the next future a better understanding of the immiscible mixture state produced in microgravity by using experimental feedback. Future simulation projects, such as those presented in [97, 107], aim to implement more optimised transports as well as atomic lensing for experimental applications.

5 Conclusion

5.1 . Summary

This manuscript presents a theoretical study dedicated to guiding and interpreting quantum gas experiments in microgravity, and more specifically in an Earth-orbiting laboratory. After analysing single-species BEC and dual-species BEC mixture experiments, we obtained a good agreement between numerical results and experimental data, validating the simulation models I developed during my research project.

The experiments studied in this manuscript share similar setup designs using atom chips. Chapter 2 serves as a toolbox to support simulations of the dynamics of Bose-Einstein condensates created with such setups. It provides a context for the data analysis of the experimental measurements realised with the Cold Atom Laboratory in Chapter 3, and adapts existing methods found for example in Refs. [56, 63, 76, 122]. My contribution to this toolbox was influenced by the analysis of data from CAL experiments with the study of BEC absorption images, and by exchanges with colleagues in Orsay and Hannover working on the interpretation of experiments with atom chips, such as the QUANTUS and MAIUS projects. The chip models give the frequencies of the trapping potential along the directions of its eigenaxes. In some cases, however, these axes are rotated with respect to the reference frame of the simulations, which is defined by the orientation of the atom chip. It is also relatively common that the imaging plane of the camera is rotated with respect to the chip. I derived unitary rotation matrices to account for the transformation between the different frames, in order to link the BEC radii fitted from the integrated data to those calculated in the simulations. Another aspect I addressed is the resolution effect of the camera, since the optics are not perfect. For short times-of-flight, when the atom cloud is dense, the observed size of the cloud is limited by a threshold due to the resolution of the optics. This leads to corrections of the size obtained from the simulations of the dynamics, which are calibrated by studying the free expansion of the atom clouds.

Chapter 3 developed results of experiments implemented on the SM2 module of the Cold Atom Laboratory for the CUAS consortium. It demonstrated the capabilities of this modular multi-user quantum gas laboratory in space and the strength of the exchange between the teams involved in the project for the elaboration of the experimental sequences, their implementation, data analysis and interpretation with simulations. Despite the limited number of experiments dedicated to the validation of the chip model, the setup was well characterised and enabled an accurate description of the

dynamics of the atom cloud. This model proved its robustness as the number of atoms fluctuated and the experimental conditions changed over time, while the ISS orbited at different altitudes during the months of operation. Using the STA method, we demonstrated that it is possible to implement rapid transport of a quantum gas over more than half a millimeter with a positioning accuracy of nearly 70 nm, and to have a tunable controlled release with velocities known at the 100 μm/s level. The implementation of the DKC method to control the size evolution of the BEC during its free expansion reduced the expansion energy to about 50 pK, extending the observation time of the atom cloud in regimes that are difficult to reproduce on ground. These performances meet the objectives set by the consortium when its proposal was selected by NASA. It also meets the demanding initial state requirements for the realization of a dual-species interferometer to test the universality of free fall with state-of-the-art precision [17]. Achieving such control over the atomic source preparation opens the path to future applications in other fields such as satellite gravimetry [132], gravitational wave detection [40, 133, 134] and space quantum communication [135, 136]. It will also lead to increased sensitivity of atom interferometers, that might be used to design pathfinders for fundamental physics tests [95] or even to explore dark sector physics and search for dark matter [137].

The analysis of the data from the imaging system helped understanding the concerns of experimentalists when designing experimental sequences, such as the parameters that can be varied or the issues of low signal-to-noise ratio. It also highlighted the different steps from the design of an experimental campaign to the final measurements. From the success of the campaigns with the SM2 science module, we have an understanding of the capabilities of the CAL machine and a blueprint of the steps to be taken to implement experiments with the new SM3 module that has replaced it.

The main result of Chapter 4 is the development of a simulation method to efficiently describe the dynamics of interacting mixtures of Bose-Einstein condensates using grid scaling. This method extends the scaled-grid method used to describe the dynamics of single-species BECs to account for the corrections introduced by the presence of the other species and the induced interspecies interactions. Fixed-grid numerical simulations are limited in grid size to ensure reasonable computational times and memory consumption. In our tests, the parameters chosen are representative of cases similar to those described in the previous Chapter 3. The superposition of the results obtained with both methods confirmed the validity of the scaled-grid approach, which was in line with our expectations, since the analytical demonstration of the frame transformation showed that the two approaches are mathematically equivalent. Similarly, the successful comparison of the atomic densities obtained with the two methods in the case of the free expansion of a mixture of K and Rb from the MAIUS team in Hannover validated the scaled-grid model. This model also successfully described the expansion results for different orientations of the setup using rotation matrices to handle the different frame transformations. It also demonstrated the critical role of the scaled-grid method in achieving fast and accurate simulations, here in less than 20 minutes for a 25 ms time-of-flight, compared to a week for a fixed-grid approach. Moreover, the simulation volume required for a fixed-grid approach would make it unrealistic to run due to the size of the grid required. Indeed, the rapid expansion of the atom clouds induces an increase in volume of about 10^4 with respect to the volume used to describe the ground state.

The interspecies interactions in a BEC mixture complicate the study of the ground state in micro-

gravity, where the positions of the trap minima for the different species are colocated. The different configurations shown in Chapter 4 also raise the influence of design choices in the experimental setup, since for some camera orientations it is not possible to distinguish the consequences of a symmetric versus an asymmetric configuration in the ground state. Nevertheless, the application of the simulation methods to images of mixtures in space obtained with the SM3 module of CAL showed that information about the global behaviour of the mixture can still be extracted, for example the centre-of-mass motion of the ensemble.

5.2 . Outlook

NASA's Cold Atom Laboratory has produced the first mixtures of BEC in space with K and Rb atoms. These mixtures provide an opportunity to test simulation models of mixture dynamics in microgravity. Upgrades of the science module are planned with a future SM3B module, which would provide better performance in terms of atom numbers and better telemetry to help troubleshoot anomalies. It will also provide a pathway for later experiments with future replacements of the CAL machine, such as with the BECCAL project, which would continue research with cold atoms in space [41]. Other facilities to perform dual-species experiments are also under development, including ^{41}K and ^{87}Rb dual-species atom interferometry with the MAIUS-B launch in the winter 2023-2024 [138]. The implementation of more experimental projects that enable the manipulation of mixtures in microgravity could help to obtain more data to test simulation models. One example is the study of the different configurations of immiscible mixtures in their ground states, which can be obtained numerically by considering different initial wave functions when using the imaginary time propagation method.

In this work, we investigated a STA method for single-species BECs based on reverse engineering of the trap displacement calculated from a desired atom trajectory. For mixture experiments, the issue of implementing fast and controlled transport is still relevant. Due to the interactions between the two species in the mixture, the trajectory of each species is different from that expected from the solution of Newton's equation of motion. Therefore, the STA method considered here is difficult to adapt to a BEC mixture. A brute force solution by trial and error or an iterative method using optimal control theory [82] could help finding a satisfying transport ramp, but such a method could be computationally very intensive in terms of time and memory resources. A long-term solution could be to study other STA protocols, such as those presented in Ref. [139] and adapt them to BEC mixtures. In the short term, we would first like to focus on controlling the size dynamics of the mixture by collimating the atom clouds using a double DKC in a telescope-like configuration [97, 107].

We observed that non-miscible mixtures in a cigar-shaped trap show a separation of the two species where, under some ideal conditions, one species sits in the center of the trapping potential while the other is split on either side along the direction of the weakest trapping frequency. This suggests that in a trap with spherical geometry, the species on the outside would form a shell around the species inside [99]. This property of immiscible mixtures can be used to create and study BEC bubbles [140, 141]. Since the calculation method presented in this manuscript uses a generic Cartesian coordinate system, it could be interesting to compare the calculation results obtained from a scaled grid method with other numerical or analytical methods used for these problems in spherical geometry.

An example of application is the case where one tries to control the expansion of shell-shaped BECs by matter-wave lensing with a DKC, as described in Ref. [142]. A numerical problem would be to observe the diffraction patterns after the lensing operation, depending on the choice of the initial grid.

The dynamics of the studied dual-species mixtures are very different depending on the interaction strength between the two species. This starts with the formation of the ground state of the mixtures, where we have shown that there are different low-lying states with almost degenerate energies. Depending on the number of atoms of each species in the mixtures, there can be a different configuration that reaches the minimum energy, corresponding to the ground state of the ensemble. The use of the coupled Gross-Pitaevskii equations is a mean-field approach that attempts to simulate the collective behaviour of the ensemble. However, focusing on few-body interactions brings a different perspective to the ensemble. By studying individual phenomena with few-body interactions, one can indeed try to infer a collective trend in the dynamics of the ensemble. Applications studying the interactions between the two species open up to the study of Feshbach molecules, where two dilute cold atomic ensembles of different species (usually alkali atoms such as K and Rb or Na and K) are brought together by tuning Feshbach resonances [143, 144]. In these regimes, two-body and three-body interactions play an important role, and Bose-Einstein condensate mixtures as low-energy and low-temperature objects could be used as initial states in such experiments. Since the system might consist of mixtures of two atom clouds with a condensed part and thermal atoms, one could try to simulate the dynamics of the condensed atoms separately to study their contribution to the evolution of the size and position of the system.

Let us conclude this work with some outlook on the realization of the UFF test with dual species mixtures and atom interferometry. The results obtained in the CAL project to control the position and size dynamics of a Rb BEC in space, as seen in this work, give us some confidence to achieve similar results with an independent mixture of K and Rb condensates in microgravity. This scenario of two non-interacting K and Rb BECs is being extensively studied for UFF tests in an Earth-orbiting satellite in a mission such as the STE-QUEST project [17, 18, 95, 97]. Simulations show that it would be possible to achieve test results up to a level of 10^{-15} in terms of the Eötvös coefficient, on par with the results from MICROSCOPE [33, 34]. By integrating the interferometric results over numerous realizations, one would improve these results to a better precision level of about 10^{-17}. In these preliminary studies, the colocation of the two species in the input state of the atom interferometers is crucial. This can be achieved with non-interacting mixtures or miscible mixtures in microgravity [97]. However, it is desirable to minimize the interaction between the two species in order to reduce their contribution to the phase terms, which are obviously of paramount importance in such measurements. The ideal case would be to suppress the interaction between the two species, and in the case of miscible, weakly interacting mixtures, the alternative would be to spatially separate the two atom clouds over the interferometer paths and keep the initial interaction time short. In my opinion, a challenge in the latter case would be to control the dynamics of the mixture, since the transport and expansion of the atom clouds will induce interactions between the two species that can be seen on the imaging system. These interactions could lead to some stripe patterns that reduce the contrast in the final results, as seen in the transport shown in Chapter 4, and consequently reduce the signal-to-noise ratio. Nevertheless, by solving the coupled GPE equations and simulating the experimental scheme in a particular configuration, one could estimate the contrast loss and assess how to mitigate this problem. It

would also help to determine whether it is possible to completely neglect the effects of interspecies interactions in the planned UFF test experiments in order to achieve state-of-the-art results.

Calculation of the size of a BEC on the camera in the Thomas-Fermi approximation

Here we write the mathematical calculations that can be used to relate the radius on the camera to the radius of the BEC in the case of the TF approximation. We use the formula of an ellipsoid, and we perform some integrations for the change of variables.

A.1 . General case

The equation of the ellipsoid with radii (R_x, R_y, R_z) in the $(Oxyz)$ frame is

$$\frac{x^2}{R_x^2} + \frac{y^2}{R_y^2} + \frac{z^2}{R_z^2} = 1 \tag{A.1}$$

and the frame transformation is written

$$\begin{pmatrix} x \\ y \\ z \end{pmatrix} = P_{chip}^{camera} \begin{pmatrix} X \\ Y \\ Z \end{pmatrix} = \begin{pmatrix} P_{11} & P_{12} & P_{13} \\ P_{21} & P_{22} & P_{23} \\ P_{31} & P_{32} & P_{33} \end{pmatrix} \begin{pmatrix} X \\ Y \\ Z \end{pmatrix} \tag{A.2}$$

The projection of the BEC on the camera plane (OXY) is an ellipse, and we want to express the radii R_X and R_Y as a function of R_x, R_y and R_z. The first step is to get the projection on the (OXY) plane along the Z axis. To do this, we have to solve the equation obtained by deriving the ellipsoid equation A.1 with respect to Z

$$\frac{2x}{R_x^2}\left(\frac{\partial x}{\partial Z}\right) + \frac{2y}{R_y^2}\left(\frac{\partial y}{\partial Z}\right) + \frac{2z}{R_z^2}\left(\frac{\partial z}{\partial Z}\right) = 0 \tag{A.3}$$

We thus get

$$F\,X + G\,Y + H\,Z = 0 \tag{A.4}$$

where

$$F = \frac{P_{11}P_{13}}{R_x^2} + \frac{P_{21}P_{23}}{R_y^2} + \frac{P_{31}P_{33}}{R_z^2} \tag{A.5a}$$

$$G = \frac{P_{12}P_{13}}{R_x^2} + \frac{P_{22}P_{23}}{R_y^2} + \frac{P_{32}P_{33}}{R_z^2} \tag{A.5b}$$

$$H = \frac{P_{13}^2}{R_x^2} + \frac{P_{23}^2}{R_y^2} + \frac{P_{33}^2}{R_z^2} \tag{A.5c}$$

Eq. (A.4) is the equation of the plane (OXY). By writing Z as a function of x, y and z thanks to the transformation (A.2) and using Eq. (A.1), which describes the ellipsoid, we finally get

$$AX^2 + BXY + CY^2 = 1 \tag{A.6}$$

where

$$A = \frac{(P_{11} - P_{13}F/H)^2}{R_x^2} + \frac{(P_{21} - P_{23}F/H)^2}{R_y^2} + \frac{(P_{31} - P_{33}F/H)^2}{R_z^2} \tag{A.7a}$$

$$B = \frac{2(P_{11} - P_{13}F/H)(P_{12} - P_{13}G/H)}{R_x^2} + \frac{2(P_{21} - P_{23}F/H)(P_{22} - P_{23}G/H)}{R_y^2}$$
$$+ \frac{2(P_{31} - P_{33}F/H)(P_{32} - P_{33}G/H}{R_z^2} \tag{A.7b}$$

$$C = \frac{(P_{12} - P_{13}G/H)^2}{R_x^2} + \frac{(P_{22} - P_{23}G/H)^2}{R_y^2} + \frac{(P_{32} - P_{33}G/H)^2}{R_z^2} \tag{A.7c}$$

Using the notations of [77], Eq. (A.6) represents the projection of the ellipsoid onto the (OXY) plane, which is an ellipse. This ellipse is characterized by its principal axes P and S. The axis P is oriented at an angle r with respect to the horizontal axis X. From the equation of a rotated ellipse, we can find the expressions for P, S and r. We get

$$A = \frac{\cos^2 r}{P^2} + \frac{\sin^2 r}{S^2} \tag{A.8a}$$

$$B = 2 \sin r \cos r \left(\frac{1}{P^2} - \frac{1}{S^2} \right) \tag{A.8b}$$

$$C = \frac{\sin^2 r}{P^2} + \frac{\cos^2 r}{S^2} \tag{A.8c}$$

Inverting this set of equations gives

$$\tan(2r) = B/(A - C) \tag{A.9a}$$

$$\frac{1}{P^2} = \frac{A + C}{2} + \frac{A - C}{2 \cos(2r)} \tag{A.9b}$$

$$\frac{1}{S^2} = \frac{A + C}{2} - \frac{A - C}{2 \cos(2r)} \tag{A.9c}$$

The principal axes P and S of the projected ellipse can be determined from these equations. Note that in the case where $r \equiv 0 \; [\pi]$, we have $P = R_X$ and $S = R_Y$.

A.2 . Application to a 2D rotation

The analytical expressions from the previous section are not very convenient at first glance due to the many notations. However, for applications where the frame transformation matrix is not full, such as in the case of a 2D rotation, these terms are simplified and easier to manipulate.

Let us consider the case where the camera is rotated by an angle α around the axis orthogonal to the chip, as described in Chapter 2. The frame transformation is then written as

$$\begin{pmatrix} x \\ y \\ z \end{pmatrix} = P_{chip}^{camera} \begin{pmatrix} X \\ Y \\ Z \end{pmatrix} = \begin{pmatrix} 0 & -\sin\alpha & -\cos\alpha \\ 0 & \cos\alpha & -\sin\alpha \\ 1 & 0 & 0 \end{pmatrix} \begin{pmatrix} X \\ Y \\ Z \end{pmatrix} = \begin{pmatrix} -Y\sin\alpha - Z\cos\alpha \\ Y\cos\alpha - Z\sin\alpha \\ X \end{pmatrix} \tag{A.10}$$

Equation (A.3) applied to this particular case yields

$$\cos\alpha \sin\alpha \left(\frac{1}{R_x^2} - \frac{1}{R_y^2} \right) Y + \left(\frac{\cos^2\alpha}{R_x^2} + \frac{\sin^2\alpha}{R_y^2} \right) Z = 0 \tag{A.11}$$

from which we can extract

$$Z = \left[\frac{(R_x^2 - R_y^2)\cos\alpha\sin\alpha}{R_x^2\sin^2\alpha + R_y^2\cos^2\alpha} \right] Y \tag{A.12}$$

Finally, using (A.10) and (A.12) we get

$$x = \left[\frac{-R_x^2\sin\alpha}{R_x^2\sin^2\alpha + R_y^2\cos^2\alpha} \right] Y \tag{A.13}$$

and

$$y = \left[\frac{R_y^2\cos\alpha}{R_x^2\sin^2\alpha + R_y^2\cos^2\alpha} \right] Y \tag{A.14}$$

In addition to the fact that $z = X$, these coordinates x and y can now be inserted into the Equation (A.1) of the ellipsoid to give

$$\frac{X^2}{R_z^2} + \frac{Y^2}{R_x^2\sin^2\alpha + R_y^2\cos^2\alpha} = 1 \tag{A.15}$$

This is the expression of an ellipse in the (XY) plane, and we can finally express its radii along the X and Y directions R_X and R_Y as

$$R_X = R_z \tag{A.16a}$$

$$R_Y = \sqrt{R_x^2\sin^2\alpha + R_y^2\cos^2\alpha} \tag{A.16b}$$

We notice that this expression is the same as the one that can be found using the variance method, which shows that both methods give the same result. However, depending on the system being studied, one may prefer to use the variance method to obtain the cloud size expression, as the notations are more straightforward.

Rotation of a BEC mixture experimental setup with respect to gravity direction

The aim of this part is to provide a quantitative comparison between experimental data and simulation results for the mixture experiment performed by the MAIUS team in the laboratory in Hannover.

Each section presents the results from a different rotation angle of the experimental setup. For completeness, we reproduce the Figures 4.10 and 4.11 from section 4.6.2 in the first section of this appendix.

Rotation angle	x_1 (µm)	y_1 (µm)	z_1 (µm)	x_2 (µm)	y_2 (µm)	z_2 (µm)
0°	-1.62	2.23	332.43	-1.76	2.24	331.35
15°	-8.79	3.29	332.35	-5.14	2.75	331.31
30°	-15.58	4.29	332.14	-8.44	3.22	331.21
45°	-21.52	5.15	331.80	-11.20	3.62	331.06
60°	-25.79	5.80	331.37	-13.35	3.93	330.86

Table B.1 – Position of the trap centre for Rb (x_1, y_1, z_1) and K (x_2, y_2, z_2) for different orientations of the setup with respect to the gravity direction. Coordinates expressed in the chip frame, origin at the centre of the chip.

Rotation angle	ω_{1,X_1} (Hz)	ω_{1,Y_1} (Hz)	ω_{1,Z_1} (Hz)	ω_{2,X_2} (Hz)	ω_{2,Y_2} (Hz)	ω_{2,Z_2} (Hz)
0°	25.3	345.1	347.1	36.5	504.1	509.8
15°	25.3	345.1	347.3	36.5	504.2	510.0
30°	25.3	345.0	348.0	36.5	504.2	510.4
45°	25.2	345.1	349.0	36.4	504.3	511.0
60°	25.1	345.3	350.1	36.4	504.5	511.7

Table B.2 – Initial trap frequency for Rb $(\omega_{1,X_1}, \omega_{1,Y_1}, \omega_{1,Z_1})$ and K $(\omega_{2,X_2}, \omega_{2,Y_2}, \omega_{2,Z_2})$ for different orientations of the setup with respect to the gravity direction.
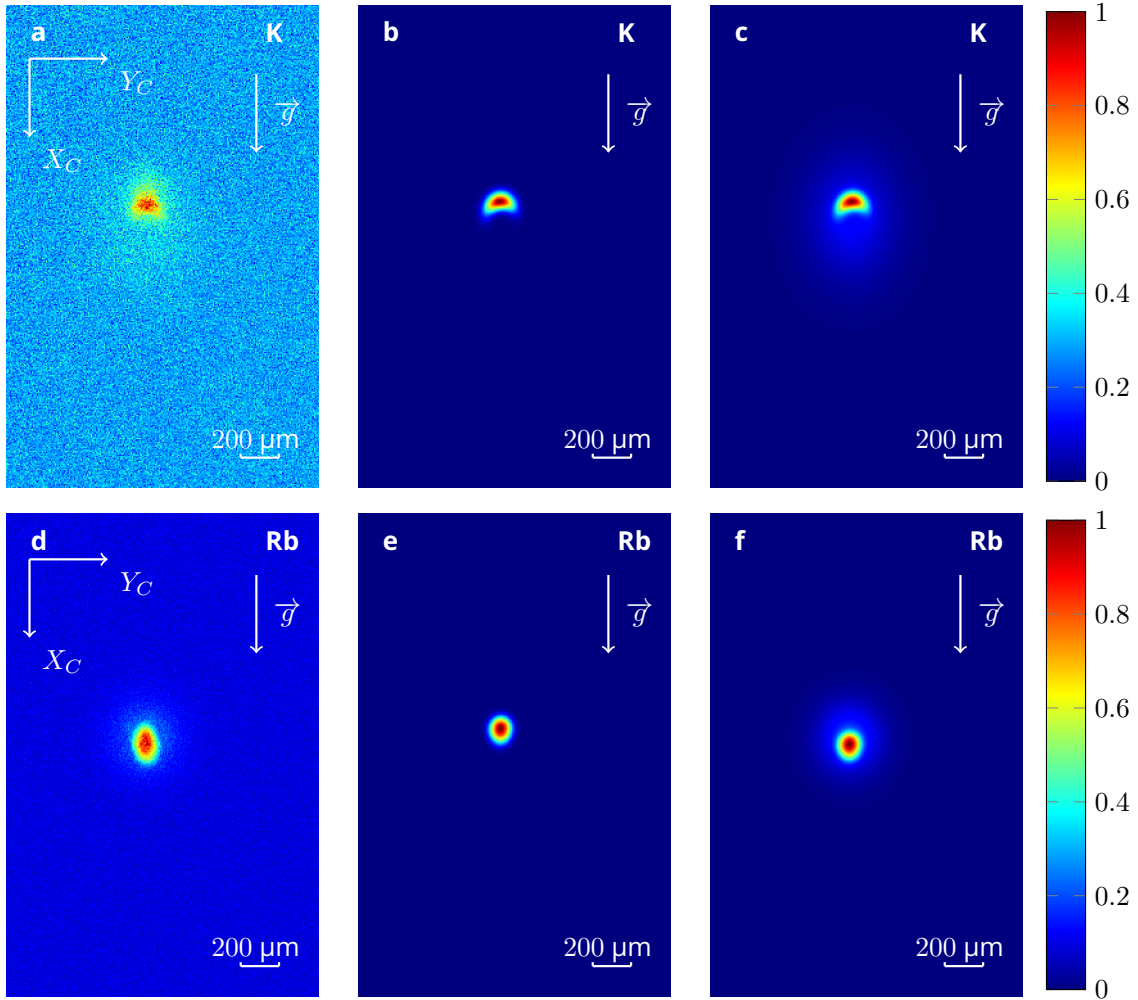
Figure B.1 – 2D atomic densities of K (first row) and Rb (second row) after a free expansion of 25 ms, starting from the initial trap described in Tables B.1 and B.2. First column : false-colour absorption images measured by the MAIUS-2 apparatus in a ground-based experiment [79]. The direction of gravity, indicated by white arrows, is vertical along the camera axis X_C, orthogonal to the atom chip. The Rb and K images are normalized for better visibility and the density scale is adjusted for each species. The fitted atom numbers are 43,900 for Rb and 14,400 for K. Second column : Condensate probability densities calculated with the scaled-grid approach in the plane (X_C, Y_C) of the camera convoluted to a 15 μm Gaussian, after 25 ms of free expansion. Third column : Calculated total probability densities including thermal atoms. The simulated Rb peak was shifted by 81.6 μm in the X_C direction and by 16.3 μm in the Y_C direction to match its position with the observation from panel **d**.
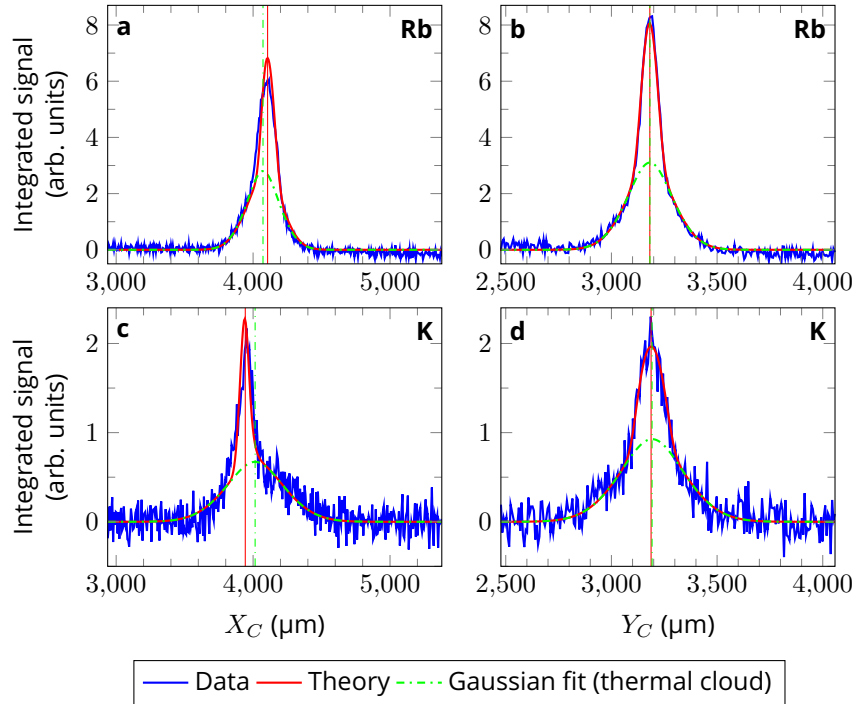
Figure B.2 – Integrated atom densities of Rb (first row) and K (second row) in arbitrary units. In the first column the integration of the 2D images shown in Figure B.1 is performed along Y_C and in the second column the integration is performed along X_C. The solid blue line is the experimental measurement and the green dashed line is the Gaussian fit describing the thermal component of the atomic cloud. The solid red line is the adjusted numerical simulation, which includes both the computed condensed and the fitted thermal components. The vertical lines correspond to the average position of the condensed part of the atomic cloud for the solid red line, and to the centre of the thermal part for the dash-dotted green line. The offsets between the positions of the condensed and thermal parts in the directions (X_C, Y_C) are $(+33.54, -0.41)$ μm for Rb and $(-40.93, -5.25)$ μm for K.
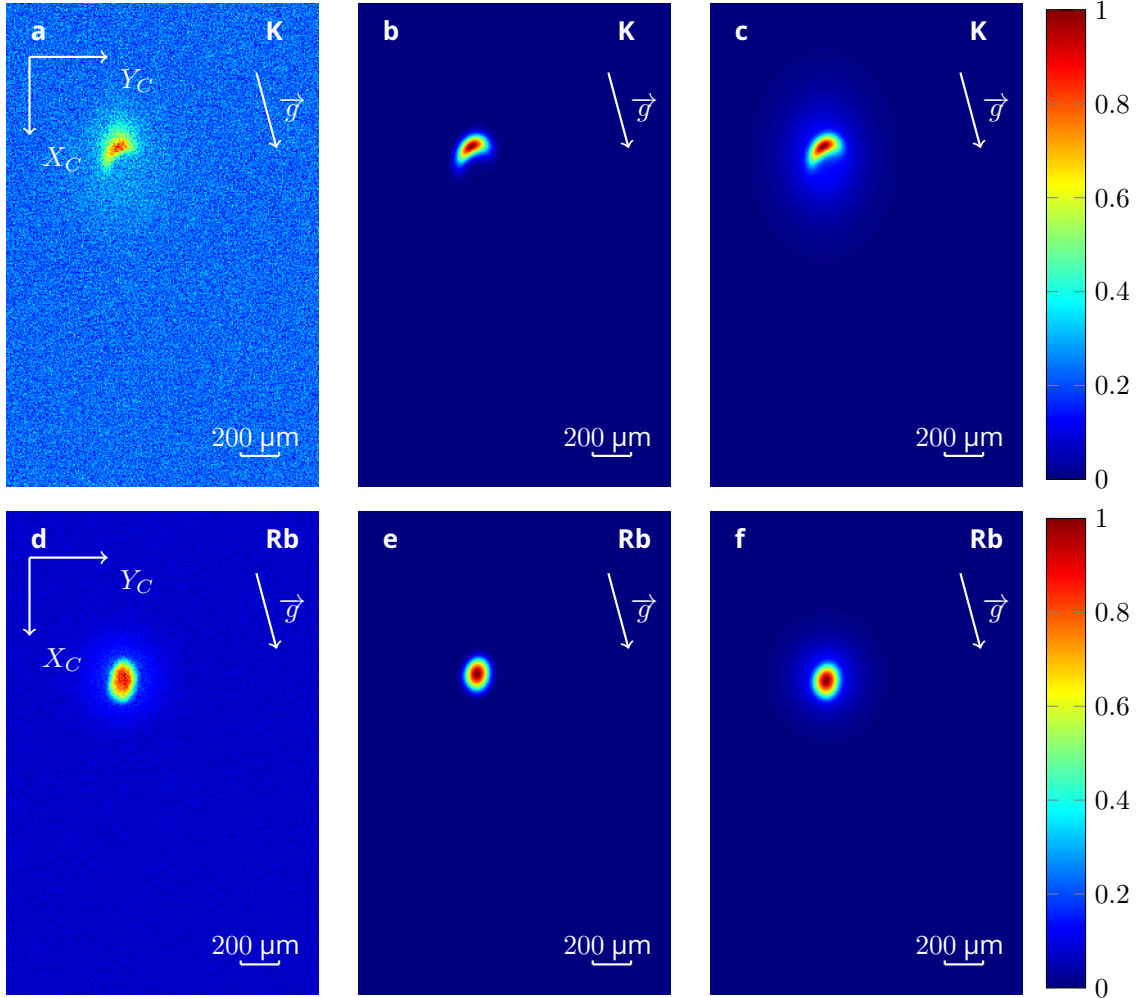
Figure B.3 – 2D atomic densities of K (first row) and Rb (second row) after a free expansion of 25 ms for the setup rotated by $\alpha = 15°$ with respect to the gravity direction, starting from the initial trap described in Tables B.1 and B.2. First column : false-colour absorption images measured by the MAIUS-2 apparatus in a ground-based experiment. The direction of gravity, indicated by white arrows, is at a $15°$ angle with respect to the camera axis X_C, orthogonal to the atom chip. The Rb and K images are normalized for better visibility and the density scale is adjusted for each species. The fitted atom numbers are 73,500 for Rb and 15,500 for K. Second column : Condensate probability densities calculated with the scaled-grid approach in the plane (X_C, Y_C) of the camera convoluted to a 15 μm Gaussian, after 25 ms of free expansion. Third column : Calculated total probability densities including thermal atoms. The simulated Rb peak was shifted by 34.9 μm in the X_C direction and by 14.2 μm in the Y_C direction to match its position with the observation from panel **d**.
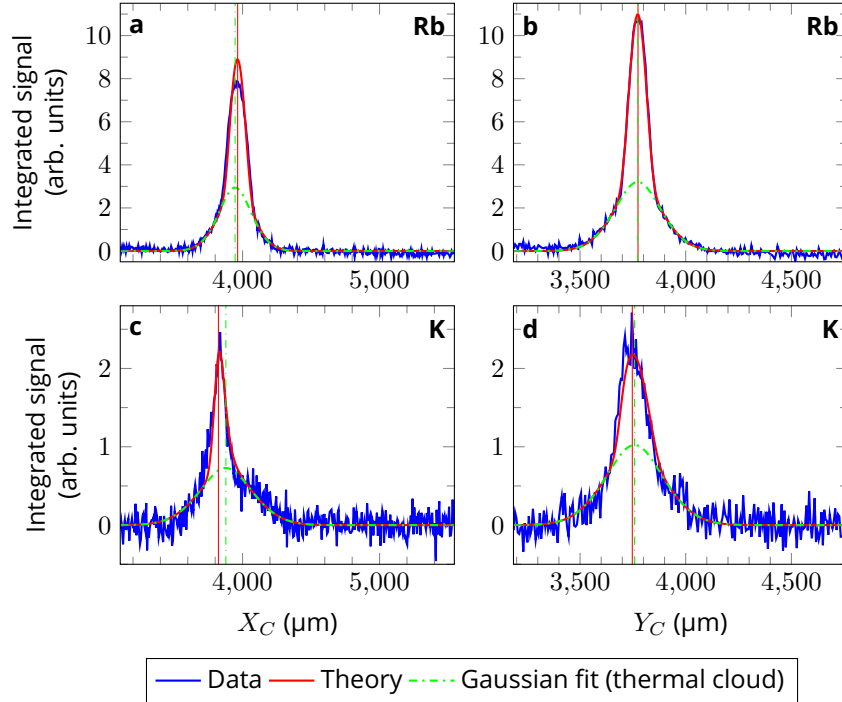
Figure B.4 – Integrated atom densities of Rb (first row) and K (second row) in arbitrary units, the setup is rotated by $\alpha = 15°$ with respect to the gravity direction. In the first column the integration of the 2D images shown in Figure B.1 is performed along Y_C and in the second column the integration is performed along X_C. The solid blue line is the experimental measurement and the green dashed line is the Gaussian fit describing the thermal component of the atomic cloud. The solid red line is the adjusted numerical simulation, which includes both the computed condensed and the fitted thermal components. The vertical lines correspond to the average position of the condensed part of the atomic cloud for the solid red line, and to the centre of the thermal part for the dash-dotted green line. The offsets between the positions of the condensed and thermal parts in the directions (X_C, Y_C) are $(+18.67, +1.06)$ µm for Rb and $(-5.44, -10.67)$ µm for K.
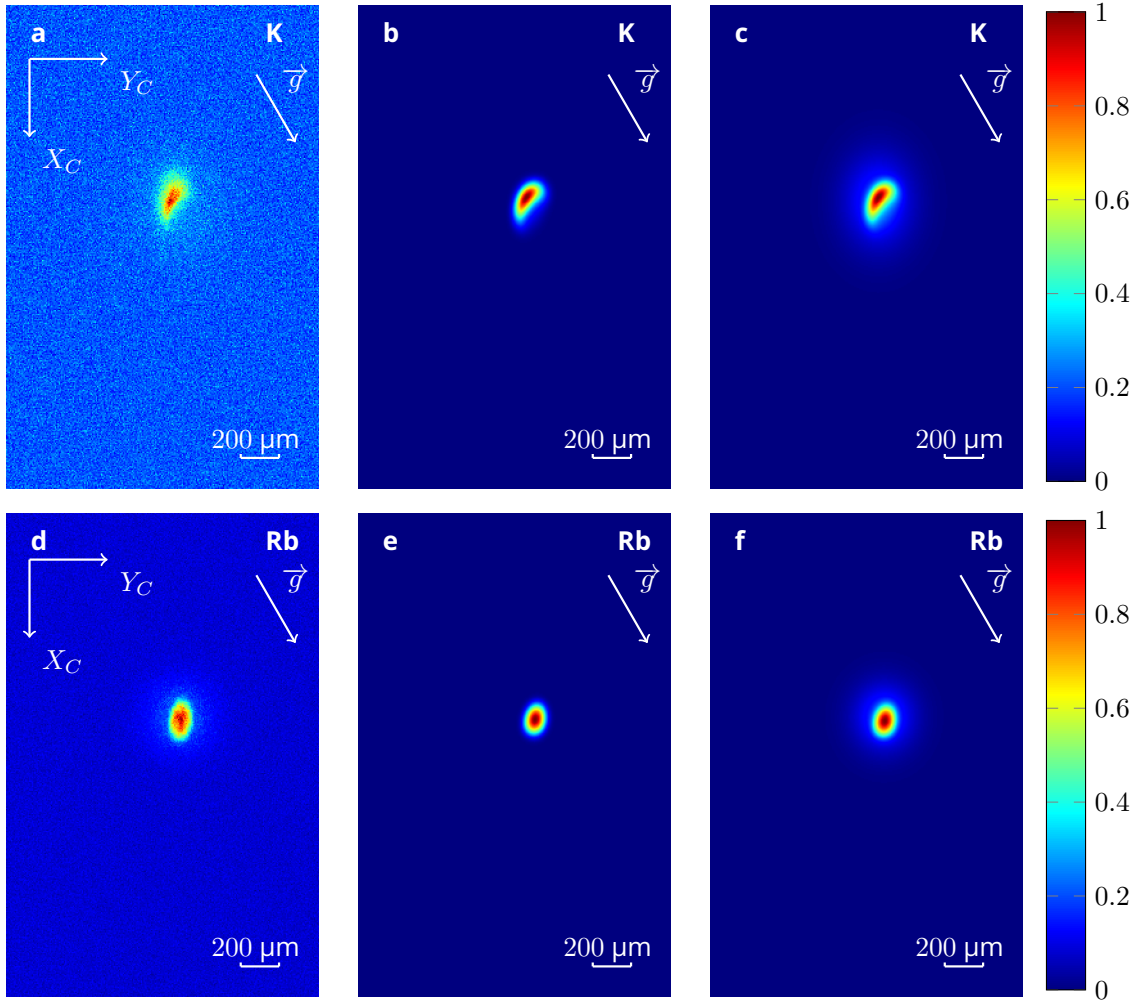
B.3 . Rotated setup, $\alpha = 30°$

Figure B.5 – 2D atomic densities of K (first row) and Rb (second row) after a free expansion of 25 ms for the setup rotated by $\alpha = 30°$ with respect to the gravity direction, starting from the initial trap described in Tables B.1 and B.2. First column : false-colour absorption images measured by the MAIUS-2 apparatus in a ground-based experiment. The direction of gravity, indicated by white arrows, is at a $30°$ angle with respect to the camera axis X_C, orthogonal to the atom chip. The Rb and K images are normalized for better visibility and the density scale is adjusted for each species. The fitted atom numbers are 46,900 for Rb and 20,200 for K. Second column : Condensate probability densities calculated with the scaled-grid approach in the plane (X_C, Y_C) of the camera convoluted to a 15 μm Gaussian, after 25 ms of free expansion. Third column : Calculated total probability densities including thermal atoms. The simulated Rb peak was shifted by 9.0 μm in the X_C direction and by 12.0 μm in the Y_C direction to match its position with the observation from panel **d**.
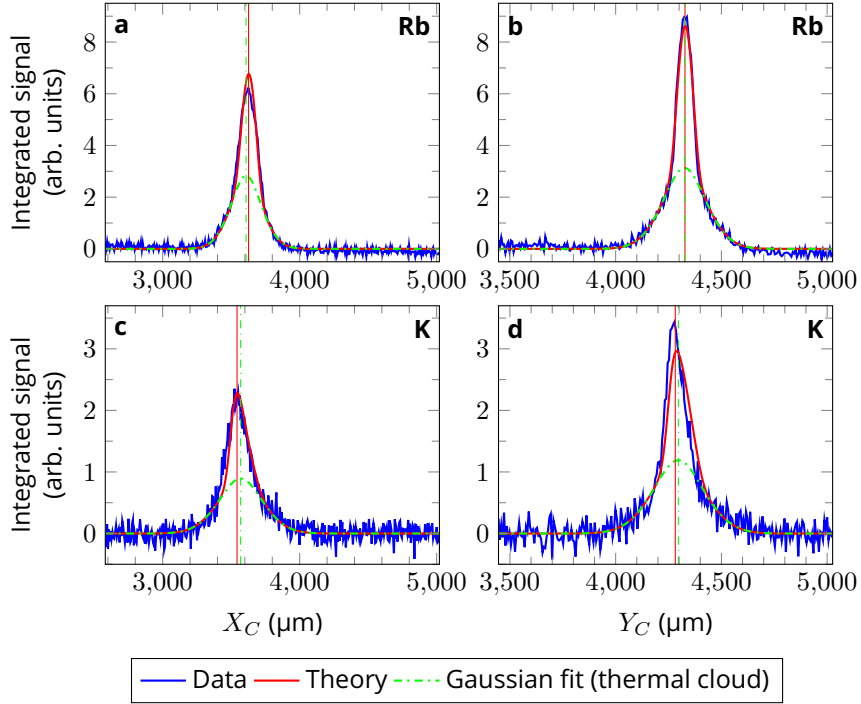
Figure B.6 – Integrated atom densities of Rb (first row) and K (second row) in arbitrary units, the setup is rotated by $\alpha = 30°$ with respect to the gravity direction. In the first column the integration of the 2D images shown in Figure B.1 is performed along Y_C and in the second column the integration is performed along X_C. The solid blue line is the experimental measurement and the green dashed line is the Gaussian fit describing the thermal component of the atomic cloud. The solid red line is the adjusted numerical simulation, which includes both the computed condensed and the fitted thermal components. The vertical lines correspond to the average position of the condensed part of the atomic cloud for the solid red line, and to the centre of the thermal part for the dash-dotted green line. The offsets between the positions of the condensed and thermal parts in the directions (X_C, Y_C) are $(+17.95, +2.50)$ µm for Rb and $(-26.28, -14.65)$ µm for K.
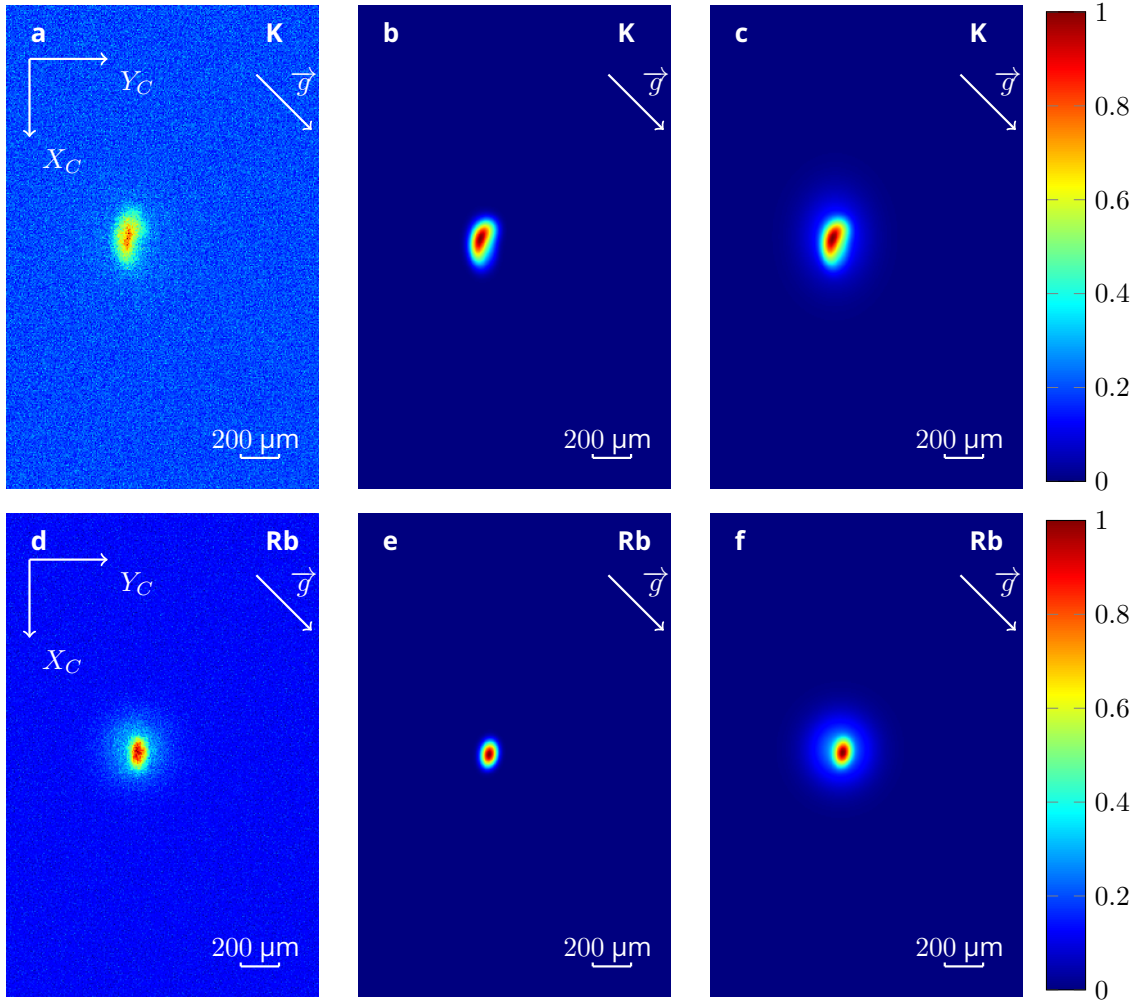
B.4 . Rotated setup, $\alpha = 45°$

Figure B.7 – 2D atomic densities of K (first row) and Rb (second row) after a free expansion of 25 ms for the setup rotated by $\alpha = 45°$ with respect to the gravity direction, starting from the initial trap described in Tables B.1 and B.2. First column : false-colour absorption images measured by the MAIUS-2 apparatus in a ground-based experiment. The direction of gravity, indicated by white arrows, is at a $45°$ angle with respect to the camera axis X_C, orthogonal to the atom chip. The Rb and K images are normalized for better visibility and the density scale is adjusted for each species. The fitted atom numbers are 15,900 for Rb and 26,400 for K. Second column : Condensate probability densities calculated with the scaled-grid approach in the plane (X_C, Y_C) of the camera convoluted to a 15 μm Gaussian, after 25 ms of free expansion. Third column : Calculated total probability densities including thermal atoms. The simulated Rb peak was shifted by 8.0 μm in the X_C direction and by 8.5 μm in the Y_C direction to match its position with the observation from panel **d**.
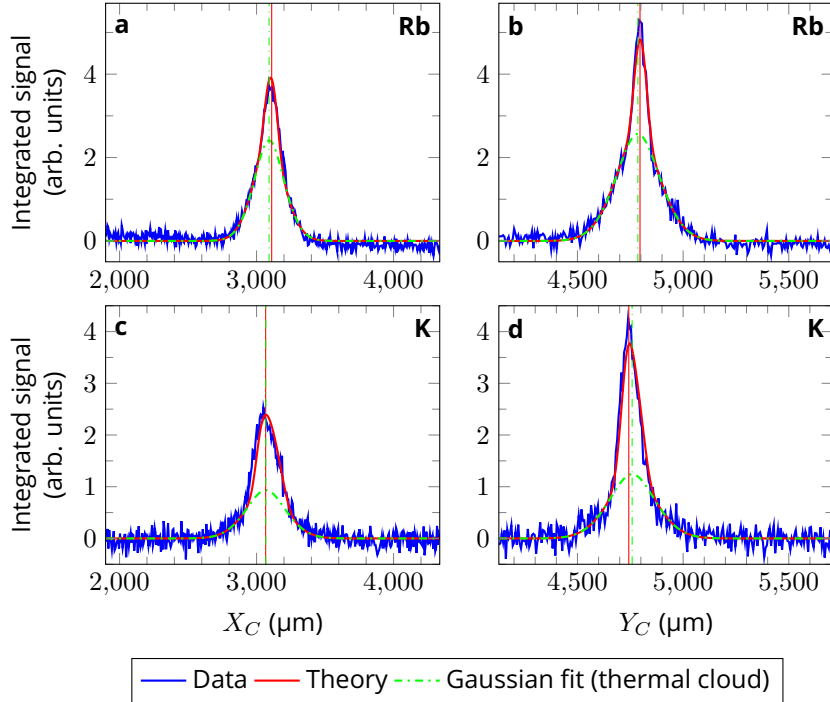
Figure B.8 – Integrated atom densities of Rb (first row) and K (second row) in arbitrary units, the setup is rotated by $\alpha = 45°$ with respect to the gravity direction. In the first column the integration of the 2D images shown in Figure B.1 is performed along Y_C and in the second column the integration is performed along X_C. The solid blue line is the experimental measurement and the green dashed line is the Gaussian fit describing the thermal component of the atomic cloud. The solid red line is the adjusted numerical simulation, which includes both the computed condensed and the fitted thermal components. The vertical lines correspond to the average position of the condensed part of the atomic cloud for the solid red line, and to the centre of the thermal part for the dash-dotted green line. The offsets between the positions of the condensed and thermal parts in the directions (X_C, Y_C) are $(+19.12, +10.18)$ μm for Rb and $(−1.08, −15.81)$ μm for K.
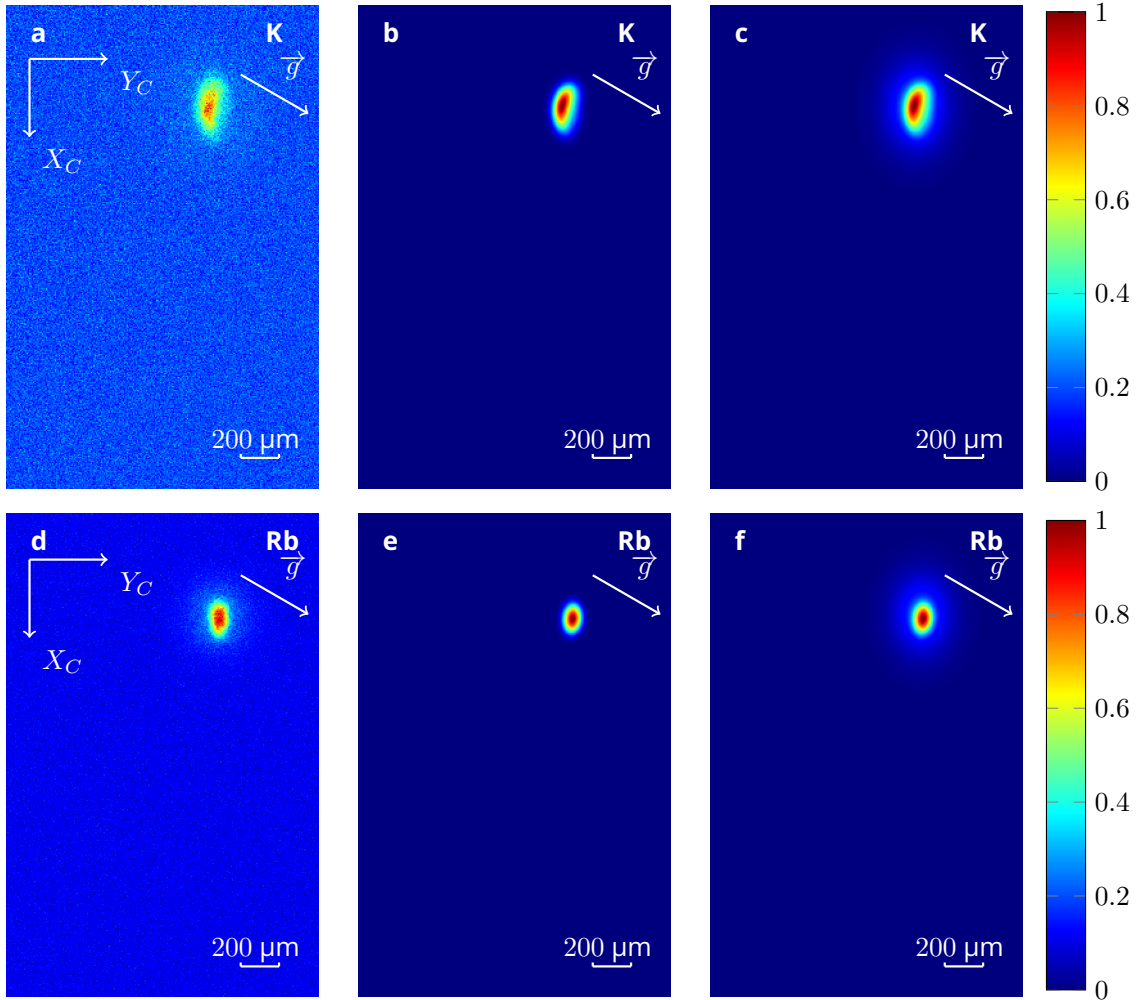
B.5 . Rotated setup, $\alpha = 60°$

Figure B.9 – 2D atomic densities of K (first row) and Rb (second row) after a free expansion of 25 ms for the setup rotated by $\alpha = 60°$ with respect to the gravity direction, starting from the initial trap described in Tables B.1 and B.2. First column : false-colour absorption images measured by the MAIUS-2 apparatus in a ground-based experiment. The direction of gravity, indicated by white arrows, is at a $60°$ angle with respect to the camera axis X_C, orthogonal to the atom chip. The Rb and K images are normalized for better visibility and the density scale is adjusted for each species. The fitted atom numbers are 27,700 for Rb and 23,200 for K. Second column : Condensate probability densities calculated with the scaled-grid approach in the plane (X_C, Y_C) of the camera convoluted to a 15 µm Gaussian, after 25 ms of free expansion. Third column : Calculated total probability densities including thermal atoms. The simulated Rb peak was shifted by 0.2 µm in the X_C direction and by 7.7 µm in the Y_C direction to match its position with the observation from panel **d**.
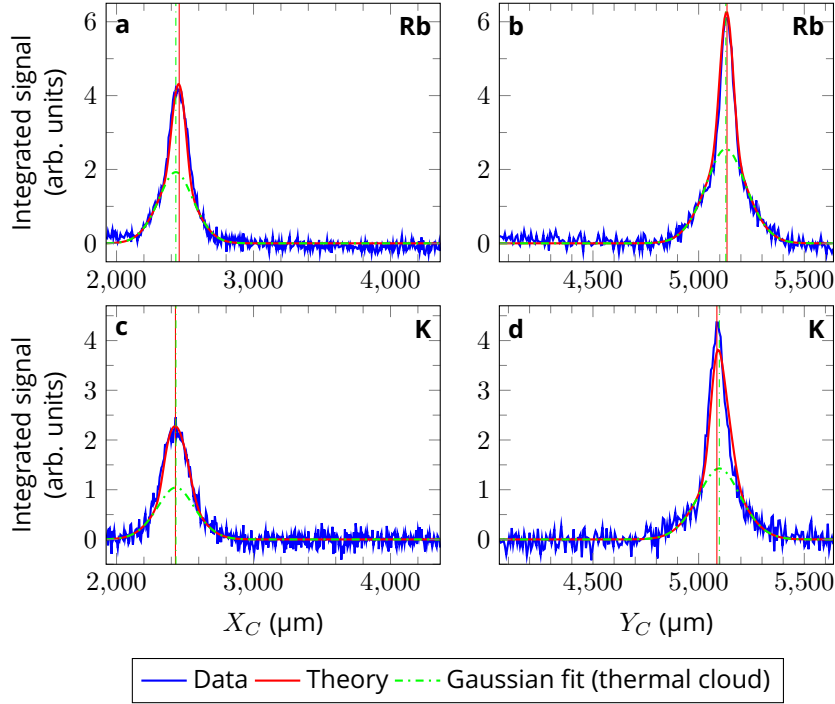
Figure B.10 – Integrated atom densities of Rb (first row) and K (second row) in arbitrary units, the setup is rotated by $\alpha = 60°$ with respect to the gravity direction. In the first column the integration of the 2D images shown in Figure B.1 is performed along Y_C and in the second column the integration is performed along X_C. The solid blue line is the experimental measurement and the green dashed line is the Gaussian fit describing the thermal component of the atomic cloud. The solid red line is the adjusted numerical simulation, which includes both the computed condensed and the fitted thermal components. The vertical lines correspond to the average position of the condensed part of the atomic cloud for the solid red line, and to the centre of the thermal part for the dash-dotted green line. The offsets between the positions of the condensed and thermal parts in the directions (X_C, Y_C) are $(+24.48, +5.50)$ μm for Rb and $(-3.47, -11.53)$ μm for K.

Bibliography

[1] C. Davisson and L. H. Germer, "Diffraction of electrons by a crystal of nickel," Phys. Rev. **30**, 705 (1927).

[2] C. Davisson and L. H. Germer, "The scattering of electrons by a single crystal of nickel," Nature **119**, 558–560 (1927).

[3] L. De Broglie, "The wave nature of the electron," Nobel lecture (1929).

[4] A. A. Michelson and E. W. Morley, "On the relative motion of the Earth and the luminiferous ether," Am. J. Sci. **s3-34**, 333–345 (1887).

[5] B. A. et al. (LIGO Scientific Collaboration and V. Collaboration) (LIGO Scientific Collaboration and Virgo Collaboration), "Observation of Gravitational Waves from a Binary Black Hole Merger," Phys. Rev. Lett. **116**, 061102 (2016).

[6] R. Colella, A. W. Overhauser, and S. A. Werner, "Observation of Gravitationally Induced Quantum Interference," Phys. Rev. Lett. **34**, 1472–1474 (1975).

[7] M. Kasevich and S. Chu, "Atomic interferometry using stimulated Raman transitions," Phys. Rev. Lett. **67**, 181–184 (1991).

[8] J. Rudolph, W. Herr, C. Grzeschik, T. Sternke, A. Grote, M. Popp, D. Becker, H. Müntinga, H. Ahlers, A. Peters, *et al.*, "A high-flux BEC source for mobile atom interferometers," New J. of Phys. **17**, 065001 (2015).

[9] M. Hauth, C. Freier, V. Schkolnik, A. Peters, H. Wziontek, and M. Schilling, "Atom interferometry for absolute measurements of local gravity," in *Volume 188: Atom Interferometry*, Proceedings of the International School of Physics "Enrico Fermi" (IOS Press, 2014) pp. 557–603.

[10] P. Storey and C. Cohen-Tannoudji, "The Feynman path integral approach to atomic interferometry. A tutorial," J. Phys. II France **4**, 1999–2027 (1994).

[11] A. Einstein, *Quantum Theory of a Monoatomic Ideal Gas A translation of Quantentheorie des einatomigen idealen Gases (Einstein, 1924)*, Vol. 1 (Sitzungsberichte Der Preuss. Akad. Der Wissenschaften, 1925).

[12] M. H. Anderson, J. R. Ensher, M. R. Matthews, C. E. Wieman, and E. A. Cornell, "Observation of Bose-Einstein Condensation in a Dilute Atomic Vapor," Science **269**, 198–201 (1995).

[13] K. B. Davis, M. O. Mewes, M. R. Andrews, N. J. van Druten, D. S. Durfee, D. M. Kurn, and W. Ketterle, "Bose-Einstein Condensation in a Gas of Sodium Atoms," Phys. Rev. Lett. **75**, 3969–3973 (1995).

[14] E. A. Cornell and C. E. Wieman, "Nobel Lecture : Bose-Einstein condensation in a dilute gas, the first 70 years and some recent experiments," Rev. Mod. Phys. **74**, 875–893 (2002).

[15] W. Ketterle, "Nobel Lecture : When atoms behave as waves : Bose-Einstein condensation and the atom laser," Rev. Mod. Phys. **74**, 1131–1151 (2002).

[16] S. S. Szigeti, J. E. Debs, J. J. Hope, N. P. Robins, and J. D. Close, "Why momentum width matters for atom interferometry with Bragg pulses," New J. Phys. **14**, 023009 (2012).

[17] H. Ahlers, L. Badurina, A. Bassi, B. Battelier, Q. Beaufils, K. Bongs, P. Bouyer, C. Braxmaier, O. Buchmueller, M. Carlesso, E. Charron, M. L. Chiofalo, R. Corgier, S. Donadi, F. Droz, R. Ecoffet, J. Ellis, F. Estève, N. Gaaloul, D. Gerardi, E. Giese, J. Grosse, A. Hees, T. Hensel, W. Herr, P. Jetzer, G. Kleinsteinberg, C. Klempt, S. Lecomte, L. Lopes, S. Loriani, G. Métris, T. Martin, V. Martín, G. Müller, M. Nofrarias, F. P. D. Santos, E. M. Rasel, A. Robert, N. Saks, M. Salter, D. Schlippert, C. Schubert, T. Schuldt, C. F. Sopuerta, C. Struckmann, G. M. Tino, T. Valenzuela, W. von Klitzing, L. Wörner, P. Wolf, N. Yu, and M. Zelan, "STE-QUEST : Space Time Explorer and QUantum Equivalence principle Space Test," (2022), arXiv:2211.15412 .

[18] T. Hensel, S. Loriani, C. Schubert, F. Fitzek, S. Abend, H. Ahlers, J.-N. Siemß, K. Hammerer, E. M. Rasel, and N. Gaaloul, "Inertial sensing with quantum gases : a comparative performance study of condensed versus thermal sources for atom interferometry," Eur. Phys. J. D **75**, 1–13 (2021).

[19] C. Misner, K. Thorne, and J. Wheeler, *Gravitation* (W. H. Freeman, 1973).

[20] L. Blanchet, A. Spallicci, and B. Whiting, *Mass and motion in general relativity*, Vol. 162 (Springer, 2011).

[21] C. Kiefer, *Quantum Gravity* (Oxford University Press, 2012).

[22] C. M. Will, "The confrontation between general relativity and experiment," Living Rev. Relativ. **17**, 1–117 (2014).

[23] R. v. Eötvös, D. Pekár, and E. Fekete, "Beiträge zum Gesetze der Proportionalität von Trägheit und Gravität," Ann. Phys. **373**, 11–66 (1922).

[24] R. H. Dicke, "Gravitation and the Universe," Memoirs of the American Philosophical Society (1970).

[25] V. B. Braginsky and V. I. Panov, "The equivalence of inertial and passive gravitational mass," General Relativity and Gravitation **3**, 403–404 (1972).

[26] E. G. Adelberger, "New tests of Einstein's equivalence principle and Newton's inverse-square law," Class. Quantum Grav. **18**, 2397 (2001).

[27] S. Schlamminger, K.-Y. Choi, T. A. Wagner, J. H. Gundlach, and E. G. Adelberger, "Test of the Equivalence Principle Using a Rotating Torsion Balance," Phys. Rev. Lett. **100**, 041101 (2008).

[28] T. A. Wagner, S. Schlamminger, J. Gundlach, and E. G. Adelberger, "Torsion-balance tests of the weak equivalence principle," Class. Quantum Grav. **29**, 184002 (2012).

[29] K. Nordtvedt, "Equivalence Principle for Massive Bodies. I. Phenomenology," Phys. Rev. **169**, 1014–1016 (1968).

[30] S. M. Merkowitz, "Tests of gravity using lunar laser ranging," Living Rev. Relativ. **13**, 1–30 (2010).

[31] J. G. Williams, S. G. Turyshev, and D. H. Boggs, "Progress in Lunar Laser Ranging Tests of Relativistic Gravity," Phys. Rev. Lett. **93**, 261101 (2004).

[32] J. G. Williams, S. G. Turyshev, and D. H. Boggs, "Lunar laser ranging tests of the equivalence principle with the Earth and Moon," Int. J. Mod. Phys. D **18**, 1129–1175 (2009).

[33] P. Touboul, G. Métris, M. Rodrigues, Y. André, Q. Baghi, J. Bergé, D. Boulanger, S. Bremer, R. Chhun, B. Christophe, *et al.*, "Space test of the equivalence principle : first results of the MICROSCOPE mission," Class. Quantum Grav. **36**, 225006 (2019).

[34] P. Touboul, G. Métris, M. Rodrigues, J. Bergé, A. Robert, Q. Baghi, Y. André, J. Bedouet, D. Boulanger, S. Bremer, P. Carle, R. Chhun, B. Christophe, V. Cipolla, T. Damour, P. Danto, L. Demange, H. Dittus, O. Dhuicque, P. Fayet, B. Foulon, P.-Y. Guidotti, D. Hagedorn, E. Hardy, P.-A. Huynh, P. Kayser, S. Lala, C. Lämmerzahl, V. Lebat, F. Liorzou, M. List, F. Löffler, I. Panet, M. Pernot-Borràs, L. Perraud, S. Pires, B. Pouilloux, P. Prieur, A. Rebray, S. Reynaud, B. Rievers, H. Selig, L. Serron, T. Sumner, N. Tanguy, P. Torresi, and P. Visser, "Result of the MICROSCOPE weak equivalence principle test," Class. Quantum Grav. **39**, 204009 (2022).

[35] R. Geiger, A. Landragin, S. Merlet, and F. Pereira Dos Santos, "High-accuracy inertial measurements with cold-atom sensors," AVS Quantum Sci. **2** (2020).

[36] P. Asenbaum, C. Overstreet, M. Kim, J. Curti, and M. A. Kasevich, "Atom-Interferometric Test of the Equivalence Principle at the 10^{-12} level," Phys. Rev. Lett. **125**, 191101 (2020).

[37] S.-W. Chiow, T. Kovachy, H.-C. Chien, and M. A. Kasevich, "$102\hbar k$ Large Area Atom Interferometers," Phys. Rev. Lett. **107**, 130403 (2011).

[38] M. Gebbe, J.-N. Siemß, M. Gersemann, H. Müntinga, S. Herrmann, C. Lämmerzahl, H. Ahlers, N. Gaaloul, C. Schubert, K. Hammerer, *et al.*, "Twin-lattice atom interferometry," Nature Comm. **12**, 2544 (2021).

[39] J.-N. Kirsten-Siemß, F. Fitzek, C. Schubert, E. M. Rasel, N. Gaaloul, and K. Hammerer, "Large-Momentum-Transfer Atom Interferometers with $\mu\mathrm{rad}$-Accuracy Using Bragg Diffraction," Phys. Rev. Lett. **131**, 033602 (2023).

[40] L. Badurina, E. Bentine, D. Blas, K. Bongs, D. Bortoletto, T. Bowcock, K. Bridges, W. Bowden, O. Buchmueller, C. Burrage, J. Coleman, G. Elertas, J. Ellis, C. Foot, V. Gibson, M. Haehnelt, T. Harte, S. Hedges, R. Hobson, M. Holynski, T. Jones, M. Langlois, S. Lellouch, M. Lewicki, R. Maiolino, P. Majewski, S. Malik, J. March-Russell, C. McCabe, D. Newbold, B. Sauer, U. Schneider, I. Shipsey, Y. Singh, M. Uchida, T. Valenzuela, M. van der Grinten, V. Vaskonen, J. Vossebeld, D. Weatherill, and I. Wilmut, "AION : an atom interferometer observatory and network," J. Cosmol. Astropart. Phys. **2020**, 011 (2020).

[41] K. Frye, S. Abend, W. Bartosch, A. Bawamia, D. Becker, H. Blume, C. Braxmaier, S.-W. Chiow, M. A. Efremov, W. Ertmer, *et al.*, "The Bose-Einstein condensate and cold atom laboratory," EPJ Quantum Technol. **8**, 1 (2021).

[42] R. A. Nyman, G. Varoquaux, F. Lienhart, D. Chambon, S. Boussen, J.-F. Clément, T. Müller, G. Santarelli, F. Pereira Dos Santos, A. Clairon, *et al.*, "ICE : a transportable atomic inertial sensor for test in microgravity," Appl. Phys. B **84**, 673–681 (2006).

[43] S. Herrmann, H. Dittus, C. Lämmerzahl, *et al.*, "Testing the equivalence principle with atomic interferometry," Class. and Quantum Grav. **29**, 184003 (2012).

[44] H. Müntinga, H. Ahlers, M. Krutzik, A. Wenzlawski, S. Arnold, D. Becker, K. Bongs, H. Dittus, H. Duncker, N. Gaaloul, *et al.*, "Interferometry with Bose-Einstein Condensates in Microgravity," Phys. Rev. Lett. **110**, 093602 (2013).

[45] C. Deppner, W. Herr, M. Cornelius, P. Stromberger, T. Sternke, C. Grzeschik, A. Grote, J. Rudolph, S. Herrmann, M. Krutzik, A. Wenzlawski, R. Corgier, E. Charron, D. Guéry-Odelin, N. Gaaloul, C. Lämmerzahl, A. Peters, P. Windpassinger, and E. M. Rasel, "Collective-Mode Enhanced Matter-Wave Optics," Phys. Rev. Lett. **127**, 100401 (2021).

[46] T. van Zoest, N. Gaaloul, Y. Singh, H. Ahlers, W. Herr, S. T. Seidel, W. Ertmer, E. Rasel, M. Eckart, E. Kajari, S. Arnold, G. Nandi, W. P. Schleich, R. Walser, A. Vogel, K. Sengstock, K. Bongs, W. Lewoczko-Adamczyk, M. Schiemangk, T. Schuldt, A. Peters, T. Könemann, H. Müntinga, C. Lämmerzahl, H. Dittus, T. Steinmetz, T. W. Hänsch, and J. Reichel, "Bose-Einstein Condensation in Microgravity," Science **328**, 1540–1543 (2010).

[47] C. Lotz, B. Piest, E. Rasel, and L. Overmeyer, "The Einstein Elevator. Space Experiments at the new Hannover Center for Microgravity Research," Europhys. News **54**, 9–11 (2023).

[48] I. Alonso, C. Alpigiani, B. Altschul, H. Araújo, G. Arduini, J. Arlt, L. Badurina, A. Balaž, S. Bandarupally, B. C. Barish, *et al.*, "Cold atoms in space : community workshop summary and proposed road-map," EPJ Quantum Technol. **9**, 1–55 (2022).

[49] D. Becker, M. D. Lachmann, S. T. Seidel, H. Ahlers, A. N. Dinkelaker, J. Grosse, O. Hellmig, H. Müntinga, V. Schkolnik, T. Wendrich, A. Wenzlawski, B. Weps, R. Corgier, T. Franz, N. Gaaloul, W. Herr, D. Lüdtke, M. Popp, S. Amri, H. Duncker, M. Erbe, A. Kohfeldt, A. Kubelka-Lange, C. Braxmaier,

E. Charron, W. Ertmer, M. Krutzik, C. Lämmerzahl, A. Peters, W. P. Schleich, K. Sengstock, R. Walser, A. Wicht, P. Windpassinger, and E. M. Rasel, "Space-borne Bose–Einstein condensation for precision interferometry," Nature **562**, 391–395 (2018).

[50] M. D. Lachmann, H. Ahlers, D. Becker, A. N. Dinkelaker, J. Grosse, O. Hellmig, H. Müntinga, V. Schkolnik, S. T. Seidel, T. Wendrich, A. Wenzlawski, B. Carrick, N. Gaaloul, D. Lüdtke, C. Braxmaier, W. Ertmer, M. Krutzik, C. Lämmerzahl, A. Peters, W. P. Schleich, K. Sengstock, A. Wicht, P. Windpassinger, and E. M. Rasel, "Ultracold atom interferometry in space," Nat. Commun. **12**, 1317 (2021).

[51] D. C. Aveline, J. R. Williams, E. R. Elliott, C. Dutenhoffer, J. R. Kellogg, J. M. Kohel, N. E. Lay, K. Oudrhiri, R. F. Shotwell, N. Yu, *et al.*, "Observation of Bose–Einstein condensates in an Earth-orbiting research lab," Nature **582**, 193–197 (2020).

[52] N. Gaaloul, M. Meister, R. Corgier, A. Pichery, P. Boegel, W. Herr, H. Ahlers, E. Charron, J. R. Williams, R. J. Thompson, W. P. Schleich, E. M. Rasel, and N. P. Bigelow, "A space-based quantum gas laboratory at picokelvin energy scales," Nat. Commun. **13**, 7889 (2022).

[53] E. R. Elliott, D. C. Aveline, N. P. Bigelow, P. Boegel, S. Botsi, E. Charron, J. P. D'Incao, P. Engels, T. Estrampes, N. Gaaloul, J. R. Kellogg, J. M. Kohel, N. E. Lay, N. Lundblad, M. Meister, M. E. Mossman, G. Müller, H. Müller, K. Oudrhiri, L. E. Phillips, A. Pichery, E. M. Rasel, C. A. Sackett, M. Sbroscia, W. P. Schleich, R. J. Thompson, and J. R. Williams, "Quantum Gas Mixtures and Dual-Species Atom Interferometry in Space," Nature **623**, 502–508 (2023).

[54] D. N. Aguilera, H. Ahlers, B. Battelier, A. Bawamia, A. Bertoldi, R. Bondarescu, K. Bongs, P. Bouyer, C. Braxmaier, L. Cacciapuoti, C. Chaloner, M. Chwalla, W. Ertmer, M. Franz, N. Gaaloul, M. Gehler, D. Gerardi, L. Gesa, N. Gürlebeck, J. Hartwig, M. Hauth, O. Hellmig, W. Herr, S. Herrmann, A. Heske, A. Hinton, P. Ireland, P. Jetzer, U. Johann, M. Krutzik, A. Kubelka, C. Lämmerzahl, A. Landragin, I. Lloro, D. Massonnet, I. Mateos, A. Milke, M. Nofrarias, M. Oswald, A. Peters, K. Posso-Trujillo, E. Rasel, E. Rocco, A. Roura, J. Rudolph, W. Schleich, C. Schubert, T. Schuldt, S. Seidel, K. Sengstock, C. F. Sopuerta, F. Sorrentino, D. Summers, G. M. Tino, C. Trenkel, N. Uzunoglu, W. von Klitzing, R. Walser, T. Wendrich, A. Wenzlawski, P. Weßels, A. Wicht, E. Wille, M. Williams, P. Windpassinger, and N. Zahzam, "STE-QUEST—test of the universality of free fall using cold atom interferometry," Class. Quantum Grav. **31**, 115010 (2014).

[55] J. P. L. NASA, "Cal project," https://coldatomlab.jpl.nasa.gov/, accessed : 06 Oct 2023.

[56] C. J. Pethick and H. Smith, *Bose–Einstein Condensation in Dilute Gases*, 2nd ed. (Cambridge University Press, 2008).

[57] Y. Castin and R. Dum, "Bose-Einstein Condensates in Time Dependent Traps," Phys. Rev. Lett. **77**, 5315–5319 (1996).

[58] H. Ammann and N. Christensen, "Delta kick cooling : A new method for cooling atoms," Phys. Rev. Lett. **78**, 2088–2091 (1997).

[59] R. Folman, P. Krüger, J. Schmiedmayer, J. Denschlag, and C. Henkel, "Microscopic Atom Optics : From Wires to an Atom Chip," in *Adv. At. Mol. Opt. Phys.*, Vol. 48, edited by B. Bederson and H. Walther (Academic Press, 2002) pp. 263–356.

[60] T. L. Gustavson, A. P. Chikkatur, A. E. Leanhardt, A. Görlitz, S. Gupta, D. E. Pritchard, and W. Ketterle, "Transport of Bose-Einstein Condensates with Optical Tweezers," Phys. Rev. Lett. **88**, 020401 (2001).

[61] S. Schmid, G. Thalhammer, K. Winkler, F. Lang, and J. H. Denschlag, "Long distance transport of ultracold atoms using a 1D optical lattice," New J. Phys. **8**, 159 (2006).

[62] R. Corgier, S. Amri, W. Herr, H. Ahlers, J. Rudolph, D. Guéry-Odelin, E. M. Rasel, E. Charron, and N. Gaaloul, "Fast manipulation of Bose–Einstein condensates with an atom chip," New J. Phys. **20**, 055002 (2018).

[63] R. Corgier, *Engineered atomic states for precision interferometry*, Ph.D. thesis, Université Paris Saclay (COmUE) ; Universität Hannover (2019).

[64] A. Pichery, M. Meister, B. Piest, J. Böhm, E. M. Rasel, E. Charron, and N. Gaaloul, "Efficient numerical description of the dynamics of interacting multispecies quantum gases," AVS Quantum Sci. **5**, 044401 (2023).

[65] J. R. Williams, C. A. Sackett, H. Ahlers, D. C. Aveline, P. Boegel, S. Botsi, E. Charron, E. R. Elliott, N. Gaaloul, E. Giese, W. Herr, J. R. Kellogg, J. M. Kohel, N. E. Lay, M. Meister, G. Müller, H. Müller, K. Oudrhiri, L. Phillips, A. Pichery, E. M. Rasel, A. Roura, M. Sbroscia, W. P. Schleich, C. Schneider, C. Schubert, B. Sen, R. J. Thompson, and N. P. Bigelow, "Interferometry of Atomic Matter Waves in the Cold Atom Lab onboard the International Space Station," (2024), arXiv:2402.14685 .

[66] W. Hänsel, P. Hommelhoff, T. Hänsch, and J. Reichel, "Bose–Einstein condensation on a microelectronic chip," Nature **413**, 498–501 (2001).

[67] T. Nirrengarten, A. Qarry, C. Roux, A. Emmert, G. Nogues, M. Brune, J.-M. Raimond, and S. Haroche, "Realization of a Superconducting Atom Chip," Phys. Rev. Lett. **97**, 200405 (2006).

[68] D. Guéry-Odelin, A. Ruschhaupt, A. Kiely, E. Torrontegui, S. Martínez-Garaot, and J. G. Muga, "Shortcuts to adiabaticity :Concepts, methods, and applications," Rev. Mod. Phys. **91**, 045001 (2019).

[69] W. Bao, D. Jaksch, and P. A. Markowich, "Numerical solution of the Gross–Pitaevskii equation for Bose–Einstein condensation," J. Comput. Phys. **187**, 318–342 (2003).

[70] W. Bao and Q. Du, "Computing the Ground State Solution of Bose–Einstein Condensates by a Normalized Gradient Flow," SIAM J. Sci. Comput. **25**, 1674–1697 (2004).

[71] X. Antoine, W. Bao, and C. Besse, "Computational methods for the dynamics of the nonlinear Schrödinger/Gross–Pitaevskii equations," Comput. Phys. Commun. **184**, 2621–2633 (2013).

120

[72] P. Ehrenfest, "Bemerkung über die angenäherte Gültigkeit der klassischen mechanik innerhalb der Quantenmechanik," Z. Physik **45**, 455–457 (1927).

[73] S. Stringari, "Collective Excitations of a Trapped Bose-Condensed Gas," Phys. Rev. Lett. **77**, 2360–2363 (1996).

[74] M. Meister, S. Arnold, D. Moll, M. Eckart, E. Kajari, M. A. Efremov, R. Walser, and W. P. Schleich, "Efficient Description of Bose–Einstein Condensates in Time-Dependent Rotating Traps," in *Adv. At. Mol. Opt. Phys.*, Vol. 66 (Elsevier, 2017) pp. 375–438.

[75] Y. Kagan, E. L. Surkov, and G. V. Shlyapnikov, "Evolution of a Bose gas in anisotropic time-dependent traps," Phys. Rev. A **55**, R18–R21 (1997).

[76] M. Eckart, *Non-equilibrium dynamics of trapped gases in controlled geometries*, Ph.D. thesis, Universität Ulm (2008).

[77] D. J. Gendzwill and M. R. Stauffer, "Analysis of triaxial ellipsoids : Their shapes, plane sections, and plane projections," Mathematical Geology **13**, 135–152 (1981).

[78] H. H. Hopkins and N. F. Mott, "On the diffraction theory of optical images," Proc. R. Soc. Lond. A **217**, 408–432 (1953).

[79] B. Piest, *Bose-Einstein condensation of K-41 and Rb-87 on an atom chip for sounding rocket missions*, Ph.D. thesis, Gottfried Wilhelm Leibniz Universität (2021).

[80] R. M. Scott, "Optical Engineering," Appl. Opt. **1**, 387–397 (1962).

[81] F. D. Smith, "Optical Image Evaluation and the Transfer Function," Appl. Opt. **2**, 335–350 (1963).

[82] S. Amri, R. Corgier, D. Sugny, E. M. Rasel, N. Gaaloul, and E. Charron, "Optimal control of the transport of Bose-Einstein condensates with atom chips," Sci. Rep. **9**, 5346 (2019).

[83] R. A. Carollo, D. C. Aveline, B. Rhyno, S. Vishveshwara, C. Lannert, J. D. Murphree, E. R. Elliott, J. R. Williams, R. J. Thompson, and N. Lundblad, "Observation of ultracold atomic bubbles in orbital microgravity," Nature **606**, 281–286 (2022).

[84] O. Zobay and B. M. Garraway, "Two-Dimensional Atom Trapping in Field-Induced Adiabatic Potentials," Phys. Rev. Lett. **86**, 1195–1198 (2001).

[85] K. Padavić, K. Sun, C. Lannert, and S. Vishveshwara, "Physics of hollow Bose-Einstein condensates," EPL **120**, 20004 (2018).

[86] A. Tononi, F. Cinti, and L. Salasnich, "Quantum Bubbles in Microgravity," Phys. Rev. Lett. **125**, 010402 (2020).

[87] E. W. Hagley, L. Deng, M. Kozuma, J. Wen, K. Helmerson, S. L. Rolston, and W. D. Phillips, "A Well-Collimated Quasi-Continuous Atom Laser," Science **283**, 1706–1709 (1999).

[88] I. Bloch, T. W. Hänsch, and T. Esslinger, "Atom Laser with a cw Output Coupler," Phys. Rev. Lett. **82**, 3008–3011 (1999).

[89] M. Meister, A. Roura, E. M. Rasel, and W. P. Schleich, "The space atom laser : an isotropic source for ultra-cold atoms in microgravity," New J. Phys. **21**, 013039 (2019).

[90] P. Naidon and S. Endo, "Efimov physics : a review," Rep. Prog. Phys. **80**, 056001 (2017).

[91] T. A. Pasquini, Y. Shin, C. Sanner, M. Saba, A. Schirotzek, D. E. Pritchard, and W. Ketterle, "Quantum Reflection from a Solid Surface at Normal Incidence," Phys. Rev. Lett. **93**, 223201 (2004).

[92] S. S. Szigeti, S. P. Nolan, J. D. Close, and S. A. Haine, "High-Precision Quantum-Enhanced Gravimetry with a Bose-Einstein Condensate," Phys. Rev. Lett. **125**, 100402 (2020).

[93] R. Corgier, N. Gaaloul, A. Smerzi, and L. Pezzè, "Delta-Kick Squeezing," Phys. Rev. Lett. **127**, 183401 (2021).

[94] H. Padé, "Mémoire sur les développements en fractions continues de la fonction exponentielle, pouvant servir d'introduction à la théorie des fractions continues algébriques," An. Sc. ENS **9**, 3 (1892).

[95] B. Battelier, J. Bergé, A. Bertoldi, L. Blanchet, K. Bongs, P. Bouyer, C. Braxmaier, D. Calonico, P. Fayet, N. Gaaloul, *et al.*, "Exploring the foundations of the physical universe with space tests of the equivalence principle," Exp. Astron. **51**, 1695–1736 (2021).

[96] A. R. Pollard, E. R. Moan, C. A. Sackett, E. R. Elliott, and R. Thompson, "Quasi-adiabatic external state preparation of ultracold atoms in microgravity," Microgravity Sci. Technol. **32**, 1175–1184 (2020).

[97] R. Corgier, S. Loriani, H. Ahlers, K. Posso-Trujillo, C. Schubert, E. M. Rasel, E. Charron, and N. Gaaloul, "Interacting quantum mixtures for precision atom interferometry," New J. Phys. **22**, 123008 (2020).

[98] S. Loriani, D. Schlippert, C. Schubert, S. Abend, H. Ahlers, W. Ertmer, J. Rudolph, J. M. Hogan, M. A. Kasevich, E. M. Rasel, and N. Gaaloul, "Atomic source selection in space-borne gravitational wave detection," New J. Phys. **21**, 063030 (2019).

[99] M. Trippenbach, K. Góral, K. Rzazewski, B. Malomed, and Y. Band, "Structure of binary Bose-Einstein condensates," J. Phys. B: At. Mol. Opt. Phys. **33**, 4017 (2000).

[100] F. Riboli and M. Modugno, "Topology of the ground state of two interacting Bose-Einstein condensates," Phys. Rev. A **65**, 063614 (2002).

[101] A. Balaž and A. I. Nicolin, "Faraday waves in binary nonmiscible Bose-Einstein condensates," Phys. Rev. A **85**, 023613 (2012).

[102] R. Pattinson, T. Billam, S. Gardiner, D. McCarron, H. Cho, S. Cornish, N. Parker, and N. Proukakis, "Equilibrium solutions for immiscible two-species Bose-Einstein condensates in perturbed harmonic traps," Phys. Rev. A **87**, 013625 (2013).

[103] J. Polo, V. Ahufinger, P. Mason, S. Sridhar, T. P. Billam, and S. A. Gardiner, "Analysis beyond the Thomas-Fermi approximation of the density profiles of a miscible two-component Bose-Einstein condensate," Phys. Rev. A **91**, 053626 (2015).

[104] K. L. Lee, N. B. Jørgensen, I.-K. Liu, L. Wacker, J. J. Arlt, and N. P. Proukakis, "Phase separation and dynamics of two-component Bose-Einstein condensates," Phys. Rev. A **94**, 013602 (2016).

[105] K. L. Lee, N. B. Jørgensen, L. J. Wacker, M. G. Skou, K. T. Skalmstang, J. J. Arlt, and N. P. Proukakis, "Time-of-flight expansion of binary Bose–Einstein condensates at finite temperature," New J. Phys. **20**, 053004 (2018).

[106] A. Wolf, P. Boegel, M. Meister, A. Balaž, N. Gaaloul, and M. A. Efremov, "Shell-shaped Bose-Einstein condensates based on dual-species mixtures," Phys. Rev. A **106**, 013309 (2022).

[107] M. Meister and A. Roura, "Efficient matter-wave lensing of ultracold atomic mixtures," Quantum Sci. Technol. **8**, 024001 (2023).

[108] G. Ferrari, M. Inguscio, W. Jastrzebski, G. Modugno, G. Roati, and A. Simoni, "Collisional Properties of Ultracold K-Rb Mixtures," Phys. Rev. Lett. **89**, 053202 (2002).

[109] G. Modugno, M. Modugno, F. Riboli, G. Roati, and M. Inguscio, "Two Atomic Species Superfluid," Phys. Rev. Lett. **89**, 190404 (2002).

[110] F. Ferlaino, C. D'Errico, G. Roati, M. Zaccanti, M. Inguscio, G. Modugno, and A. Simoni, "Feshbach spectroscopy of a $\mathrm{K}-\mathrm{Rb}$ atomic mixture," Phys. Rev. A **73**, 040702 (2006).

[111] S. B. Papp, J. M. Pino, and C. E. Wieman, "Tunable Miscibility in a Dual-Species Bose-Einstein Condensate," Phys. Rev. Lett. **101**, 040402 (2008).

[112] S. Ronen, J. L. Bohn, L. E. Halmo, and M. Edwards, "Dynamical pattern formation during growth of a dual-species Bose-Einstein condensate," Phys. Rev. A **78**, 053613 (2008).

[113] G. Thalhammer, G. Barontini, L. De Sarlo, J. Catani, F. Minardi, and M. Inguscio, "Double Species Bose-Einstein Condensate with Tunable Interspecies Interactions," Phys. Rev. Lett. **100**, 210402 (2008).

[114] A. Burchianti, C. D'Errico, S. Rosi, A. Simoni, M. Modugno, C. Fort, and F. Minardi, "Dual-species Bose-Einstein condensate of $^{41}\mathrm{K}$ and $^{87}\mathrm{Rb}$ in a hybrid trap," Phys. Rev. A **98**, 063616 (2018).

[115] K. E. Wilson, A. Guttridge, J. Segal, and S. L. Cornish, "Quantum degenerate mixtures of Cs and Yb," Phys. Rev. A **103**, 033306 (2021).

[116] F. Jia, Z. Huang, L. Qiu, R. Zhou, Y. Yan, and D. Wang, "Expansion Dynamics of a Shell-Shaped Bose-Einstein Condensate," Phys. Rev. Lett. **129**, 243402 (2022).

[117] L. Lehtovaara, J. Toivanen, and J. Eloranta, "Solution of time-independent Schrödinger equation by the imaginary time propagation method," J. Comput. Phys. **221**, 148–157 (2007).

[118] D. S. Hall, M. R. Matthews, J. R. Ensher, C. E. Wieman, and E. A. Cornell, "Dynamics of Component Separation in a Binary Mixture of Bose-Einstein Condensates," Phys. Rev. Lett. **81**, 1539–1542 (1998).

[119] K. M. Mertes, J. W. Merrill, R. Carretero-González, D. J. Frantzeskakis, P. G. Kevrekidis, and D. S. Hall, "Nonequilibrium Dynamics and Superfluid Ring Excitations in Binary Bose-Einstein Condensates," Phys. Rev. Lett. **99**, 190402 (2007).

[120] G. Hechenblaikner, E. Hodby, S. A. Hopkins, O. M. Maragò, and C. J. Foot, "Direct Observation of Irrotational Flow and Evidence of Superfluidity in a Rotating Bose-Einstein Condensate," Phys. Rev. Lett. **88**, 070406 (2002).

[121] M. Edwards, C. W. Clark, P. Pedri, L. Pitaevskii, and S. Stringari, "Consequence of Superfluidity on the Expansion of a Rotating Bose-Einstein Condensate," Phys. Rev. Lett. **88**, 070405 (2002).

[122] M. Meister, *Novel concepts for ultra-cold quantum gases in microgravity*, Ph.D. thesis, Universität Ulm (2019).

[123] M. Feit, J. Fleck, and A. Steiger, "Solution of the Schrödinger equation by a spectral method," J. Comput. Phys. **47**, 412–433 (1982).

[124] I.-K. Liu, R. W. Pattinson, T. P. Billam, S. A. Gardiner, S. L. Cornish, T.-M. Huang, W.-W. Lin, S.-C. Gou, N. G. Parker, and N. P. Proukakis, "Stochastic growth dynamics and composite defects in quenched immiscible binary condensates," Phys. Rev. A **93**, 023628 (2016).

[125] D. J. McCarron, H. W. Cho, D. L. Jenkin, M. P. Köppinger, and S. L. Cornish, "Dual-species Bose-Einstein condensate of $^{87}\mathrm{Rb}$ and $^{133}\mathrm{Cs}$," Phys. Rev. A **84**, 011603 (2011).

[126] J. Reichel and V. Vuletic, *Atom Chips*, 1st ed. (Wiley, 2011).

[127] K. Pearson, "LIII. On lines and planes of closest fit to systems of points in space," The London, Edinburgh, and Dublin Philosophical Magazine and Journal of Science **2**, 559–572 (1901).

[128] H. Hotelling, "Analysis of a complex of statistical variables with principal components," J. Educ. Psy. **24**, 498–520 (1933).

[129] S. R. Segal, Q. Diot, E. A. Cornell, A. A. Zozulya, and D. Z. Anderson, "Revealing buried information : Statistical processing techniques for ultracold-gas image analysis," Phys. Rev. A **81**, 053601 (2010).

[130] T. Lévèque, C. Fallet, J. Lefebve, A. Piquereau, A. Gauguet, B. Battelier, P. Bouyer, N. Gaaloul, M. Lachmann, B. Piest, E. Rasel, J. Müller, C. Schubert, Q. Beaufils, and F. Pereira Dos Santos, "CARIOQA : Definition of a Quantum Pathfinder Mission," (2022), arXiv:2211.01215 .

[131] K. L. Lee and N. P. Proukakis, "Non-equilibrium atomic condensates and mixtures : collective modes, condensate growth and thermalisation," J. Phys. B: At. Mol. Opt. Phys. **49**, 214003 (2016).

[132] A. Trimeche, B. Battelier, D. Becker, A. Bertoldi, P. Bouyer, C. Braxmaier, E. Charron, R. Corgier, M. Cornelius, K. Douch, N. Gaaloul, S. Herrmann, J. Müller, E. Rasel, C. Schubert, H. Wu, and F. P. dos Santos, "Concept study and preliminary design of a cold atom interferometer for space gravity gradiometry," Class. Quantum Grav. **36**, 215004 (2019).

[133] S. Dimopoulos, P. W. Graham, J. M. Hogan, M. A. Kasevich, and S. Rajendran, "Gravitational wave detection with atom interferometry," Phys. Lett. B **678**, 37–40 (2009).

[134] B. Canuel, A. Bertoldi, L. Amand, *et al.*, "Exploring gravity with the MIGA large scale atom interferometer," Sci. Rep. **8**, 14064 (2018).

[135] S.-K. Liao, W.-Q. Cai, W.-Y. Liu, *et al.*, "Satellite-to-ground quantum key distribution," Nature **549**, 43–47 (2017).

[136] J.-G. Ren, P. Xu, H.-L. Yong, *et al.*, "Ground-to-satellite quantum teleportation," Nature **549**, 70–73 (2017).

[137] Y. A. El-Neaj, C. Alpigiani, S. Amairi-Pyka, *et al.*, "AEDGE : Atomic Experiment for Dark Matter and Gravity Exploration in Space," EPJ Quantum Technology **7**, 6 (2020).

[138] M. Elsen, B. Piest, F. Adam, O. Anton, P. Arciszewski, W. Bartosch, D. Becker, K. Bleeke, J. Böhm, S. Boles, *et al.*, "A Dual-Species Atom Interferometer Payload for Operation on Sounding Rockets," Microgravity Sci. Technol. **35**, 48 (2023).

[139] D. Guéry-Odelin and J. G. Muga, "Transport in a harmonic trap : Shortcuts to adiabaticity and robust protocols," Phys. Rev. A **90**, 063425 (2014).

[140] A. Wolf, P. Boegel, M. Meister, A. Balaž, N. Gaaloul, and M. A. Efremov, "Shell-shaped Bose-Einstein condensates based on dual-species mixtures," Phys. Rev. A **106**, 013309 (2022).

[141] N. Lundblad, D. C. Aveline, A. Balaž, E. Bentine, N. P. Bigelow, P. Boegel, M. A. Efremov, N. Gaaloul, M. Meister, M. Olshanii, C. A. R. S. de Melo, A. Tononi, S. Vishveshwara, A. C. White, A. Wolf, and B. M. Garraway, "Perspective on quantum bubbles in microgravity," Quantum Sci. Technol. **8**, 024003 (2023).

[142] P. Boegel, A. Wolf, M. Meister, and M. A. Efremov, "Controlled expansion of shell-shaped Bose–Einstein condensates," Quantum Sci. Technol. **8**, 034001 (2023).

[143] J. P. D'Incao, M. Krutzik, E. Elliott, and J. R. Williams, "Enhanced association and dissociation of heteronuclear Feshbach molecules in a microgravity environment," Phys. Rev. A **95**, 012701 (2017).

[144] T. Hartmann, T. A. Schulze, K. K. Voges, P. Gersema, M. W. Gempel, E. Tiemann, A. Zenesini, and S. Ospelkaus, "Feshbach resonances in $^{23}\mathrm{Na} + ^{39}\mathrm{K}$ mixtures and refined molecular potentials for the NaK molecule," Phys. Rev. A **99**, 032711 (2019).

Academic Curriculum Vitae

Personal Data

Name :	Annie Pichery
Born :	16 April 1996 in Versailles, France
Nationality :	French

Education

Oct 2019 – present	Joint Phd with the Institute of Quantum Optics, Leibniz Universität Hannover (Germany) and ISMO, Paris-Saclay University (France) Thesis : *Theoretical study of quantum gas experiments in an Earth-orbitingresearch laboratory*
2018 – 2019	Master M2 LOM (Laser Optics Matter) at Institut d'Optique Graduate School (Palaiseau, France)
2015 – 2018	Engineering School Institut d'Optique Graduate School (Palaiseau,France) 2017–2018 : Msc Physics with Distinction at Imperial College London 2016–2017 : Second year student with parallel studies in first year of Master's degree in fundamental physics at Paris-Sud University (Orsay, France) 2015–2016 : Obtention of the Bachelor's degree (*Licence*) in fundamental physics at Paris-Sud University with *Assez Bien* honours (Orsay, France) studied in parallel
2013 – 2015	Intensive studying in mathematics and physics with a dominant in mathematics for the nation-wide competitive examination, for admission to the top engineering institutions in France (MPSI than MP) at lycée Hoche (Versailles, France)
2010 – 2013	Lycée Hoche (high school) (Versailles, France) 2013 : Scientific *Baccalauréat* with *Très Bien* distinction

Complete list of publications

- Naceur Gaaloul, Matthias Meister, Robin Corgier, **Annie Pichery**, Patrick Boegel, Waldemar Herr, Holger Ahlers, Eric Charron, Jason R. Williams, Robert J. Thompson, Wolfgang P. Schleich, Ernst M. Rasel, and Nicholas P. Bigelow, "A space-based quantum gas laboratory at picokelvin energy scales", *Nature Communications*, **13**, 7889 (2022).

- **Annie Pichery**, Matthias Meister, Baptist Piest, Jonas Böhm, Ernst Maria Rasel, Eric Charron, and Naceur Gaaloul, "Efficient numerical description of the dynamics of interacting multispecies quantum gases", AVS Quantum Science **5**, 044401 (2023).

- Ethan R. Elliott, David C. Aveline, Nicholas P. Bigelow, Patrick Boegel, Sofia Botsi, Eric Charron, José P. D'Incao, Peter Engels, Timothé Estrampes, Naceur Gaaloul, James R. Kellogg, James M. Kohel, Norman E. Lay, Nathan Lundblad, Matthias Meister, Maren E. Mossman, Gabriel Müller, Holger Müller, Kamal Oudrhiri, Leah E. Phillips, **Annie Pichery**, Ernst M. Rasel, Charles A. Sackett, Matteo Sbroscia, Wolfgang P. Schleich, Robert J. Thompson, and Jason R. Williams, "Quantum Gas Mixtures and Dual-Species Atom Interferometry in Space", *Nature*, **623**, 502-508 (2023).

- Jason R. Williams, Charles A. Sackett, Holger Ahlers, David C. Aveline, Patrick Boegel, Sofia Botsi, Eric Charron, Ethan R. Elliott, Naceur Gaaloul, Enno Giese, Waldemar Herr, James M. Kohel, Matthias Meister, Gabriel Müller, Holger Müller, Kamal Oudrhiri, Leah Phillips, **Annie Pichery**, Ernst M. Rasel, Albert Roura, Matteo Sbroscia, Wolfgang P. Schleich, Christian Schneider, Christian Schubert, Bejoy Sen, Robert J. Thompson, and Nicholas P. Bigelow, "Interferometry of Atomic Matter-Waves in a Cold Atom Lab onboard the International Space Station", arXiv:2402.14685 (2024).